

CHARACTERISTICS OF THE HIGH SPEED GAS-LIQUID INTERFACE

Christopher Jude Weiland

Dissertation submitted to the faculty of the Virginia Polytechnic Institute and State University in
partial fulfillment of the requirements for the degree of

Doctor of Philosophy
In
Mechanical Engineering

Pavlos P. Vlachos, Committee Chair
Jon J. Yagla, Member
Eugene F. Brown, Member
Demetri P. Telionis, Member
Andrew T. Duggleby, Member

12.02.2009
Blacksburg, Virginia

Keywords: Submerged Round Gas Jet, Submerged Rectangular Gas Jet, Water Piercing Missile
Launcher, Supercavitation

Copyright 2010, Christopher J. Weiland

CHARACTERISTICS OF THE HIGH SPEED GAS-LIQUID INTERFACE

Christopher Jude Weiland

ABSTRACT

The objective of this dissertation was to investigate physical characteristics of high speed gas-liquid interfaces for the cases of subsonic, transonic, and supersonic gas jets submerged underwater and the transient development of an underwater projectile reaching the supercavitating state. These studies are motivated by the need to understand the basic physics associated with a novel submersible missile launcher termed the Water Piercing Missile Launcher (WPML).

This dissertation presents the first study of high speed round and rectangular gas jets submerged underwater utilizing a global optical measurement technique. This technique allows quantitative measurement of the entire gas jet and the interfacial motion. Experimental results indicate that the penetration of the gas jets into a quiescent liquid is strongly influenced by the injection mass flow and the nozzle geometry. In contrast, the oscillations of the interface are influenced by the injection Mach number. The transition from a momentum driven to a buoyant jet is determined using a characteristic length scale that appears to be in good agreement with experimental observations. Moreover, the unsteadiness of the interface appears to be governed by both Kelvin-Helmholtz and Rayleigh-Taylor instabilities.

This dissertation also contains the first study of a projectile accelerating to reach the supercavitating state. Experimental results show that the transient development of the supercavity is governed by the formation of a vortex ring. Nuclei are shed from the forebody of the accelerating projectile and are entrained in the vortex ring core where they are subjected to low pressure and subsequently expand rapidly. A characteristic time scale for this supercavity development is presented.

This dissertation is dedicated to my family.

ACKNOWLEDGEMENTS

There are numerous people who have contributed to the successful completion of this PhD program. First, Dr. Pavlos Vlachos deserves recognition as my advisor. Dr. Vlachos has taught me what it means to be a successful academic and I like to think that I have absorbed some of these qualities. Because of him I plan to pursue an academic position. Dr. Vlachos was the one who convinced me to begin graduate studies and I truly thank him for giving me this opportunity.

I thank my dissertation committee for agreeing to help guide this research. The committee was composed of Dr. Jon Yagla, Dr. Eugene Brown, Dr. Demetri Telionis, and Dr. Andrew Duggleby. Dr. Sunghwan Jung served as a proxy for Dr. Duggleby on short notice and I sincerely appreciate this!

Dr. Jon Yagla deserves significant recognition as my first mentor while I worked at the Naval Surface Warfare Center, Dahlgren Division. He has shaped this engineer's mind and philosophy of science more than he probably knows and served as a role model for success in both work and life.

I thank the Naval Surface Warfare Center, Dahlgren Division for sponsoring this research. The two technical monitors for this work were Mr. John Busic and Dr. Jon Yagla. I appreciate their support of this work.

Throughout this effort I have sacrificed much of my personal time and my family has had to endure the result of this. To them, I sincerely appreciate your support and love.

My friends and lab mates have helped me in so many ways. Kelley Stewart, Dave Hubble, Alicia Williams, Dave Griffiths, Andy Gifford, Mike Brady, Satya Karri, John Charonko, Adric Eckstein, Ali Etebari, Nick Cardwell...the list could go on. I sincerely enjoyed our time at Virginia Tech together. I hope I have been able to help you as much as you have helped me.

ATTRIBUTION

This dissertation is composed of an introduction, conclusion, and four Chapters. These four Chapters are written in journal format as all will be submitted to archival journals for publication. The following individuals serve as co-authors on one or more Chapters.

Dr. Pavlos P. Vlachos – Ph.D. (Department of Engineering Sciences and Mechanics, Virginia Tech) is the committee chair and has provided advice on the works presented herein. Dr. Vlachos took the original images presented in Chapter 5 during Post-Doctoral research at Virginia Tech which were subsequently analyzed by the author.

Dr. Jon J. Yagla – Ph.D. (Aerospace Engineering and Engineering Science, Arizona State University) is a committee member and inventor of the Water Piercing Missile Launcher. He provided considerable insight on the topics presented in Chapter 2. Dr. Yagla is a co-author of Chapter 2.

TABLE OF CONTENTS

Abstract.....	ii
Acknowledgements.....	iv
Attribution.....	v
List of Figures.....	ix
List of Tables.....	xviii
1. Introduction.....	1
1.1 Background and Motivation.....	1
1.2 Objective and Structure of Dissertation.....	3
1.3 Statement of Originality.....	5
1.4 References.....	6
2. Concept Analysis and Laboratory Observations on a Water Piercing Missile Launcher.....	8
2.1 Abstract.....	8
2.2 Nomenclature.....	9
2.3 Introduction.....	9
2.4 Experimental Methods and Modeling.....	14
2.5 Results.....	22
2.6 Conclusions.....	24
2.7 Acknowledgements.....	24
2.8 References.....	24
3. The Penetration of Submerged Round Turbulent Gas Jets in Water.....	26
3.1 Abstract.....	26
3.2 Nomenclature.....	27
3.3 Introduction.....	27
3.4 Experimental Methods.....	30
3.4.1 Operation and Instrumentation Measurements Details.....	32
3.4.2 Photographic Measurements and Edge Detection.....	34
3.5 Results and Discussion.....	35
3.5.1 Analysis of Jet Pinch-Off Location.....	35
3.5.2 Jet Penetration Distance.....	41
3.5.3 Unsteady Interface Characteristics.....	47
3.5.4 Kelvin-Helmholtz versus Rayleigh-Taylor Instabilities.....	51
3.6 Conclusions.....	52
3.7 Acknowledgements.....	53

3.8	References	54
4.	The Effect of Mach Number and Aspect Ratio on the Interfacial Characteristics of a Submerged Rectangular Gas Jet	56
4.1	Abstract	56
4.2	Nomenclature	57
4.3	Introduction	57
4.4	Experimental Methods and Facilities	60
4.4.1	Operation and Instrumentation Measurements Details.....	64
4.4.2	Photographic Measurements and Edge Detection	65
4.5	Results and Discussion.....	66
4.5.1	Analysis of the Jet Pinch-Off	66
4.5.2	Jet Penetration Distance	69
4.5.3	Unsteady Interfacial Characteristics	76
4.6	Conclusions	79
4.7	Acknowledgements	81
4.8	References	81
5.	Time-Scale for Critical Growth of Partial and Supercavitation Development Over Impulsively Translating Projectiles.....	83
5.1	Abstract	83
5.2	Nomenclature	84
5.3	Introduction	85
5.4	Experimental Methods and Processing Techniques	88
5.4.1	Image Processing Techniques	90
5.4.2	Projectile Trajectory and Cavity Shape Analysis Methods.....	91
5.4.3	Determination of Supercavity Growth Time Scales	94
5.5	Non-Dimensional Time Scale	96
5.6	Results and Discussion.....	97
5.6.1	The Archetypal Cavity Formation Process	97
5.6.2	The Gas Leakage Effect.....	101
5.6.3	Critical Time Scale for Partial and Supercavity Formation	103
5.7	On the Similarity Between the Formation Number for Vortex Rings and the CGTS ..	109
5.8	Conclusions	111
5.9	References	112
6.	Conclusions.....	114
6.1	Is the WPML Feasible?	114

6.2	How Do Submerged Gas Jets Behave?	115
6.3	WPML Failure – What Happens to Missile?	115
6.4	Future Work.....	116
7.	Appendix A: Image Collection, Processing, and Image Analysis Details	118
7.1	Introduction	118
7.2	Photographic Measurement Details	118
7.3	Edge Detection Algorithm.....	120
7.3.1	Image Digitization	121
7.3.2	Median Filter.....	122
7.3.3	Image Fill	123
7.3.4	Morphological Functions	124
7.3.5	Edge Detection.....	125
7.4	Image Analysis Steps	127
7.4.1	Determination of the Jet Pinch-Off Location.....	128
7.4.2	Computation of the Jet Penetration Distance.....	131
7.5	Edge Detection Code.....	138
7.5.1	MATLAB Code: Write Detected Edges From Raw Images to .txt Files	138
7.5.2	MATLAB Code: Linearize Detected Edges for Data Analysis	141
7.6	References	144
8.	Appendix B: Jet Penetration Data.....	150
8.1	Introduction	150
8.2	Round Jets	151
8.3	Rectangular Jets – Aspect Ratio 2	157
8.4	Rectangular Jets – Aspect Ratio 10.....	164
8.5	Rectangular Jets – Aspect Ratio 20.....	171

LIST OF FIGURES

Figure 1.1. The WPML is composed of two concentric cylinders. Rocket motor exhaust is directed along the missile line of fire which forms a gas jet underwater (A). The missile travels through this exhaust jet, presumably never contacting water (B). The missile exits the water and transitions to external flight (C).....	2
Figure 1.2. The WPML feasibility study process is divided into three sections. Each section is explored in greater detail in one of four chapters of this dissertation.....	4
Figure 2.1. The WPML geometry.	11
Figure 2.2. Missile launch from WPML at shallow depth.....	12
Figure 2.3. Time-averaged interface position of gas jets at both subsonic and supersonic velocities in a 0.3 (left) and 0.7 (right) m/s cross flow. The supersonic gas jets are much less susceptible to cross flow.	13
Figure 2.4. The high speed gas jet is classified into the near, transition, and far regions. Even in the presence of cross flow the jet is mostly columnar and upright in the near region, after which the transition region shows characteristics of both jet and plume behavior. In the far region the jet is dominated by the cross flow and aligns itself with the cross flow direction.	16
Figure 2.5. The jet tip trajectories from several scale tests (Yagla et al, 2006) were reduced using the nondimensional variables given by Equations 1.5 and 1.6. The jet tip trajectory follows a power law relationship.....	17
Figure 2.6. Curvature of gas jet due to cross flow. Near the submarine hull the gas jet is straight and columnar but due to the action of cross flow the gas jet will curve so as to align itself with the cross flow.	18
Figure 2.7. Reduction of experimental data yields values of the C_l coefficient for submerged gas jets in water. The coefficient varies in value up until about 5 diameters, which is consistent for the development length of a submerged gas jet in water.	20
Figure 2.8. A generic burn curve used to simulate the thrusting force which drives missile flight. This curve was artificially created to simulate the appropriate sized thrust for a missile of this class.....	22
Figure 2.9. Jet deflection under several cross flow velocities. The artillery missile jet characteristics were used to compute the steady-state windward position of the gas jet. The dotted vertical line represents the leading edge radius of the launcher. Impingement of the jet on the radius of the launcher defines the maximum launch depth.....	23
Figure 2.10. The operational envelope of a large artillery missile is affected by the launch depth and cross flow velocity. The optimal (left) and maximum (right) launch conditions are shown.	24

Figure 3.1. View of the acrylic tank and the injector. The flow pressure was monitored at several points inside the base and at the nozzle throat and exit. Perforated sheets helped to maintain a uniform surface by breaking any large scale surface motions. The injector was flush-mounted to the bottom of the acrylic tank. 32

Figure 3.2. Schematic of the instrumentation and control system. Gas flow is started and stopped using a fast acting pneumatic valve controlled by LabVIEW software, which also triggers all instrumentation. 33

Figure 3.3. Steps used to detect the jet boundary. The process neglects outliers such as bubbles torn from the interface to accurately track the phase boundary. The horizontal scale bar represents 0.0254m. 35

Figure 3.4. The images show the process of jet pinch-off in a 0.8 Mach jet. The first image is shown 1292ms after the gas jet was begun and subsequent images are shown at 1ms intervals. 36

Figure 3.5. The interface position in time is shown at 10 diameters downstream from the nozzle exit. This information was computed for each test run at each downstream pixel location. 37

Figure 3.6. Graph of the average pinch-off location for all Mach numbers. Three trials for each Mach number were averaged to obtain these curves. The Mach 1.8 jet did not pinch-off. All of the jets consistently reached a maximum number of pinch-offs at $10 < y/L_0 < 15$ 38

Figure 3.7. The cumulative time fraction of stable jetting behavior is plotted against the time between successive pinch-offs. The time between successive pinch-off events is indicative of the pinch-off frequency. The inset picture is a zoomed in portion to show greater detail. 40

Figure 3.8. Although it was shown that the jets pinch-off at several frequencies, the jet pinch-off frequency shown here is the largest contributor to the pinch-off phenomenon. The jet pinch-off frequency for Mach 1.8 is 0 Hz as the jet never pinched off. 41

Figure 3.9. Gas holdup contours for a Mach 0.4 jet (left) and Mach 0.9 jet (right). The gas holdup is a statistical mapping of how far gas penetrates into the surrounding water. The transonic gas jet penetrates further into the quiescent fluid statistically than the subsonic gas jet. 42

Figure 3.10. The jet penetration distance is calculated using only the jet attached to the orifice (circle) and including bubbles advected downstream (square). The Mach 0.4 jet did not maintain a permanent penetration distance 98.5% of the measurement time and the Mach 1.8 jet never pinched off (penetration length of at least $85 y/L_0$). 46

Figure 3.11. A comparison of methods to delineate bubbling and jetting. The left plot shows the pinch-off time fraction against the jet penetration length defined in this paper. The right plot shows the pinch-off time fraction against the average interface position. 47

Figure 3.12. In general, the interface unsteadiness increases downstream and decreases for higher Mach numbers. The average deviation calculation was only performed on locations which were not pinched-off for 80% of the total recorded time. 48

Figure 3.13. The spatial growth rate decreases with increasing Mach number. The growth rate is a nondimensional scale representing the rate of interface unsteadiness downstream and is given by the slope of the best fit line passing through the AD points. 50

Figure 3.14. The submerged gas jet exhibits a high oscillatory motion as a function of Mach number. The relative importance of the two instabilities associated with the gas jet is dependent on both Mach number and axial position, but these results indicate that the RT is just as important as KH in governing the interfacial stability. 52

Figure 4.1 View of the injector inside the acrylic tank. Perforated sheets helped to control surface disturbances. A steel angle bracket was bolted to the injector to secure it upright. 62

Figure 4.2 The injector is composed of three pieces, the two outer aluminum side plates and the nozzle insert. Picture on left shows outer aluminum piece while the right picture shows the subsonic/sonic aspect ratio 2 nozzle insert. 63

Figure 4.3. Schematic of the instrumentation and control system. Gas flow was started and stopped using a fast acting pneumatic valve controlled by LabVIEW software, which also triggered all instrumentation. 64

Figure 4.4. Steps used to detect the jet boundary. The process neglects outliers such as bubbles torn from the interface to accurately track the phase boundary. 66

Figure 4.5 The number of pinch-off events observed for each Mach number and aspect ratio. The number of pinch-off events was normalized by the total observation distance divided by the width of the nozzle. 67

Figure 4.6. Spatial distribution of pinch-off events for AR 10. For all Mach numbers except Mach 1.5 the jets have a maximum in pinch-off events at $y/L_Q \approx 3-5$. The Mach 1.5 jet did not pinch-off. 68

Figure 4.7. The axial position having the most pinch-off events is dependent on the aspect ratio of the nozzle. Tests for nozzles AR 10 Mach 1.5 and AR 20 Mach numbers 1.3 and 1.5 showed no pinch-off events over the measured domain. 69

Figure 4.8. Gas holdup contours for a AR 2 Mach 0.4 jet (left) and Mach 1.0 jet (right). The sonic gas jet penetrates further into the quiescent fluid statistically than the subsonic gas jet. 71

Figure 4.9. The jet penetration distance increases with increasing aspect ratio and Mach number. The unconnected data points correspond to cases in which the jet penetration distance was greater than the field of view; the jet penetrated at least this distance. 72

Figure 4.10. The jet penetration distance increases with mass flow according to a power law relationship.....	73
Figure 4.11. On left and right the jet penetration distance is scaled by L_Q and the square root of the nozzle area, respectively. The latter term appears to collapse the data more effectively.	74
Figure 4.12. The average jet spreading angle is a function of both aspect ratio and Mach number. Generally, the spreading angle is greater for supersonic flows and higher AR nozzles.	75
Figure 4.13. Average deviation of interface for AR 2 nozzle.	77
Figure 4.14. Average deviation of interface for AR 10 nozzle.	77
Figure 4.15. Average deviation of interface for AR 20 nozzle.	78
Figure 4.16. Spatial growth rate for all aspect ratio nozzles. The growth rate is a nondimensional scale representing the rate of interface unsteadiness downstream and is given by the slope of the best fit line passing through the AD points.	79
Figure 5.1: Experimental setup and sequence of events during projectile egress (left to right) showing the acceleration of the body in the water. Note that the charge gases leak into the quiescent water after the aft end of the projectile has cleared the barrel.	89
Figure 5.2. Image processing procedure (left to right) of a typical image is composed of several steps: 1) threshold and digitized image, 2) median filtering, and 3) final edge detection with estimated projectile location. Barrel is located at coordinates (0,0).	91
Figure 5.3: Projectile and cavity tip vertical positions in time.	92
Figure 5.4: Projectile and cavity normalized velocities in time. Time=0 corresponds to egress of projectile tip from barrel.	93
Figure 5.5: Ratio of projectile cavity area to projected projectile area as a function of time. Time=0 corresponds to egress of projectile tip from barrel.	94
Figure 5.6: Change Point Analysis of Figure 5.5 showing the computed location of the CGTS.	96
Figure 5.7. Plot of area ratios for all tested projectiles against the formation time. Inset picture shows zoomed-in detail. Note the clear division between two regimes which seems to occur near a formation time of 3.	98
Figure 5.8. Supercavity development over aspect ratio 5 blunt projectile with maximum speed of 24 m/s ($\sigma=0.33$). The images are shown at 0.24 ms intervals. Growing cavity is denoted by arrows. Note the forebody of the projectile is covered by small bubbles in images A-I. The formation time (CGTS) of the test case was computed to be about 4.3.	100

Figure 5.9. Cavity development for projectile of aspect ratio of $L_P/D_P=2.5$ and $\sigma=0.18$ shown at $\Delta t=0.24\text{ms}$. Initial cavity is shown by arrow. Note the forebody of the projectile is covered by bubbles in images A and B.....	101
Figure 5.10. Supercavity development over projectile ($L_P/D_P=2.5$ $\sigma=0.25$) and corresponding cavity development shown at 1.6 ms intervals. Note that the cavity extends from the projectile forebody to the barrel in images B-D.	102
Figure 5.11. Supercavity development over projectile of $L_P/D_P=5$ and $\sigma=0.34$ shown at 1.6 ms intervals. Initial cavities are clearly seen in images A-C, which interact with barrel gases in image D (arrow).....	103
Figure 5.12. The critical time of the supercavity development process over the range of parameters tested.....	104
Figure 5.13. Predicted pressures which can drive the CGTS. Circles represent archetypal development cases and diamonds represent gas leakage cases.	107
Figure 5.14. The maximum recirculation time scale computed from the digital images. In all cases the actual CGTS was greater than would be expected if the re-entrant jet were responsible for rapid cavity growth.....	108
Figure 5.15. Theoretical values for the CGTS as a function of the running mean velocity. The experimental data is shown as either confirmed gas leakage or archetypal formation processes.	110
Figure 6.1. The WPML feasibility study process is divided into three sections. Each section is explored in greater detail in one of four chapters of this dissertation.....	114
Figure 7.1. A schematic of the shadowphotography system is shown on the left and consists of a high-speed camera, a distributed light source, and a light diffuser (white sheet). On right is shown the actual test layout.	119
Figure 7.2. Recorded shadowgraph images for a Mach 0.8 round jet at several instances in time. Note the clear distinction of the phase interface.	120
Figure 7.3. Various thresholds applied to the original image result in a varying level of information being filtered. The horizontal scale bar represents 0.0254m.	122
Figure 7.4. The median filter is used to smooth irregularities in the binary image. Only small median sizes are used to prevent filtering of actual interface data.	123
Figure 7.5. The digitization and other filtering operations can yield holes, or regions within the known gas jet identified as liquid. These regions are automatically identified and filled.	124

Figure 7.6. The morphological disk element is traversed around the image to filter small detached bubbles.....	125
Figure 7.7. The final step consists of edge detection where the perimeter of the orifice-attached jet is determined. This perimeter is overlaid with the original image to show the degree of accuracy in determining the perimeter.....	126
Figure 7.8. Steps used to detect the jet boundary. The process neglects outliers such as bubbles torn from the interface to accurately track the phase boundary. The horizontal scale bar represents 2.54 cm.....	127
Figure 7.9. The computed jet interface positions are linearized and separated into left and right sides, denoted by the symbol color. Only the orifice attached jet is retained for study.....	129
Figure 7.10. The minimum location where the gas jet became discontinuous is shown as a black dot. The x axis corresponds to axial position and the y axis corresponds to time. The slope of the black dots is the velocity of the pinch-off location.....	130
Figure 7.11. The axial position corresponding to the orifice attached jet position was recorded and summed for all times.....	131
Figure 7.12. First three time steps of jet penetration determination, which is computed by binary image addition. The left images only add orifice attached jets together and all pinched-off bubbles are neglected in the image addition. In the right images no portion of the gas jet is neglected in the image addition.....	133
Figure 7.13. Last three time steps of jet penetration determination, which is computed by binary image addition. The left images only add orifice attached jets together and all pinched-off bubbles are neglected in the image addition. In the right images no portion of the gas jet is neglected in the image addition.....	134
Figure 7.14. A comparison of probe (left) and optical (right) techniques for judging the presence of gas at a simultaneous point in space.....	136
Figure 7.15. Unprocessed images are shown at 4 ms intervals. The red circle denotes the position of the probe. The gas jet tends to pinch off which is the source of the erroneous probe based measurements.....	137
Figure 7.16. Simulated probe response (left) and the optical response (right) for the images shown in Figure 7.15.....	138
Figure 8.1. Mach 0.4 jet penetration trials: orifice attached jets only.....	151
Figure 8.2. Mach 0.4 jet penetration trials: entire jet.....	151
Figure 8.3 Mach 0.6 jet penetration trials: orifice attached jets only.....	152

Figure 8.4. Mach 0.6 jet penetration trials: entire jet.....	152
Figure 8.5. Mach 0.8 jet penetration trials: orifice attached jets only.....	153
Figure 8.6. Mach 0.8 jet penetration trials: entire jet.....	153
Figure 8.7. Mach 0.9 jet penetration trials: orifice attached jets only.....	154
Figure 8.8. Mach 0.9 jet penetration trials: entire jet.....	154
Figure 8.9. Mach 1.1 jet penetration trials: orifice attached jets only.....	155
Figure 8.10. Mach 1.1 jet penetration trials: entire jet.....	155
Figure 8.11. Mach 1.8 jet penetration trials: orifice attached jets only.....	156
Figure 8.12. Mach 1.8 jet penetration trials: entire jet.....	156
Figure 8.13. Mach 0.5 jet penetration trials: orifice attached jets only.....	157
Figure 8.14. Mach 0.5 jet penetration trials: entire jet.....	157
Figure 8.15 Mach 0.6 jet penetration trials: orifice attached jets only.....	158
Figure 8.16. Mach 0.6 jet penetration trials: entire jet.....	158
Figure 8.17. Mach 0.8 jet penetration trials: orifice attached jets only.....	159
Figure 8.18. Mach 0.8 jet penetration trials: entire jet.....	159
Figure 8.19. Mach 1.0 jet penetration trials: orifice attached jets only.....	160
Figure 8.20. Mach 1.0 jet penetration trials: entire jet.....	160
Figure 8.21. Mach 1.1 jet penetration trials: orifice attached jets only.....	161
Figure 8.22. Mach 1.1 jet penetration trials: entire jet.....	161
Figure 8.23. Mach 1.3 jet penetration trials: orifice attached jets only.....	162
Figure 8.24. Mach 1.3 jet penetration trials: entire jet.....	162
Figure 8.25. Mach 1.5 jet penetration trials: orifice attached jets only.....	163
Figure 8.26. Mach 1.5 jet penetration trials: entire jet.....	163

Figure 8.27. Mach 0.5 jet penetration trials: orifice attached jets only.....	164
Figure 8.28. Mach 0.5 jet penetration trials: entire jet.....	164
Figure 8.29 Mach 0.6 jet penetration trials: orifice attached jets only.....	165
Figure 8.30. Mach 0.6 jet penetration trials: entire jet.....	165
Figure 8.31. Mach 0.8 jet penetration trials: orifice attached jets only.....	166
Figure 8.32. Mach 0.8 jet penetration trials: entire jet.....	166
Figure 8.33. Mach 1.0 jet penetration trials: orifice attached jets only.....	167
Figure 8.34. Mach 1.0 jet penetration trials: entire jet.....	167
Figure 8.35. Mach 1.1 jet penetration trials: orifice attached jets only.....	168
Figure 8.36. Mach 1.1 jet penetration trials: entire jet.....	168
Figure 8.37. Mach 1.3 jet penetration trials: orifice attached jets only.....	169
Figure 8.38. Mach 1.3 jet penetration trials: entire jet.....	169
Figure 8.39. Mach 1.5 jet penetration trials: orifice attached jets only.....	170
Figure 8.40. Mach 1.5 jet penetration trials: entire jet.....	170
Figure 8.41. Mach 0.5 jet penetration trials: orifice attached jets only.....	171
Figure 8.42. Mach 0.5 jet penetration trials: entire jet.....	171
Figure 8.43 Mach 0.6 jet penetration trials: orifice attached jets only.....	172
Figure 8.44. Mach 0.6 jet penetration trials: entire jet.....	172
Figure 8.45. Mach 0.8 jet penetration trials: orifice attached jets only.....	173
Figure 8.46. Mach 0.8 jet penetration trials: entire jet.....	173
Figure 8.47. Mach 1.0 jet penetration trials: orifice attached jets only.....	174
Figure 8.48. Mach 1.0 jet penetration trials: entire jet.....	174
Figure 8.49. Mach 1.1 jet penetration trials: orifice attached jets only.....	175

Figure 8.50. Mach 1.1 jet penetration trials: entire jet.....	175
Figure 8.51. Mach 1.3 jet penetration trials: orifice attached jets only.....	176
Figure 8.52. Mach 1.3 jet penetration trials: entire jet.....	176
Figure 8.53. Mach 1.5 jet penetration trials: orifice attached jets only.....	177
Figure 8.54. Mach 1.5 jet penetration trials: entire jet.....	177

LIST OF TABLES

Table 3.1. Test matrix for all Mach numbers tested. All jets were shot at 0.46m water depth and the properties shown here were calculated for the nozzle exit.	31
Table 4.1. Test matrix for all Mach numbers tested. All jets were shot at 0.46m water depth and the properties shown here were calculated for the nozzle exit.	61
Table 5.1: Experimental test matrix.	90

1. INTRODUCTION

1.1 Background and Motivation

The study of high speed fluid flowing from an orifice into quiescent fluid, defined as a jet, is a classic subject in fluid mechanics. Helmholtz (1868), Kelvin (1871), and Rayleigh (1879) were among the first who studied this problem. Although the literature contains a large body of works on single phase jets [(Dimotakis et al. 1983); (Wang and Law 2002)] such as a water jet in a water environment, there is relatively little work on the behavior of submerged gas jets in water. Here the term ‘behavior’ is used broadly encompassing gas jet characteristics such as the unsteady motion of the gas-liquid interface and how far the gas jet penetrates into the liquid bath. Past studies of submerged gas jets have identified a transition in jet behavior which occurs at a gas injection speed of Mach 1 [(McNallan and King 1982); (Mori et al. 1982)]. At injection speeds lower than Mach 1 the gas jet enters a flow regime characterized by rapid jet breakup into bubbles. This flow regime is termed bubbling [(Sahai and Guthrie 1982); (Ruzicka et al. 1997)]. At Mach 1 a steady jetting regime is maintained. The effect of increased injection Mach numbers past this point is unknown. Additionally, there have been no studies of the effect of exit geometry on the gas jet characteristics. Loth and Faeth (1990) studied submerged planar gas jets exhausted at Mach 1, but no studies of rectangular jets have been attempted. In past experimental studies of submerged gas jets researchers have used point measurement techniques, such as pitot [(Loth and Faeth 1989); (Loth and Faeth 1990)] or electroresistivity [(Castillejos and Brimacombe 1987); (Ito et al. 1991); (Sano et al. 1986)] probes to study the submerged gas jet behavior. These probe measurement techniques are both intrusive and incomplete, as the only instantaneous information which may be gathered is at one point in space. The probe techniques require one to average in time the jet behavior, and do not yield any global instantaneous measurements.

The high speed gas-liquid interface encountered in submerged gas jets is also found in the wholly different phenomenon of supercavitation [(Plesset and Prosperetti 1977); (Matveev 2003)]. Supercavitation implies large scale cavitation where the gas envelop is long enough to cover a translating body underwater. The translating body must move at great speed to create the supercavity which, with the exception of the forebody, is completely covered in gas. There are,

however, no studies known to the author which study the development of the supercavity as an underwater body accelerates from rest to a speed which permits supercavitation.

A unique application of a high speed submerged gas jet is the Water Piercing Missile Launcher (WPML). The WPML is a new submersible missile launcher platform currently under development by the United States Navy for use in submarines [(Yagla et al. 2004; Weiland et al. 2005); (Yagla et al. 2006); (Yagla et al. 2008)]. The WPML geometry and the launch of a missile using WPML technology is shown schematically in Figure 1.1. The WPML is composed of two concentric cylinders and is capped with a hemisphere. The basic premise of the launcher is to provide a dry path for missile travel while underwater. When a missile is launched underwater, motor exhaust gases are directed along the line of fire where they form a high speed gas jet which leads the missile (Figure 1.1A). The missile travels through this exhaust jet (Figure 1.1B) and does not contact water. Last the missile exits the free surface (Figure 1.1C).

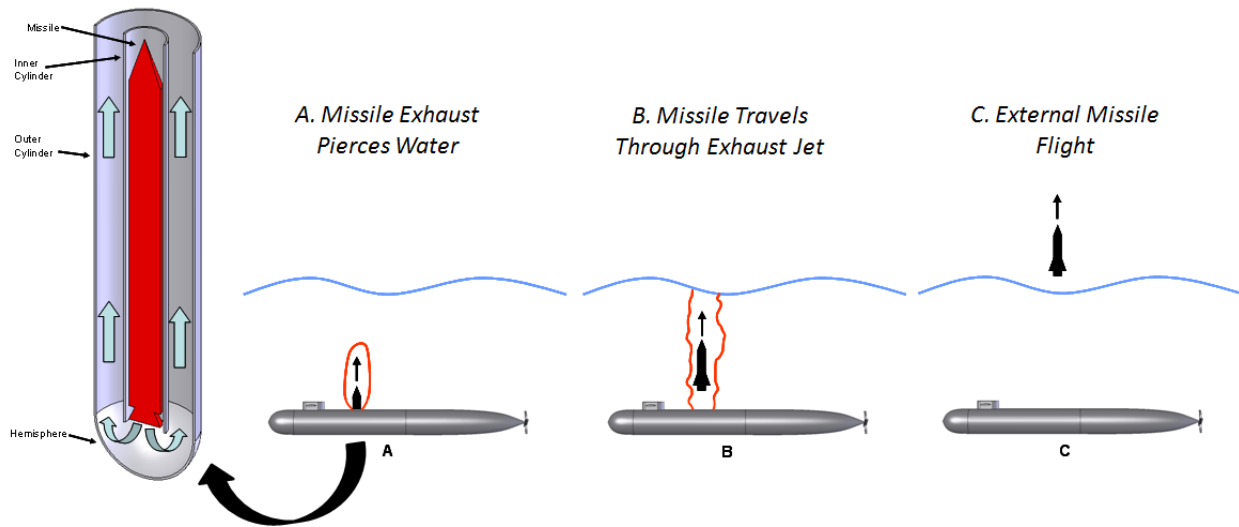


Figure 1.1. The WPML is composed of two concentric cylinders. Rocket motor exhaust is directed along the missile line of fire which forms a gas jet underwater (A). The missile travels through this exhaust jet, presumably never contacting water (B). The missile exits the water and transitions to external flight (C).

In contrast to the current missile launcher technology the WPML has several differences namely 1) the method in which the missile is ejected from the launcher and 2) the environment in which the missile travels from the launcher to the free surface. Past launchers utilized an additional device (gas generator, compressed gas, etc) to blow the missile out of the launcher. This is termed a cold launch. The WPML requires the missile to exit the launcher under its own thrust from inside the submarine hull which is termed a hot launch. The WPML uses the rocket

exhaust gases to create a high speed underwater jet which forms a dry environment for missile flight while underwater. Because the underwater flight environment is dry, non-marinated weapons could potentially be launched as they remain dry throughout their flight path. To the author's knowledge such a missile launcher has never been fielded before.

There are three basic questions which must be answered if the WPML is to deserve consideration as a launcher technology. These questions are:

1. Is it possible to maintain a stable jet column and what are the optimal gas jet properties?
2. Given that all buoyant gas jets will eventually transition into a plume, what is the maximum jet length we can expect a stable jet column?
3. What happens to the missile if the WPML gas jet fails near the launcher exit?

All of these questions stem from a lack of knowledge about the high speed gas-liquid interface. This dissertation represents the first step in understanding the physics which govern the high speed gas-liquid interface.

1.2 Objective and Structure of Dissertation

The objective of this dissertation is to provide an understanding of the basic characteristics of the high speed gas-liquid interface utilizing an optical measurement technique to record global instantaneous measurements. Specifically two examples of these flows are studied: a submerged high speed gas jet and a projectile accelerating to reach the supercavitating state.

The implications of these interfacial characteristics on the WPML are also explored. Thus the dissertation is a mixture of basic and applied science. The dissertation is divided into three sections which, in addition to increasing the understanding of basic science, are meant to provide some answers with regards to the questions posed in the previous section and are shown in Figure 1.2.

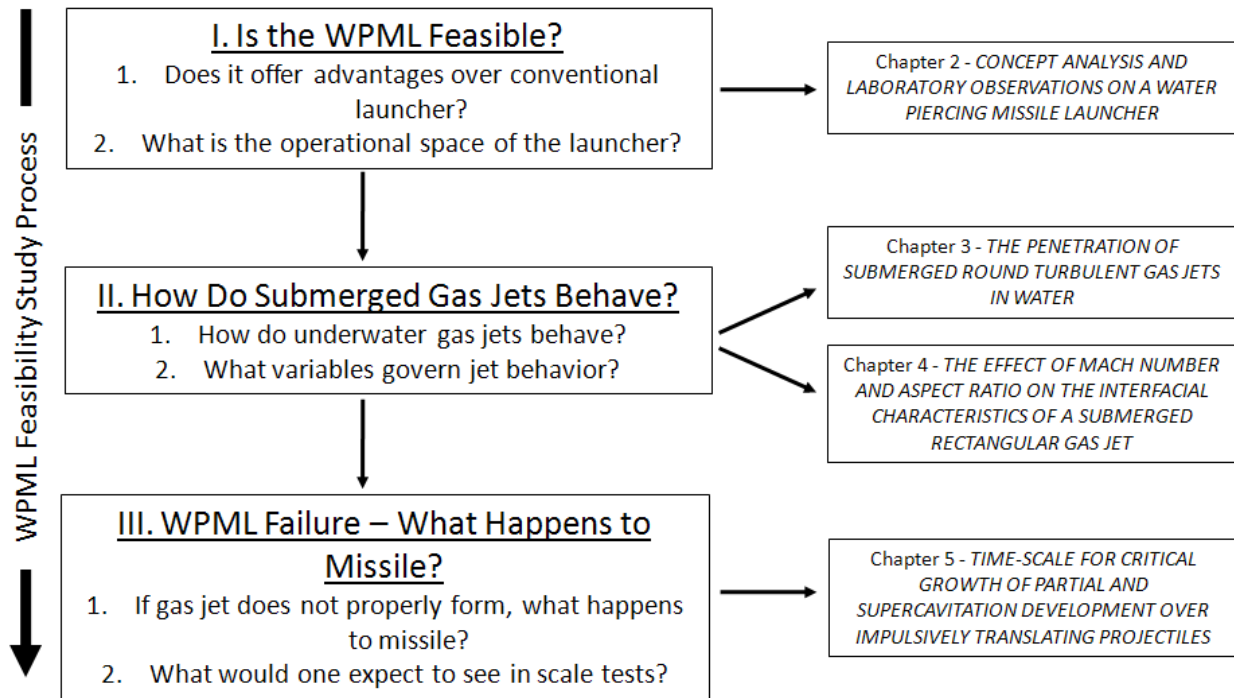


Figure 1.2. The WPML feasibility study process is divided into three sections. Each section is explored in greater detail in one of four chapters of this dissertation.

Section I answers the most basic question, specifically if the WPML concept is valid. In particular, the two questions which are addressed are: 1) if the WPML offers any advantages over the conventional launching technology and 2) what the operational space of such a launcher is expected to be. Section I is addressed in Chapter 2 and is an engineering analysis of the WMPL.

Section II studies the basic physics of the submerged high speed gas jet. An optical measurement technique, as opposed to probe measurement techniques, provides quantitative information about the global characteristics of high speed submerged gas jets. Both geometry and Mach number effects are explored by varying the nozzle geometry from circular to rectangular and varying the injection Mach number from subsonic to supersonic. In the case of rectangular gas injection the nozzle aspect ratio was also studied. The results are divided into Chapter 3, which presents the results for a round nozzle and Chapter 4, which presents the results for rectangular nozzles.

Section III studies the transient development of a supercavity over an accelerating underwater body. An optical technique similar to that employed in Chapters 2 and 3 is used to study the projectile motion and the cavity development. The results of this study have implications as the scenario of gas jet failure during a WPML launch. Such a failure could be

due to the gas jet being imperfectly formed due to some technical malfunction or perhaps the weapon was fired outside of its operational envelope. In this scenario the normal WPML operation as shown in Figure 1.1 does not occur. Chapter 6 summarizes the important findings from this dissertation.

The individual chapters are presented in a journal manuscript format as all will be submitted to archival journals for publication. At the time of this writing Chapter 2 is presently under review in the Journal of Ocean Engineering. Chapters 3 and 4 will be submitted to the International Journal of Multiphase Flow or another journal of similar quality. Chapter 5 will be submitted to Experiments in Fluids or another journal of similar caliber.

1.3 Statement of Originality

Since at the time of this writing the WPML is a relatively new concept, and little quantitative work on the submerged behavior of high speed gas jets has been presented in the literature, this dissertation contains many original scholarly contributions to both basic fluid mechanics and the WPML concept. A brief review of these contributions follows.

- In Chapter 2, originality is claimed for the computation and analysis of the WPML operational envelope. The submerged interface data was generously provided by Dr. Jon Yagla of the Naval Surface Warfare Center, Dahlgren Division.
- In Chapters 3 and 4, originality is claimed for the whole field measurements and subsequent analysis of the submerged round and rectangular gas jets. In particular, there have been no studies which analyze the concept of pinch off and jet penetration in a rigorous fashion as is presented in this dissertation. Nor have there been any studies on the unsteady motion of the interface which divides a submerged gas jet and the ambient fluid.
- In Chapter 3, originality is claimed for the term L_{M^*} which attempts to predict the average jet penetration distance. The term predicts fairly well the average jet penetration distance.
- In Chapter 5, originality is claimed for the time scale of supercavity development over impulsively launched projectiles. A mechanism was introduced to predict this time scale, and data was shown to support this mechanism.

1.4 References

- Castillejos, A. H. and J. K. Brimacombe (1987). "Measurement of Physical Characteristics of Bubbles in Gas-Liquid Plumes .1. an Improved Electroresistivity Probe Technique." Metallurgical Transactions B-Process Metallurgy **18**(4): 649-658.
- Dimotakis, P. E., R. C. Miakelye and D. A. Papantoniou (1983). "Structure and Dynamics of Round Turbulent Jets." Physics of Fluids **26**(11): 3185-3192.
- Helmholtz, H. v. (1868). "On discontinuous movements of fluids." Phil. Mag. **36**(4): 9.
- Ito, K., S. Kobayashi and M. Tokuda (1991). "Mixing Characteristics of a Submerged Jet Measured Using an Isokinetic Sampling Probe." Metallurgical Transactions B-Process Metallurgy **22**(4): 439-445.
- Kelvin, W. (1871). "Hydrokinetic solutions and observations." Phil. Mag. **42**(4): 15.
- Loth, E. and G. M. Faeth (1989). "Structure of Underexpanded Round Air Jets Submerged in Water." International Journal of Multiphase Flow **15**(4): 589-603.
- Loth, E. and G. M. Faeth (1990). "Structure of plane underexpanded air jets into water." AICHE Journal **36**(6): 818-826.
- Matveev, K. I. (2003). "On the Limiting Parameters of Artificial Cavitation." Ocean Engineering **30**(9): 1179-1190.
- McNallan, M. J. and T. B. King (1982). "Fluid-Dynamics of Vertical Submerged Gas Jets in Liquid-Metal Processing Systems." Metallurgical Transactions B-Process Metallurgy **13**(2): 165-173.
- Mori, K., Y. Ozawa and M. Sano (1982). "Characterization of Gas-Jet Behavior at a Submerged Orifice in Liquid-Metal." Transactions of the Iron and Steel Institute of Japan **22**(5): 377-384.
- Plesset, M. S. and A. Prosperetti (1977). "Bubble Dynamics and Cavitation." Annual Reviews in Fluid Mechanics **9**(1): 145-185.
- Rayleigh, J. (1879). "On the instability of jets." Proc. Lond. Math. Soc. **10**: 10.
- Ruzicka, M. C., J. Drahos, J. Zahradnik and N. H. Thomas (1997). "Intermittent transition from bubbling to jetting regime in gas-liquid two phase flows." International Journal of Multiphase Flow **23**(4): 671-682.
- Sahai, Y. and R. I. L. Guthrie (1982). "Hydrodynamics of Gas Stirred Melts .1. Gas-Liquid Coupling." Metallurgical Transactions B-Process Metallurgy **13**(2): 193-202.
- Sano, M., H. Makino, Y. Ozawa and K. Mori (1986). "Behavior of Gas-Jet and Plume in Liquid-Metal." Transactions of the Iron and Steel Institute of Japan **26**(4): 298-304.
- Wang, H. W. and A. W. K. Law (2002). "Second-order integral model for a round turbulent buoyant jet." Journal of Fluid Mechanics **459**: 397-428.
- Weiland, C., P. Vlachos and J. Yagla (2005). A Novel Launcher for Submarine Self-Defense. 4th Biennial National Forum on Weapon System Effectiveness. Austin, TX, AIAA.

- Yagla, J., J. Basic, S. Koski, B. Myruski, C. Weiland and P. Vlachos (2008). Launcher Dynamics Environment of a Water Piercing Missile Launcher. 24th International Symposium on Ballistics. New Orleans, LA, NDIA.
- Yagla, J., K. Deloach and C. Weiland (2004). The Water Piercing Missile Launcher. 21st International Symposium on Ballistics. Adelaide, Australia, NDIA.
- Yagla, J., M. Soifer, K. Deloach, C. Weiland and P. Vlachos (2006). The Water Piercing Missile Launcher. Submarine Technology Symposium. Laurel, MD, The Johns Hopkins University Applied Physics Laboratory.

2. CONCEPT ANALYSIS AND LABORATORY OBSERVATIONS ON A WATER PIERCING MISSILE LAUNCHER

Chris J. Weiland¹ and Pavlos P. Vlachos²
Virginia Tech Mechanical Engineering Dept

Jon J. Yagla³
DTI Associates, Dahlgren, Virginia

¹ Graduate Research Assistant, Virginia Tech Mechanical Engineering Department

² Associate Professor, Virginia Tech Mechanical Engineering Department

³ Consultant to Naval Surface Warfare Center Dahlgren Division

Under Review in the Journal of Ocean Engineering

2.1 Abstract

The Water Piercing Missile Launcher (WPML) is a new concept for launching missiles from submerged platforms such as a submarine. The WPML employs a high speed gas jet, using rocket exhaust as the gas source, to create a dry path underwater through which a missile can pass without contacting water. This paper presents modeling and analysis of the operational characteristics of the WPML in launching a generic artillery missile using available engineering literature. The gas jet is deflected due to cross flow and the gas jet trajectory is computed through a semi-empirical relationship commonly used to describe single phase jet deflection. The jet deflection, which requires an experimentally determined constant to predict jet deflection, is computed using experimental data of a WPML gas jet. Uncoupled simulations of the rocket exhaust jet tip and missile dynamics are shown to demonstrate how such a launcher could be utilized in launching a generic artillery missile. Results indicate that under some conditions it is necessary to restrain the missile in the launcher for some time, dependent on the launch depth, to prevent the missile overtaking the gas jet tip. Since the WPML requires the missile to be launched from inside the submarine hull it is imperative to minimize the restraint time. The results indicate the optimal launch depth, in terms of maximizing the launch depth while minimizing missile restraint time, is 14 m given an 8 m/s submarine speed. The maximum depth at which the launcher can operate with a submarine speed of 4 m/s is 20 m.

Keywords: Water Piercing Missile Launcher, Concentric Canister Launcher, Submerged Gas Jet

2.2 Nomenclature

B – buoyancy flux
 C – experimental constants for jet deflection
 d_{jet} – distance between jet tip and launcher
 D – hydraulic diameter
 D^* – nondimensional distance between jet tip and launcher
 g – gravity
 L_M – momentum length
 L_Q – development length
 M – momentum flux
 Q – volume flux
 t – time
 t^* – nondimensional time
 U – submarine speed/cross flow velocity
 W – gas jet speed at launcher exit
 $WPML$ – water piercing missile launcher
 x – cross flow position from launcher
 z – axial position from launcher
 z_B – ratio of jet buoyancy to cross flow effects
 z_M – ratio of jet to cross flow momentum

2.3 Introduction

For the past several years, the Water Piercing Missile Launcher (WPML) has been studied both conceptually and experimentally as the next generation missile launching platform for submarines [(Yagla et al. 2004); (Yagla et al. 2008)]. Due to its unique design, the WPML is thought to offer several advantages over conventional launchers, such as increased launch depth and increased submarine speed at launch. The primary differences between the WPML and the current launch technology are the method in which the missile is ejected from the launcher and the environment the missile travels in from the launcher to the free surface. While past launchers utilized a gas generator device to blow the missile out of the launcher, and only after the missile left the free surface did the rocket motor ignite, the WPML requires the missile to exit the launcher under its own thrust. The WPML uses the rocket exhaust gases to create a high speed underwater jet which forms a dry environment for missile flight while underwater. An additional advantage of the WPML is that since missiles operate in the gas jet underwater, non-marinated weapons could be launched as they remain dry throughout their flight path.

The WPML utilizes a unique geometry and several forward thinking concepts to combine many attractive features into one launcher, such as an integrated gas management system for each missile tube and a distributed electronic architecture (Yagla 1997). The WPML is a scalable

and modular design that includes all the necessary electronics to launch a missile in a single canister. Electronic commonality between the canisters allows for each submarine to carry many different types of missiles with a plug-and-play capability.

The WPML utilizes a unique geometry so that the launcher serves as an integrated gas management system. The launcher is comprised of two concentric cylinders joined at the aft end with a hemisphere (Figure 2.1). The missile is launched and initially guided from the inner cylinder. After ejection from the motor nozzle, rocket gases (arrows in Figure 2.1) strike the hemisphere and are turned 180-degrees. The exhaust gases travel through the annular region formed by the inner and outer cylinders where they exit the launcher from the fore end along the missile line of fire. These high energy exhaust gases form a jet which penetrates into the environment. As a result of this gas management system missiles can be hot-launched from inside the ship hull without complicated systems to redirect exhaust.

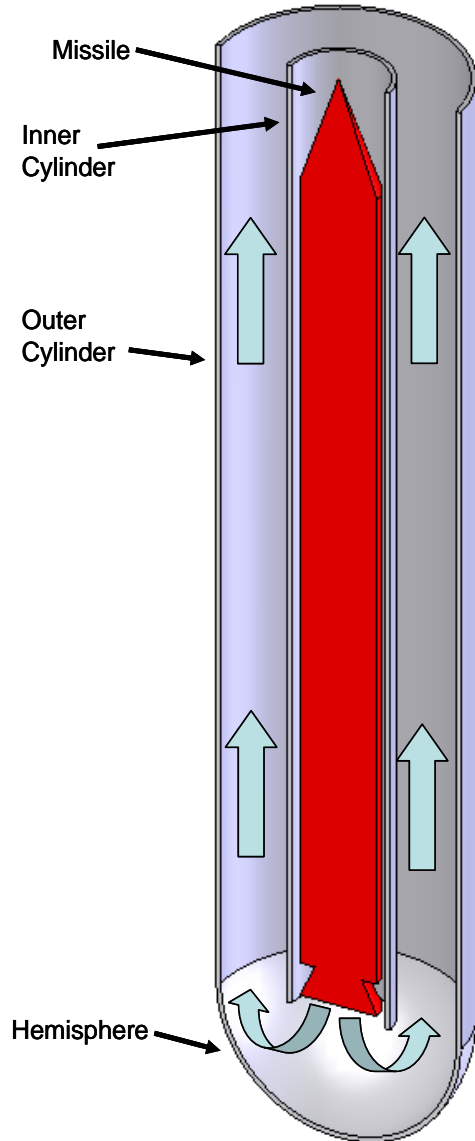


Figure 2.1. The WPML geometry.

When the WPML is submerged, the high speed gas jet interacts with the surrounding water to form a complex multiphase flow system. For shallow missile launches the WPML acts in a “water piercing” fashion. The gaseous jet ejected by the launcher extends from the submarine hull to the free surface providing a dry environment for the missile to travel through as it moves towards the free surface. A schematic that depicts the conceptual operation of a submerged WPML is shown in Figure 2.2 (gas jet in red, free surface as blue curve). Upon ignition of the rocket motor, the gas jet discharges into the water and leads the missile (Figure 2.2A). When the missile has gained enough thrust to exit the launcher or a missile restraint system releases the missile after a predetermined amount of time, the gas jet is well ahead of the missile and the

missile flies through this gaseous jet (Figure 2.2B). Note the presence of a continuous gas jet from the submarine hull to the free surface, which prohibits water from contacting the ascending missile. The missile exits the free surface (Figure 2.2C), presumably having never contacted water as long as the gas jet remains continuous from the launch platform to the free surface. This has been confirmed experimentally by firing missiles with moisture sensors located on the surface of the missile (Yagla et al. 2006). Utilizing the WPML the missile launching system becomes idealized and simplistic as many of the supporting systems normally required for underwater missile launch become unnecessary. In particular for an underwater missile launch two important subsystems of conventional launchers can be eliminated: A) the missile pressurization system which elevates the pressure inside the missile skin prior to launch and is designed to prevent water intrusion through the missile skin as it moves underwater and B) the gas generator system which generates high pressure and drives the missile out of the launch tube. The former is eliminated as the missile travels inside the exhaust jet and never contacts water while the latter is eliminated since the missile exits the launch tube under its own thrust.

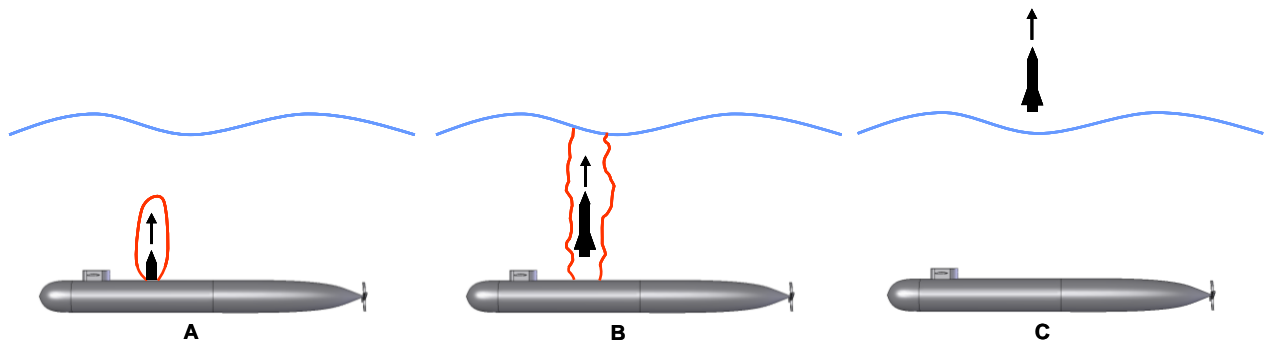


Figure 2.2. Missile launch from WPML at shallow depth.

Extensive experimentation on the gas jet dynamics has been conducted to determine the feasibility of such a design at both laboratory (Weiland and Vlachos 2007) and practical scales [(Weiland et al. 2005); (Yagla et al. 2006)]. The results of these experimental studies indicate that the stability and penetration of the gas jet into the surrounding water is adequate to allow a missile launch under some conditions. The gas jet is affected by a number of issues such as the launch depth, submarine speed at launch, other cross flow currents in the ocean, and the gas jet characteristics (such as speed) at the launcher exit. Empirical evidence suggests these factors will only play a significant role if the cross flow velocity is high and/or the launch depth is deep. An example demonstrating the effect of cross flow on the curvature of the gas jet is given in

Figure 2.3, which shows the time-averaged stagnation side interface position for several gas injection Mach numbers exhausted from a laboratory sized WPML (1.9 and 0.95 cm outer and inner cylinder diameters, respectively) in a 0.3 (left) and 0.7 (right) m/s cross flow (Weiland et al, 2007). The interface positions were acquired using high speed shadow-photography and then digitally processed to reveal only the interface position. The susceptibility of the gas jet to cross flow curvature is directly related to the gas injection speed, with supersonic gas jets remaining upright for over 16 diameters length over the range of cross flow velocities tested. If the continuity of the gas jet is compromised due to a large launch depth or if the gas jet bends excessively due to cross flow the WPML will fail to provide a dry environment for missile travel.

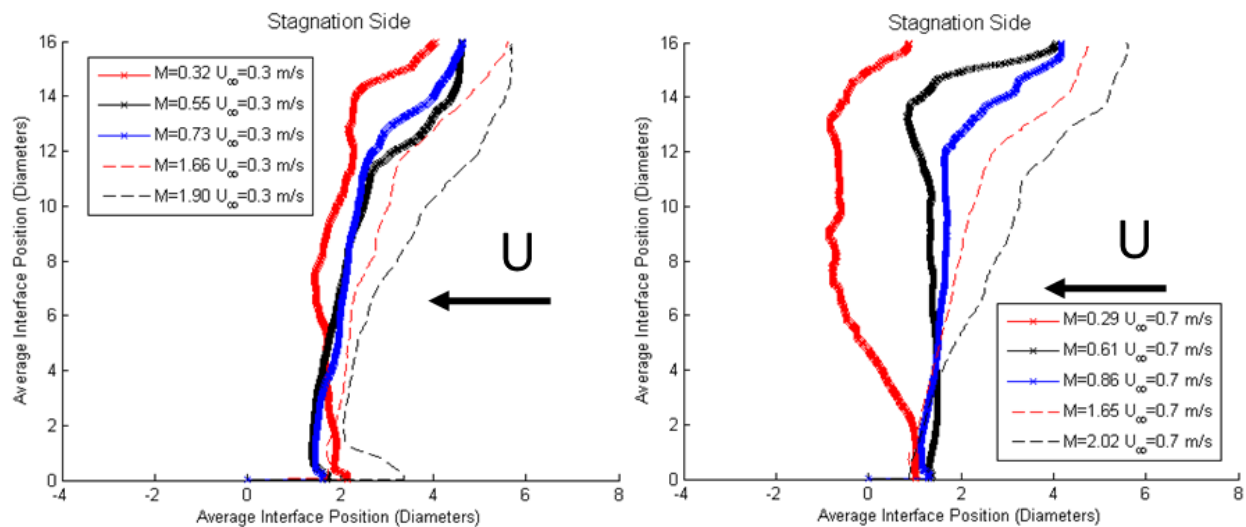


Figure 2.3. Time-averaged interface position of gas jets at both subsonic and supersonic velocities in a 0.3 (left) and 0.7 (right) m/s cross flow. The supersonic gas jets are much less susceptible to cross flow.

Although research into the basic gas jet physics is ongoing, there have been no conceptual studies of what limitations are imposed on the WPML. The conceptual analysis presented in this paper is important to the WPML development as the concept behind the WPML, namely utilizing a high speed gas jet to provide a dry path for missile travel, has not been attempted before and a successful launch requires the missile to remain within the gas jet. These limitations are primarily due to deep missile launches and can include A) the deflection of the gas jet due to submarine translation, B) breakup of the gas jet due to hydrodynamic instabilities of the interface, and C) inadequate jet tip penetration such that the missile overtakes the gas jet during underwater flight. These physical limitations are inescapable if the submarine is either moving too quickly and/or the launch is too deep. The first limitation prevents the gas jet from maintaining a straight path through which the missile can travel and thus the missile, which

presumably will travel in a straight line from the launcher to the water surface, will enter a wet environment. The second limitation concerns the continuity of the jet; if the jet breaks up into many small bubbles as opposed to a continuous jet flow the missile will enter a wet environment. The third limitation can be overcome by simply increasing the missile restraint time and allowing the jet to penetrate further before the missile is released.

This paper presents a conceptual analysis of the operational characteristics of a WPML in launching a generic artillery missile. A brief overview of how the jet physics have been modeled from empirical data for use in our computations is given and the limitations of the WPML concept are discussed.

2.4 Experimental Methods and Modeling

The basic premise of the launcher is to provide a dry environment, via a continuous and upright gas jet, for a missile launch underwater. Among the ways a missile launch can fail are: 1. Classic jet instabilities such as Kelvin-Helmholtz (KH), which is due to shear between the gas jet and the water, can lead to jet breakup (i.e. a discontinuity in the gas jet), 2. The leading edge of the jet can transform into a plume which can pinch off and rise to the free surface independently as a large bubble, and 3. Cross flow can bend the jet so as to encroach on the missile line of fire. The Rayleigh-Taylor (RT) instability, which is due to the acceleration of a fluid by a less dense fluid, also contributes to the destabilization of the gas jet through rapid pulsations of the gas jet near the launcher. In the context of our problem, we consider a stable jet to be a semi-columnar gas pocket whose radius does not increase significantly as it rises to the surface, no section of which impinges on the missile. To ensure this last criterion if the gas jet bends due to cross flow we establish the minimum allowable radius of the gas jet equal to the radius of the outer diameter of the WPML.

The WPML operational space is greatly dependent on the location where the flow transitions from a jet to a plume. The two regions are defined by their source of momentum flux: in a jet the momentum flux is given by a large pressure difference between the nozzle and ambient fluid while in a plume the momentum flux is given by buoyancy. The transition from jet to plume is inevitable given enough distance from the nozzle and is dependent on several variables. These variables include the annulus area, the gas exit velocity, the cross flow speed, the launch depth,

and the missile thrust. In this section these variables will be used to model the operational space of the WPML in launching a generic artillery missile.

Near the launcher exit, the missile exhaust is nearly columnar due to the high velocity of the exhaust gas from the annular space. In this region, the exhaust is classified as a jet whose source of momentum flux is due to the pressure difference between the rocket motor and ambient environment. As the jet evolves in space, it loses speed and expands radially due to entrainment of ambient water into the gas flow. At some point from the launcher the jet will transition into a plume, where the source of momentum flux is due to buoyancy. The high speed gas is buoyant due to a density variation between the gas and the surrounding water, and this buoyancy action can have a considerable effect on the jet behavior.

We can classify the development of a buoyant jet, based on the source of momentum flux, as the near and far fields which are dependent on the distance from the launcher exit (Figure 2.4). In the near region, the flow is considered a jet and is mostly columnar and stands upright in the presence of cross flow. The transition zone contains characteristics of both plume and jet behavior. In the far region the flow is considered a plume which aligns itself with the direction of cross flow. Identification of the transition region is important as the behaviors of the jet and plume are markedly different, and the probability of a successful launch is diminished if the jet transitions to a plume too quickly from the launcher exit. This transition point is classically given by L_m , a characteristic length scale defined by Equation 2.1. Physically L_m corresponds to the ratio of momentum to buoyancy effects and thus this parameter dictates the character of the buoyant gas jet as jet-like ($d_{jet} \ll L_m$) or plume-like ($d_{jet} \gg L_m$). This term does not give an exact prediction of the transition point but rather an estimate.

$$L_M = \frac{M^{3/4}}{B^{1/2}} \quad 2.1$$

M is the momentum flux and B is the buoyancy flux at the WPML exit, defined by equations 2.2 and 2.3, respectively. Here D is the launcher hydraulic diameter, W is the gas exit speed, g is the gravitational acceleration, ρ_∞ is the ambient fluid density, and ρ_e is the gas density at the launcher exit. Q is the volume flux and is given by Equation 2.4.

$$M = \frac{1}{4} \pi D^2 W^2 \quad 2.2$$

$$B = Qg \frac{(\rho_{\infty} - \rho_e)}{\rho_e} \quad 2.3$$

$$Q = \frac{1}{4} \pi D^2 W \quad 2.4$$

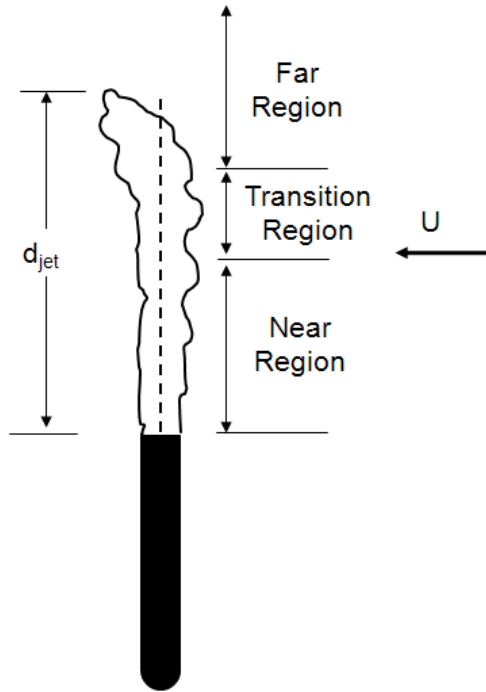


Figure 2.4. The high speed gas jet is classified into the near, transition, and far regions. Even in the presence of cross flow the jet is mostly columnar and upright in the near region, after which the transition region shows characteristics of both jet and plume behavior. In the far region the jet is dominated by the cross flow and aligns itself with the cross flow direction.

It is noted that the evolution of the high speed jet into a plume is inevitable, as all buoyant jets will eventually transition into a plume given enough distance from the source. This transition is detrimental to the WPML performance as the plume A) rises more slowly than the jet and thus the missile can overtake the gas jet tip more easily and B) aligns itself with the direction of cross flow which causes the gas jet to encroach on the missile flight path.

For our calculations of the gas jet there are essentially two aspects which must be modeled. The first is the speed of the gas jet tip as it propagates from the launcher exit. This is critical in order to define a missile restraint time which prevents the missile from overtaking the gas jet. The second is the trajectory of the gas jet due to cross flow. The jet tip speed is taken directly from experimental data of scale sized WPMLs operating underwater with a rocket motor. Details of these tests can be found in Yagla et al (2006). The motion of the underwater jet was tracked using high speed photography and the gas jet tip speed was non-dimensionalized via Equations

2.5 and 2.6, which were determined from a Buckingham analysis of the relevant variables. The result of the non-dimensionalization of the jet tip trajectory data from several scale tests is shown in Figure 2.5. The results indicate the jet tip trajectory is described by a power law relationship.

$$t^* = \left(\frac{W}{L_M} \right) t \quad 2.5$$

$$D^* = \frac{d_{jet}}{L_m} \quad 2.6$$

Here W is the initial gas exit velocity from the WPML annulus, t is the time beginning from the moment the jet first leaves the launcher, and d_{jet} is the downstream distance of the jet tip.

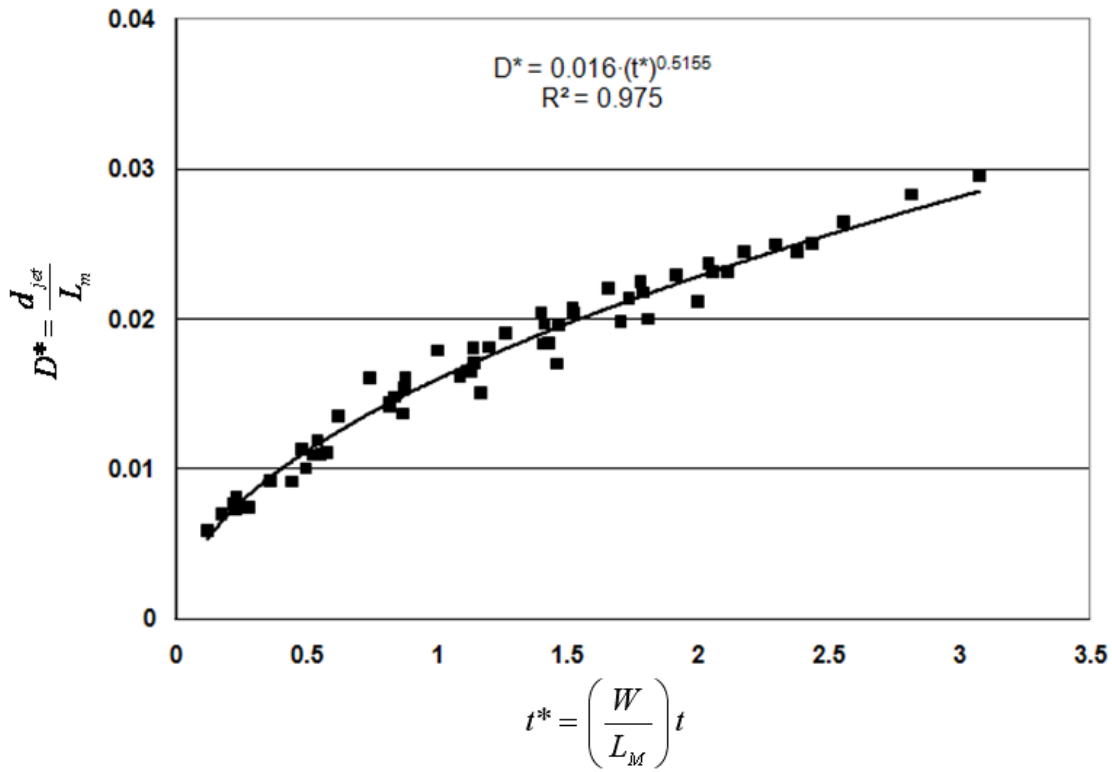


Figure 2.5. The jet tip trajectories from several scale tests (Yagla et al, 2006) were reduced using the nondimensional variables given by Equations 1.5 and 1.6. The jet tip trajectory follows a power law relationship.

Equations 2.1-2.6 effectively scale the experimental high speed gas jet data into the reduced form shown in Equation 2.7. This scaling reduces the jet tip position as a function of time for several sizes of WPMLs so that the position of the jet tip (in the jetting regime) from the WPML exit can be predicted.

$$D^* = 0.016(t^*)^{0.5155} \quad 2.7$$

It should also be noted that the behavior of the gas jet will change as the jet loses forward momentum and transitions into a plume. At this point, the flow is buoyancy driven and it is the action of the buoyancy force which accounts for all movement of the plume. The behavior of the jet will change at this point, and the validity of Equation 2.7 may be called into question. However for the applications presented in this paper our knowledge of the near-jet flow region is sufficient to model launch scenarios because for the launcher to be effective and not bend under the effect of cross flow it must operate in the jetting regime. Thus no modeling of far field effects is required.

Curvature of the high speed gas jet due to cross flow is problematic if the gas jet curves into the missile line of fire as shown by the cartoon in Figure 2.6. Cross flow is defined as the velocity which acts on the jet perpendicular to the line of fire and includes cross currents in the ocean and the submarine velocity itself. Many submarines maintain control using lifting surfaces and must always remain in motion. Although multiple cross flows could be present, we only consider the speed of the submarine as the source of the cross flow.

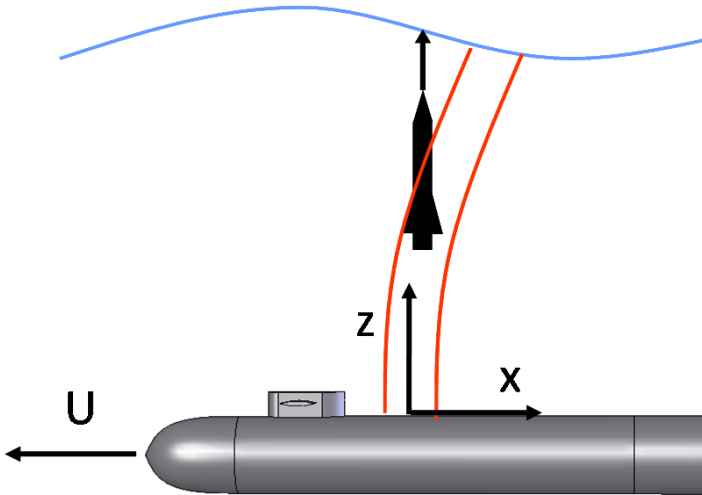


Figure 2.6. Curvature of gas jet due to cross flow. Near the submarine hull the gas jet is straight and columnar but due to the action of cross flow the gas jet will curve so as to align itself with the cross flow.

Two important non-dimensional scaling groups for modeling the cross flow scenario are given in Equations 2.8 and 2.9. Physically, Equation 2.8 corresponds to the distance from the launcher at which the gas jet velocity is of the same order as the cross flow velocity. Equation 2.9 corresponds to buoyancy to cross flow effects and denotes the distance from the launcher where the vertical velocity of the plume is of the order as the cross flow velocity.

$$z_M = \frac{M^{1/2}}{U} \tag{2.8}$$

$$z_B = \frac{B}{U^3} \quad 2.9$$

U is the cross flow speed, restricted here to include only the submarine speed. The bending of the gas jet, as well as the change in nature of the gas jet (i.e. jet, plume, or bent plume) is described mathematically using equations 2.10-2.12. Equation 2.10 describes the stagnation side jet deflection for a pure jet, Equation 2.11 describes the jet deflection for a plume, and Equation 2.12 describes the jet deflection for a bent plume in which cross flow effects thoroughly dominate the gas behavior. These equations originated from simple scaling arguments of the time-averaged momentum equations, which describe the jet in cross flow problem and details can be found in the book by Fischer et al (1979).

$$\frac{\bar{z}}{z_M} = C_1 \left(\frac{x}{z_M} \right)^{1/2} \quad \text{for } L_Q \leq \bar{z} \leq L_M \quad 2.10$$

$$\frac{\bar{z}}{z_B} = C_3 \left(\frac{x}{z_B} \right)^{3/4} \quad \text{for } L_M \leq \bar{z} \leq L_B \quad 2.11$$

$$\frac{\bar{z}}{z_B} = C_4 \left(\frac{x}{z_B} \right)^{2/3} \quad \text{for } z_B \leq \bar{z} \quad 2.12$$

Here z denotes the distance from the launcher exit and the overbar denotes that these equations show the mean location of the jet. The C variables are empirical constants given by the literature for single phase jets (Fischer et al. 1979), x is the downstream distance from the jet exit, and L_Q is a non-dimensional characteristic length scale that is defined in Equation 2.13. This term physically represents the development length of the jet as it transitions to self-similar flow due to merging of the nozzle shear layers.

$$L_Q = \frac{Q}{M^{1/2}} \quad 2.13$$

The C variables listed in Equations 2.10-2.12 have been reported for single phase jets and thus are not applicable to submerged gas jets. Additionally, the spreading of the jet due to mass entrainment must be accounted for to accurately resolve the jet curvature in cross flow. Empirical evidence from a wide range of both laboratory and large scale WPMLs shows a jet half-angle of about 10 degrees. Since we are only interested in the portion of the jet in the jetting regime, only C_1 must be identified to compute the jet deflection. Equation 2.10 can be rearranged to compute the C_1 constant from experimental data. Empirical evidence suggests C_1

should be taken as 0.58 as shown in Figure 2.7, which uses experimental data of the jet displacement in a 1.54 m/s cross flow using rocket exhaust as the gas source. The large jump in the C_I value between 1 and 2 diameters most likely results from a mixture of normal developmental and additional compressibility effects which are absent in a buoyant liquid jet in cross flow. After approximately 5 diameters the constant C_I settles into a practically constant value whose average is 0.58. The decline of the C_I constant from about 2.1 to 0.58 after about 4 diameters is thought to be a manifestation of the jet development length which is consistent with the theoretical development length of 5 diameters for gas jets submerged in liquid (Abramovich 1963). Note that a liquid jet in liquid cross flow has been shown to have an average C_I value of about 2.1 (Fischer et al. 1979).

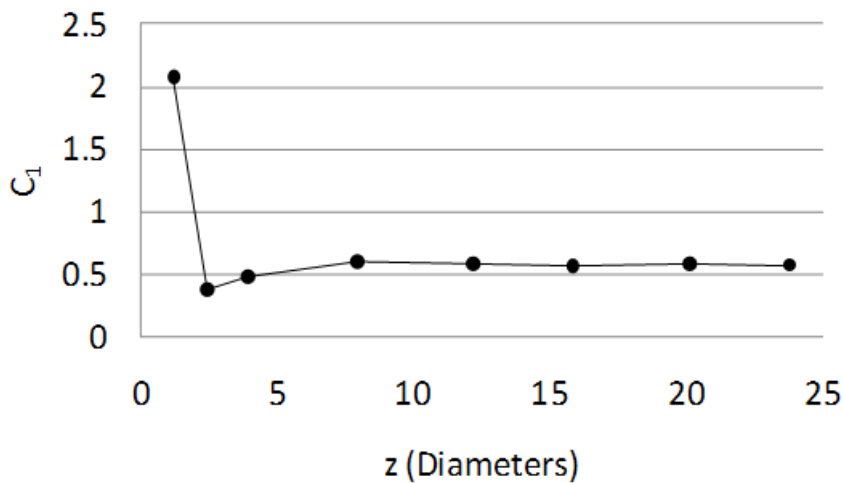


Figure 2.7. Reduction of experimental data yields values of the C_I coefficient for submerged gas jets in water. The coefficient varies in value up until about 5 diameters, which is consistent for the development length of a submerged gas jet in water.

Using the aforementioned equations, we can compute the curvature, trajectory, and nature of the gas jet given the appropriate launch parameters. The total jet deflection is calculated using the superposition of the jet spreading due to turbulent entrainment and deflection from cross flow. It is now obvious that there are several variables which govern the performance of a WPML including the annulus area, the gas exit velocity, the cross flow speed, the launch depth, and the missile thrust. These variables define the operating space of the launcher as presented in Equations 2.1-2.13.

Modeling of the high speed gas jet using the relationships shown above were used in uncoupled numerical simulations of a missile/jet system. The missile flight dynamics were calculated using a finite difference code written by the author and are meant to give order-of-

magnitude guidelines to explore the WPML limitations. This code has been used to predict the trajectory and performance of a small missile using a rocket motor used in the scale WPML tests with success (Yagla et al. 2006). A generic artillery missile with a maximum thrust of 90 kN and a mass of 1500 kg was chosen for study. The generic missile is 5m in length and 0.75m in diameter giving an aspect ratio of 6.5. The WPML used in these calculations had an annular area of 0.2124 m² from which to exhaust. In all of the calculations we have imposed the jet exit Mach number as 1.5 ($W=1460$ m/s). We have chosen this exit velocity to coincide with very near the theoretical limit of Mach 1.2 for optimal hydrodynamic stability of a submerged high speed gas jet in water (Chen and Richter 1997). The Mach number is defined in the gas phase only at the exit plane of the WPML. At this exit speed, convective and absolute instabilities in the gas jet are low while still attaining good jet penetration performance. We do not model the instabilities of the gas jet; only the effects of jet curvature impinging on the line of fire define the limitations of the launcher. Research into these hydrodynamic instabilities is on-going, but laboratory scale tests of the launcher have shown that the high speed gas jet at supersonic Mach numbers can maintain suitable stability with and without cross flow for many seconds and is in fact a function of the jet Mach number (Weiland and Vlachos 2007).

The missile was treated as a lumped unit with a time-varying mass. Thrust and drag are the only forces governing the missile motion. The thrust curve used in these simulations is shown in Figure 2.8. Drag forces were computed using the instantaneous missile velocity and the coefficient of drag which was taken as 0.14 as is typical for artillery missiles of this size, an example of which is the Tactical Missile System (Laughlin and Brooks 1996). The gas jet properties were computed using a one-dimensional code (LAX) developed at the Naval Surface Warfare Center Dahlgren Division. LAX implements a compressible, finite volume, Lax-Wendroff upwind scheme to solve for flow variables inside the WPML annulus. The code accounts for viscous wall friction and heat loss due to conduction through the walls and has been utilized with great success in predicting the internal WPML ballistics (Yagla et al. 2006).

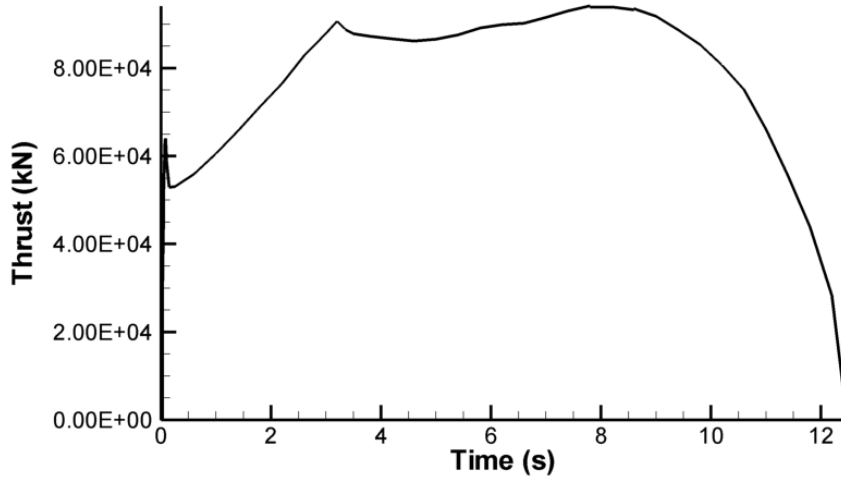


Figure 2.8. A generic burn curve used to simulate the thrusting force which drives missile flight. This curve was artificially created to simulate the appropriate sized thrust for a missile of this class.

2.5 Results

The primary limitation of the WPML is due to the effect of cross flow. This is demonstrated using Equation 2.10 to compute the stagnation side jet deflection under several cross flow velocities and is shown in Figure 2.9. The vertical dotted line represents the leading edge (radius) of the WPML and impingement of the jet boundary on this position denotes the maximum launch depth.

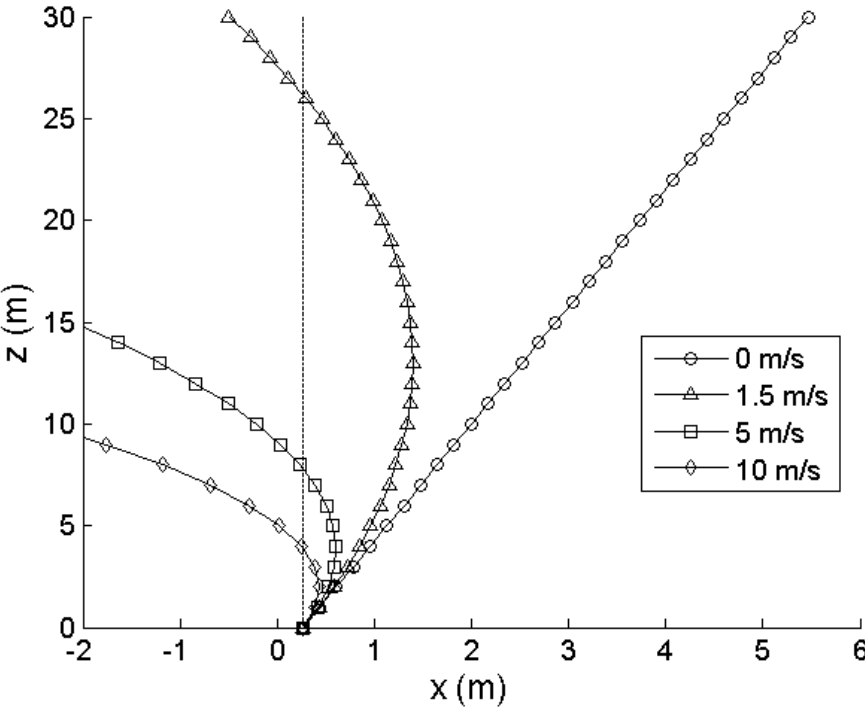


Figure 2.9. Jet deflection under several cross flow velocities. The artillery missile jet characteristics were used to compute the steady-state windward position of the gas jet. The dotted vertical line represents the leading edge radius of the launcher. Impingement of the jet on the radius of the launcher defines the maximum launch depth.

Calculations of the missile and jet trajectories indicate the operational limitations of the WPML considered in this paper as shown in Figure 2.10 for optimal (left) and maximum (right) launch conditions. Here the term optimal refers to minimizing missile restraint time while maximizing launch depth. It is imperative to minimize the missile restraint time as the WPML requires the missile to be launched from inside the submarine hull. The optimal launch point (left plot of Figure 2.10), in terms of maximizing launch depth while minimizing the missile restraint time, is shown as the intersection of both the time release and cross flow curves which occurs at about 14 m depth, 8 m/s cross flow, and a 2 s missile restraint time. The maximum operating conditions are shown in the right plot of Figure 2.10. A maximum launch point occurs at 20 m, 4 m/s cross flow, and a 4.5 s missile restraint time. These results are highly dependent on the missile launched and the characteristics of the launcher will change accordingly.

Note that as anticipated both depth and cross flow act to minimize the launch depth. The launch depth of the artillery missile is heavily weighted on the restraint time of the missile since one of the simulation requirements was that the missile cannot overtake the exhaust jet. Although increasing the missile restraint time allows the gas jet to penetrate further into the surrounding water before being overtaken by the missile, it presents an additional problem as it might not be possible to restrain a missile for long periods of time inside the launcher. For example, the right plot of Figure 2.10 indicates that a launch depth of 20 m requires a 4.5 s missile restraint time. If the heat management is inadequate inside the launcher catastrophic material failure could occur. An alternative is to replace missile exhaust with compressed gas for

the first portion of the launch to minimize the restraint time of the ignited missile motor.

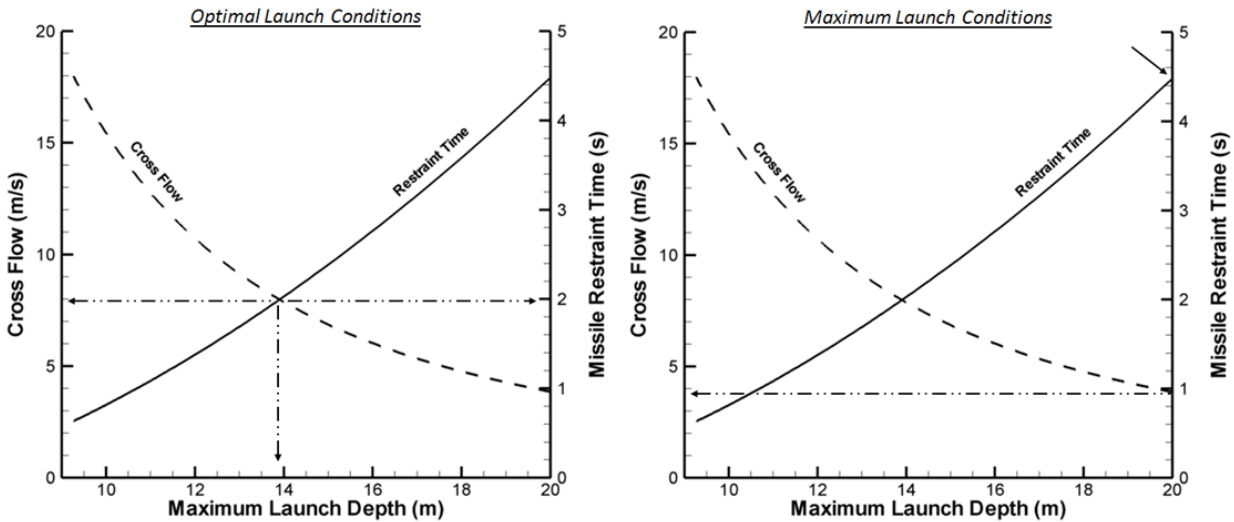


Figure 2.10. The operational envelope of a large artillery missile is affected by the launch depth and cross flow velocity. The optimal (left) and maximum (right) launch conditions are shown.

2.6 Conclusions

The Water Piercing Missile Launcher (WPML) is an effective missile launcher in both surfaced and submerged roles and due to its scalable design can be applied to a wide range of missiles. Based on empirical evidence and the numerical simulations presented in this paper, the WPML concept is shown as a viable launcher for underwater bodies. The results indicate the optimal launch depth, in terms of maximizing launch depth while minimizing the missile restraint time, for a generic artillery missile occurs at about 14 m depth for a 8 m/s submarine speed. The maximum launch depth occurs at about 20 m given a cross flow speed of 4 m/s and a missile restraint time of 4.5 s.

2.7 Acknowledgements

This work was supported by the Naval Surface Warfare Center, Dahlgren Division. The authors wish to acknowledge the support of program manager Mr. John Busic.

2.8 References

- Abramovich, G. (1963). The Theory of Turbulent Jets. Cambridge, M.I.T. Press.
- Chen, K. and H. J. Richter (1997). "Instability analysis of the transition from bubbling to jetting in a gas injected into a liquid." International Journal of Multiphase Flow **23**(4): 699-712.
- Fischer, H., E. List, et al. (1979). Mixing in Inland and Coastal Water. New York, Academic Press.

- Laughlin, J. and W. Brooks (1996). Adaptation of the Army Tactical Missile System to Undersea Operations, Lockheed Martin.
- Weiland, C. and P. Vlachos (2007). Experimental Study of the Stability and Trajectory of a High Speed Gas Jet Under the Influence of Liquid Cross Flow. ASME Joint U.S.-European Fluids Engineering Meeting. San Diego, CA.
- Weiland, C., P. Vlachos, et al. (2005). A Novel Launcher for Submarine Self-Defense. 4th Biennial National Forum on Weapon System Effectiveness. Austin, TX, AIAA.
- Yagla, J. (1997). "Concentric Canister Launcher." Naval Engineers Journal **109**(3): 18.
- Yagla, J., J. Basic, et al. (2008). Launcher Dynamics Environment of a Water Piercing Missile Launcher. 24th International Symposium on Ballistics. New Orleans, LA, NDIA.
- Yagla, J., K. Deloach, et al. (2004). The Water Piercing Missile Launcher. 21st International Symposium on Ballistics. Adelaide, Australia, NDIA.
- Yagla, J., M. Soifer, et al. (2006). The Water Piercing Missile Launcher. Submarine Technology Symposium. Laurel, MD, The Johns Hopkins University Applied Physics Laboratory.

3. THE PENETRATION OF SUBMERGED ROUND TURBULENT GAS JETS IN WATER

Chris J. Weiland¹ and Pavlos P. Vlachos²
Virginia Tech Mechanical Engineering Dept

¹ Graduate Research Assistant, Virginia Tech Mechanical Engineering Department

² Associate Professor, Virginia Tech Mechanical Engineering Department

To Be Submitted to the International Journal of Multiphase Flow

3.1 Abstract

Direct measurements of the interfacial behavior of submerged high speed gas jets with speeds ranging from subsonic to supersonic Mach numbers were performed using high speed digital photography and shadowgraphs. The results indicate that the jets preferentially pinch-off near the axial position which in previous experimental work has been shown to correspond to the location of the maximum streamwise velocity turbulence fluctuations. Using the optical method presented in this paper, the data indicates that the electroresistivity probe technique used by past researchers to quantify the jet penetration into the ambient fluid biases the measurement by up to 30 diameters as the probe cannot identify true jet continuity as opposed to advecting bubbles. We introduce a theoretical jet penetration distance based on a simple force balance of the jet cross-section which compares reasonably well with the measured data. An experimental jet penetration distance is introduced and is defined as the 98.5% contour of the orifice attached gas jet presence over the measurement time. Measurements of the interface acceleration coupled with estimations of the internal gas jet velocity suggest that entrainment and stability are governed by both Rayleigh-Taylor and Kelvin-Helmholtz mechanisms.

Keywords: *submerged gas jet, interfacial stability, buoyant jet*

3.2 Nomenclature

a – interfacial acceleration
 A – jet cross sectional area
 AD – average deviation
 D – orifice diameter
 F – force
 g – gravity
 KH – Kelvin-Helmholtz
 L – length scale
 M – Mach number
 P – pressure
 R – Radius of jet
 RMS – root-mean-square
 RT – Rayleigh-Taylor
 t – time
 u – axial velocity
 x – radial position
 y – axial position
 α – void fraction
 ρ – density
 σ – surface tension
 Ψ – relative importance of RT to KH
 Φ – self-similar jetting parameter

Subscripts
 B – buoyancy
 c – centerline property
 g – gas
 M – momentum
 o – orifice
 Q – geometric
* – modified length scale
 ∞ – ambient fluid

3.3 Introduction

The problem of jet stability is a classic subject in fluid mechanics [(Lin and Benney 1962); (Birkhoff 1962)]. Helmholtz (1868), Kelvin (1871), and Rayleigh (1879) were among the first who laid the mathematical foundations of instability theory governing jets. While the structure and stability of single phase jets have been studied for quite some time [(Dimotakis et al. 1983); (Wang and Law 2002)], multiphase systems formed by a gas jet submerged in liquid are infrequently studied. The submerged gas jet forms a complex multiphase system which is important to the metallurgical (Wraith and Chalkly 1977), chemical (Darmana et al. 2005), and nuclear (Chawla 1975) industries. The metallurgical industry uses submerged gas jets for liquid

metal stirring and gas-metal reactions, but it has been shown that if the gas jet enters the bubbling regime close to the gas injection nozzle significant pressure fluctuations on the nozzle tip ensue which tends to cause nozzle erosion. For example, nozzle erosion decreases productivity and efficiency (Sahai and Guthrie 1982). Thus understanding the conditions that control the stability of the gas jet is important to prolonging the life of the gas injection tip and determining the hydrodynamics and efficiency of the mixing process. These multiphase phenomena are of interest to the nuclear industry for fast breeder reactor technology as the postulated core disruptive accident involves the penetration of nuclear fuel vapor into cold liquid sodium. This interaction has potentially disastrous results for the reactor and thus understanding the dynamics and penetration of the gas jet into the ambient fluid is of utmost importance (Epstein et al. 2001).

Numerous past studies have confirmed the presence of two regimes which characterize the development of the gas flow after leaving the nozzle. At low flow rates the bubbling regime is observed, characterized by the production of bubbles that break near the orifice and rise independently in the direction dictated by gravitational or density effects. A number of studies have concentrated on this regime [(Brodkey 1967);(Ruzicka et al. 1997);(Cieslinski and Mosdorf 2005)]. At higher flow rates a gaseous jet is produced which under some circumstances remains relatively stable and only far downstream of the orifice do bubbles break off from this jet. This study is devoted to the latter regime, namely the study of the characteristics of a submerged high speed gas jet and its transition from a jet to a bubbly plume. Only a small number of previous investigations exploring the physics of these processes are available in the literature.

Identification of a single nondimensional number capable of predicting the transition from bubbling to jetting has dominated the motivation for understanding submerged gas jets. Mori et al (1982) was among the first to define a useful quantitative metric to describe the bubbling/jetting transition point. They showed experimentally that the sonic flow region defines the transition point between bubbling and jetting behavior for nitrogen injected into a mercury bath. The bubbling regime was distinguished from the jetting regime by the fraction of time gas at the orifice had the same diameter as the orifice. McNallan and King (1982) studied the effects of several gases (argon, nitrogen, and helium) injected into several liquid baths (water, molten tin, tin-lead alloy, and iron) by high speed photography. They identified the bubbling to jetting transition to occur near the sonic point or more reliably, at a mass flux of $40 \text{ g/cm}^2\text{s}$ which

corresponded to the sonic point for all gases but helium. This disparity was not explained. Loth and Faeth (1989) conducted measurements on round turbulent gas jets injected vertically into quiescent water at various under-expanded jetting conditions. The under-expansion of a compressible gas jet is due to an imperfectly matched pressure condition at the exit plane of the nozzle. If the nozzle exit pressure is higher or lower than the ambient fluid the flow is termed under-expanded or over-expanded, respectively (Shapiro 1953). Imperfectly expanded jets require some additional process, such as shock or oblique waves, to restore the exhausted gas to the ambient pressure (Liepmann and Roshko 1957). Using a pitot-probe device, Loth and Faeth measured the presence of a shock cell structure downstream of the orifice. Ito et al (1991) sampled the internal flow using a specialized sampling probe to define the slip velocity and entrainment between the two phases. Both the work of Loth and Faeth (1989) and Ito et al (1991) relied on point measurements of the of the flow field resulting in temporally averaged results to describe the jet.

In trying to define a critical number which dictates the transition from bubbling to jetting, past researchers relied largely on the conventional explanation for the bubbling to jetting transition: the rate of formation of bubbles was such that successive bubbles merged to form a continuous jet and the rate at which bubbles were fractured from this jet was less than their formation rate. More recent explanations for this transition center on hydrodynamic stability theory, namely the Rayleigh-Taylor (RT) and Kelvin-Helmholtz (KH) instabilities and the rate at which instabilities evolve and propagate. Kitscha and Kocamustafaogullari (1989) and (Zhao and Irons (1990) were among the first to identify the importance of such instability mechanisms in dictating the bubbling to jetting transition point and explained that jetting occurs when perturbations travel on the phase boundary faster than they can accumulate. The model of (Zhao and Irons (1990) compares reasonably well with experimental results. Chen and Richter (1997) conducted a thorough perturbation analysis of a compressible gas jet injected into an unbounded inviscid liquid environment. They computed the transonic regime as the bubbling/jetting transition point, and argue the physical mechanism for this behavior as the accumulation of vorticity which is generated by compressibility effects: flow in the subsonic region will have density changes leading to the production of vorticity while the opposite is true in the supersonic regime. This is similar to the classic definition of the KH instability as the stability of a vortex sheath (Batchelor 1967) . Jetting is predicted to occur for supersonic gas flows.

Herein we present direct measurements of the interface using shadowgraphs and high speed digital photography. A robust image processing algorithm analyzed the phase boundary from the experimental images. In this paper we employ these measurements to quantify A) the dependence of gas jet pinch-off on Mach number, B) the penetration of submerged gas jets as a function of Mach number, C) the effect of Mach number on interface unsteadiness, and D) the relative importance of the RT and KH mechanisms on the interface motion.

3.4 Experimental Methods

The experiments were conducted in the Advanced Experimental Thermofluid Engineering Research Laboratory of the Mechanical Engineering Department at Virginia Tech. The experimental setup is shown in Figure 3.1 and consists of a clear acrylic tank, an injector assembly, pressure and temperature sensors, a fast acting valve which impulsively switched on the gas injection, and a high speed camera which recorded shadowgraph images of the underwater jet. The tests were controlled by a LabVIEW program which simultaneously triggered the high speed camera (Photron APX-RX), monitored various gas pressures and temperatures, and opened the fast acting valve which delivered gas flow to the injector. This allowed for the establishment of an accurate reference time, and synchronization between the sensor and the recorded images. The test matrix is shown in Table 3.1 where the Reynolds and Richardson numbers are calculated based on the initial (orifice exit) properties. Here P_e refers to the pressure in the exit plane of the nozzle, P_H is the hydrostatic pressure calculated from a barometric load cell and a known water depth, P_o is the stagnation pressure inside the injector, and T_o is the reservoir temperature. The hydrostatic pressure was practically constant across all shots at approximately 1.05×10^5 Pa.

Table 3.1. Test matrix for all Mach numbers tested. All jets were shot at 0.46m water depth and the properties shown here were calculated for the nozzle exit.

Mach Number	P_e (Pa $\times 10^5$)	P_o (Pa $\times 10^5$)	P_e/P_H	P_e/P_o	T_o (K)	Mass Flow (kg/s)	Velocity (m/s)	Reynolds No	Richardson No
0.39	1.05	1.16	1.01	0.90	301.7	0.0013	134	3.05E+04	0.035
0.61	1.06	1.37	1.02	0.78	301.8	0.0021	205	4.65E+04	0.0223
0.77	1.09	1.61	1.05	0.67	302.0	0.0029	255	5.78E+04	0.0174
0.91	1.15	1.96	1.10	0.58	301.8	0.0033	294	6.66E+04	0.0144
1.14	1.10	2.46	1.06	0.45	301.3	0.0049	353	8.00E+04	0.0118
1.85	1.08	6.66	1.04	0.16	301.9	0.0145	496	1.13E+05	0.0073

The injectors were composed of a base and a nozzle. Nozzles were rapid prototyped having a constant exit diameter and a varying throat diameter to achieve the desired Mach number. The Mach number was defined in the gas phase only at the exit plane of the nozzle. The nozzles were attached to a base common to all nozzles with several o-rings forming an airtight seal between the base and nozzle. The assembly was flush-mounted to the bottom plate of the acrylic tank. Air was delivered to the nozzle via five gas injection ports evenly spaced about the base. The injectors were submerged in an acrylic tank at a constant depth of 0.46 m with a wave breaker constructed from 3 layers of perforated sheet to limit surface waves and provide a constant hydrodynamic pressure, which was calculated using a Druck PTX-7217 barometric load cell (range: 79–120 kPa absolute, 0.1% full scale accuracy) to measure the atmospheric pressure and a known and closely controlled water depth. Although past researchers have shown that wave dampers do little to change the flow characteristics [(Loth and Faeth 1989); (Dai et al. 2006)], the wave damper has the added benefit of forcing the ambient water to reach a stagnant state more quickly after a test.

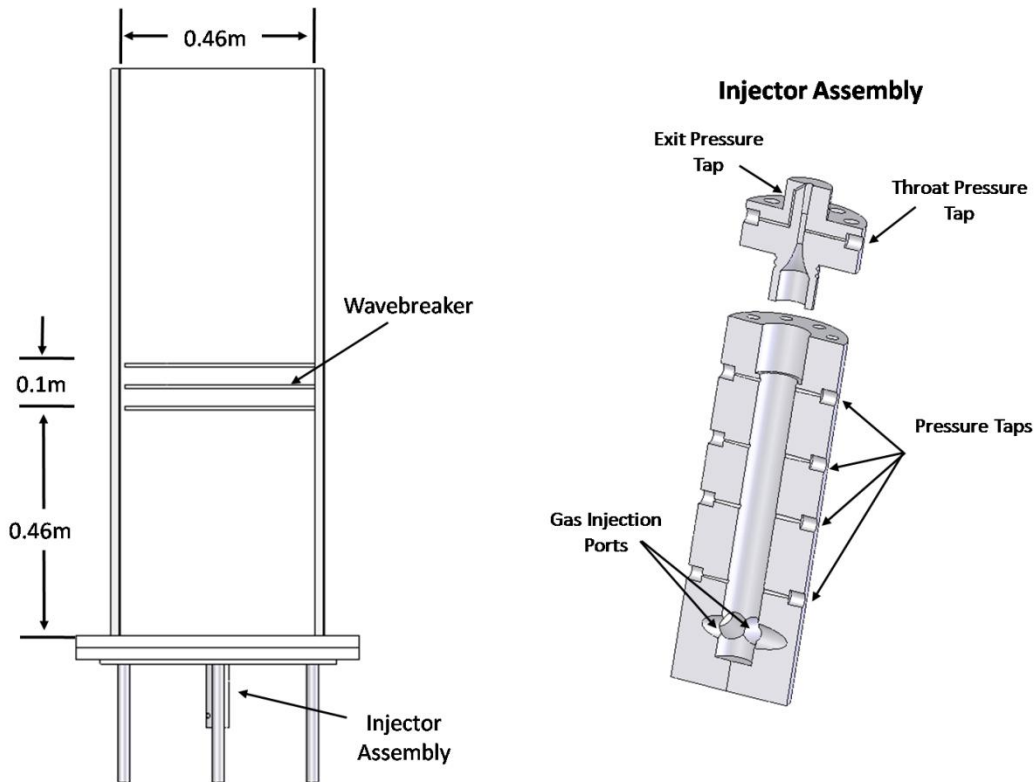


Figure 3.1. View of the acrylic tank and the injector. The flow pressure was monitored at several points inside the base and at the nozzle throat and exit. Perforated sheets helped to maintain a uniform surface by breaking any large scale surface motions. The injector was flush-mounted to the bottom of the acrylic tank.

3.4.1 Operation and Instrumentation Measurements Details

A schematic illustrating the instrumentation and control system is shown in Figure 3.2. The system was designed to deliver a constant mass flow to the injector. A pressure reservoir (0.23m^3 volume) was used in conjunction with a gas pressure regulator (Generant model 2GDR-1000B-V-B) that was insensitive to backpressure changes (1.7 kPa output change in flow pressure given 0.69 MPa input change) in reservoir pressure. The pressure downstream of the gas regulator was monitored to ensure a constant delivery pressure. Prior to each test the pressure reservoir was charged from an external gas source until the maximum pressure was attained. The manual valve was then closed to prohibit any line pressure spikes from interfering with the injector gas flow. During a test, the change in the vessel pressure and temperature was monitored to calculate the mass flow rate delivered to the injector using the ideal gas equation. In all cases dried air was used as the working fluid and untreated tap water was used as the quiescent fluid.

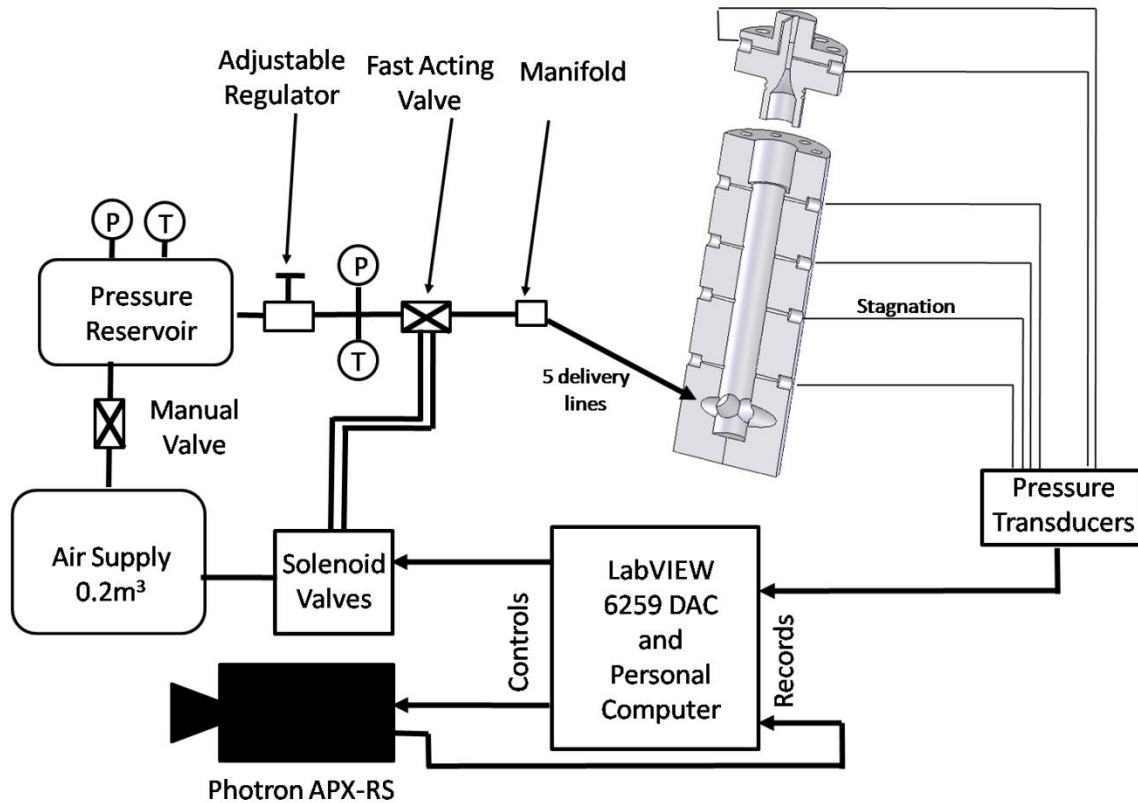


Figure 3.2. Schematic of the instrumentation and control system. Gas flow is started and stopped using a fast acting pneumatic valve controlled by LabVIEW software, which also triggers all instrumentation.

The system was controlled by LabVIEW software in conjunction with a National Instruments 6259 16-bit DAC. Upon running the software, a low voltage signal is transmitted to both the Photron camera and a solenoid valve which causes the camera to begin recording and the fast acting valve (W.E. Anderson $\frac{3}{4}$ " NPT, model ABV1DA103) to open simultaneously. The fast acting valve has an opening time of about 0.03s. Not shown in Figure 3.2 are 10 Clippard (model EV-2-24) solenoid valves controlled by the DAC which deliver compressed gas to the pressure lines while the injector is off. The compressed gas prohibited water intrusion into the pressure lines.

Pressure measurements were taken at a 1 kHz sampling rate with Druck 7217-PTX transducers with an accuracy of 2% full scale. Several ranges of transducers were used to measure signals of different expected pressure ranges in an effort to minimize errors. Temperature measurements were made at the pressure reservoir and just downstream of the adjustable pressure regulator using type K thermocouples with an Omega thermocouple to analog converter (model SMCJ-K) for a total accuracy of ± 3 deg C. The Mach number was

calculated using the isentropic law relating pressure and Mach number. The stagnation pressure was measured at a position several inches downstream of the gas injection ports. Due to propagation of uncertainties in the pressure measurements the error in the Mach number measurements at the nozzle exit was approximately 1% (Mach 1.8) - 7% (Mach 0.4). Considerable effort went into ensuring, in the case of the sonic and supersonic nozzles, that the gas jets were perfectly expanded by monitoring the exit pressure and the known hydrostatic pressure. The experimental pressure ratios are shown Table 3.1. Values of $P_e/P_H=1$ indicate a perfectly expanded jet.

3.4.2 *Photographic Measurements and Edge Detection*

A Photron FASTCAM APS-RX in conjunction with a Canon VX-16 telephoto lens was used to digitally record shadowgraph images of the test section at 1 kHz sampling rate for 14 seconds. The typical magnification used in the tests was approximately 477 $\mu\text{m}/\text{pixel}$. Eight 250W halogen lamps evenly distributed over the test section were arranged behind a white sheet to distribute light evenly over the test section. Acquired images were processed in MATLAB to detect the gas jet boundary in time. As the shadowgraph produces a projection of the gas jet onto a two-dimensional image, no three-dimensional information is collected. The jet boundary is computed using the steps shown in Figure 3.3. First the image is digitized based on a threshold pixel intensity to distinguish the gas phase from the ambient liquid and a 7x7 pixel median filter is applied to smooth any irregularities such as bubbles fractured from the jet. Next a circular disk morphological element was applied to the digitized image and after dilation and erosion the perimeter of the resulting structure was identified. As shown in Figure 3.3 the detected boundary agrees quite well with the experimental image. To ensure the nozzle gas flow reached steady-state behavior the jet boundaries were tracked $\frac{1}{2}$ second after the gas jet was initiated. In the context of this work “steady-state” refers to the initial start up jet formed when the gas jet is switched on. All jets had reached the free surface prior to analysis. The computed edges were tracked and their positions recorded for all times which allowed not only the computation of interfacial position, frequencies, velocities, and accelerations but also every pinch-off event in time was identified. Details on the image processing may be found in Appendix A.

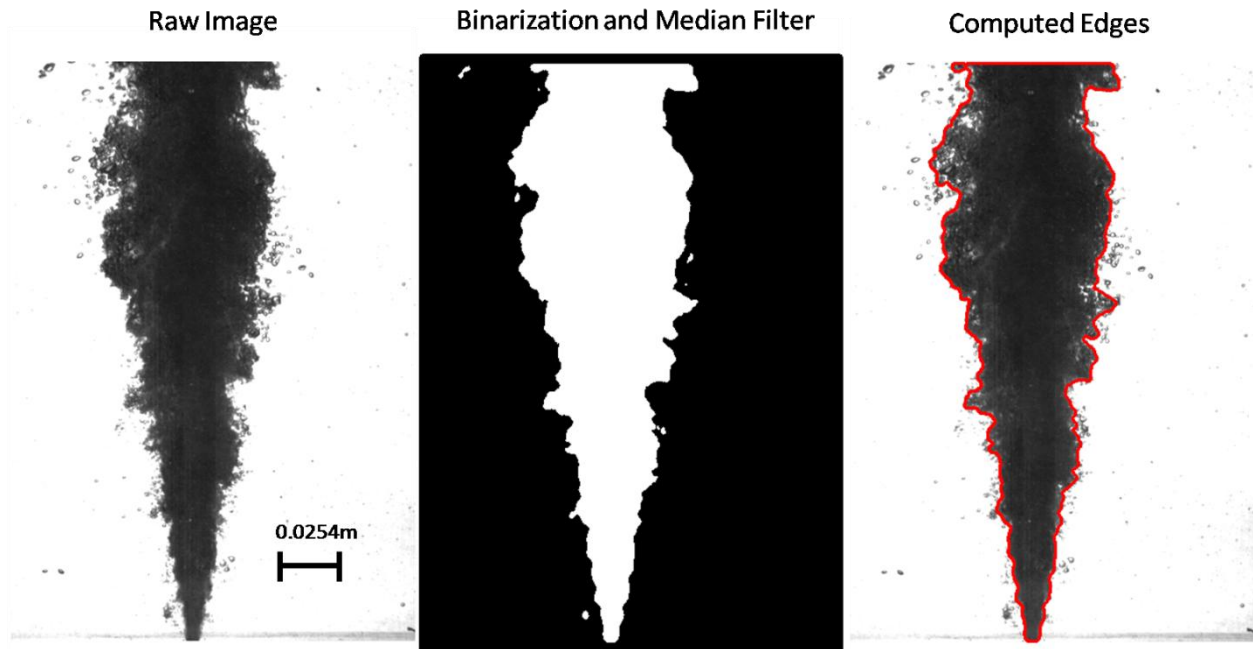


Figure 3.3. Steps used to detect the jet boundary. The process neglects outliers such as bubbles torn from the interface to accurately track the phase boundary. The horizontal scale bar represents 0.0254m.

3.5 Results and Discussion

In this paper we employ photographic measurements to quantify A) the dependence of gas jet pinch-off on Mach number, B) the penetration of submerged gas jets as a function of Mach number, C) the effect of Mach number on interface unsteadiness, and D) the relative importance of the RT and KH mechanisms on the interface motion. As far as the authors know, this is the first time quantitative measurements of the entire jet have been attempted to yield insight into global jet properties.

3.5.1 Analysis of Jet Pinch-Off Location

One of the goals of this work was to quantitatively explore the relationship between jet pinch-off and the injection Mach number at a constant hydrostatic pressure. The term pinch-off refers to the state in which the gas jet is no longer continuous from the nozzle to the free surface. The process of events leading up to jet pinch-off is shown in Figure 3.4 for a Mach 0.8 jet. The jet is considered continuous between 1292ms-1295ms with pinch-off occurring at 1296ms. The jet remains pinched-off in the remainder of the times shown.

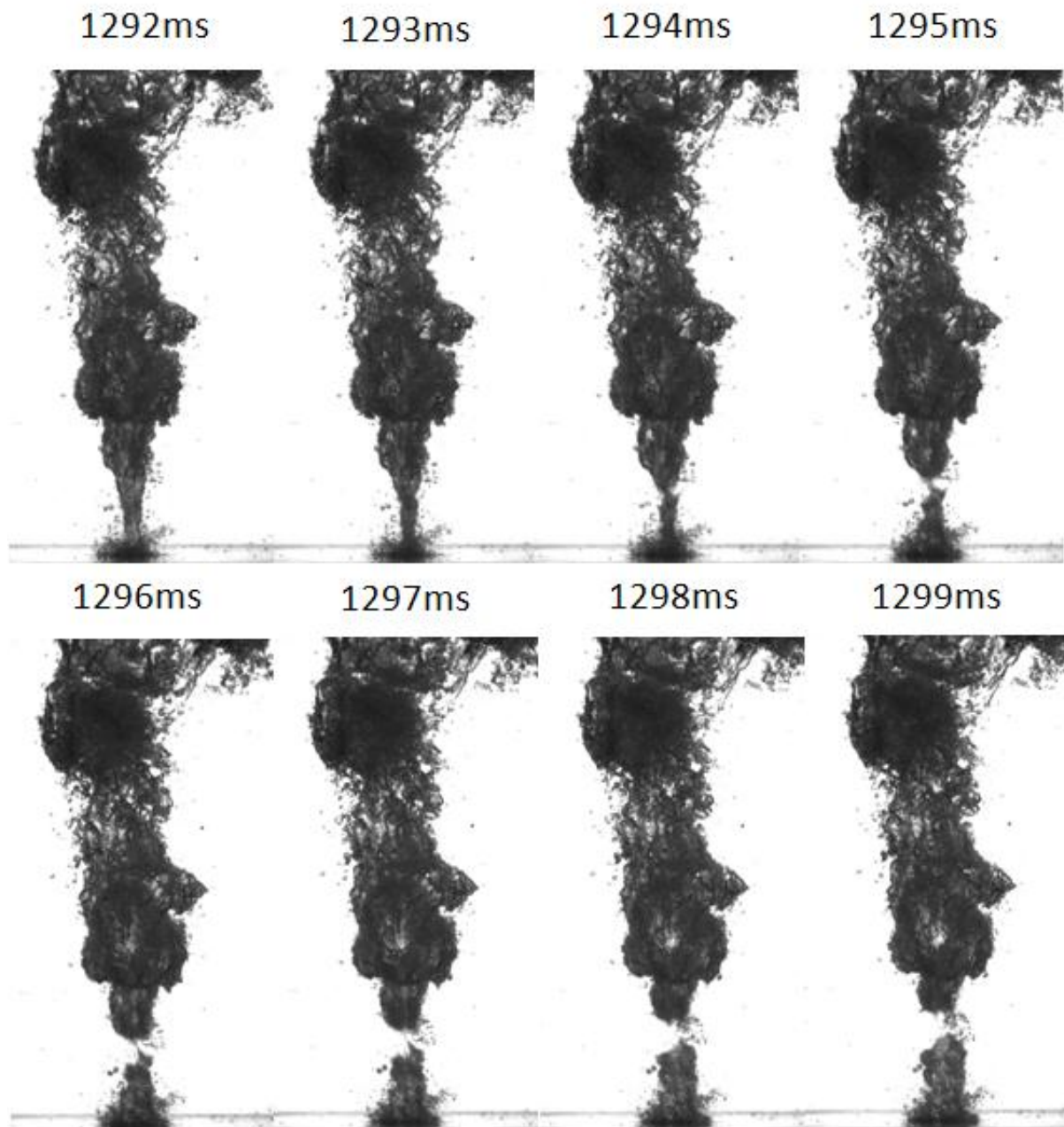


Figure 3.4. The images show the process of jet pinch-off in a 0.8 Mach jet. The first image is shown 1292ms after the gas jet was begun and subsequent images are shown at 1ms intervals.

The method presented herein builds upon the methods used by past researchers [(Wraith and Chalkly 1977); (Ozawa and Mori 1986)] in their determination of jetting or bubbling behavior. To meet this goal the jet interface was tracked using edge detection on high speed digital images as shown in Figure 3.3. An example of interface tracking at a fixed position 10 diameters downstream of the nozzle exit is shown in Figure 3.5 for Mach 0.4 and 1.8. One second of time is shown for clarity. Figure 3.5 shows the position of the interface in time at a fixed distance of

10 diameters downstream from the nozzle exit. The Mach 0.4 jet clearly has several positions, such as approximately 2.63 and 2.73 seconds, where both the left and right interfaces occupy the same radial position. This situation denotes a pinch-off event and this procedure of pinch-off detection was automated in MATLAB. Further details on the interface imaging and pinch-off detection may be found in Appendix A.

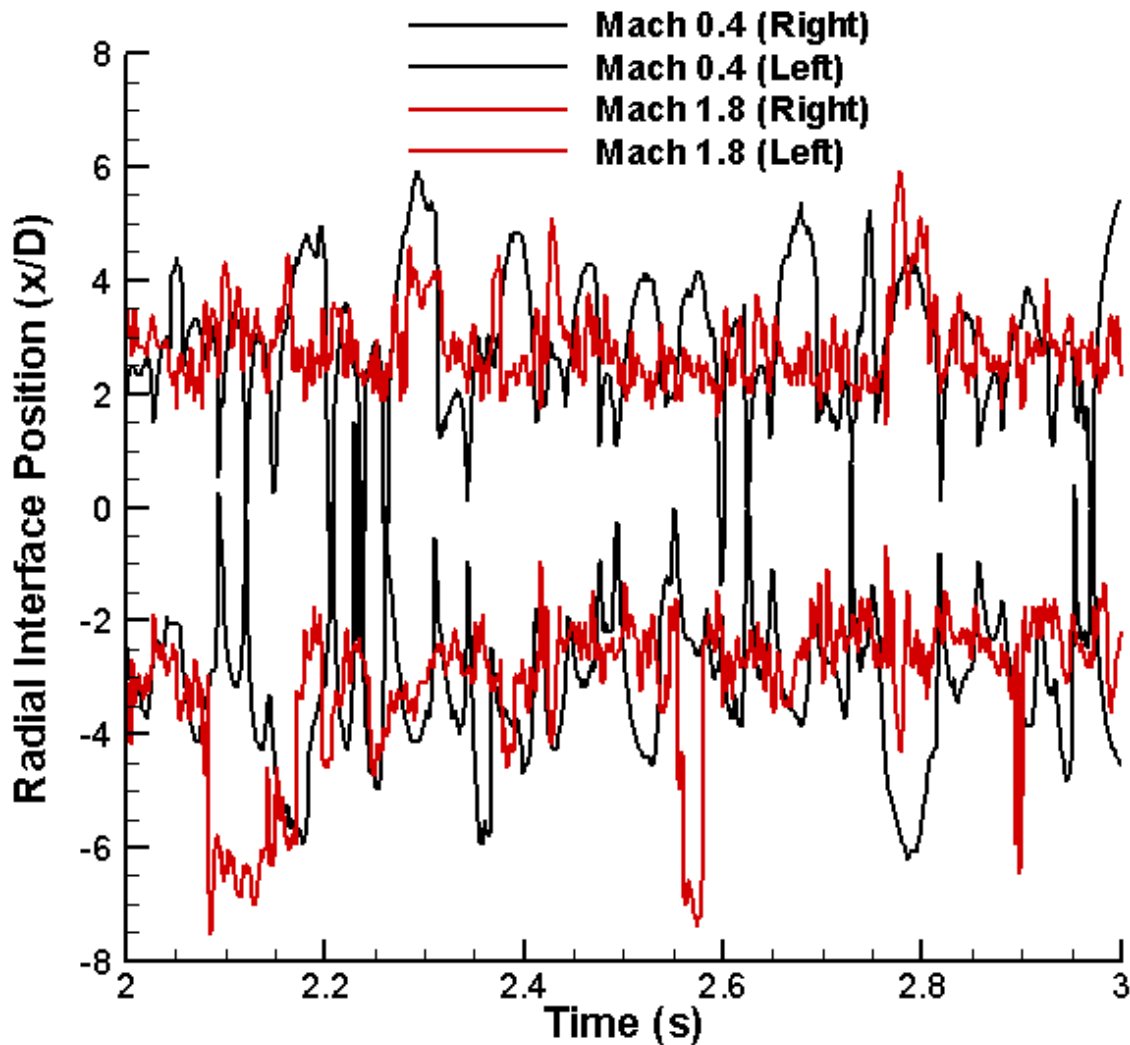


Figure 3.5. The interface position in time is shown at 10 diameters downstream from the nozzle exit. This information was computed for each test run at each downstream pixel location.

The jet pinch-off locations were recorded and their spatial distribution was determined by summing across all times for each downstream position. The normalized average distribution of pinched-off jet location across three trials for each Mach number is shown in Figure 3.6 plotted against downstream position y/L_Q . L_Q ($1.13D$) is a geometric length scale associated with the jet development which for a round jet is simply the square root of the orifice area (Fischer et al.

1979). The number of pinch-off measurements is normalized by the maximum number of pinch-off observations that occurred at any point. For example, the Mach 1.1 jet was pinched-off the most at $y/L_Q \approx 14$, and thus the entire Mach 1.1 curve shown was normalized by the number of pinch-off events sustained at $y/L_Q \approx 14$. The location of the pinch-off events is very repeatable for all cases and occurs between $10 < y/L_Q < 15$, with $y/L_Q \approx 14$ corresponding to the peak value location. Mach 0.4 deviates from this behavior demonstrating a broader range of pinch-off locations. This can be attributed to a more bubbly behavior and as a result the pinch-off location is more distributed.

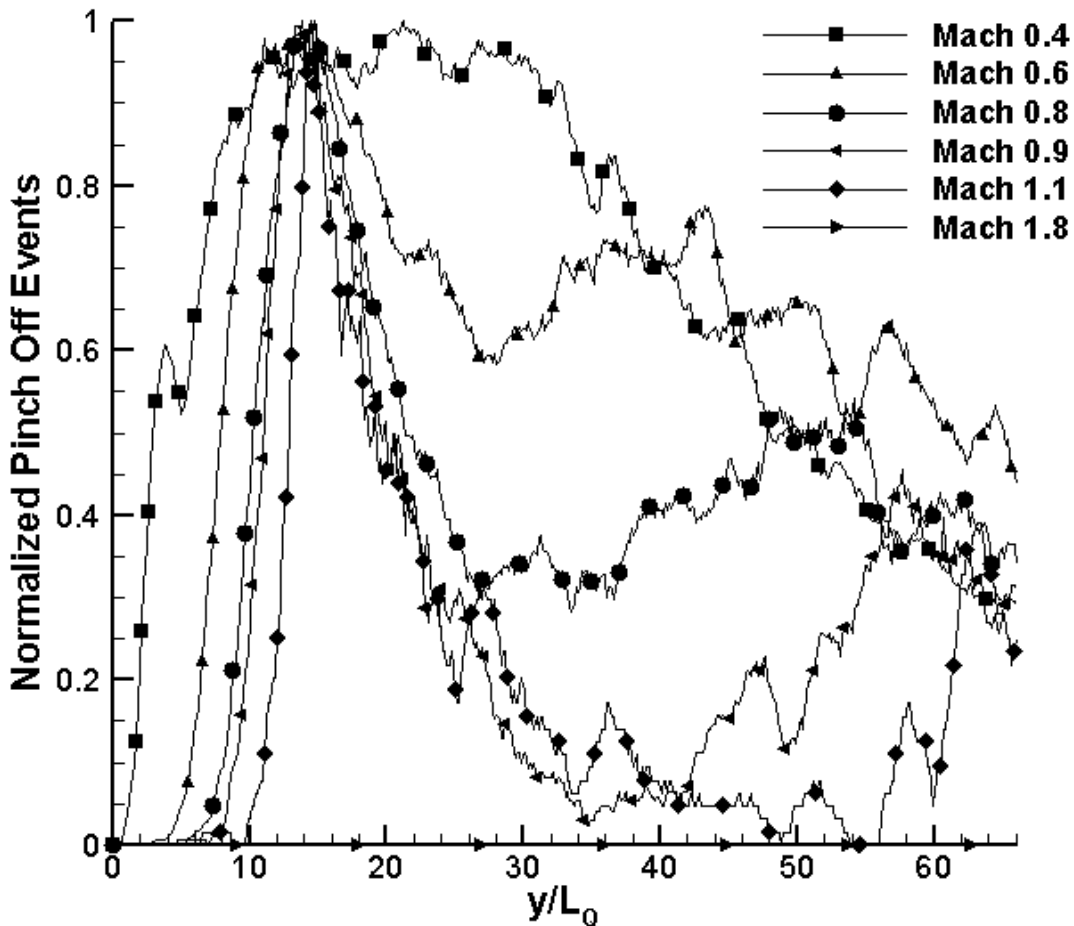


Figure 3.6. Graph of the average pinch-off location for all Mach numbers. Three trials for each Mach number were averaged to obtain these curves. The Mach 1.8 jet did not pinch-off. All of the jets consistently reached a maximum number of pinch-offs at $10 < y/L_Q < 15$.

This finding can perhaps be explained from the internal characteristics of a turbulent gas jet. Although our experiments cannot quantify its internal characteristics, previous research has shown that for single phase jets (i.e. gas jet in gas environment) the streamwise turbulence intensity reaches a peak at $y/L_Q \approx 10$ after which point it steadily decays [(Crow and Champagne

1971); (Fischer et al. 1979)]. This decay point signals the development of self-similar flow. Although our results indicate the maximum number of pinch-offs occurs at a nominal value of $y/L_Q \approx 10-14$ and the literature shows a peak value occurring at $y/L_Q \approx 10$, the similarity between these two values indicates a correlation between pinch-off location and the location of maximum turbulence intensity. This correlation suggests the two may be linked and it is likely that the turbulence acts as a perturbation on the interface to drive its unsteadiness hence leading to pinch-off.

The jet goes through intermittent periods where the jet maintains a continuous presence from the orifice to the free surface, pinch-off where the single jet fractures into multiple independent bubbles, and recovery where pinched-off bubbles re-form into a continuous jet. This behavior is indicative of jetting or bubbling, since by definition a continuous jet cannot pinch-off. This unsteady behavior is quantified by the time interval of continuous jetting and is shown in Figure 3.7. Here this time interval is plotted against the cumulative time fraction of a continuous jet where the inset shows greater detail over a reduced interval. This Figure not only denotes the total time period for which a gas jet did not pinch-off, but also shows the distribution of time intervals between pinch-off events. The total measurement time was 13.5s. Only pinch-off events lasting 2 ms or more are included as the Nyquist frequency is 500 Hz. For example, the Mach 0.4 jet maintained a continuous presence without pinch-off for about 30% of its life over the time measurement period while the Mach 0.9 and 1.1 jets did not pinch-off for 95% and 96% of the measurement period, respectively. It is readily apparent that the higher Mach numbers have longer periods of jet stability before pinch-off occurs since more time is spent in a longer time interval of continuous jetting behavior. The Mach 1.8 jet never pinched off and therefore is not included in this plot.

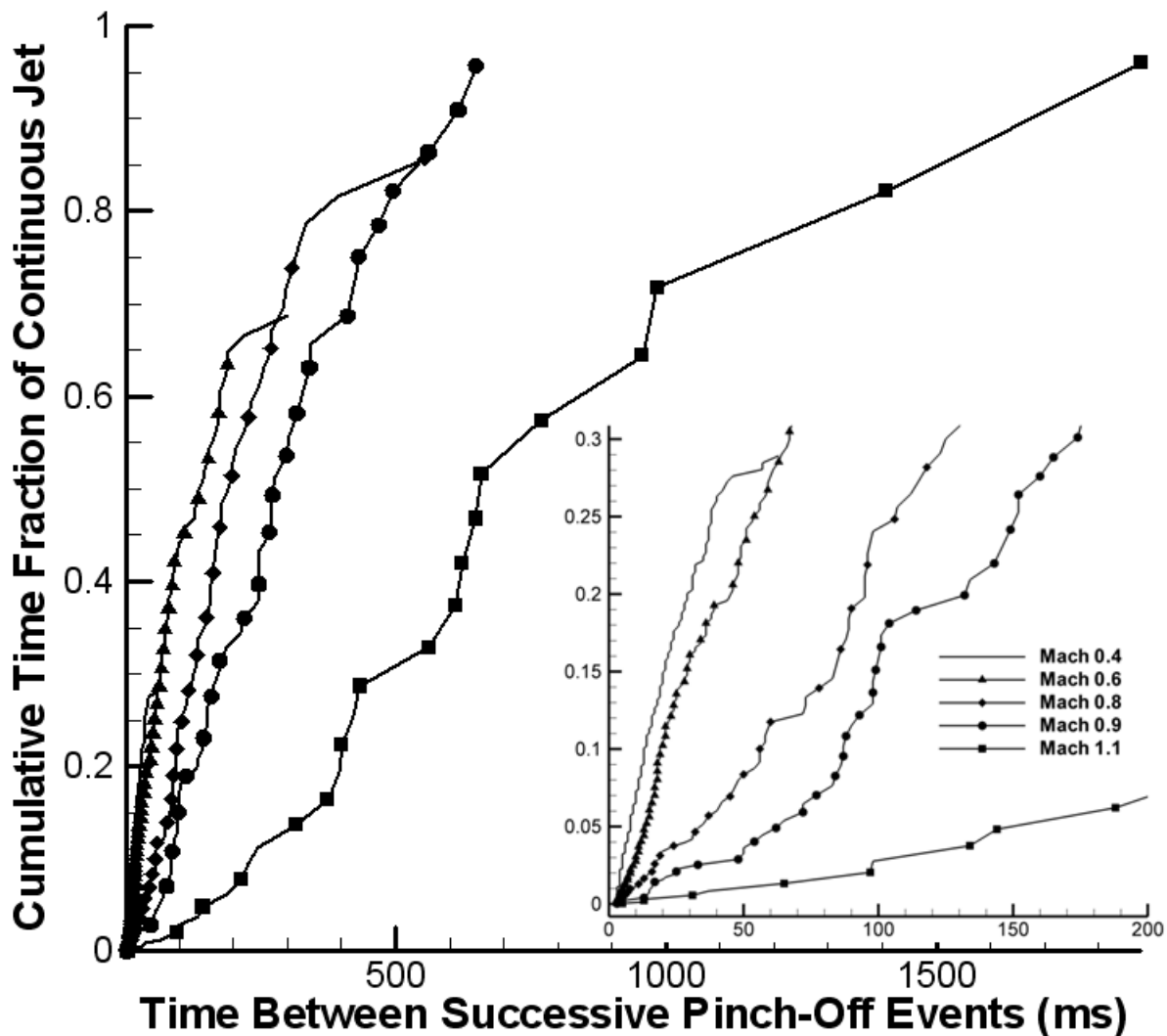


Figure 3.7. The cumulative time fraction of stable jetting behavior is plotted against the time between successive pinch-offs. The time between successive pinch-off events is indicative of the pinch-off frequency. The inset picture is a zoomed in portion to show greater detail.

The pinch-off frequency can be estimated from the inverse time interval between successive pinch-off events which, as can be seen in Figure 3.7, occurs over a range of frequencies. The maximum contributor, in terms of time fraction spent at this pinch-off frequency, is shown in Figure 3.8. The Mach 1.8 jet had a pinch-off frequency of 0 Hz since it never pinched off. The pinch-off frequency drops rapidly as Mach number is increased which is in agreement with Figure 3.7 and other qualitative observations.

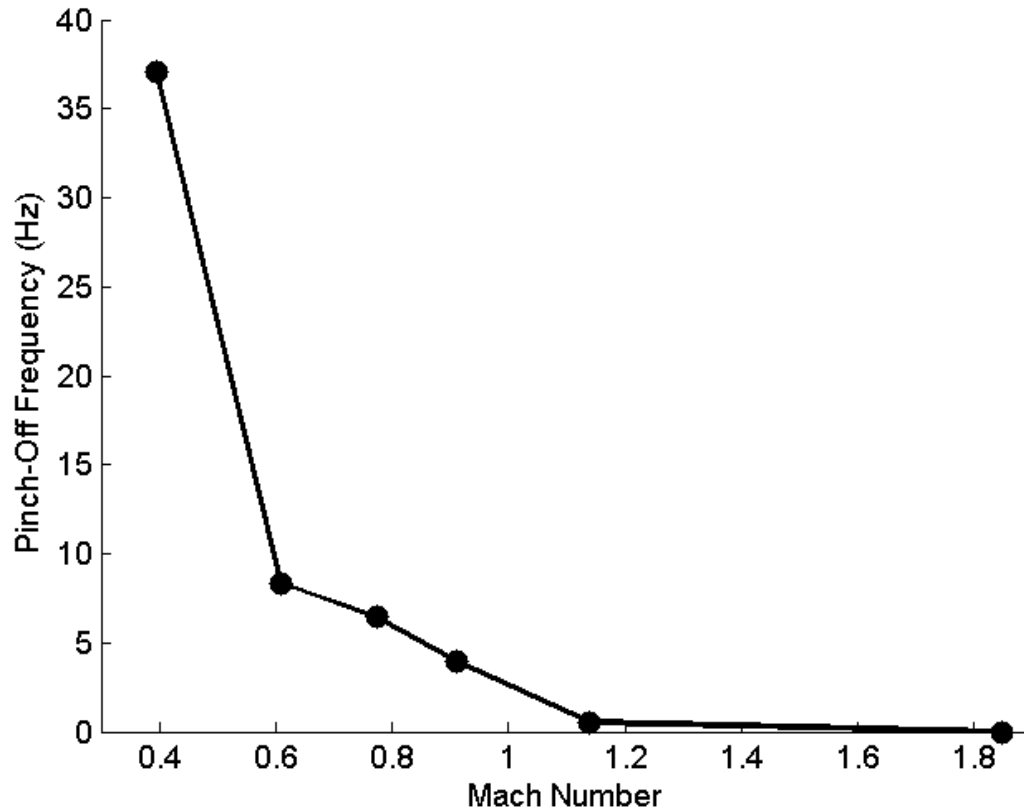


Figure 3.8. Although it was shown that the jets pinch-off at several frequencies, the jet pinch-off frequency shown here is the largest contributor to the pinch-off phenomenon. The jet pinch-off frequency for Mach 1.8 is 0 Hz as the jet never pinched off.

3.5.2 Jet Penetration Distance

The length of gas jet penetration into the ambient water is thought to be governed by several parameters, such as the size of the nozzle, the water depth, and Mach number. In the present tests only the variation in jet penetration with Mach number was studied. The jet penetration can only be described statistically as all gas jets pulsate and undulate through their natural motions. Several previous works [(Castillejos and Brimacombe 1987), (Ozawa and Mori 1986), and (Ito et al. 1991)] have measured the mean void fraction using electroresistive or optical probes lowered into the water and traversed through space. Ozawa and Mori (1986) use this method to determine what they call gas holdup, which is a statistical mapping of how far gas penetrates into the surrounding water. If water was present at the measurement point an electrical circuit was completed and registered a value of 1 and if gas was present a value of 0 was recorded. By summing up all of these values in time for many points in space the time fraction of gas penetration at that point was calculated. Here we implement a similar approach but instead we use our non-invasive imaging that measures the position of the gas jet spatially at each instant of

time. From the digitized images, as shown in Figure 3.3, we sum the values of each pixel over time and divide by the measurement duration to arrive at a time fraction of gas presence for all pixel locations as shown in Figure 3.9 where the color contour indicates the percentage of time that a certain location in the field of view was occupied by gas. A comparison of the Mach 0.4 and Mach 0.9 jets show obvious differences, especially in the length of a gaseous core which occupies a volume for a large percentage of the test record. To quantify and compare this distance between the test cases, we define the jet penetration distance as the maximum centerline location of 98.5% gas occupation averaged over $\pm 0.5D$ about the centerline.

One advantage of this approach is that it enables distinguishing between bubbles that have fractured from the gas jet column and an orifice attached continuous jet, which is not possible using the electroresistive probe. We determine the length of the gas jet penetration only for orifice-attached gas jets, meaning that our calculations ignore any portion of the gas jet that has ruptured and is rising to the surface as an independent bubble.

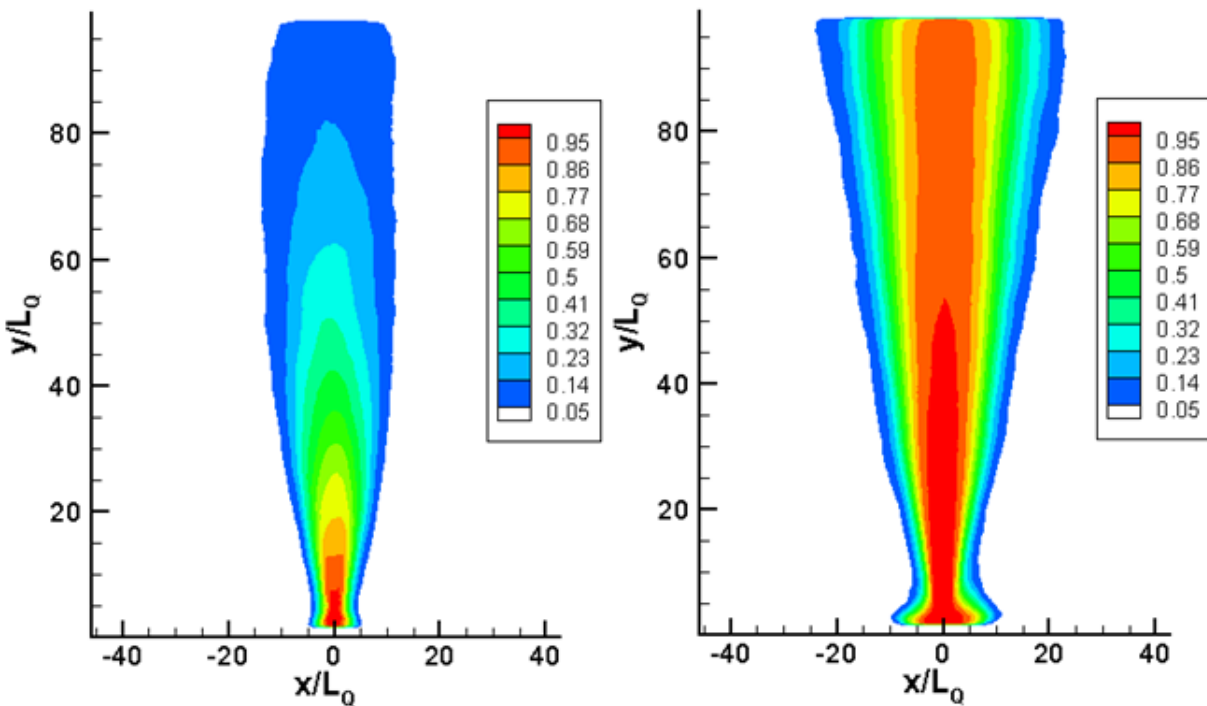


Figure 3.9. Gas holdup contours for a Mach 0.4 jet (left) and Mach 0.9 jet (right). The gas holdup is a statistical mapping of how far gas penetrates into the surrounding water. The transonic gas jet penetrates further into the quiescent fluid statistically than the subsonic gas jet.

Prediction of the jet penetration distance is difficult due to the large density variation between gas and liquid, compressibility of the gas jet, and the inherently unsteady processes

which govern jet pinch-off. Assuming a static force balance on a circular cross section of the jet, we expect the transition from jetting to bubbling to occur at an axial position when momentum and buoyancy forces are approximately equal. This is traditionally described by the parameter L_M in single phase flows (Fischer et al. 1979) to quantify the location from the orifice where the flow is driven by momentum ($y \ll L_M$) or buoyancy effects ($y \gg L_M$). L_M thus corresponds to a distance downstream from the orifice where the ratio of momentum to buoyancy effects is equal as shown in Equation 3.1. D is the orifice diameter, u_o is the gas exit speed, g is the gravitational acceleration, ρ_∞ is the ambient fluid density, and ρ_o is the gas density at the launcher exit.

$$L_M = \frac{\left(\frac{1}{4}\pi D^2 u_o^2\right)^{3/4}}{\left(\left(\frac{1}{4}\pi D^2 u_o\right)g \frac{(\rho_\infty - \rho_o)}{\rho_o}\right)^{1/2}} \quad 3.1$$

The multiphase system encountered in this work is much different from the single phase case as the jet properties vary greatly over axial position. Tross (1974) showed through experiments that submerged gas jets exhibit self-similar behavior and provided relationships to calculate the dynamic pressure, void fraction, and other internal characteristics of submerged gas jets, which were later used as an experimental comparison to the numerical computations of Loth and Faeth (1989) in predicting the evolution of the internal characteristics, such as void fraction of dynamic pressure, of submerged underwater jets. The experimental and numerical results agree reasonably well.

As a first approximation the jet penetration distance is estimated through a static force balance on the gas jet interface where the internal gas jet pressure and the external hydrostatic pressure are the only forces considered. Dynamic forces due to the undulations of the gas jet are not considered. Thus the jet penetration distance corresponds to the distance from the orifice where the internal gas jet pressure cannot withstand the hydrostatic pressure which subsequently leads to collapse of the jet. We estimate the axial position where the gas jet and hydrostatic pressures are equal using the experimental and theoretical framework presented by Tross (1974). According to this work the velocity and void fraction distributions are given by Equations 3.2-3.3 and ζ is a length scale for variable density jets given by Equation 3.4. Here r is radius at

which the velocity u is evaluated, y_N is the distance from the nozzle, and the subscripts c , ∞ , and o denote centerline, ambient, and exit conditions respectively.

$$\frac{u}{u_c} = 0.9975e^{-77.7\left(\frac{r}{\zeta}\right)^2} \quad 3.2$$

$$\frac{\alpha}{\alpha_c} = 0.9897e^{-46.9\left(\frac{r}{\zeta}\right)^2}$$

3.3

$$\zeta = 8.4y_N\left(\frac{\rho_\infty}{\rho_c}\right)^{1/2} \quad 3.4$$

The centerline velocity (u_c), void fraction (α_c), and density (ρ) are given by Equations 3.5-3.8 where the constants computed by Tross are consolidated into bulk constants. Φ is a semi-empirical function which describes the downstream evolution of the gas jet.

$$\Phi = 1 + 2189\left(\frac{y_N}{\rho_o^{1/2}}\right) \quad 3.5$$

$$\frac{1}{\alpha_c} = 3 \times 10^{-4} \rho_o \Phi + \left(1 - \frac{\rho_o}{\rho_\infty}\right) \quad 3.6$$

$$\rho_c = \alpha_c \rho_o + (1 - \alpha_c) \rho_\infty \quad 3.7$$

$$u_c = 2.56\left(\frac{u_o}{\Phi}\right) \quad 3.8$$

The axial position where the dynamic jet and hydrostatic pressures are equal occurs when $L_{M^*} = 1$ in Equation 3.9, which is rearranged into the form given by Equation 3.10 which directly predicts the pinch-off point. Substitution of Equations 3.2-3.8 into Equation 3.10 yields the jet penetration length which was solved for here. The subscript c denotes a centerline property which varies with axial position, g is gravity, y_{N^*} is the predicted pinch-off point, and y_D is the nozzle depth. Note that cases for which $y_{N^*} > y_D$ the jet is not predicted to pinch-off.

$$L_{M^*} = \frac{\rho_c u_c^2}{\rho_\infty - \rho_c} \frac{y_D - y_N}{g} \quad 3.9$$

$$y_{N^*} = y_D - \frac{\rho_c u_c^2}{\rho_\infty - \rho_c} \frac{1}{g} \quad 3.10$$

Both the experimental results from this work and the predicted jet penetration distances are shown in Figure 3.10. The vertical bars represent repeatability across the three trials for each Mach number. The penetration distance including only orifice-attached jets that neglect

independent bubbles which have fractured from the gas jet is shown in Figure 3.10 as open circles. The penetration distance is also computed from the experimental data to simulate the response of an electroresistivity probe by including bubbles that have pinched off from the gas jet and are rising independently and is shown with open squares. Appendix A explains the process of calculating the jet penetration from the experimental data in detail. The orifice attached only jets have a smaller penetration distance than when also considering pinched off bubbles in the measurement, and it is apparent that electroresistivity probes over-estimate the gas jet penetration, particularly at larger Mach number flows. The shaded gray areas indicate the error bounds of the two analytic jet penetration estimates. Estimations of the uncertainty in L_M were computed from a propagation of error calculation while L_{M^*} errors were estimated at 15% (Loth 1988).

The predicted pinch-off points using L_M and L_{M^*} are shown in Figure 3.10 as well. While L_M greatly and consistently overestimates the pinch-off point by about 10-30 diameters, L_{M^*} agrees quite well with the experimental jet penetration distance for the subsonic cases (Mach 0.4, 0.6, 0.8, and 0.9) after which the similarity decreases. The reason for this divergence between theory and experiment is unclear. The Mach 0.4 case is also over predicted and is probably due to this case pertaining to bubbly flow. In other words the unsteadiness of the jet was so great that the mean internal jet characteristics presented by Tross do not hold. It is interesting to note that while L_M predicts a linear jet penetration distance, both experimental and L_{M^*} predictions indicate a quadratic relationship between jet penetration and Mach number, with the experimental data having approximately twice the growth rate of L_{M^*} . The jet penetration distance measured by the simulated electroresistivity probe technique appears to indicate an inflection point near or at the sonic point, but it is unclear if this is in agreement with the actual (orifice attached) penetration distance due to a lack of Mach numbers tested between 1.1 and 1.8. The Mach 1.8 jet is predicted to never pinch-off as $y_{N^*} > y_D$ for all axial positions measured which is in agreement with the experimental results over the limited depths observed.

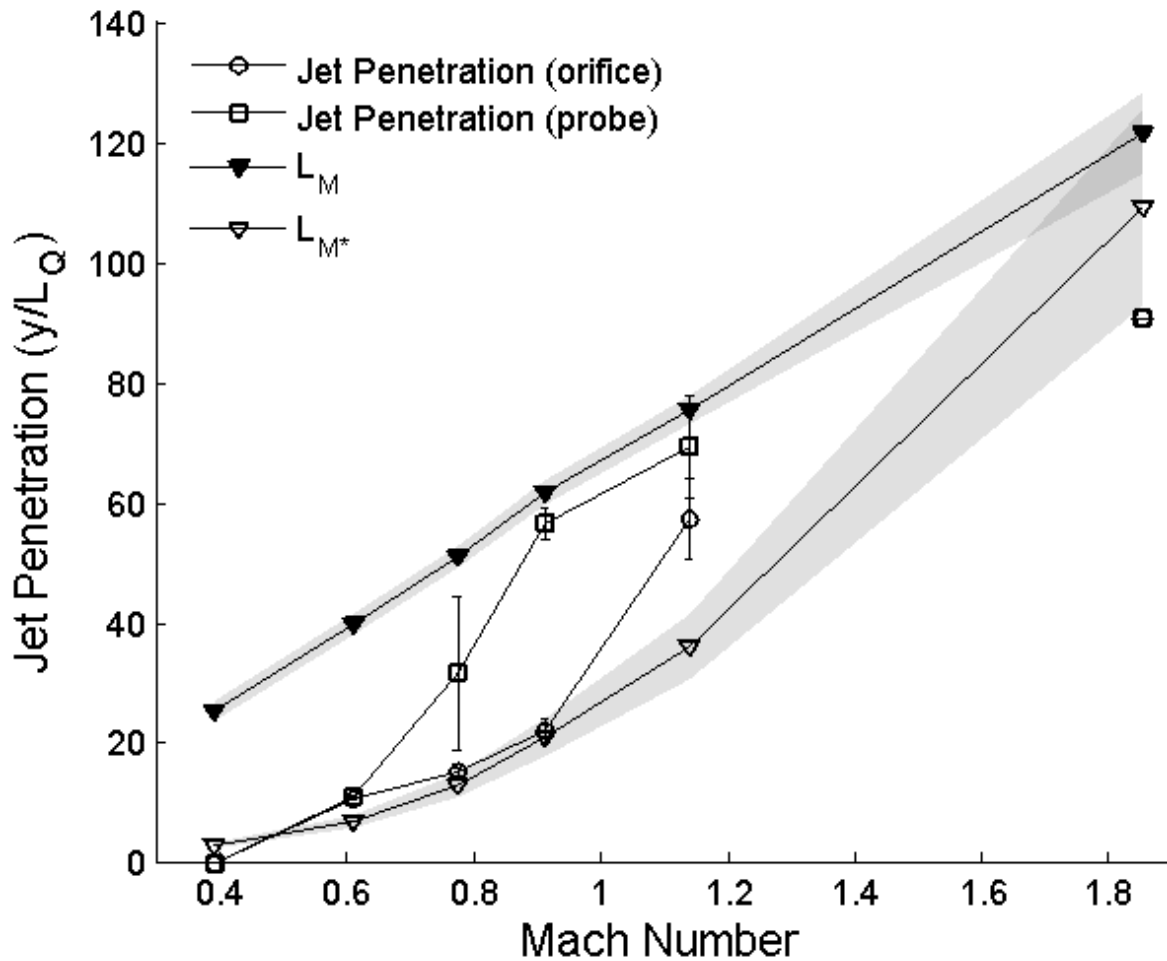


Figure 3.10. The jet penetration distance is calculated using only the jet attached to the orifice (circle) and including bubbles advected downstream (square). The Mach 0.4 jet did not maintain a permanent penetration distance 98.5% of the measurement time and the Mach 1.8 jet never pinched off (penetration length of at least $85 y/L_Q$).

Figure 3.11 compares two metrics for delineating between bubbly and jetting flows. The left plot shows the pinch-off time fraction, or the amount of time the gas jet remained in a pinched-off configuration out of the total measurements period (13.5s), versus the jet penetration distance defined in this paper using the 98.5% contour of orifice attached gas jets. The right plot shows the pinch-off time fraction versus the average interface position at 0.8 mm ($y/L_Q=0.14$) downstream of the orifice. The former metric was defined in this paper and the latter has been used as a metric to define jetting/bubbling behavior in a past work (Mori et al. 1982). As shown in these plots the jet penetration length appears to be a better metric, as the average orifice diameter has no correlation to the pinch-off time fraction. The pinch-off time fraction is clearly a measure of bubbling or jetting behavior over a sampled distance. The reason the latter metric is

less effective is because while some jets can maintain a significant presence at the orifice, and would thus be labeled as jetting, they tend to pinch-off further downstream exhibiting clear bubbly flow behavior. Thus a global measurement technique, such as the optical method presented in this paper, is required to capture this effect. Consider the Mach 0.6 and 0.8 curves in Figure 3.6 which, although they exhibit distinctive peaks in the pinch-off location at $y/L_Q \approx 14$, also include pinch-off locations downstream of $y/L_Q \approx 14$. Obviously this cannot be captured by electrodes at the orifice only, which therefore cannot capture the true dynamics of the flow.

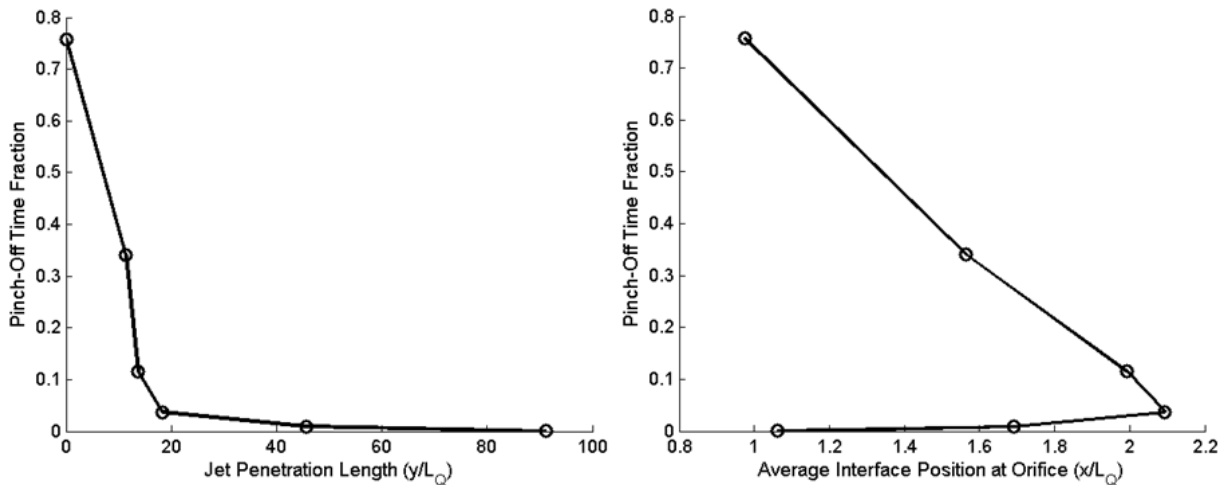


Figure 3.11. A comparison of methods to delineate bubbling and jetting. The left plot shows the pinch-off time fraction against the jet penetration length defined in this paper. The right plot shows the pinch-off time fraction against the average interface position.

3.5.3 Unsteady Interface Characteristics

The average deviation (AD) of the interface radial position was calculated along the jet for all locations where the jet maintained a presence for 80% of the recorded time over a period of 13.5s and is shown in Figure 3.12. The signal was mean-removed prior to calculating the AD values and thus only the unsteadiness of the interface was computed. General trends of the results indicates downstream positions yield more interfacial unsteadiness while larger Mach numbers yield less interfacial unsteadiness.

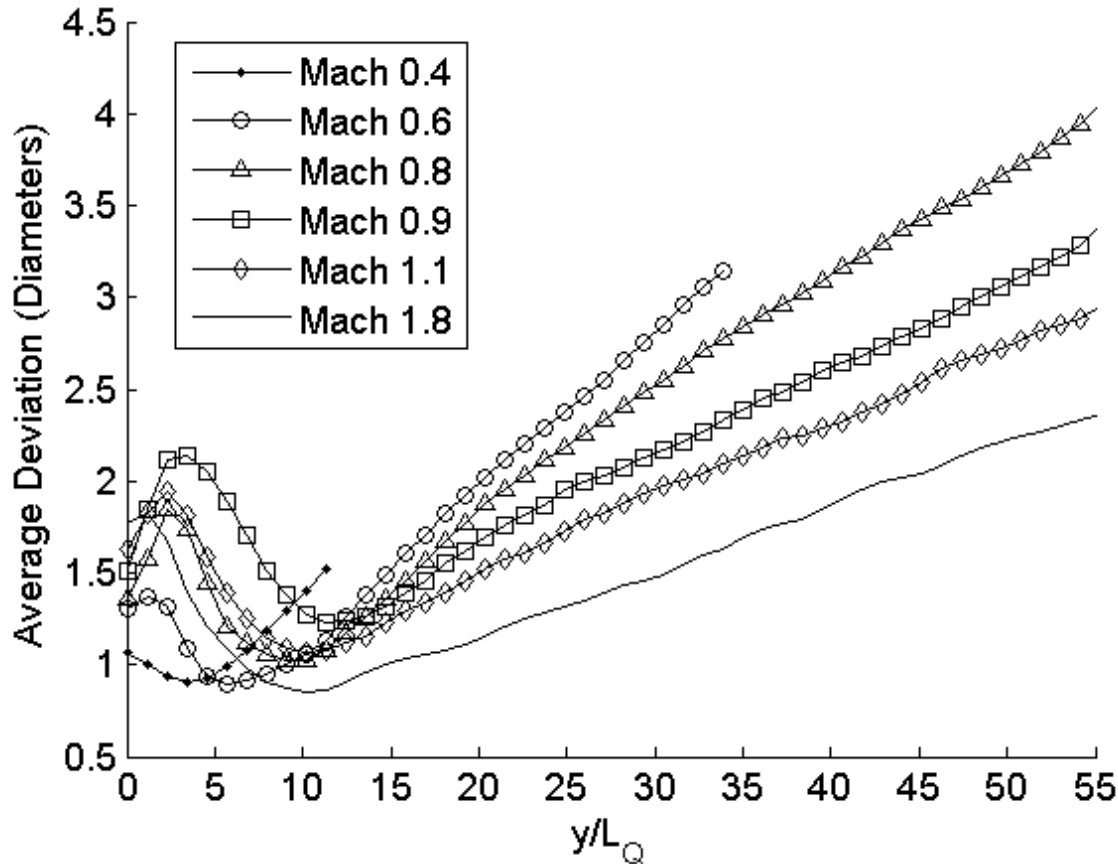


Figure 3.12. In general, the interface unsteadiness increases downstream and decreases for higher Mach numbers. The average deviation calculation was only performed on locations which were not pinched-off for 80% of the total recorded time.

Further analysis of the interfacial unsteadiness yields several interesting observations. The first is that at approximately $y/L_Q \approx 10-11$ Mach numbers 0.6, 0.8, 0.9, and 1.1 undergo a switch in their trends of interfacial unsteadiness. Prior to this location the Mach 0.9 and 1.1 jets have higher unsteadiness but downstream of this point the subsonic Mach numbers have higher unsteadiness. The Mach 0.4 and 1.8 jets do not follow this trend, as the Mach 0.4 jet rapidly overtakes all other jets at $y/L_Q \approx 10$ and the Mach 1.8 jet has the lowest unsteadiness after $y/L_Q \approx 8$. It is readily apparent from these and other observations that Mach 0.4 corresponds to a bubbly flow as opposed to a jetting flow. Given the switch in interfacial behavior for almost all of the Mach numbers at $y/L_Q \approx 10-11$, this position appears to be the jet development length described for single phase jets [(Crow and Champagne 1971); (Fischer et al. 1979)], although in the present experiment we cannot confirm whether this development length is due to internal turbulence levels, compressibility effects, or some other phenomena.

The second observation is that the transonic and supersonic gas jets may have higher unsteadiness near the orifice due to compressibility effects. The presence of a shock cell structure in submerged gas jets was confirmed experimentally by Loth and Faeth (1989) through static pressure measurements just downstream of the orifice. As the interface rapidly expands and contracts near the orifice, this character is felt downstream in the form of a propagating interfacial wave. If the propagating interfacial wave is large enough in amplitude it will induce large interfacial motions which can lead to pinch-off. In the case of transonic and supersonic jets, the rapid oscillation of the gas-liquid interface near the orifice quickly generates a bubbly flow through the Rayleigh-Taylor instability. It is plausible that this bubbly flow surrounding the gas jet near the orifice acts as a damping mechanism to lessen subsequent impulsive oscillations of the interface, which in turn propagates a wave of smaller amplitude downstream. The subsonic gas jets, on the other hand, tend to exhibit low frequency oscillations which do not produce this damping mechanism, and thus all interfacial motions are propagated downstream where they contribute to the overall unsteadiness of the interface.

The third observation is that a maximum in interfacial unsteadiness occurs near the sonic point at $y/L_Q \approx 4.5$ which then decreases in the supersonic region. This result seems to corroborate the work of Chen and Richter (1997) in a qualitative sense as 1) they computed the bubbling to jetting transition to occur at the sonic point and as indicated by the upper subset picture in Figure 3.10 a large jump appears in the gas jet penetration length with a subsequent decrease in the number of pinch-off events in the supersonic regime and 2) they computed that a maximum in the axisymmetric temporal and spatial growth rates occur at the sonic point and which then quickly reduce at supersonic Mach numbers. Although in this work we do not compute growth rates we can infer interface stability based on the unsteadiness of the interface. Here stability is defined by the motion of the interface; a perfectly stable interface is composed of a slowly diverging column of gas rising from the orifice to the free surface with no motion of the interface. Thus it follows that as the interface AD values become smaller the jet approaches a perfectly stable interface. Based on this interpretation, the sonic point does appear to be the least stable Mach number. Additionally, if the interface unsteadiness can be linked to stability, then the slope of the AD versus downstream position is indicative of the spatial instability growth rate. As shown in Figure 3.12 for $y/L_Q > 10$ the slope decreases with increasing Mach number, indicating increasing Mach number yields more stable jets with lower growth rates.

Although stability and the unsteady interface motions reported here are fundamentally different they are phenomenology similar. This is apparent from the results reported here as increased interfacial motions are experimentally correlated to a less stable jet exhibiting a greater number of pinch-off events. Thus, the growth of the interface unsteadiness as it evolves downstream of the orifice may be linked to the spatial growth rate of the interface unsteadiness. The growth rate is presented in Figure 3.13 as the slope of the best fit line which passes through the AD points shown in Figure 3.12. The line was fitted after the inflection point of the AD curve to ensure the jet is fully developed. The results show a steadily decreasing spatial growth rate as Mach number increases. These results are somewhat in agreement with the calculations of Chen and Richter (1997). Although they compute the supersonic regime to be the most stable which is in agreement with the results shown here, they computed a steadily increasing growth rate up to the sonic point which is clearly not seen here. The reason for this discrepancy is not clear, although Chen and Richter (1997) assumed an idealized interface with no mixing which is not realized here.

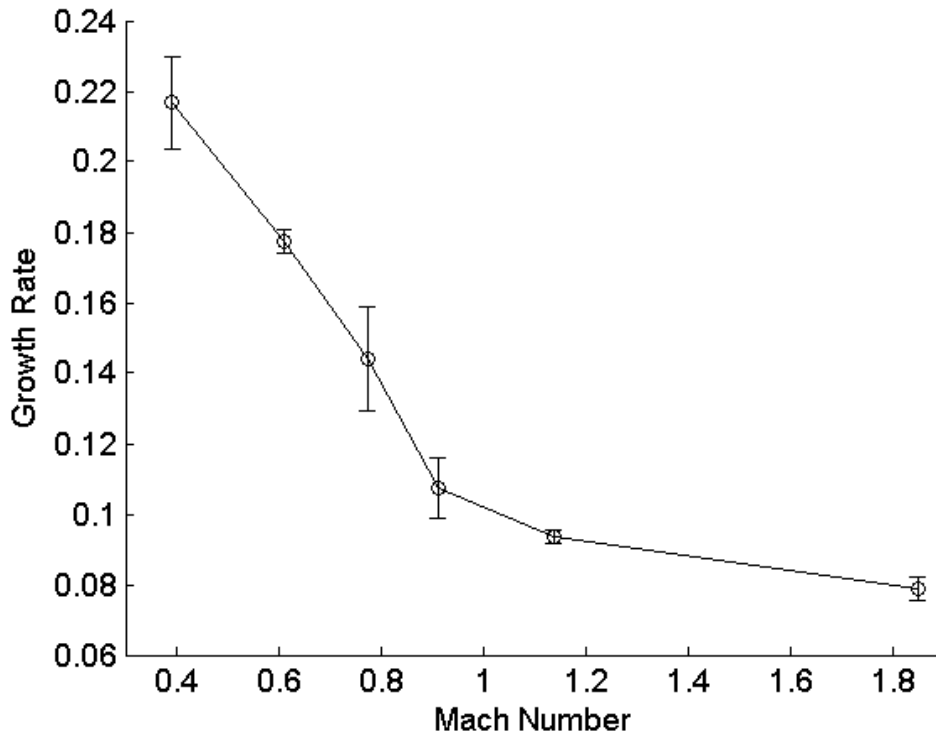


Figure 3.13. The spatial growth rate decreases with increasing Mach number. The growth rate is a nondimensional scale representing the rate of interface unsteadiness downstream and is given by the slope of the best fit line passing through the AD points.

3.5.4 Kelvin-Helmholtz versus Rayleigh-Taylor Instabilities

The submerged gas jet, due to the large density difference between the jet and the surrounding fluid and the high speed jet flow at the interface, will be subject to both Rayleigh-Taylor (RT) and Kelvin-Helmholtz (KH) instability mechanisms. For jets typically only the KH instability is considered as the dominant mechanism (Chawla 1975). Here we investigate the relative importance between the two mechanisms on the interface in a manner similar to Epstein et al (2001), who estimated entrainment rates in an expanding underwater gas bubble. The relative importance of the instability mechanisms was given by Epstein et al and is shown in Equation 3.11, where ρ is density (∞ or g denoting liquid or gas, respectively), a is the interfacial acceleration, u is the gas flow velocity, R is the interfacial radial position, and σ is the surface tension between water and air. The surface tension is assumed constant along the interface. Kelvin-Helmholtz instability dominates for $\Psi \ll 1$ and Rayleigh-Taylor instability dominates for $\Psi \gg 1$.

$$\Psi = \frac{\sigma \rho_l a_{r=R}}{\rho_g^2 u_{r=R}^4} \quad 3.11$$

Equation 3.11 requires the acceleration of the interface and the gas velocity near the interface (at position $r=R$) since these drive the RT and KH instabilities, respectively. We use the theoretical framework and experimental measurements of Tross (1974) presented earlier in Equations 3.2-3.8 to estimate $u(r,y)$. For each axial position, the mean interface position calculated from the experimental data gives the radial position r of the interface. Using this radial position and the framework developed by Tross allows calculation of the average gas jet velocity near the interface. The interfacial acceleration is computed directly from the recorded interface position in time and the RMS of the interface acceleration time history is taken for use in Equation 3.11 to calculate the average relationship. All derivatives were taken as central differences and the averaging RMS calculation of the interface signal helps to reduce errors associated with twice differentiating the interface signal. The results are shown in Figure 3.14. Note that the interface accelerations were only calculated for locations where the interface existed 80% of the time, in order to ensure accurate interface acceleration computations. These results indicate that for all of the jets tested the effects of the RT instability are of the same importance as the KH instability. It should be noted that these results are heavily dependent upon the estimation of $u(r)$. If the centerline velocity is used in Equation 3.11 as the velocity the results indicate that the supersonic

gas jets are computed to be dominated by KH instability and the subsonic gas jets show tendencies of both RT and KH instability mechanisms based on their distance from the orifice. However, it is important to consider that it is not the centerline jet velocity which drives the KH instability, but rather the gas velocity near the interface.

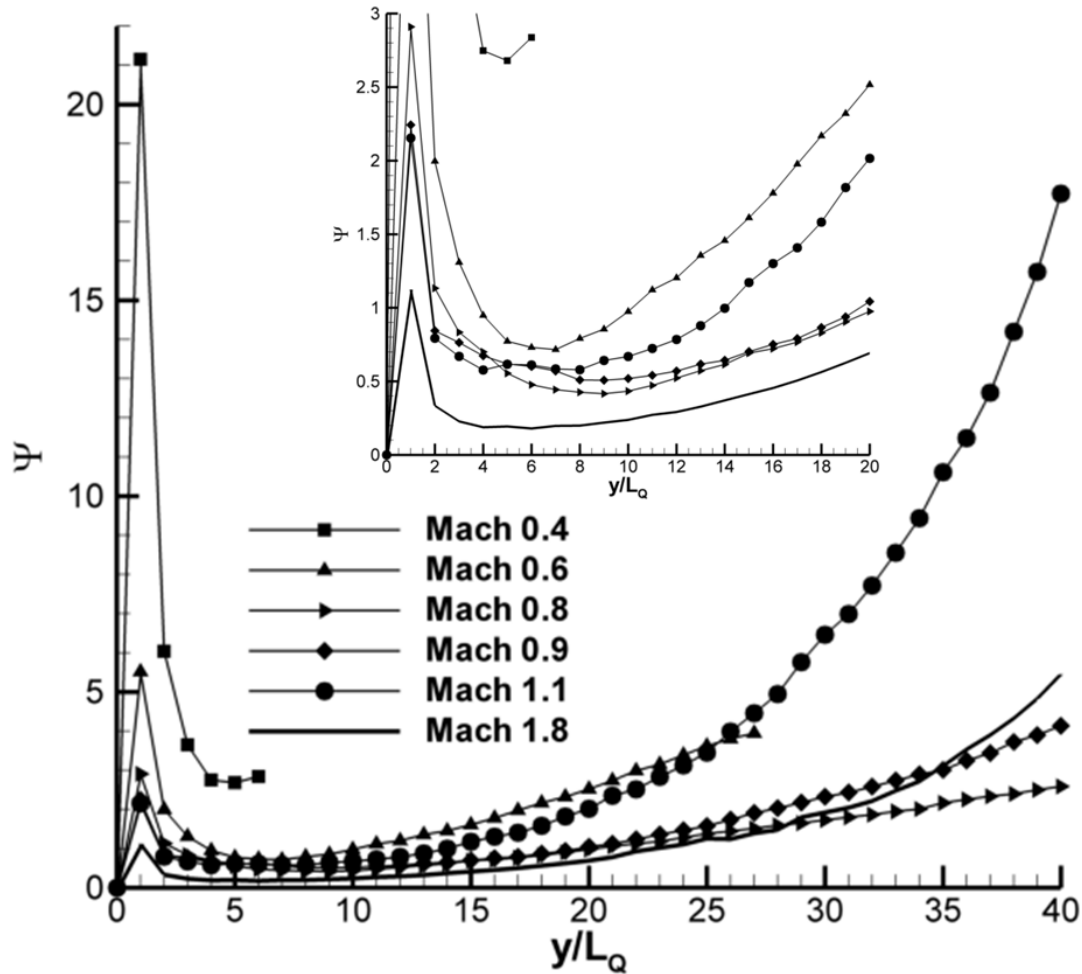


Figure 3.14. The submerged gas jet exhibits a high oscillatory motion as a function of Mach number. The relative importance of the two instabilities associated with the gas jet is dependent on both Mach number and axial position, but these results indicate that the RT is just as important as KH in governing the interfacial stability.

3.6 Conclusions

Direct measurements of the interfacial behavior of submerged high speed gas jets ranging from subsonic to supersonic Mach numbers were performed using high speed digital photography. While past researchers have relied on pressure history at the injection point or electrode contact circuits to determine the jetting/bubbling transition point, as far as the authors

know, this work is the first to directly measure the entire interface in both space and time simultaneously. There are several main conclusions of this work:

1. Buoyant jets were observed to consistently pinch-off at a spatial location corresponding to the maximum axial velocity turbulence fluctuations, namely on the interval $10 < y/L_Q < 15$. This suggests that buoyant jets are very sensitive to the internal turbulence levels, which experiments have shown reach a peak at $y/L_Q \sim 10$ in single phase jets.
2. The electroresistive probe technique used by many researchers to establish a jet penetration distance inherently biases the measurement by as much as 30 diameters. This is due to the probe technique not distinguishing between orifice attached jets – crucial to the definition of jetting – and bubbles which break from the jet and advect upwards.
3. The jet penetration distance defined in this paper is an improved metric for defining jetting as opposed to the bubble diameter at the orifice. A simple force balance on the gas jet based on measurements by others agrees reasonably well with the experimentally measured jet penetration distance. The classic jetting length L_M does not perform well for estimating this distance for buoyant gas jets.
4. The jet unsteadiness near the orifice is a function of the Mach number and reaches a peak near the sonic point suggesting that these are the least stable in terms of interfacial motion. The sonic point was observed to be the bubbling/jetting transition point as the jet penetration distance increased markedly after this point. The spatial instability growth rate was shown to decrease as the Mach number was increased.
5. The RT and KH instability mechanisms are in constant competition as driving mechanisms for instability and mixing along the interface. The results presented herein show that in the average, the RT is equally important as KH for all Mach numbers if an estimate on the axial velocity near the interface is used. This estimate is very sensitive to the gas velocity used in the calculation.

3.7 Acknowledgements

This research was sponsored by the Naval Surface Warfare Center, Dahlgren Division. Mr. John Busic and Dr. Jon Yagla served as the technical monitors. Their support is gratefully acknowledged.

3.8 References

- Batchelor, G. K. (1967). An Introduction to Fluid Dynamics, Cambridge University Press.
- Birkhoff, G. (1962). "Helmholtz and Taylor Instability." Proc. Sym. App. Math **13**: 21.
- Brodkey, R. S. (1967). The Phenomena of Fluid Motions, Dover.
- Castillejos, A. H. and J. K. Brimacombe (1987). "Measurement of Physical Characteristics of Bubbles in Gas-Liquid Plumes .1. an Improved Electroresistivity Probe Technique." Metallurgical Transactions B-Process Metallurgy **18**(4): 649-658.
- Chawla, T. C. (1975). "Kelvin-Helmholtz Instability of Gas-Liquid Interface of a Sonic Gas Jet Submerged in a Liquid." Journal of Fluid Mechanics **67**(FEB11): 513-537.
- Chawla, T. C. (1975). "Rate of Liquid Entrainment at Gas-Liquid Interface of a Liquid Submerged Sonic Gas Jet." Nuclear Science and Engineering **56**(1): 1-6.
- Chen, K. and H. J. Richter (1997). "Instability analysis of the transition from bubbling to jetting in a gas injected into a liquid." International Journal of Multiphase Flow **23**(4): 699-712.
- Cieslinski, J. T. and R. Mosdorf (2005). "Gas bubble dynamics - experiment and fractal analysis." International Journal of Heat and Mass Transfer **48**(9): 1808-1818.
- Crow, S. C. and F. H. Champagne (1971). "Orderly structure in jet turbulence." Journal of Fluid Mechanics **48**(03): 547-591.
- Dai, Z. Q., B. Y. Wang, L. X. Qi and H. H. Shi (2006). "Experimental study on hydrodynamic behaviors of high-speed gas jets in still water." Acta Mechanica Sinica **22**(5): 443-448.
- Darmana, D., N. G. Deen and J. A. M. Kuipers (2005). "Detailed modeling of hydrodynamics, mass transfer and chemical reactions in a bubble column using a discrete bubble model." Chemical Engineering Science **60**(12): 3383-3404.
- Dimotakis, P. E., R. C. Miakelye and D. A. Papantoniou (1983). "Structure and Dynamics of Round Turbulent Jets." Physics of Fluids **26**(11): 3185-3192.
- Epstein, M., H. Fauske, S. Kubo, T. Nakamura and K. Koyama (2001). "Liquid entrainment by an expanding core disruptive accident bubble - a Kelvin/Helmholtz phenomenon." Nuclear Engineering and Design **210**: 24.
- Fischer, H., E. List, R. Koh, J. Imberger and N. Brooks (1979). Mixing in Inland and Coastal Water. New York, Academic Press.
- Helmholtz, H. v. (1868). "On discontinuous movements of fluids." Phil. Mag. **36**(4): 9.
- Ito, K., S. Kobayashi and M. Tokuda (1991). "Mixing Characteristics of a Submerged Jet Measured Using an Isokinetic Sampling Probe." Metallurgical Transactions B-Process Metallurgy **22**(4): 439-445.
- Kelvin, W. (1871). "Hydrokinetic solutions and observations." Phil. Mag. **42**(4): 15.
- Kitscha, J. and G. Kocamustafaogullari (1989). "Breakup Criteria for Fluid Particles." International Journal of Multiphase Flow **15**(4): 573-588.
- Liepmann, H. and A. Roshko (1957). Elements of Gasdynamics. New York, John Wiley & Sons.
- Lin, C. C. and D. J. Benney (1962). "On the Instability of Shear Flows." Proc. Sym. App. Math **13**: 24.
- Loth, E. (1988). Study of Underexpanded Turbulent Air Jets in Water. Ann Arbor, The University of Michigan. **PhD**.
- Loth, E. and G. M. Faeth (1989). "Structure of Underexpanded Round Air Jets Submerged in Water." International Journal of Multiphase Flow **15**(4): 589-603.
- McNallan, M. J. and T. B. King (1982). "Fluid-Dynamics of Vertical Submerged Gas Jets in Liquid-Metal Processing Systems." Metallurgical Transactions B-Process Metallurgy **13**(2): 165-173.

- Mori, K., Y. Ozawa and M. Sano (1982). "Characterization of Gas-Jet Behavior at a Submerged Orifice in Liquid-Metal." Transactions of the Iron and Steel Institute of Japan **22**(5): 377-384.
- Ozawa, Y. and K. Mori (1986). "Effect of Physical-Properties of Gas and Liquid on Bubbling Jetting Phenomena in Gas Injection into Liquid." Transactions of the Iron and Steel Institute of Japan **26**(4): 291-297.
- Rayleigh, J. (1879). "On the instability of jets." Proc. Lond. Math. Soc. **10**: 10.
- Ruzicka, M. C., J. Drahos, J. Zahradnik and N. H. Thomas (1997). "Intermittent transition from bubbling to jetting regime in gas-liquid two phase flows." International Journal of Multiphase Flow **23**(4): 671-682.
- Sahai, Y. and R. I. L. Guthrie (1982). "Hydrodynamics of Gas Stirred Melts .1. Gas-Liquid Coupling." Metallurgical Transactions B-Process Metallurgy **13**(2): 193-202.
- Shapiro, A. (1953). The Dynamics and Thermodynamics of Compressible Fluid Flow. New York, John Wiley & Sons.
- Tross, S. (1974). Characteristics of a Turbulent, Two-Phase, Submerged, Free Jet. Mechanical Engineering. University Park, The Pennsylvania State University. **Masters Thesis**.
- Wang, H. W. and A. W. K. Law (2002). "Second-order integral model for a round turbulent buoyant jet." Journal of Fluid Mechanics **459**: 397-428.
- Wraith, A. and M. Chalkly (1977). Advances in Extractive Metallurgy. M. Jones. London, IMM.
- Zhao, Y. F. and G. A. Irons (1990). "The Breakup of Bubbles into Jets During Submerged Gas Injection." Metallurgical Transactions B-Process Metallurgy **21**(6): 997-1003.

4. THE EFFECT OF MACH NUMBER AND ASPECT RATIO ON THE INTERFACIAL CHARACTERISTICS OF A SUBMERGED RECTANGULAR GAS JET

Chris J. Weiland¹ and Pavlos P. Vlachos²
Virginia Tech Mechanical Engineering Dept

¹ Graduate Research Assistant, Virginia Tech Mechanical Engineering Department

² Associate Professor, Virginia Tech Mechanical Engineering Department

To Be Submitted to the International Journal of Multiphase Flow

4.1 Abstract

Gas jets formed by rectangular nozzles submerged in water were studied using a non-invasive photographic technique which allowed simultaneous measurements of the entire interface. Three aspect ratios were considered corresponding to 2, 10, and 20 with all nozzles sharing a common width. As far as the authors know this study represents the first time the effects of aspect ratio and Mach number on a submerged gas jet have been studied. The results indicate aspect ratio and Mach number play a large role in dictating both the unsteadiness of the interface and the penetration of the gas jet into the surrounding liquid medium. The jet pinch-off is shown to have a logarithmic decay with increasing Mach number and when appropriately scaled by the total viewing length and a geometric length scale (L_Q) is relatively constant across all aspect ratio nozzles. The location of pinch-off is also a function of aspect ratio, with the subsonic aspect ratio 2 nozzles showing maximum pinch-off at $y/L_Q \approx 23-26$ while sonic and supersonic Mach numbers have peaks over the range $y/L_Q \approx 11-14$. The AR 10 and 20 nozzles show no dependence on Mach number with the maximum number of pinch-off events observed over the interval $y/L_Q \approx 3-5$. Jet spreading which is indicative of liquid entrainment is also shown to increase with Mach number and aspect ratio. The jet penetration also increases with increasing Mach number and aspect ratio. The spatial instability growth rate was deduced from the downstream evolution of the interfacial unsteadiness and it is shown that the nozzle with aspect ratio of 2 follows a different trend than the aspect ratio 10 and 20 nozzles, suggesting a fundamentally different mechanism dominates the stability of large aspect ratio rectangular gas jets.

Keywords: *submerged gas jet, interfacial stability, buoyant jet*

4.2 Nomenclature

A – orifice exit area (m^2)
 AR – aspect ratio (l/w)
 l – length of nozzle (long dimension)
 L_Q – length scale (l)
 M – Mach number
 P – pressure (Pa)
 T – temperature (K)
 x – radial position (m)
 y – axial position (m)
 w – width of nozzle (short dimension)

Subscripts

e – exit conditions
 H – hydrostatic conditions
 o – stagnation conditions
 p – penetration distance

4.3 Introduction

While the structure and stability of single phase jets have been studied extensively for quite some time, two-phase flow systems formed by a submerged compressible gas jet have received very little attention. The metallurgical industry uses submerged round gas jets for liquid metal stirring and gas-metal reactions as the gas jet enhances mixing efficiency through the high surface to volume ratio of the bubbly mixture [(Mori et al. 1982); (Sano et al. 1986)]. Since the focus of submerged gas injection in most cases is usually on enhancing mixing and mass transfer, rectangular jets are excellent for achieving these goals. Single phase rectangular jets naturally exhibit higher mixing at the interface than circular jets when the aspect ratio increases past approximately 10 (Zaman 1999). Although most studies have focused on round [(Loth and Faeth 1989); (Zhao and Irons 1990)] or planar (Loth and Faeth 1990) gas jets injected into quiescent liquid, the present study focuses on the injection of a rectangular gas jet exhausted into quiescent liquid. In particular, we seek to characterize the effects of aspect ratio and Mach number on the interfacial structure formed by the two-phase system.

While gas jets submerged in liquid are not understood very well, single phase plane and rectangular jets are extensively analyzed [(Deo et al. 2007); (Gutmark and Wygnanski 1976)]. Planar jets include end-walls at either end of the nozzle span to limit three-dimensional effects while rectangular jets omit the end-walls. Here we review both planar and rectangular jets in order to illustrate some of the physics common to both configurations.

Of particular interest to the present study is the existence of ordered structure in the plane jet. The experiments of Antonia et al (1983) support the existence of counter-rotating spanwise structures through space-time correlations of point measurements in the planar jet. Near the jet exit prior to merging of the shear layers, these structures are symmetric about the centerline. The structures are asymmetric after the shear layers merge. Gordeyev and Thomas [(1999); (2000)] provided an exhaustive analysis of the similarity region of a turbulent planar jet and directly observed the asymmetry of the large scale structures. They note that these structures interact with one another, which could explain the “jet flapping” commonly observed in plane jets. The jet was acoustically excited above and below the long dimension of the nozzle orifice at the fundamental frequency while varying the phase between the two acoustic excitation sources. They found that many aspects of the jet such as spreading rates, velocity fluctuations, and their spectral distributions can be effectively controlled through artificial excitation, which is a further manifestation of the importance of the shear layer merger on the bulk jet properties.

Single phase rectangular jets have also been studied although with much less frequency than planar or axisymmetric jets. Rectangular jets, with no end-plate to limit three-dimensional effects near the nozzle, have been shown to have three-dimensional effects and provide a convenient flow field for studying three-dimensional effects in shear layers [(Sforza et al. 1966); (Lozanova and Stankov 1998)]. Hot-wire measurements by Krothapalli et al (1981) and the work of Sforza et al (1966) indicate three regions in the development of a rectangular jet, namely the potential core (initial) region, a two-dimensional (characteristic) region, and an axisymmetric (fully developed) region; the latter two regions are characterized by their velocity profiles and decay rates, which resemble either two-dimensional planar or axisymmetric velocity profiles respectively. The results of Krothapalli et al (1981) and others suggest that the two-dimensional region begins to develop when the shear layers from the small nozzle dimension merge, and the axisymmetric character develops when the shear layers from the large nozzle dimension merge. In the axisymmetric region all memory of the original nozzle configuration is lost. Sforza et al (1966) identify a fourth region in which the flow is fully axisymmetric far downstream of the orifice.

For the case of rectangular jets as opposed to planar jets the path to a fully axisymmetric flow is enhanced due to mixing at the corners of the rectangular nozzle, which introduce sharp gradients and tend to smear rapidly and enhance mixing. Tam and Thies (1993) derived the

equations of stability for a rectangular jet using a vortex sheet model and numerically showed four linearly independent families of instability waves. The first and third are due to the nozzle corners, and as such tend to dampen out as the jet mixes and becomes more axisymmetric. Thus the literature contains two competing explanations for why the rectangular jet transitions towards an axisymmetric configuration: the sharp gradients located at the nozzle corners and the merging of the jet shear layers. In planar jets, it is commonly accepted that the merger of the shear layers (from the small nozzle dimension) play a role in the mean jet characteristics, such as potential core length, although some evidence suggests that aspect ratio may play a role as well (Deo et al. 2007).

The effect of aspect ratio on mean flow characteristics in rectangular jets has been studied in some detail. Common to large (>5) aspect ratio rectangular jets is the saddle-shaped mean streamwise velocity profile [(Krothapalli et al. 1981); (Sforza et al. 1966); (Sfeir 1979)]. Quinn (1991) studied two rectangular nozzles having aspect ratios of 2 and 10 and confirmed the presence of the saddle-shaped mean streamwise velocity profile for aspect ratio 10 and its failure to exist for an aspect ratio 2 nozzle. Tsuchiya and Horikoshi (1986) studied small aspect ratio rectangular jets as well, with nozzles having aspect ratios less than 5. They found a large difference in the turbulence intensity as a function of aspect ratio. Krothapalli et al (1981) also reported the effects of aspect ratio on the development of single phase rectangular jets and note that the downstream distance where the velocity profile follows similarity seems to depend on aspect ratio, mainly due to merging of the shear layers located in the plane of the long nozzle dimension. Using hot-wire anemometer measurements Sfeir (1979) confirmed the importance of aspect ratio on velocity decay and more importantly, showed the departure from two-dimensional effects which are related to the nozzle aspect ratio.

The injection of gas into liquid introduces an additional level of complexity in the jet character, which is marked by unsteadiness and pulsating of the phase interface. The submerged jet can even rupture into bubbles which rise independently, a phenomenon known as pinch-off. When pinch-off occurs near the orifice damage to the submerged injector can occur (Sahai and Guthrie 1982). To prevent damage to the injector it is common for submerged jets in both planar and round configurations to operate with a sonic (convergent) nozzle. Loth and Faeth (1990) reported the internal structure of vertical underexpanded planar nozzles. Underexpansion ratios as high as 4 were tested and as a result pressure measurements taken inside the gas jet showed

the presence of a shock-cell expansion region downstream of the nozzle exit for the first time. Also, void fraction measurements indicated that the half-widths were 2 to 3 times greater than that of single phase plane jets. However their measurements, such as the interface position, are only time averaged quantities. In fact all past measurements of multiphase gas systems known to the authors utilize time averaged quantities to deduce physical mechanisms responsible for the observed behaviors. These analysis methods conflict with what many past studies have shown, namely that the interface is dynamic and constantly evolving.

The goal of the present experiment is to study the interfacial character of the submerged rectangular gas jet. While the nozzle and flow system were instrumented to provide measurements of the internal nozzle Mach number at the jet exit plane, no measurements of the internal jet structure were taken. In particular, compressibility (Mach 0.4-1.5) and aspect ratio (2, 10, and 20) were varied to ascertain their effects on the jet penetration and interface characteristics, which was measured directly using high speed digital photography. To the authors' knowledge, this study represents the first study of submerged rectangular gas jets and the first time quantitative time-resolved measurements of the interface position have been attempted.

4.4 Experimental Methods and Facilities

The experiments were conducted in the Advanced Experimental Thermofluid Engineering Research Laboratory of the Mechanical Engineering Department at Virginia Tech. The experimental setup is shown in Figure 4.1 and consists of a clear acrylic tank, an injector assembly, pressure and temperature sensors, a fast acting valve which impulsively switched on the gas injection, and a high speed camera which recorded shadowgraph images of the underwater jet. The tests were controlled by a LabVIEW program which simultaneously triggered the high speed camera (Photron APX-RX), monitored various gas pressures and temperatures, and opened the fast acting valve which delivered gas flow to the injector. This allowed for the establishment of an accurate reference time, and synchronization between the sensors and the recorded images. The test matrix is shown in Table 4.1 where all properties, such as the Reynolds and Richardson numbers, are calculated based on the initial (orifice exit) properties. Here the Reynolds number uses the nozzle width (short dimension) as the

characteristic length scale. The Mach number is calculated for the gas phase only at the exit of the nozzle.

Table 4.1. Test matrix for all Mach numbers tested. All jets were shot at 0.46m water depth and the properties shown here were calculated for the nozzle exit.

	Mach Number	P_e (Pa $\times 10^5$)	P_o (Pa $\times 10^5$)	P_e/P_o	P_e/P_H	T_o (K)	Mass Flow (kg/s)	Velocity (m/s)	Reynolds No ($\times 10^4$)
AR 2	0.50	1.05	1.13	0.93	1.013	300.2	0.0010	165	1.72
	0.63	1.05	1.17	0.90	1.014	300.6	0.0013	210	2.14
	0.82	1.05	1.27	0.83	1.014	300.7	0.0018	270	2.70
	0.97	1.05	1.51	0.70	1.016	300.8	0.0023	320	3.14
	1.10	1.09	2.28	0.48	1.052	299.9	0.0034	340	3.46
	1.36	1.04	3.07	0.34	1.006	300.1	0.0047	401	4.08
	1.50	1.04	3.71	0.28	1.002	300.8	0.0050	430	4.38
AR 10	0.48	1.03	1.09	0.94	0.989	300.6	0.0040	165	1.64
	0.64	1.03	1.15	0.89	0.99	300.7	0.0055	210	2.16
	0.84	1.04	1.29	0.81	0.999	300.4	0.0078	270	2.76
	1.01	1.06	1.55	0.69	1.025	300.2	0.0105	320	3.24
	1.07	1.09	1.98	0.55	1.047	299.8	0.0125	340	3.40
	1.36	1.04	2.79	0.37	0.999	300.6	0.0176	401	4.10
	1.52	1.04	3.57	0.29	1.003	300.5	0.0201	430	4.42
AR 20	0.47	1.05	1.10	0.95	1.01	300.3	0.0074	165	1.62
	0.60	1.05	1.16	0.91	1.014	300.2	0.0100	210	2.02
	0.80	1.06	1.24	0.85	1.02	300.7	0.0142	270	2.65
	1.00	1.08	1.44	0.75	1.037	300.6	0.0192	320	3.20
	1.13	1.07	1.68	0.64	1.031	300.9	0.0207	340	3.56
	1.30	1.05	2.22	0.47	1.009	299.8	0.0262	401	3.96
	1.57	1.03	3.27	0.31	0.995	299.6	0.0343	430	4.52

The injector was rigidly held upright in an acrylic tank using a steel bracket bolted to the injector as shown in Figure 4.1. The injectors were submerged in an acrylic tank at a constant depth of 0.46 m with a wave breaker constructed from 3 layers of perforated sheet to limit surface waves and provide a constant hydrodynamic pressure, which was calculated using a Druck PTX-7217 barometric load cell (range: 79–120 kPa absolute, 0.1% full scale accuracy) to measure the atmospheric pressure and a known and closely controlled water depth. Although past researchers have shown that wave dampers do little to change the flow characteristics [(Loth and Faeth 1989); (Dai et al. 2006)], the wave damper has the added benefit of forcing the ambient water to reach a quiescent conditions more quickly after a test.

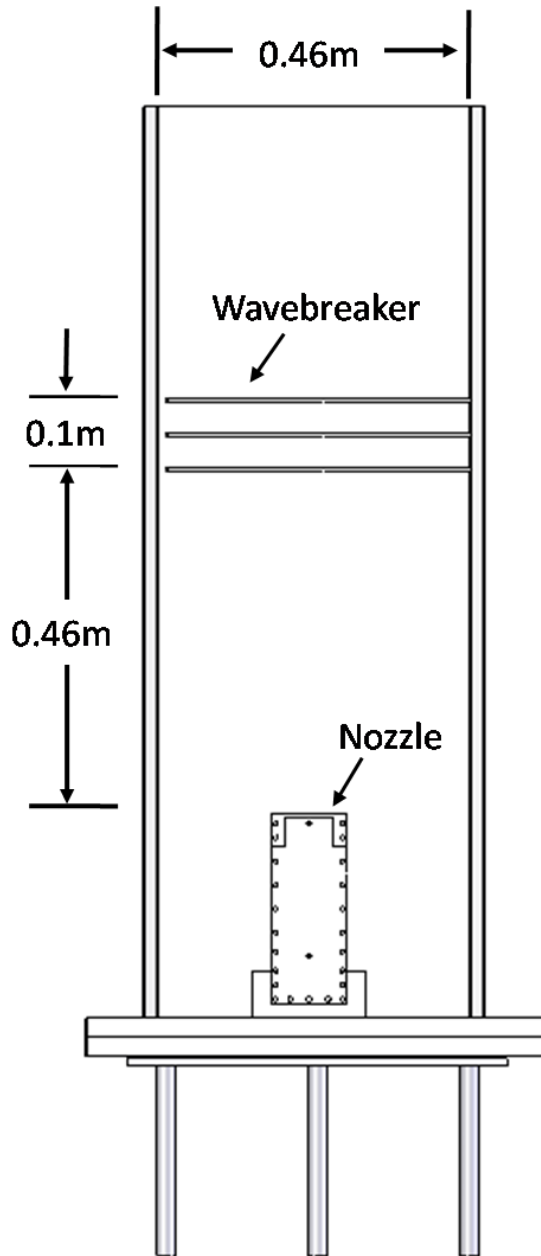


Figure 4.1 View of the injector inside the acrylic tank. Perforated sheets helped to control surface disturbances. A steel angle bracket was bolted to the injector to secure it upright.

Three injectors having aspect ratios of 2, 10, and 20 were studied with a common width (w) of 1.5mm (0.0625 inches) with three lengths (l). The nozzles were cut from Acrylic sheet using a Universal Laser CNC laser cutter to dimensions specified in CAD drawings. The nozzle dimensions were measured to ensure accuracy. For each aspect ratio four nozzles were CNC laser cut: one nozzle for the subsonic (Mach 0.5, 0.6, and 0.8) and sonic test cases and one for each supersonic Mach number (1.2, 1.3, and 1.5). Three trials of each test case were recorded. The nozzles were sandwiched between two aluminum plates as shown in Figure 4.2 and held together with a system of bolts around its perimeter. This unit consisting of the two aluminum side plates and the nozzle insert will hereafter be referred to as the injector. The left picture of Figure 4.2 illustrates the aluminum sides which sandwich the interchangeable nozzle insert, shown as the right picture. Vacuum grease placed between the nozzle insert and the aluminum sides formed a high pressure seal prohibiting gas leakage from all sides. Air was delivered via two gas injection ports and the stagnation pressure was measured in the gas inlet chamber.

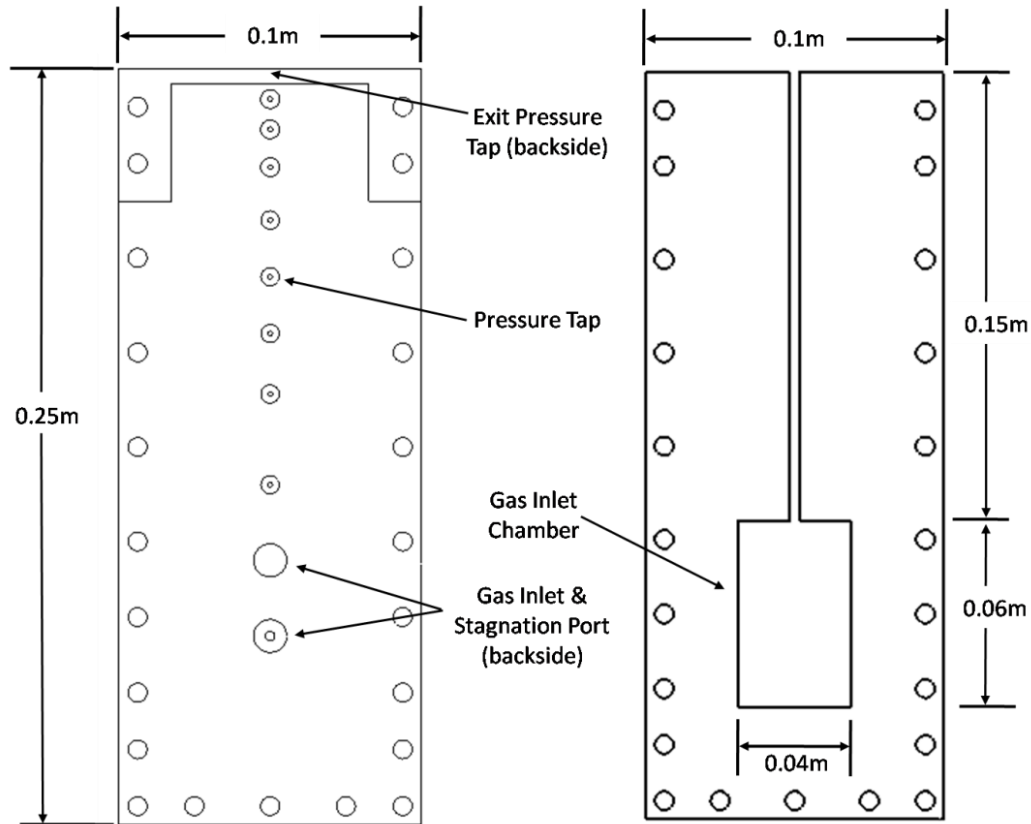


Figure 4.2 The injector is composed of three pieces, the two outer aluminum side plates and the nozzle insert. Picture on left shows outer aluminum piece while the right picture shows the subsonic/sonic aspect ratio 2 nozzle insert.

4.4.1 Operation and Instrumentation Measurements Details

A schematic illustrating the instrumentation and control system is shown in Figure 4.3. The system was designed to deliver a constant mass flow to the injector. A pressure reservoir (0.23m³ volume) was used in conjunction with a gas pressure regulator (Generant model 2GDR-1000B-V-B) that was insensitive to backpressure changes (1.7 kPa output change in flow pressure given 0.69 MPa input change) in reservoir pressure. The pressure downstream of the gas regulator was monitored to ensure a constant delivery pressure. Prior to each test the pressure reservoir was charged from an external gas source until the maximum pressure was attained. The manual valve was then closed to prohibit any line pressure spikes from interfering with the injector gas flow. During each test, the change in the vessel pressure and temperature was monitored to calculate the mass flow rate delivered to the injector using the ideal gas equation. In all cases dried air was used as the working fluid and untreated tap water was used as the quiescent fluid.

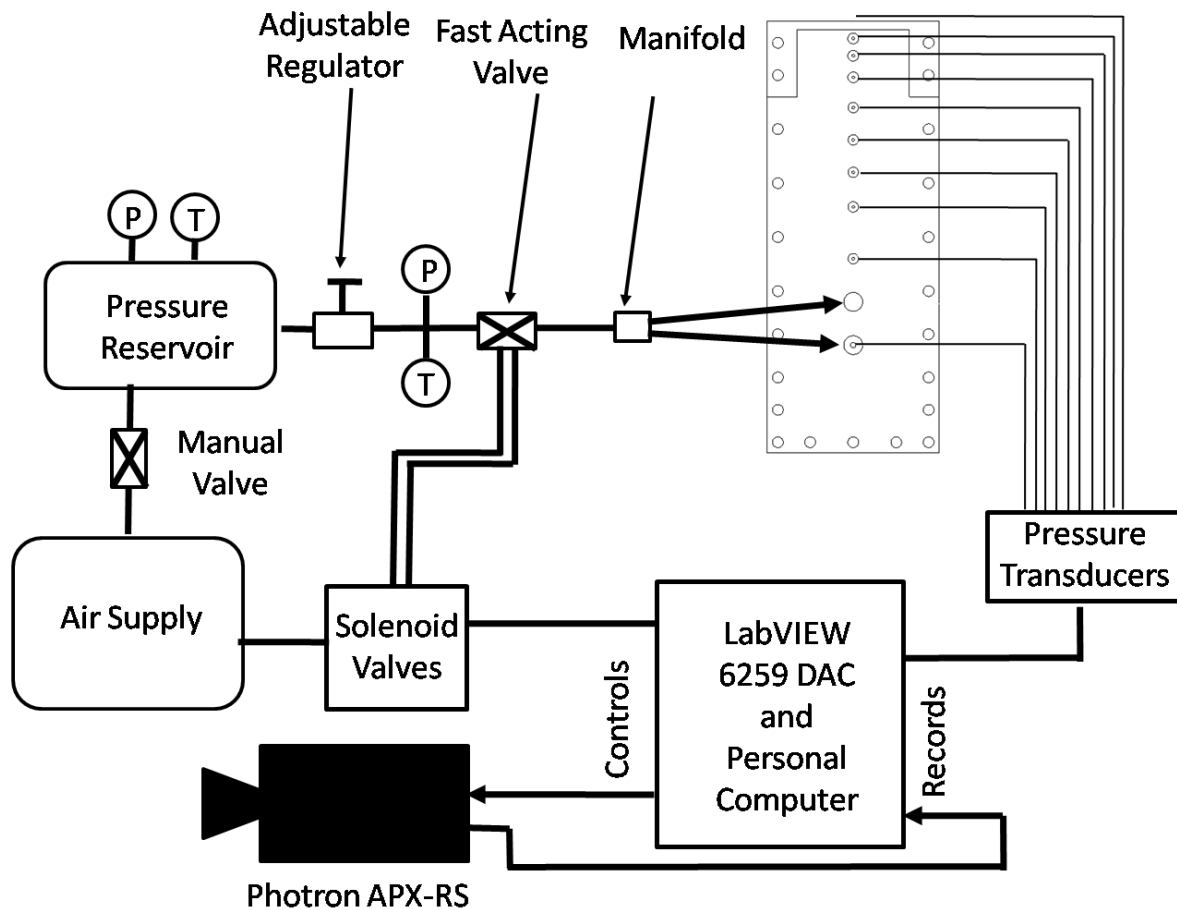


Figure 4.3. Schematic of the instrumentation and control system. Gas flow was started and stopped using a fast acting pneumatic valve controlled by LabVIEW software, which also triggered all instrumentation.

The system was controlled by LabVIEW software in conjunction with a National Instruments 6259 16-bit DAC. Upon running the software, a low voltage signal is transmitted to both the Photron camera and a solenoid valve which causes the camera to begin recording and the fast acting valve (W.E. Anderson $\frac{3}{4}$ " NPT, model ABV1DA103) to open simultaneously. The fast acting valve has an opening time of about 0.03s. Not shown in Figure 4.3 are 10 Clippard (model EV-2-24) solenoid valves controlled by the DAC which deliver compressed gas to the pressure lines while the injector is off. The compressed gas prohibited water intrusion into the pressure lines.

Pressure measurements were taken at a 1 kHz sampling rate with Druck 7217-PTX transducers with an accuracy of 2% full scale. Several ranges of transducers were used to measure signals of different expected pressure ranges in an effort to minimize errors. Transducers with a range of 0-0.35 MPa were used to measure pressures at and downstream of the nozzle throat while upstream of the nozzle throat transducers with a range of 0-0.70 MPa were used. Temperature measurements were made at the pressure reservoir and just downstream of the adjustable pressure regulator using type K thermocouples with an Omega thermocouple to analog converter (model SMCJ-K) for a total accuracy of +/- 3 deg C. The Mach number was calculated using the isentropic law relating pressure and Mach number. Due to propagation of uncertainties in the pressure measurements, the error in the Mach number measurements at the nozzle exit was approximately 1% (Mach 1.8) - 7% (Mach 0.4). Considerable effort went into ensuring, in the case of the sonic and supersonic nozzles, that the gas jets were perfectly expanded by monitoring the exit pressure and the known hydrostatic pressure.

4.4.2 Photographic Measurements and Edge Detection

A Photron FASTCAM APS-RX in conjunction with a Canon VX-16 telephoto lens was used to digitally record shadowgraph images of the test section at 1 kHz sampling rate for 9 seconds. The typical magnification used in the tests was approximately 388 $\mu\text{m}/\text{pixel}$. Eight 250W halogen lamps evenly distributed over the test section were arranged behind a white sheet to distribute light evenly over the test section. Acquired images were processed in MATLAB to detect the gas jet boundary in time. As the shadowgraph produces a projection of the gas jet onto a two-dimensional image, no three-dimensional information is collected. The jet boundary is computed using the steps shown in Figure 3.3. First the image is digitized based on a threshold pixel intensity to capture the gas phase and a 7x7 pixel median filter is applied to smooth any

irregularities such as bubbles fractured from the jet. Next a circular disk morphological element was applied to the digitized image and after dilation and erosion the perimeter of the resulting structure was identified. As shown in Figure 3.3 the detected boundary agrees quite well with the experimental image. To ensure the jet reached steady-state behavior the jet boundaries were tracked $\frac{1}{2}$ second after the gas jet was initiated. All jets had reached the free surface prior to analysis. The computed edges were tracked and their positions recorded for all times which allowed not only the computation of interfacial position, frequencies, velocities, and accelerations but also every pinch-off event in time was identified.

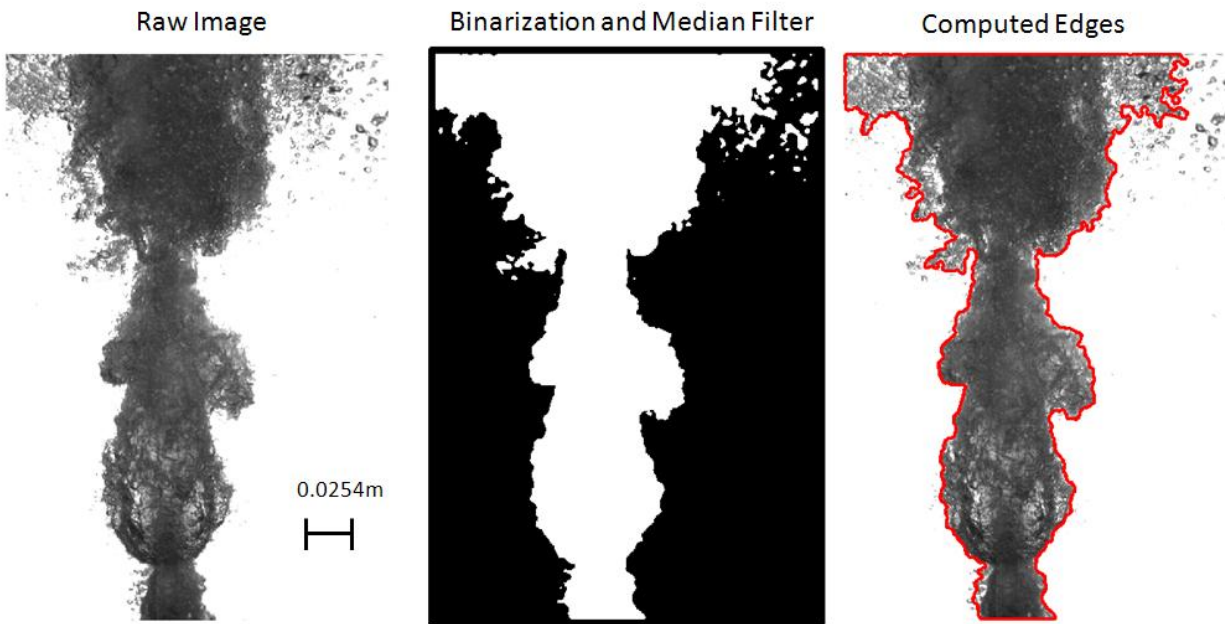


Figure 4.4. Steps used to detect the jet boundary. The process neglects outliers such as bubbles torn from the interface to accurately track the phase boundary.

4.5 Results and Discussion

In this paper we employ photographic measurements to quantify the effects of Mach number and aspect ratio (AR) on A) the spatial distribution of gas jet pinch-off, B) the penetration of submerged gas jets in water, and C) interfacial unsteadiness.

4.5.1 Analysis of the Jet Pinch-Off

One of the goals of this research was to quantify the effect of jet aspect ratio and Mach number on the jet pinch-off distribution. The phenomenon of pinch-off is largely due to the large density variation between the gas jet and the ambient water. At some downstream position the gas jet can no longer support the local hydrostatic pressure and the gas jet will pinch-off. At this

downstream location the flow is driven by buoyancy as opposed to momentum. Using the high speed photography and analysis methods presented above the distribution of pinch-off locations is quantified herein.

The number of pinch-off events for each aspect ratio and Mach number is shown in Figure 4.5. In several test cases no pinch-off events were observed namely AR 10 Mach 1.5 and AR 20 Mach 1.3 and 1.5. The number of pinch-off events is scaled by the total viewing length available divided by the length of the nozzle (l), which for a rectangular nozzle is also the geometric length scale L_Q (Fischer et al. 1979). This geometric length scales the jet development in single phase (i.e. gas jet in ambient gas environment) jets. As shown in Figure 4.5 the number of pinch-off events has a logarithmic decay with increasing Mach number and when appropriately scaled appears to be somewhat constant across all aspect ratio nozzles. These results indicate that increasing Mach number decreases the likelihood of a pinch-off event as Mach number is increased.

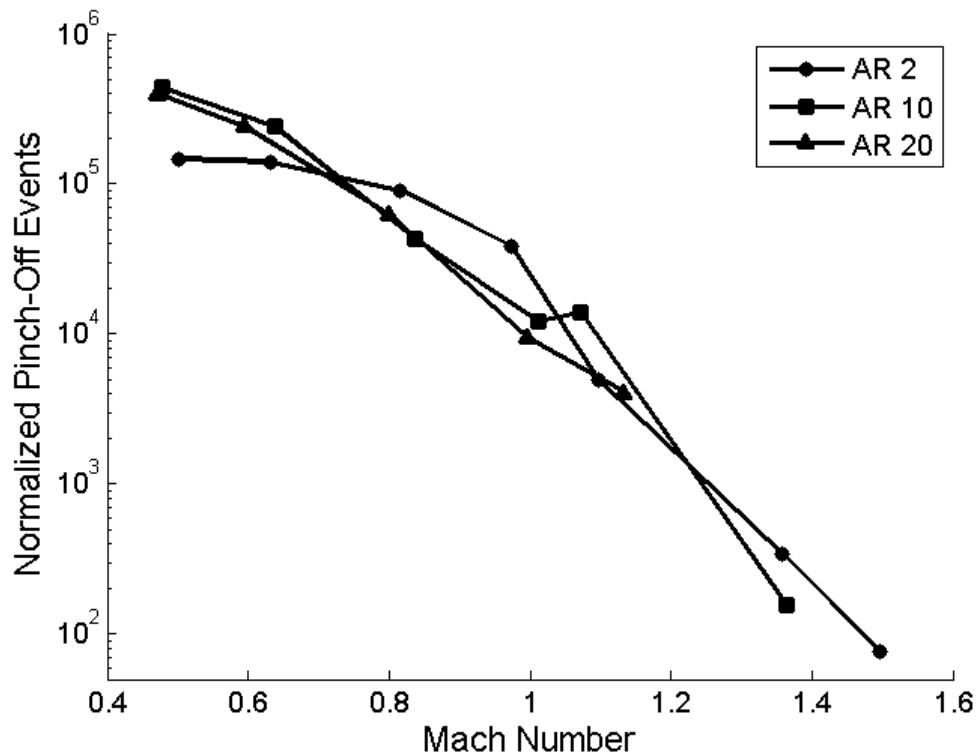


Figure 4.5 The number of pinch-off events observed for each Mach number and aspect ratio. The number of pinch-off events was normalized by the total observation distance divided by the width of the nozzle.

The spatial distribution of pinch-off events was experimentally observed to be dependent on the aspect ratio of the injector. An example of this is shown in Figure 4.6 for the AR 10 nozzle

which shows a peak in the number of pinch-off events at $y/L_Q \approx 3-5$. The subsonic Mach numbers 0.5, 0.6, and 0.8 show a broader range of pinch-off locations ranging from $y/L_Q \approx 3-9$ while the sonic and supersonic jets typically show peaks of smaller width.

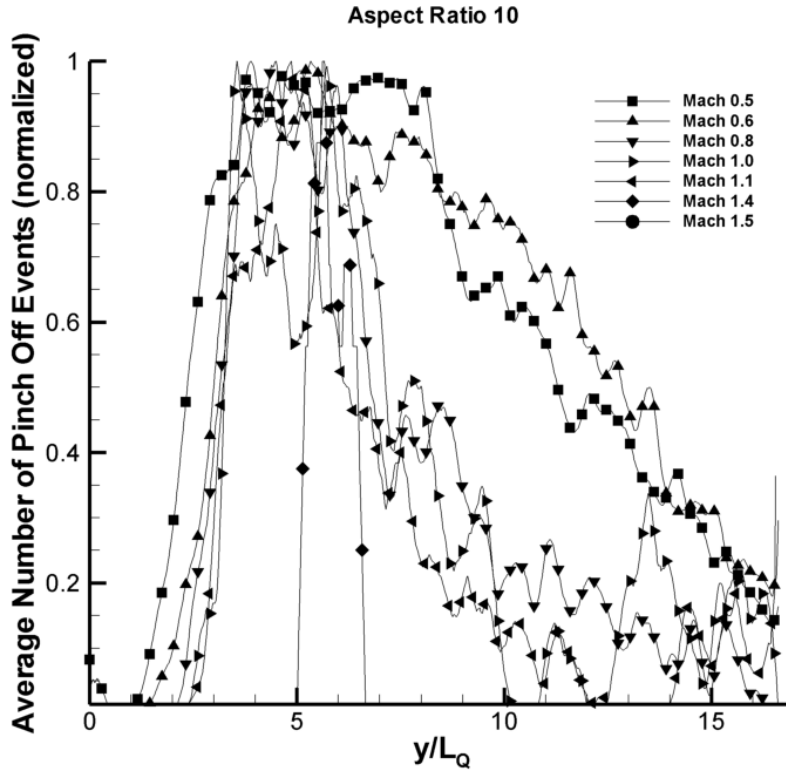


Figure 4.6. Spatial distribution of pinch-off events for AR 10. For all Mach numbers except Mach 1.5 the jets have a maximum in pinch-off events at $y/L_Q \approx 3-5$. The Mach 1.5 jet did not pinch-off.

The axial location of maximum pinch-off events for all aspect ratio nozzles and Mach numbers is shown in Figure 4.7. Values of zero indicate the jet did not pinch-off, namely AR 10 Mach 1.5 and AR 20 Mach numbers 1.3 and 1.5. The AR 2 nozzles show a remarkable dependence on Mach number with subsonic Mach numbers having peaks between $y/L_Q \approx 23-26$ while sonic and supersonic Mach numbers have peaks over the range $y/L_Q \approx 11-14$. The latter range of values corresponds to the experimentally observed location of maximum streamwise turbulence levels in round gas jets [(Crow and Champagne 1971); (Fischer et al. 1979)]. The AR 10 and 20 nozzles show no dependence on Mach number with the maximum number of pinch-off events observed over the interval $y/L_Q \approx 3-5$.

The variance in pinch-off location with aspect ratio suggests that aspect ratio plays a fundamental role in the development of rectangular jets. Quinn (1992) showed through measurements of AR 2, 10, and 20 single phase gas jets that the streamwise turbulence

fluctuations reach a maximum near $y/L_Q \approx 10-15$ for the AR 2 nozzle and $y/L_Q \approx 5$ for the AR 10 and 20 nozzles. These results are remarkably similar to those shown here and it is possible that the streamwise turbulence levels act as a perturbing factor on the interface, being directly responsible for pinch-off. Additionally, the axial position of $y/L_Q \approx 3$ (Sfeir 1979) and $y/L_Q \approx 5$ (Trentacoste and Sforza 1967) were shown to correspond to the axial position of “axis switching,” where the jet cross section increases significantly in the nozzle width dimension. This point corresponds to the departure of the jet from two-dimensional to axisymmetric flow behavior, and the tendency of rectangular gas jets to switch major axes during evolution suggests this point to be a prime location for pinch-off to occur.

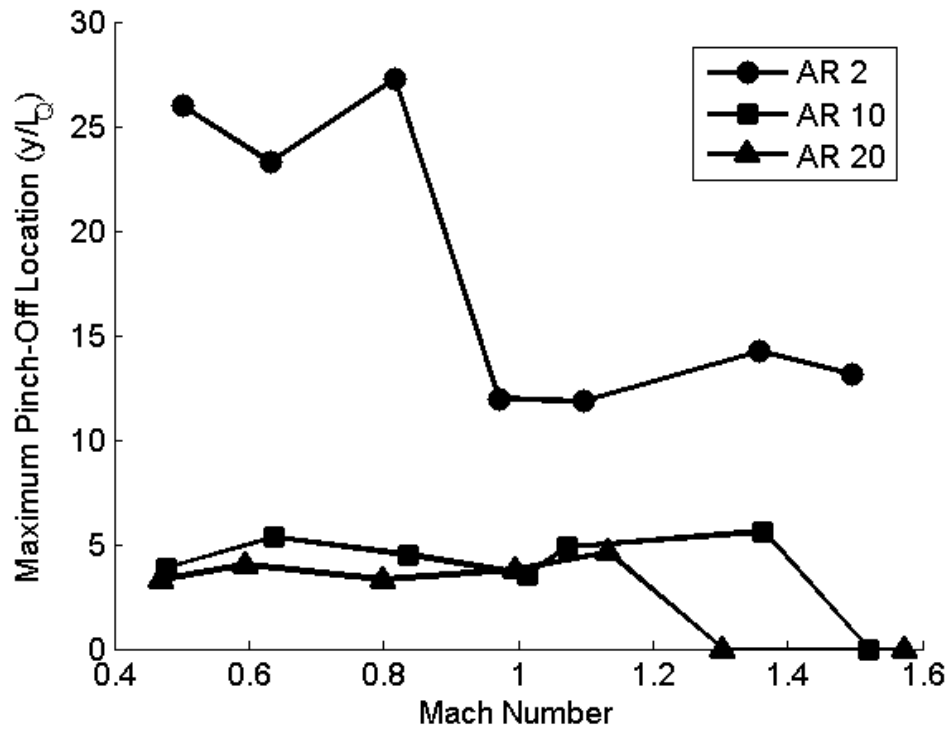


Figure 4.7. The axial position having the most pinch-off events is dependent on the aspect ratio of the nozzle. Tests for nozzles AR 10 Mach 1.5 and AR 20 Mach numbers 1.3 and 1.5 showed no pinch-off events over the measured domain.

4.5.2 Jet Penetration Distance

The length of gas jet penetration into the ambient water is governed by the Mach number and aspect ratio. The jet penetration distance is defined as the maximum length along the jet centerline the gas jet maintains a presence over the test sample for 98.5% of the measured time. The penetration distance must be described statistically as submerged gas jets naturally pulsate and the penetration distance varies in time. Several previous works have measured the

penetration distance of submerged round gas jets using electroresistive or optical probes lowered into the water and traversed through space [(Castillejos and Brimacombe 1987), (Ozawa and Mori 1986), and (Ito et al. 1991)]. Ozawa and Mori (1986) use this method to determine what they call gas holdup, which is a statistical mapping of how far gas penetrates into the surrounding water. If water was present at the measurement point an electrical circuit was completed and registered a value of 1 and if gas was present a value of 0 was recorded. By summing up all of these values in time for many points in space the time fraction of gas penetration at that point was calculated. Here we implement a similar approach but instead we use our non-invasive imaging that measures the position of the gas jet spatially at each instant of time. From the digitized images, as shown in Figure 3.3, we sum the values of each pixel over time and divide by the measurement duration to arrive at a time fraction of gas presence for all pixel locations as shown in Figure 3.9 where the color contour indicates the percentage of time that a certain location in the field of view was occupied by gas. A comparison of the Mach 0.4 and Mach 0.9 jets show obvious differences, especially in the length of a gaseous core which occupies a volume for a large percentage of the test record.

One advantage of this approach is that it enables distinguishing between bubbles that have fractured from the gas jet column and an orifice attached continuous jet, which is not possible using the electroresistive probe. We determine the length of the gas jet penetration only for orifice-attached gas jets, meaning that our calculations ignore any portion of the gas jet that has ruptured and is rising to the surface as an independent bubble.

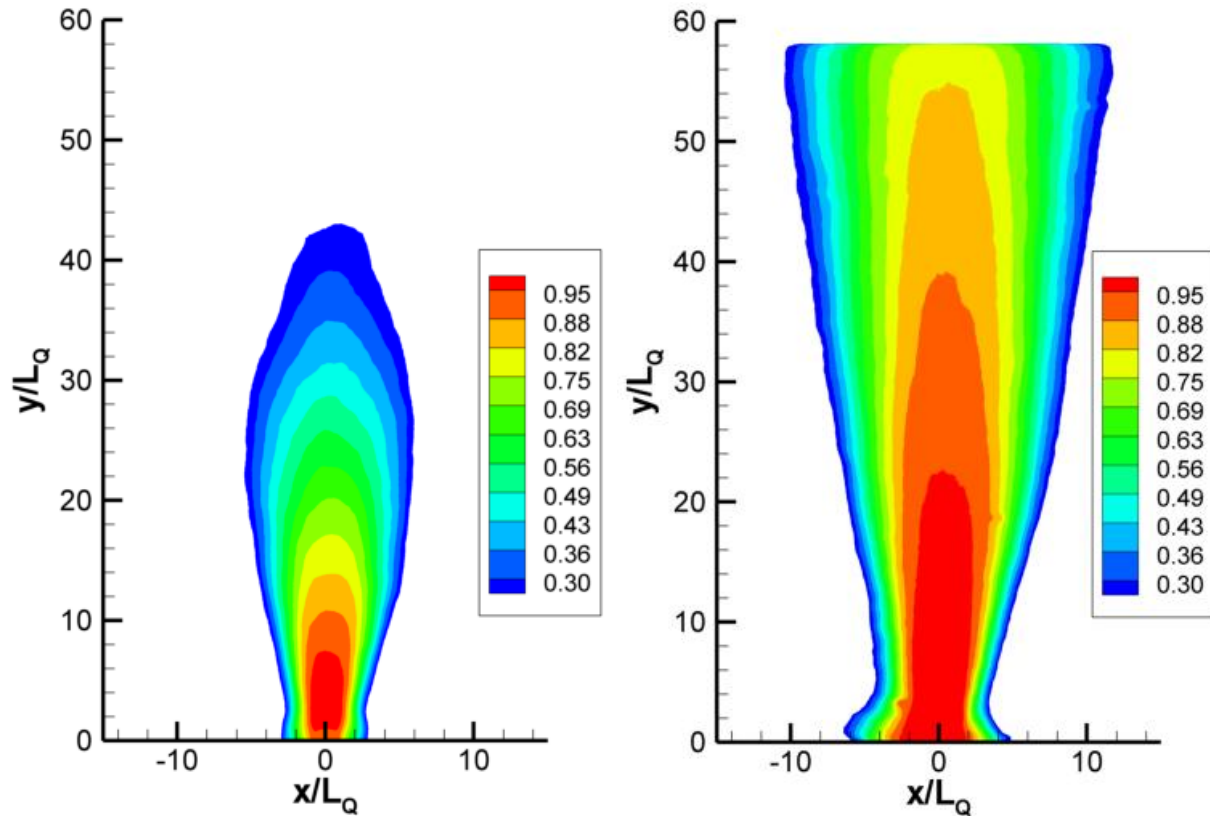


Figure 4.8. Gas holdup contours for a AR 2 Mach 0.4 jet (left) and Mach 1.0 jet (right). The sonic gas jet penetrates further into the quiescent fluid statistically than the subsonic gas jet.

The jet penetration distance for all aspect ratio nozzles is shown in Figure 4.9 as a function of Mach number. Cases for which the jet penetration was greater than the sampled viewing area are shown as disconnected points. In general, increasing aspect ratio and increasing Mach number yields greater penetration distances. The bubbling to jetting transition point is the sonic point as a large jump in penetration length occurs at or after this Mach number. The jet penetration increases non-linearly in the supersonic regime, with at least the AR 2 nozzle having a trend indicative of a cubic relationship such as $y_P \approx C(M - 1)^{1/3}$, where y_P is the jet penetration distance, C is a constant dependent on aspect ratio, and M is the injection Mach number. The fact that the inflection point occurs at the sonic point is further proof that the transition from bubbling to jetting occurs at the sonic point in rectangular jets. The sonic point is taken as the bubbling to jetting transition point in round submerged gas jets as well [(McNallan and King 1982); (Mori et al. 1982)], indicating a fundamental change in the jet dynamics after this point.

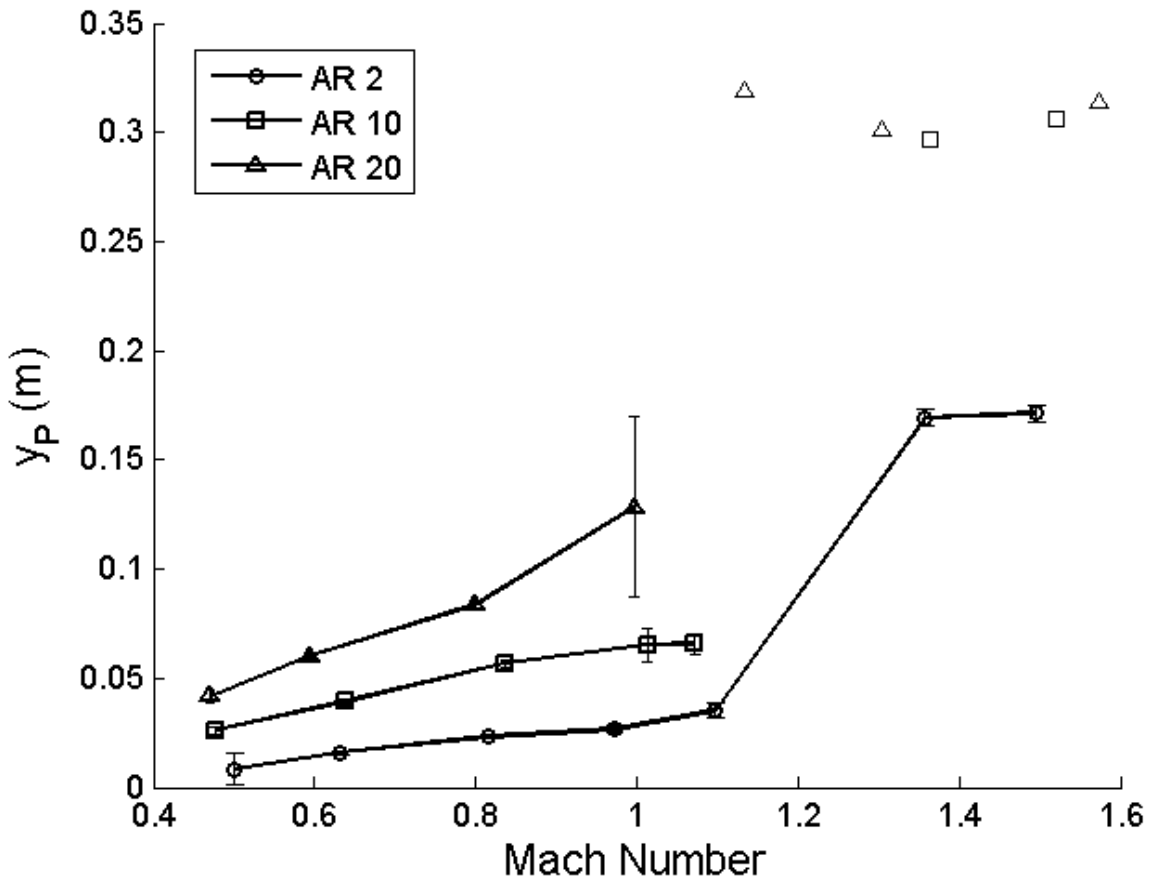


Figure 4.9. The jet penetration distance increases with increasing aspect ratio and Mach number. The unconnected data points correspond to cases in which the jet penetration distance was greater than the field of view; the jet penetrated at least this distance.

In light of the nearly linear jet penetration distance with Mach number in the subsonic and sonic regimes it is anticipated that some scaling relationship exists between the different aspect ratio jet penetration distances. As shown in Figure 4.10 the jet penetration in physical units increases with the power law relationship $y_p = 1.95m^{0.74}$ which gives a coefficient of determination of 0.93. This relationship was fit using a least squares algorithm.

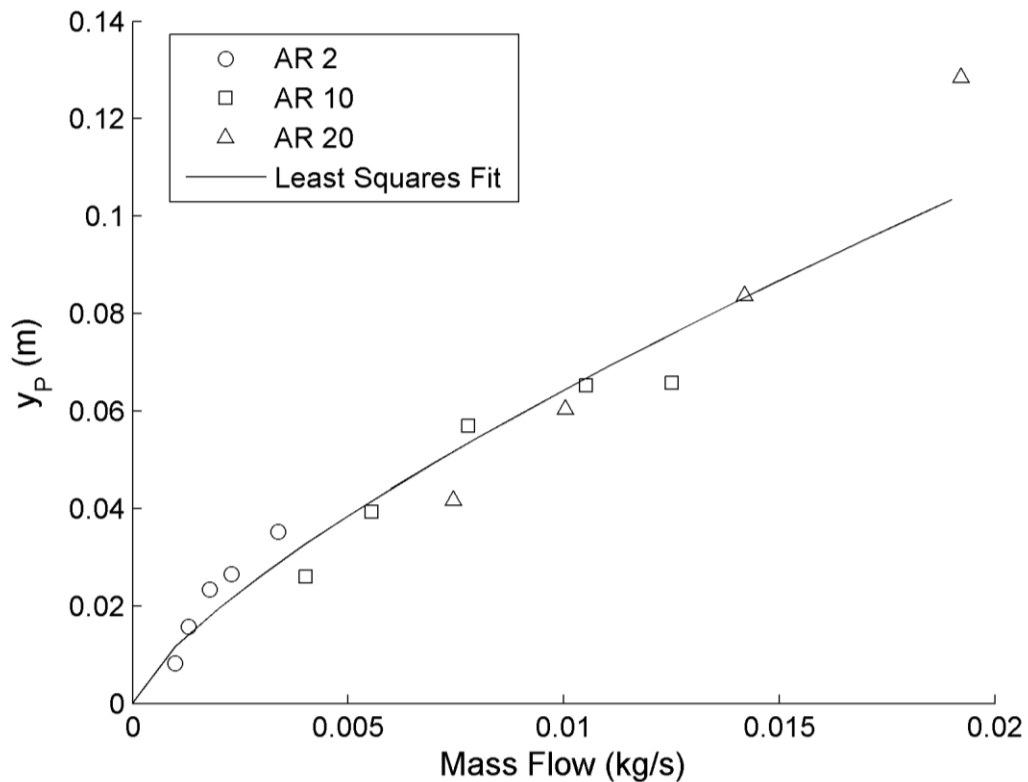


Figure 4.10. The jet penetration distance increases with mass flow according to a power law relationship.

The nondimensional jet penetration distance is shown in the left plot of Figure 4.11 and is scaled by the developmental length L_Q . For rectangular nozzles this length is simply the long dimension of the nozzle (l). The AR 10 and 20 nozzle curves collapse reasonably well using L_Q to scale the jet penetration length. The AR 2 curve does not scale similarly. This may be a manifestation of the fact that the AR 2 nozzle is nearly axisymmetric after a smaller development length than the AR 10 and 20 nozzles. The effects of aspect ratio on rectangular jet development have been well documented. Krothapalli et al (1981) has reported the effects of aspect ratio on the development of single phase rectangular jets and note that the downstream distance where the velocity profile follows similarity seems to depend on aspect ratio, mainly due to merging of the shear layers located in the plane of the long nozzle dimension. Using hot-wire anemometer measurements Sfeir (1979) confirmed the importance of aspect ratio on velocity decay and showed the departure from two-dimensional effects which are influenced by the nozzle aspect ratio. Thus, both the AR 10 and 20 nozzles are less axisymmetric near the nozzle and require a larger development length to reach the axisymmetric zone where all memory of the original rectangular configuration is lost (Sforza et al. 1966).

The right plot of Figure 4.11 shows the jet penetration distance scaled by the square root of the nozzle area and the curves collapse reasonably well with a nearly linear trend. Interestingly, the square root of the nozzle area is used as the development length L_Q used in round jets and it appears to scale the jet penetration distance more effectively than the value of L_Q used in rectangular jets (l). This is somewhat artificial, however, as both the square root of the exit area and L_Q are related simply through the square root of the aspect ratio.

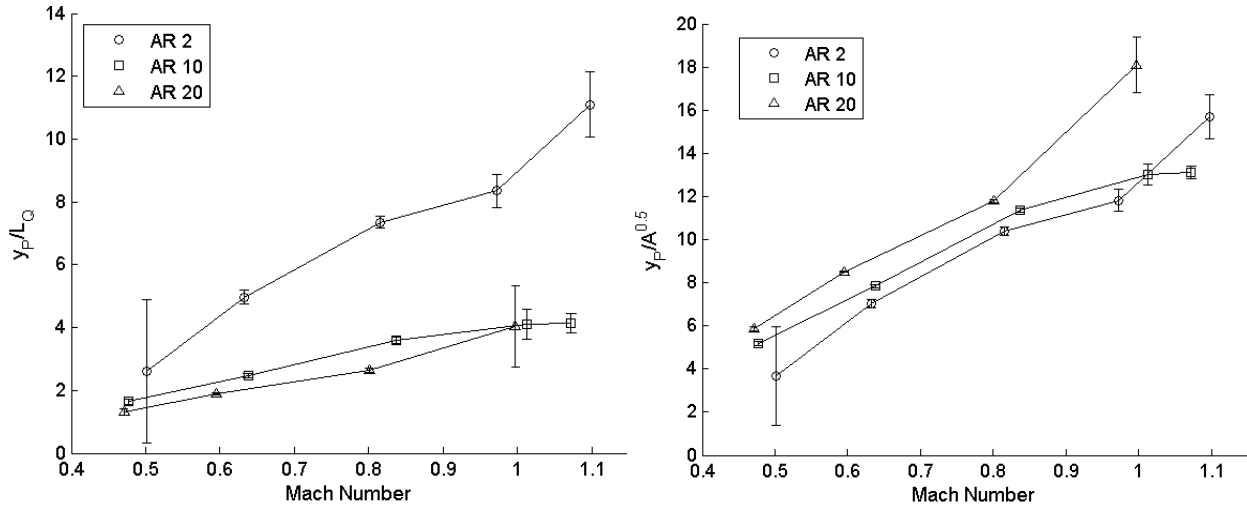


Figure 4.11. On left and right the jet penetration distance is scaled by L_Q and the square root of the nozzle area, respectively. The latter term appears to collapse the data more effectively.

The jet spreading rate, which is indicative of mixing and entrainment at the interface, was found to be a function of both Mach number and aspect ratio as shown in Figure 4.12. In general, increasing aspect ratio and Mach number increase the spreading rate. The trend of increasing jet spreading angle with increasing aspect ratio has been noted in a number of studies of single phase rectangular [(Quinn 1992); (Tsuchiya and Horikoshi 1986); (Lozanova and Stankov 1998)] and planar (Deo et al. 2007) jets. Zaman (1999) measured the entrainment on Mach 0.95 jets of aspect ratio 2-38 and found that entrainment rates increased significantly only for $AR \geq 10$. In our data, this trend is also observed. Prior to Mach 1.35 both the AR 2 and AR 10 have about the same spreading rates, while the AR 20 jet has a much greater spreading rate. The similarity in jet spreading for the AR 2 and 10 nozzles suggests the entrainment rate mechanisms may be similar.

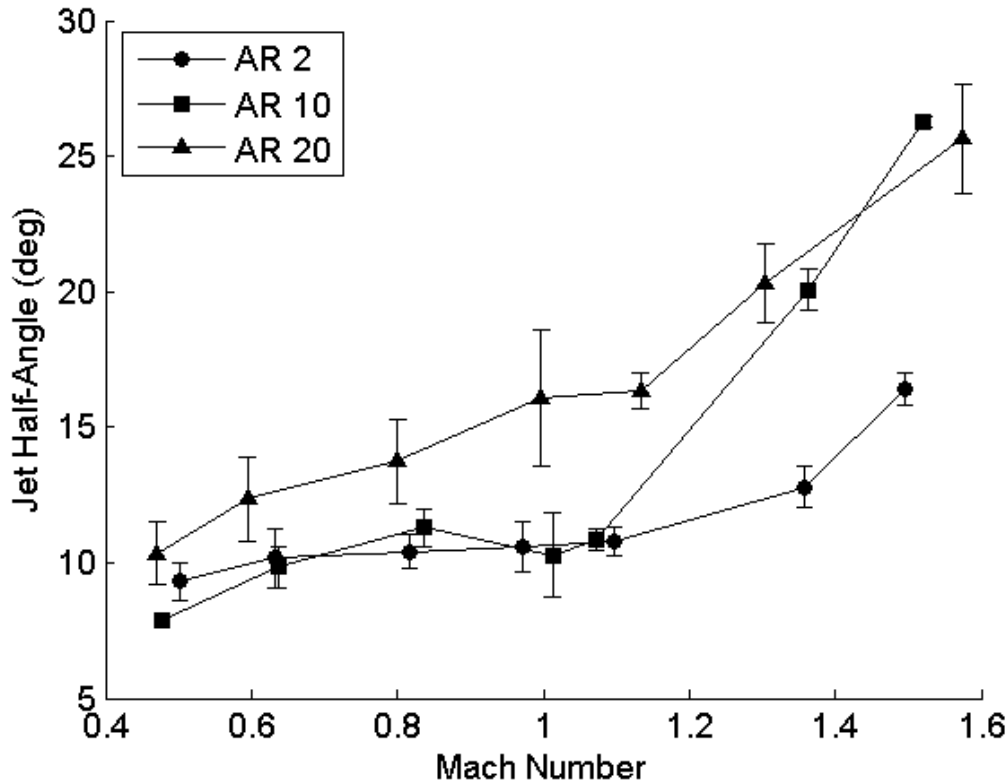


Figure 4.12. The average jet spreading angle is a function of both aspect ratio and Mach number. Generally, the spreading angle is greater for supersonic flows and higher AR nozzles.

It is fairly intuitive that increasing the aspect ratio moves the jet away from a near-axisymmetric case (AR 2) into a fully three-dimensional case. The sharp gradients at the corners of a large aspect ratio jet are quickly smeared due to instabilities which tend to enhance mixing (Tam and Thies 1993). The effect of Mach number on the spreading rate is less clear. It is interesting to note in Figure 4.12 the effect of Mach number on the AR 10 nozzle. After maintaining a slowly increasing spreading angle throughout the subsonic and transonic domain the spreading angle quickly increases near Mach 1.35. After this point the spreading rate becomes similar to values obtained for the AR 20 nozzle. This is in contrast to the AR 20 nozzle, which shows a strongly increasing jet spreading rate as Mach number is increased.

Based on these results, it is hypothesized that the interfaces generated by submerged rectangular gas jets are primarily influenced by instabilities whose relative strength is dependent on the aspect ratio. Stability may be directly linked to entrainment, as interfacial wave production and subsequent collapse leads to entrainment of ambient fluid into the jet, and therefore exerts a strong influence on the jet spreading rate. Mach number plays a secondary role and as seen in Figure 4.12 is apparently a triggering mechanism which can take a nominally

stable jet, such as seen in the subsonic AR 10 nozzle with a jet spreading rate similar to the subsonic AR 2 nozzle, and rapidly increase the jet spreading rate. After the transonic regime the AR 10 spreading ratio increases drastically and is comparable to the AR 20 spreading rate. Although the AR 2 nozzle also shows an increase in the jet spreading past Mach 1.1 it does not increase to the extent seen in the AR 10 and 20 nozzles. In other words, cases AR 2 and 20 correspond to mostly stable and unstable jetting behavior in the subsonic and sonic regimes with AR 10 corresponding to a nominally stable jet until appropriately perturbed. This perturbation could come in the form of compressibility effects, such as shock-cell structures (Loth and Faeth 1990) or screech feedback mechanisms [(Zaman 1999); (Zaman et al. 2002)].

4.5.3 *Unsteady Interfacial Characteristics*

The interfacial unsteadiness was directly computed by taking the average deviation (AD) of the interface position and the results are shown in Figure 4.13-Figure 4.15 for the AR 2-10 nozzles, respectively. All dimensions are normalized by width (w) of the rectangular nozzle. With the exception of the AR 20 Mach 0.5 test supersonic nozzles generated the most unsteadiness near the nozzle and the least downstream of $y/w \sim 10 - 12$. The correspondence of this switch in interfacial behavior after $y/w \sim 10 - 12$ interface unsteadiness suggests that the shear layers emanating from the width of the nozzle plays a large role in governing the jet development by directly contributing to the stability of the interface. The magnitude of the interfacial movement increases with increasing aspect ratio as well. In general, increasing Mach number is seen to have a stabilizing effect on the interface with supersonic gas jets having less interfacial motion than subsonic jets.

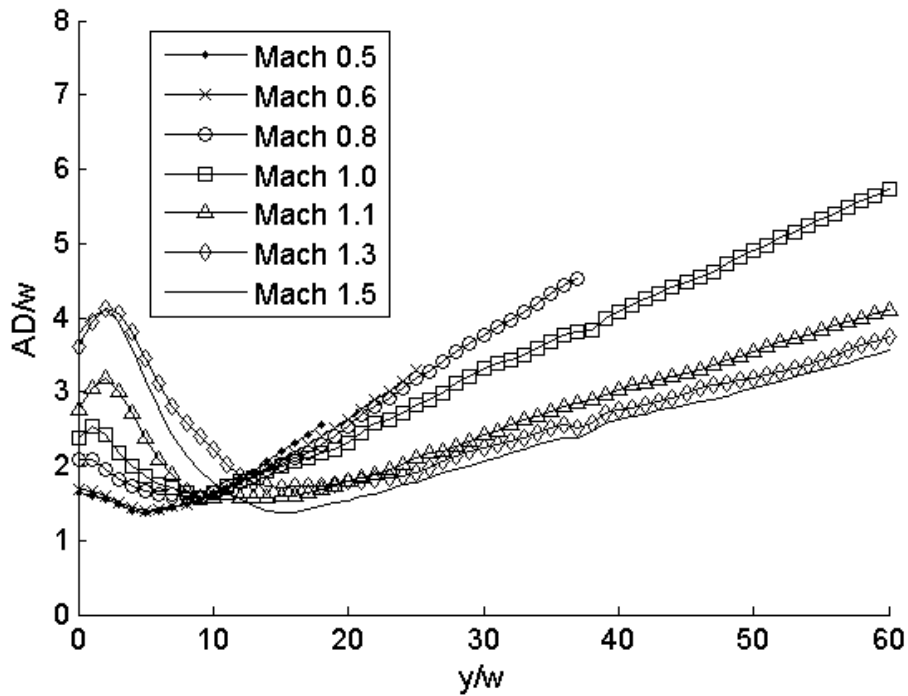


Figure 4.13. Average deviation of interface for AR 2 nozzle.

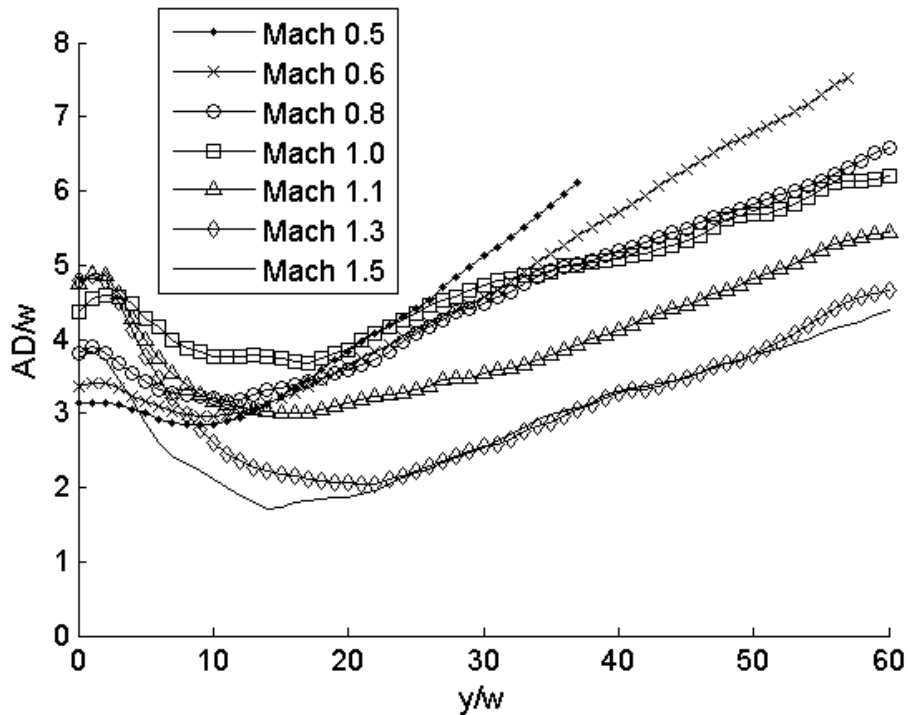


Figure 4.14. Average deviation of interface for AR 10 nozzle.

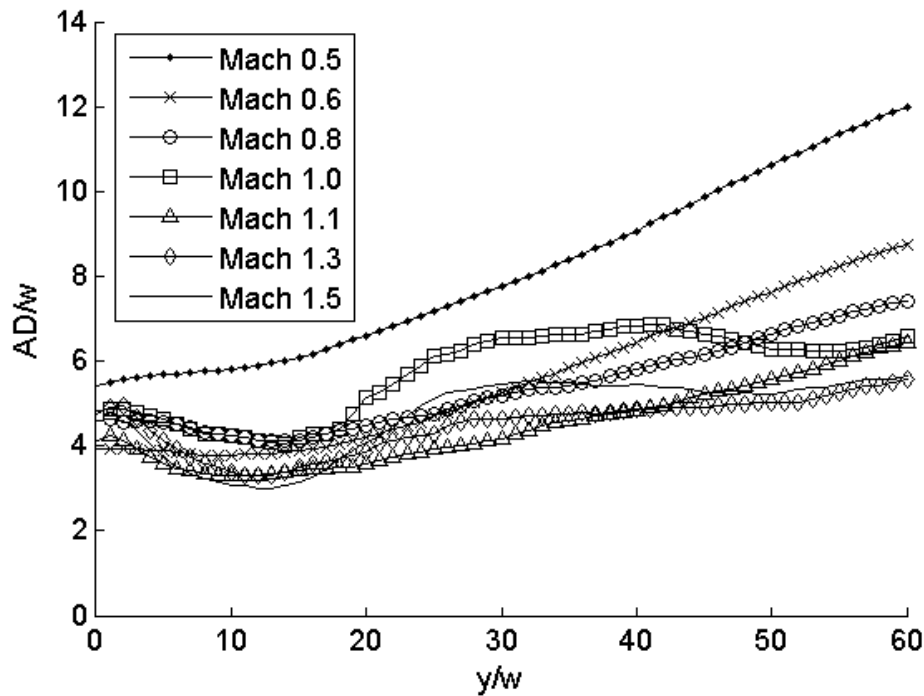


Figure 4.15. Average deviation of interface for AR 20 nozzle.

Although stability and the unsteady interface motions reported here are fundamentally different they are phenomenology similar. This is apparent from the results reported as increased interfacial motions are experimentally correlated to a less stable jet exhibiting a greater number of pinch-off events (consider Figure 4.5). Thus, the growth of the interface unsteadiness as it evolves downstream of the orifice may be linked to the spatial growth rate of the interface unsteadiness. This is plotted for all Mach numbers and aspect ratios in Figure 4.16. The scale is nondimensional and was computed from the slope of the line which best fits the data shown in Figure 4.13-Figure 4.15. The line is fitted after approximately $y/w \sim 12$ to ensure the jet is fully developed. The characteristics of the AR 2 nozzle is qualitatively similar to the results of Chen and Richter (1997), as the spatial growth rate increases to a maximum in the sonic region and then rapidly decreases in the supersonic regime. The AR 10 and 20 cases follow a separate trend, having decreasing spatial growth rates until the sonic point and increasing growth rates in the supersonic regime. A manifestation of the increased growth rate in the supersonic regime for the AR 10 and 20 nozzles is also seen in Figure 4.12 as in the supersonic regime these nozzles had much greater spreading angles, and thus entrainment of local fluid. These results are interesting in that the AR 2 case corresponds to a nearly axisymmetric gas injection case whereas the AR 10 and 20 are fully three-dimensional by virtue of their large aspect ratios. This difference in

growth rate as a function of aspect ratio suggests a different instability mechanism which governs rectangular, as opposed to circular, submerged gas jets. While several analytical studies have been conducted on submerged round gas jet stability [(Chen and Richter 1997); (Chawla 1975); (Subramaniam et al. 1999)], there are no studies known to the authors which analytically explore the interfacial stability of rectangular gas injection in water. Future research should pursue an analytical approach to yield insight into this problem.

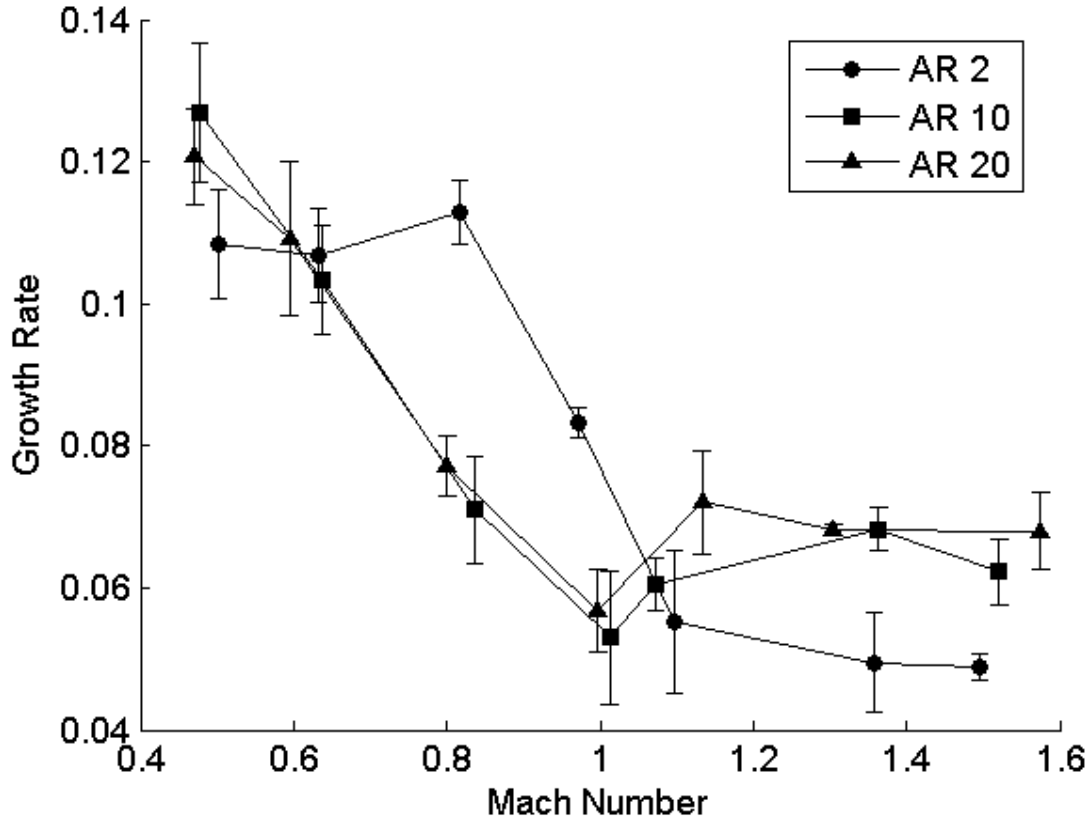


Figure 4.16. Spatial growth rate for all aspect ratio nozzles. The growth rate is a nondimensional scale representing the rate of interface unsteadiness downstream and is given by the slope of the best fit line passing through the AD points.

4.6 Conclusions

Gas jets formed by rectangular nozzles submerged in water were studied using a non-invasive photographic technique which allowed simultaneous measurements of the entire interface. Three aspect ratios were studied corresponding to 2, 10, and 20 with all nozzles sharing a common width. As far as the authors know this study represents the first time the effects of aspect ratio on a submerged gas jet have been studied. The main conclusions of this work are:

6. Buoyant jets were observed to consistently pinch-off at a spatial location corresponding to the maximum axial velocity turbulence fluctuations when normalized by the length scale L_Q . The number of pinch-off events decreases in a logarithmic fashion with increasing Mach number.
7. The jet penetration increases linearly for all aspect ratio nozzles in the subsonic and transonic regimes. After this point the jet penetration distance increases in a nonlinear fashion. The AR 2 nozzle showed a jet penetration trend of $y_p \approx C(M - 1)^{1/3}$, but the penetration of the supersonic AR 10 and 20 test cases was so great that this distance was not measureable.
8. The jet spreading rate, which is indicative of entrainment, shows dependence on both aspect ratio and Mach number. The AR 2 and 10 nozzles show similar spreading rates until the transonic regime, after which point both increase. However, the AR 20 nozzle has a much greater spreading rate regardless of Mach number. The AR 10 spreading rate increased to the level of the AR 20 nozzle in the supersonic regime, indicating the AR 10 nozzle sustained a significant change in its interfacial behavior as it became supersonic. The mechanism for the switch in behavior for the AR 10 nozzle in the supersonic regime is not clear.
9. The jet unsteadiness near the orifice is a function of the Mach number and aspect ratio. In general increasing Mach number decreases unsteadiness and increasing aspect ratio increases unsteadiness. All nozzles showed a switch in interfacial unsteadiness after $y/w \sim 10 - 12$, with supersonic jets be the least stable prior to this point and the most stable after this point.
10. The increase in interface unsteadiness downstream was computed and is indicative of the spatial instability growth rate. The results indicate that the AR 2 nozzle follows a trend similar to that predicted by Chen and Richter (1997) while the AR 10 and 20 nozzles follow a separate trend. This suggests a fundamentally different mechanism for interfacial stability in rectangular jets as opposed to round jets.

4.7 Acknowledgements

This research was sponsored by the Naval Surface Warfare Center, Dahlgren Division. Mr. John Busic and Dr. Jon Yagla served as the technical monitors. Their support is gratefully acknowledged.

4.8 References

- Antonia, R., L. Browne, S. Rajagopalan and A. Chambers (1983). "On the organized motion of a turbulent plane jet." Journal of Fluid Mechanics **134**: 17.
- Castillejos, A. H. and J. K. Brimacombe (1987). "Measurement of Physical Characteristics of Bubbles in Gas-Liquid Plumes .1. an Improved Electroresistivity Probe Technique." Metallurgical Transactions B-Process Metallurgy **18**(4): 649-658.
- Chawla, T. C. (1975). "Kelvin-Helmholtz Instability of Gas-Liquid Interface of a Sonic Gas Jet Submerged in a Liquid." Journal of Fluid Mechanics **67**(FEB11): 513-537.
- Chen, K. and H. J. Richter (1997). "Instability analysis of the transition from bubbling to jetting in a gas injected into a liquid." International Journal of Multiphase Flow **23**(4): 699-712.
- Crow, S. C. and F. H. Champagne (1971). "Orderly structure in jet turbulence." Journal of Fluid Mechanics **48**(03): 547-591.
- Dai, Z. Q., B. Y. Wang, L. X. Qi and H. H. Shi (2006). "Experimental study on hydrodynamic behaviors of high-speed gas jets in still water." Acta Mechanica Sinica **22**(5): 443-448.
- Deo, R. C., J. Mi and G. J. Nathan (2007). "The influence of nozzle aspect ratio on plane jets." Experimental Thermal and Fluid Science **31**(8): 825-838.
- Fischer, H., E. List, R. Koh, J. Imberger and N. Brooks (1979). Mixing in Inland and Coastal Water. New York, Academic Press.
- GORDEYEV, S. V. and F. O. THOMAS (1999). "Temporal subharmonic amplitude and phase behaviour in a jet shear layer: wavelet analysis and Hamiltonian formulation." Journal of Fluid Mechanics **394**(-1): 205-240.
- Gordeyev, S. V. and F. O. Thomas (2000). "Coherent structure in the turbulent planar jet. Part 1. Extraction of proper orthogonal decomposition eigenmodes and their self-similarity." Journal of Fluid Mechanics **414**(-1): 145-194.
- Gutmark, E. and I. Wygnanski (1976). "The planar turbulent jet." Journal of Fluid Mechanics **73**: 30.
- Ito, K., S. Kobayashi and M. Tokuda (1991). "Mixing Characteristics of a Submerged Jet Measured Using an Isokinetic Sampling Probe." Metallurgical Transactions B-Process Metallurgy **22**(4): 439-445.
- Krothapalli, A., D. Baganoff and K. Karamcheti (1981). "On the mixing of a rectangular jet." Journal of Fluid Mechanics Digital Archive **107**(-1): 201-220.
- Loth, E. and G. M. Faeth (1989). "Structure of Underexpanded Round Air Jets Submerged in Water." International Journal of Multiphase Flow **15**(4): 589-603.
- Loth, E. and G. M. Faeth (1990). "Structure of plane underexpanded air jets into water." AICHE Journal **36**(6): 818-826.
- Lozanova, M. and P. Stankov (1998). "Experimental investigation on the similarity of a 3D rectangular turbulent jet." Experiments in Fluids **24**(5): 470-478.

- McNallan, M. J. and T. B. King (1982). "Fluid-Dynamics of Vertical Submerged Gas Jets in Liquid-Metal Processing Systems." Metallurgical Transactions B-Process Metallurgy **13**(2): 165-173.
- Mori, K., Y. Ozawa and M. Sano (1982). "Characterization of Gas-Jet Behavior at a Submerged Orifice in Liquid-Metal." Transactions of the Iron and Steel Institute of Japan **22**(5): 377-384.
- Ozawa, Y. and K. Mori (1986). "Effect of Physical-Properties of Gas and Liquid on Bubbling Jetting Phenomena in Gas Injection into Liquid." Transactions of the Iron and Steel Institute of Japan **26**(4): 291-297.
- Quinn, W. (1991). "Passive Near-Field Mixing Enhancement in Rectangular Jet Flows." AIAA Journal **29**(4): 4.
- Quinn, W. (1992). "Turbulent Free Jet Flows Issuing from Sharp-Edged Rectangular Slots: The Influence of Slot Aspect Ratio." Experimental Thermal and Fluid Science **5**: 12.
- Sahai, Y. and R. I. L. Guthrie (1982). "Hydrodynamics of Gas Stirred Melts .1. Gas-Liquid Coupling." Metallurgical Transactions B-Process Metallurgy **13**(2): 193-202.
- Sano, M., H. Makino, Y. Ozawa and K. Mori (1986). "Behavior of Gas-Jet and Plume in Liquid-Metal." Transactions of the Iron and Steel Institute of Japan **26**(4): 298-304.
- Sfeir, A. (1979). "Investigation of Three-Dimensional Turbulent Rectangular Jets." AIAA Journal **17**(10): 5.
- Sforza, P., M. Steiger and N. Trentacoste (1966). "Studies on Three-Dimensional Viscous Jets." AIAA Journal **4**(5): 6.
- Subramaniam, K., R. N. Parthasarathy and K. M. Chiang (1999). "Three-dimensional temporal instability of compressible gas jets injected in liquids." Aiaa Journal **37**(2): 202-207.
- Tam, C. and A. Thies (1993). "Instability of rectangular jets." Journal of Fluid Mechanics **248**: 23.
- Trentacoste, N. and P. Sforza (1967). "Further Experimental Results for Three-Dimensional Free Jets." AIAA Journal **5**(5): 6.
- Tsuchiya, Y. and C. Horikoshi (1986). "On the spread of rectangular jets." Experiments in Fluids **4**(4): 197-204.
- Zaman, K. B. M. Q. (1999). "Spreading characteristics of compressible jets from nozzles of various geometry." Journal of Fluid Mechanics **383**: 31.
- Zaman, K. B. M. Q., M. D. Dahl, T. J. Bencic and C. Y. Loh (2002). "Investigation of a 'transonic resonance' with convergent divergent nozzles." Journal of Fluid Mechanics **463**(-1): 313-343.
- Zhao, Y. F. and G. A. Irons (1990). "The Breakup of Bubbles into Jets During Submerged Gas Injection." Metallurgical Transactions B-Process Metallurgy **21**(6): 997-1003.

5. TIME-SCALE FOR CRITICAL GROWTH OF PARTIAL AND SUPERCAVITATION DEVELOPMENT OVER IMPULSIVELY TRANSLATING PROJECTILES

Chris J. Weiland¹ and Pavlos P. Vlachos²
Virginia Tech Mechanical Engineering Dept

¹ Graduate Research Assistant, Virginia Tech Mechanical Engineering Department
² Associate Professor, Virginia Tech Mechanical Engineering Department

To Be Submitted to Experiments in Fluids

5.1 Abstract

A physical mechanism is proposed to explain an experimentally observed critical time scale that governs the partial cavity development over blunt free flying cylindrical projectiles. The projectiles were ejected using a modified gas-gun mechanism consisting of a barrel and explosive charge. Upon ignition, high-pressure gases forced a projectile down the launch barrel and into quiescent water. Results indicate that initial small cavities created at the projectile forebody are convected downstream where they subsequently grow towards the forebody, partially enveloping the projectile in a vapor cavity. The time at which the initially stable bubbles rapidly expand signifies that the partial cavity development process has begun. When this time quantified and is non-dimensionalized appropriately, a time-scale for the critical growth (CGTS) for the cavitation is revealed. A plausible explanation of the partial cavity development process observed in these experiments is that the process is due to the interaction between small cavitation bubbles shed from the projectile forebody and the vortex ring generated by the impulsively started projectile. This interaction mediates the destabilization and spontaneous growth of small unstable bubbles resulting in the formation of partial cavitation over the projectile. An additional supercavitation formation mechanism was observed and is attributed to the launch mechanism. This process is not due to pure hydrodynamic cavitation, but rather an effect we term “gas leakage” whereby the driving gases contaminated the aft flow field near the projectile and thus facilitated supercavitation to occur on a reduced time scale. This mechanism practically corresponds to off-body ventilated supercavitation.

Keywords: *transient cavity development, supercavitation*

5.2 Nomenclature

Symbols

A – area

a – vortex core radius

C_g – dissolved gas content in parts per million (ppm)

C_p – pressure coefficient

CPA – Change Point Analysis

CS – cumulative sums

CSGT – Critical Supercavity Growth Time

D – diameter

H – translated projectile distance

L – length

N – number of signal points

P – pressure

R – radius

Re – Reynolds number based on projectile diameter and speed

S – signal

t – time

TSGT – Terminal Supercavity Growth Time

U – speed

y – position downstream barrel

β – Henry's constant

γ – standard deviation

σ – cavitation index

ρ – density

τ – dummy variable

Γ – vortex circulation

Θ – velocity program

Subscripts

∞ – ambient conditions

p – projectile

s – saturation

c – cavity

o – initial condition

core – vortex core

v – vapor

min – minimum

max – maximum

critical – critical condition to unstable bubble growth

j – re-entrant jet

x – signal position

Superscripts

np – n-point calculation

5.3 Introduction

Supercavitation is an effective method to overcome viscous drag resistance underwater and achieve extreme velocities through the basic premise of minimizing the amount of wetted surface. Its use has found applications in both civilian and military technologies. Surface ships have used a similar concept for a number of years to reduce frictional drag on ship hulls by injecting a thin layer of gas between the ship hull and the surrounding water. This process is termed a ventilated supercavity (Matveev 2003) and is different from natural supercavitation as the latter requires hydrodynamic effects to generate the surrounding gases through vaporization. Supercavitating munitions for mine-clearing operations and terminal torpedo defense have been used in military applications (Hrubes 2001). While cavitation is to be avoided in most engineering applications, examples of which include ship propellers or pumps where the collapsing cavitation bubbles cause considerable surface damage and noise, supercavitation is highly desired in the context of minimizing viscous drag over underwater bodies translating at high speed.

Supercavitation refers to the most extreme form of cavitation in that a single gas or vapor envelope surrounds and translates with a moving body. Frictional drag is minimized as the amount of wetted surface decreases (Amromin and Mizine 2003). By definition, the supercavity is larger than the projectile length, with the total supercavity length being dependent on the degree of supercavitation. With slender axisymmetric shapes, supercavities develop into elongated ellipsoids, beginning at the forebody and trailing behind. At the closure region of the cavity, phenomena such as detachment, cavity shedding and tail-slapping occur which can develop critical instabilities that compromise stable projectile motion (Stutz and Reboud 1997; Gopalan and Katz 2000; Stutz and Reboud 2000; Callenaere et al. 2001) and create great challenges for the stability and control of supercavitating vehicles (Kirschner et al. 2002; Lin et al. 2008).

Despite the extensive previous research very little has been done to investigate the transient dynamics of the initial cavity growth. The motivation for this research is to address this limitation and contribute to the understanding of supercavitation development over impulsively translated bodies of revolution. To reach the supercavitating state, high-speed bodies must transition from a first stage of cavitation inception to partial/attached cavitation to fully developed supercavitation (Savchenko 2001). Cavitation inception corresponds to the explosive

growth of gas or vapor-filled microbubbles (nuclei) in response to a decrease in pressure below a critical point, usually considered to be the vapor pressure of water. Partial cavitation corresponds to a body only partially covered by a gaseous cavity (Le et al. 1993; Varghese et al. 2005). The similarity parameter that has evolved from this understanding is the cavitation index (σ), which describes the receptivity of the flow to cavitation and is given by Equation 5.1. Here p_∞ is the pressure in the ambient fluid, p_c is the cavity pressure, ρ_∞ is the density of the liquid, and U_p is the body speed. For purely hydrodynamic supercavitation, p_c is the vapor pressure (p_v) of water at its current thermodynamic state.

$$\sigma = \frac{p_\infty - p_c}{\frac{1}{2} \rho_\infty U_p^2} \quad 5.1$$

For a translating underwater body, the primary factor influencing cavitation inception is the interaction of the viscous flow and the associated pressure field. Boundary layer effects such as flow separation and reattachment often accompany cavitation inception (Keller 1979) and regions of turbulent or separated flow can potentially induce cavitation due to the large pressure fluctuations that local nuclei experience (Katz 1984). This dynamic process is described by the Rayleigh-Plesset equation (Rayleigh 1917; Plesset and Prosperetti 1977; Prosperetti 1982), from which Blake (Blake Jr 1949) defined a critical pressure threshold necessary to drive an oscillating bubble into unstable growth (Brennen and Earls 1995). The coupling of the pressure field and the nuclei distribution controls the onset of unstable bubble growth and thus one can postulate that the onset of cavitation can be predicted if these variables are properly described.

Cavitation inception over axisymmetric bodies of revolution has been thoroughly studied in water tunnels. These include measurements of the cavitation inception with the addition of artificial nuclei through hydrolysis (Kondama et al. 1979) or turbulence grid generators (Keller 1979). Past experiments have shown that cavitation inception always starts near the forebody, where viscous effects typically dominate the flow field. Huang (Huang 1979) conducted a comprehensive study of cavitation inception measurements on six axisymmetric headforms in a water tunnel facility. He concluded that the cavitation inception appeared in different fashions based on the local flow regime. Headforms resulting in a natural transition to turbulent flow with no possibility of laminar separation resulted in the growth and collapse of small bubbles as they moved into and out of the low-pressure transition region. However, headforms that

exhibited laminar separation were characterized by attached ring-cavitation. These measurements offer a great deal of insight about the generation of microbubbles due to a specific headform shape, and as we will show later it is these microbubbles which are susceptible to develop into partial cavitation. Supercavitation over translating bodies has also been studied in the past, although not as extensively. These experiments typically involve shooting high-speed projectiles into a water reservoir, including projectiles shot fast enough to approach the speed of sound in water (Shi et al. 2000; Hrubes 2001). These studies are typically qualitative in nature and largely concentrate on measurements of the supercavity shape itself, and not the supercavitation development process.

In all of our test cases laminar separation occurred at the headform where the initial cavitation appeared and was subsequently swept downstream. The large-scale cavitation began at or near the aft end of the projectile and grew in volume, traveling upwards until it reached the fore end. A similar effect was noted in the experiments of Arakeri and Acosta (Arakeri and Acosta 1973) who found bubbles were advected downstream from the separation point and entrained in the separated region in water tunnel tests. Their results are quite different from the results presented here for several reasons. First, their measurements were performed in a water tunnel yielding a quasi-steady flow field. This is inherently different from the notion of an impulsively launched body. Second, the bubbles located in the separation bubble that advected upstream were very small and no coalesce was observed. In the present study, we will show the rapid growth in volume of a single or multiple bubbles which apparently fills the entire separated flow region. Arakeri and Acosta specifically noted that the bubbles they measured did not increase in size substantially.

The present work explores the impulsive motion of an axisymmetric body of revolution whose initial motion produces a vortex ring. The nuclei produced at the forebody are swept downstream, presumably in the shear layer, and are entrained in the vortex ring where they migrate to the core. It is well known from studies of supercavitation phenomena wherein fluid moves over a stationary body, that cavitation is often initiated in the centers of vortices, where the pressure is lower compared to the surrounding fluid and often provides the starting point for cavitation (Arndt 2002). Thus, we propose that the mechanism observed herein, responsible for supercavity or partial cavity development over an impulsively translated body of revolution is

due to the interaction of small bubbles generated at the forebody of the projectile and the local pressure field caused by the vortex ring.

It is important to note that the experiments presented in this work aim to characterize the development of the supercavity on macroscopic scales and not the nucleization process. The interested reader is referred to Rood (Rood 1989; Rood 1991) for an overview of the mechanisms of cavitation inception and the difficulties associated with inception studies.

5.4 Experimental Methods and Processing Techniques

The goal of the project was to visualize and quantify the development of a partial cavity over an impulsively started blunt projectile. The impulsive launch of the projectile, as opposed to a water tunnel study, simulates the launch dynamics of a real vehicle attempting to reach the supercavitating state. Note that, because the nucleization processes were not of interest for these experiments, normal tap water was used and no effort was made to regulate the water quality or measure the nuclei potential. It is therefore assumed that the water is weak with a significant nuclei population and as such inception will begin when the local pressure nears the vapor pressure.

The projectile was shot into a water tank vertically under quiescent flow conditions. The projectile was accelerated by means of an explosive charge inside a modified nail gun. From hereon we will refer to this launch method as the gas-gun method. The expanding gases drove a piston to accelerate the projectile to test speed. Vertical firing of the launch mechanism with the barrel adequately submerged (fully submerged projectiles) as shown in Figure 5.1 was implemented in order to eliminate any free surface penetration effects. Prior to launch, the projectile was kept at the tip of the barrel to prevent the ejection of water from preceding the projectile egress, which would result in vortex ring production. Note that the plots presented in the analysis section are inverted, with respect to the coordinate system shown in Figure 5.1, such that in the processed images the projectiles move from bottom to top.

Blunt cylindrical unguided projectiles were fired at initial velocities that ranged between 19 to 40 m/s. Under test conditions, these velocities correspond to a range of peak cavitation indices from approximately $\sigma=0.13$ to $\sigma=0.53$ calculated at the time when cavitation ensues. Since the projectiles must accelerate to reach test speed, the concept of a cavitation index becomes ill-defined. Therefore, we define the cavitation-index velocity at the moment when

cavitation ensues on a large scale, and this in turn allows for the computation of the cavitation index. The projectiles were manufactured from Teflon and were 2.5 cm and 5 cm in length with a common diameter of 1 cm, thus giving aspect ratios of 2.5 and 5. Given these two aspect ratios, the test parameters are shown in Table 5.1. A Phantom IV high-speed digital camera was used to image the test section that was illuminated with 500 Watt halogen lamps. The test section was sampled from 1900 Hz to 6000 Hz. The spatial resolution at these sampling frequencies ranged from 128x512 to 256x256 pixels.

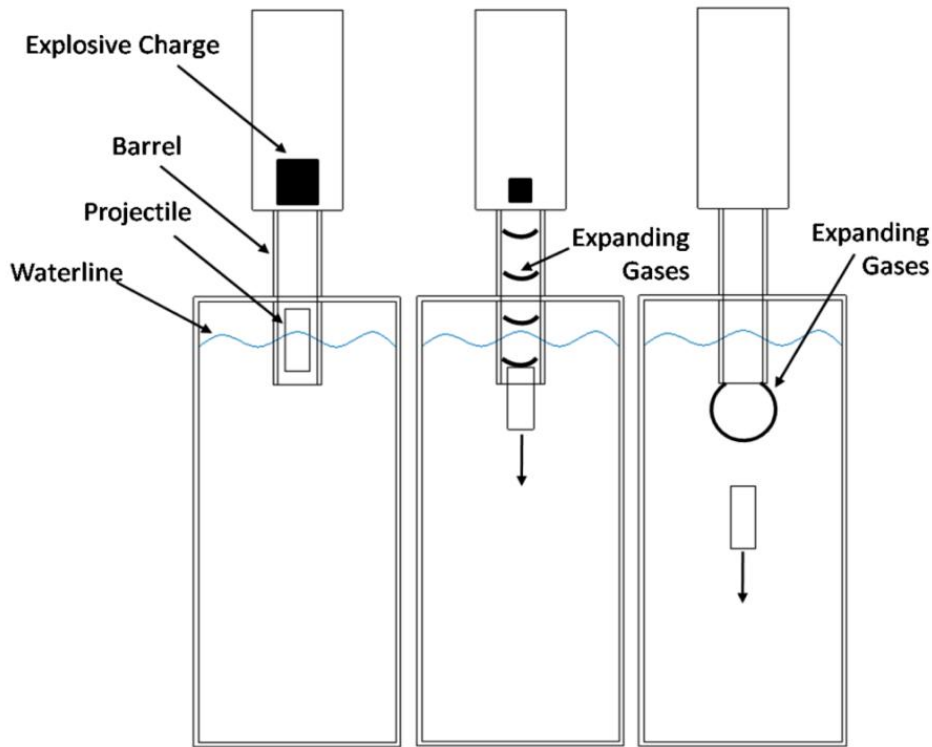


Figure 5.1: Experimental setup and sequence of events during projectile egress (left to right) showing the acceleration of the body in the water. Note that the charge gases leak into the quiescent water after the aft end of the projectile has cleared the barrel.

Table 5.1: Experimental test matrix.

Shot #	Aspect Ratio	Proj Speed (m/s)	Re ($\times 10^5$)	Cav Index
1	5	24	2.4	0.33
2	5	23	2.3	0.34
3	5	19	1.9	0.52
4	5	23	2.2	0.37
5	5	33	3.3	0.17
6	5	26	2.6	0.28
7	5	24	2.4	0.33
8	5	38	3.8	0.13
9	5	26	2.5	0.29
10	5	23	2.2	0.37
11	2.5	25	2.4	0.31
12	2.5	19	1.9	0.52
13	2.5	29	2.8	0.23
14	2.5	33	3.3	0.17
15	2.5	31	3.0	0.20

5.4.1 Image Processing Techniques

To accurately track the cavity and projectile positions, image-processing algorithms were developed in MATLAB to automatically detect the cavity and projectile positions in time. The gas interface detection scheme consists of three steps: pixel intensity thresholding, median filtering, and image dilation as shown in Figure 5.2 with the estimated projectile position shown in gray. The projectile position is estimated from the computed projectile tip and the known geometry of the projectile. The threshold pixel intensity algorithm filters all values below a given brightness level. Next, the image was median-filtered to compare pixels with others in its neighborhood and eliminate high frequency noise components, examples of which include particles or other spurious reflections. The boundary is identified next. Note that in the processed image in Figure 5.2 all cavity boundaries are shown, including the boundary of the driving gases near the barrel position which is shown at coordinates (0,0). Only cavities attached to the projectile were analyzed and we specifically focused on the growth of small bubbles near the aft end of the projectile that rapidly grow in volume. Therefore, faint cavities such as can be seen in the wake of the projectile in Figure 5.2 are ignored in the analysis as it does not contribute to the bulk cavity development we aim to study here.

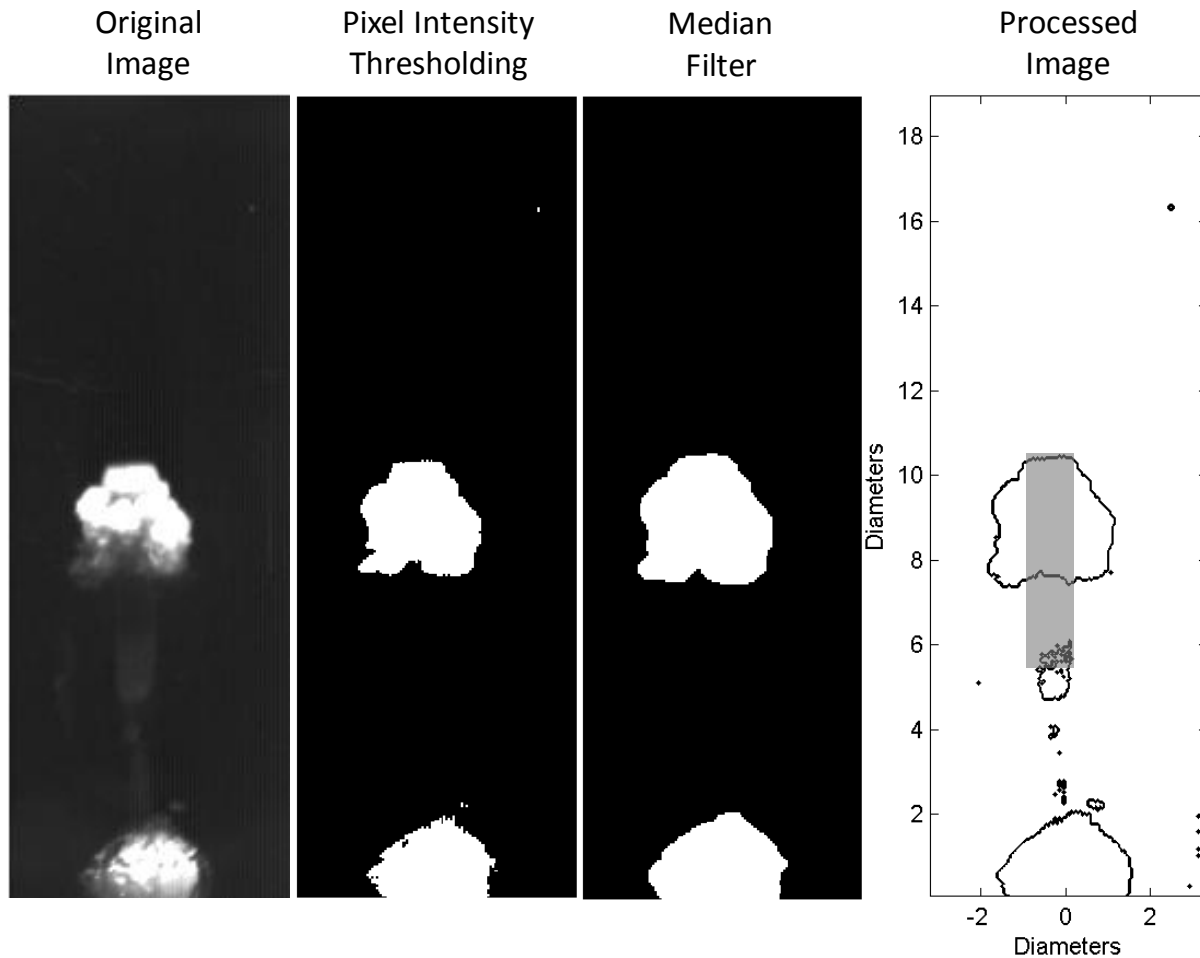


Figure 5.2. Image processing procedure (left to right) of a typical image is composed of several steps: 1) threshold and digitized image, 2) median filtering, and 3) final edge detection with estimated projectile location. Barrel is located at coordinates (0,0).

5.4.2 Projectile Trajectory and Cavity Shape Analysis Methods

The image processing analysis tracks the cavity and projectile boundaries and thus quantitative information about the projectile trajectory and supercavity development can be computed. The MATLAB function was written to automatically track the supercavity boundary and compute the projectile tip velocity. Time derivatives were estimated using a 2nd order central finite difference scheme of the computed projectile or cavity tip locations. Errors associated with this method are $\sim O(\Delta t^2)$, where Δt is the time step between consecutive images. In these experiments the sampling frequency ranged from 1900 Hz to 6000 Hz ($0.166 \text{ ms} < \Delta t < 0.526 \text{ ms}$).

The data analysis methods are illustrated here for a representative test case. The test case chosen is that of a blunt projectile of aspect ratio 5 translating at a maximum speed of 24 m/s

($\sigma=0.33$). The simultaneous projectile and cavity vertical (streamwise) positions are shown in Figure 5.3 plotted against time. Respectively, Figure 5.4 shows the corresponding velocities of both the projectile and the cavity normalized against the initial projectile velocity. The analysis of such plots enables us to determine the time of the initial cavity development as well as the convective speed of the cavity with respect to the projectile. For example, by observing Figure 5.3 and Figure 5.4, we note that the cavity tip originated at 1.5 diameters downstream of the projectile forebody at time $t=1.2$ ms, with all times referenced to the time at which the projectile tip left the barrel. Also these figures show that at approximately $t=3.8$ ms the cavity had accelerated forward, reaching the projectile tip. Note that until 5 diameters (~ 2 ms) downstream of the launch barrel the projectile was still accelerating.

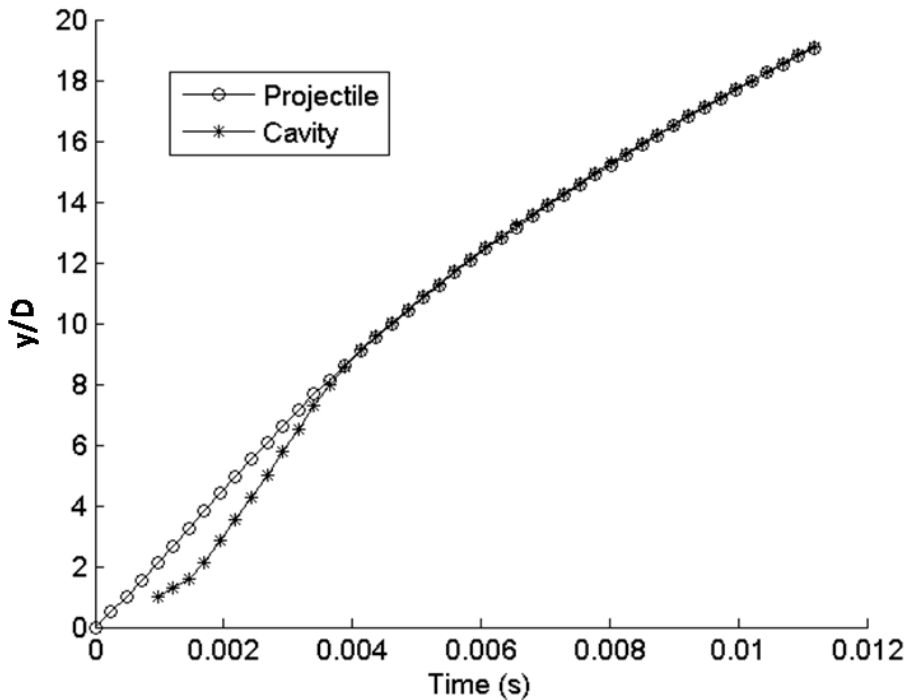


Figure 5.3: Projectile and cavity tip vertical positions in time.

As shown in Figure 5.3 and Figure 5.4, the cavity first appeared near the aft end of the projectile. At a later time in the development process, this small cavity (which was typically symmetric about the projectile) rapidly grew in size and subsequently enveloped the projectile. This is better illustrated by analyzing the area ratio between the cavity and the projectile as shown in Figure 5.5 for the example case. The small initial cavity retained its size for approximately 1.3 ms (region A, 0.9 ms – 2.2 ms) as it translated with the projectile. At approximately 2.2 ms (region B), rapid growth of the initial cavitation appeared and is reflected

in the rapid growth of the area ratio. During this period the projectile is first enveloped by the partial cavity. After this time the area ratio fluctuated as the cavity continued to develop and the projectile flight became unstable. Identifying what physical mechanism that governs the rapid growth of the initially small cavities (region A) into a fully developed partial cavity (region B) is the focus of the remaining analysis.

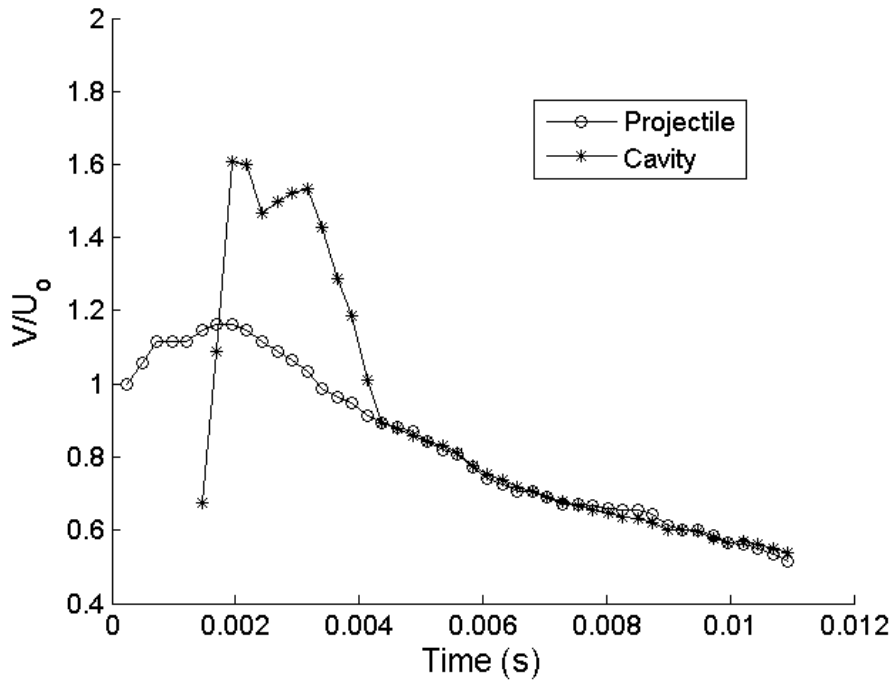


Figure 5.4: Projectile and cavity normalized velocities in time. Time=0 corresponds to egress of projectile tip from barrel.

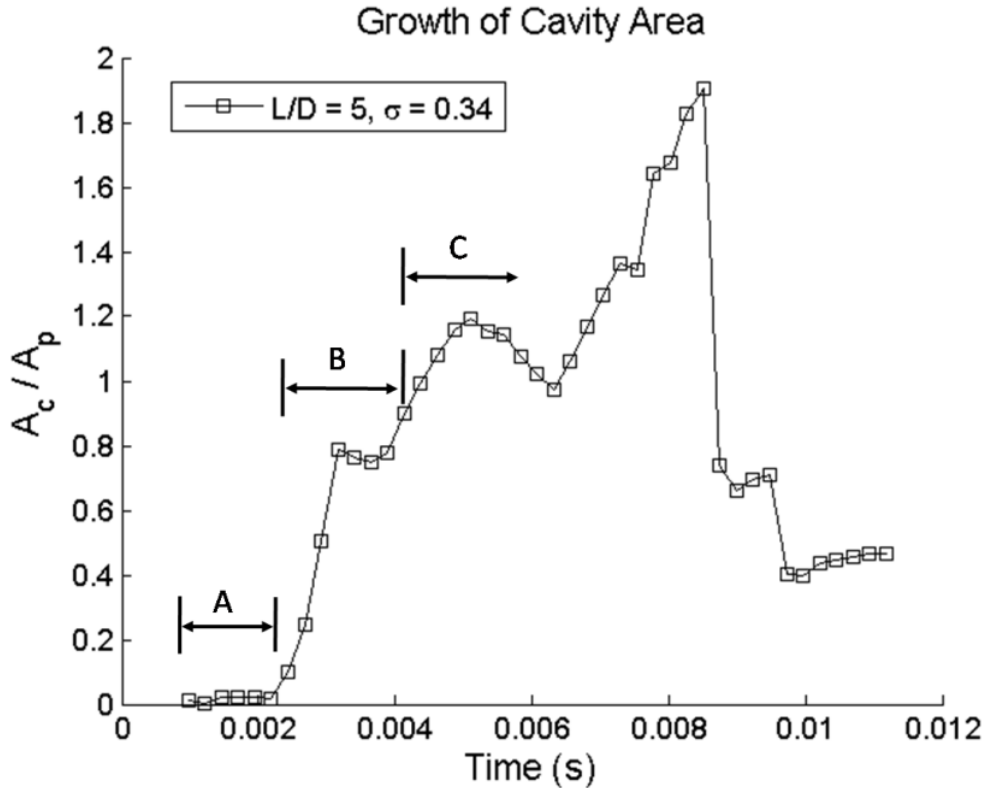


Figure 5.5: Ratio of projectile cavity area to projected projectile area as a function of time. Time=0 corresponds to egress of projectile tip from barrel.

5.4.3 Determination of Supercavity Growth Time Scales

Observations similar to the ones illustrated by Figure 5.3-Figure 5.5 were made across all experimental trials and revealed the existence of two critical time scales that characterize the cavity development process: the critical growth time and terminal growth time. The first is the time at which the initial cavitation bubble rapidly grows in size. We term this the critical growth time scale (CGTS) and it represents the spontaneous growth of the initial cavitation bubble. This time is manifested by the explosive growth of the ratio of projected cavity area to projectile area, such as where region A transitions into region B in Figure 5.5.

The second critical time scale occurs when the cavity is fully developed. This is termed the terminal growth time scale (TGTS) and is defined as the time at which the cavity and projectile translate with the same velocity (99% with respect to each other). The TSGT can be identified in Figure 5.4 at approximately 4.4 ms. The velocity time history serves as a better metric for determining the TSGT than the respective area measurements because the developed supercavity will shed gases and thus alter the cavity area ratios bounded to the projectile, making identification of this time scale difficult.

For repeatable determination of the CGTS, Change Point Analysis (CPA) was used to statistically detect changes in the area ratio signal (Hinkley 1970; Hinkley 1971). CPA relies on a statistical cumulative sum estimation of variations, such as the mean or median of a signal, in order to detect significant changes in a spatially or temporally varying signal. These changes are identified by the local minima or maxima in the cumulative sum. The CPA calculation of a one dimensional signal S (composed of x number of measurement points) proceeds as follows. First the n -point (np , an odd number) standard deviation (γ^{np}) of all points are computed as shown in Equation 5.2. The mean signal \bar{S} is computed for each signal point j between the bounds $j \pm [np/2]$. Brackets denote the floor function which rounds the number to the next lowest integer value. Note that the total signal size is diminished by $np-1$ number of points. Second the mean standard deviation of the signal is computed ($\bar{\gamma}$) as shown in Equation 5.3. Last the cumulative sum (CS) is computed for each point as shown in Equation 5.4 where $CS_1=0$. In our analysis, a 5-point standard deviation (γ^5) of the area ratio was computed.

$$\gamma_j^{np} = \sqrt{\frac{1}{np} \sum_{j=[np/2]}^{x-[np/2]} S_j - \bar{S}_{j \pm np/2}}^2 \quad 5.2$$

$$\bar{\gamma} = \frac{\sum_{j=1}^{x-np-1} \gamma_j^{np}}{x-np-1} \quad 5.3$$

$$CS_i = CS_{i-1} + (\gamma_i^{np} - \bar{\gamma}) \quad 5.4$$

The result of the CPA analysis for the signal shown in Figure 5.5 is shown in Figure 5.6. The local minimum of the CPA value is seen approximately at $t=2.2$ ms (marked with arrow) and denotes that a significant change in the area ratio signal has occurred. This point in time is defined as the CGTS. This analysis was performed on all of the test cases to determine the CGTS as a function of all test parameters. Note that the subsequent maxima and minima at later times reflect other changes in the area ratio as shown in Figure 5.5. Since we are concerned with identifying the change in stability of the initial cavitation bubble, we ignore these later maxima and minima and only consider the first one.

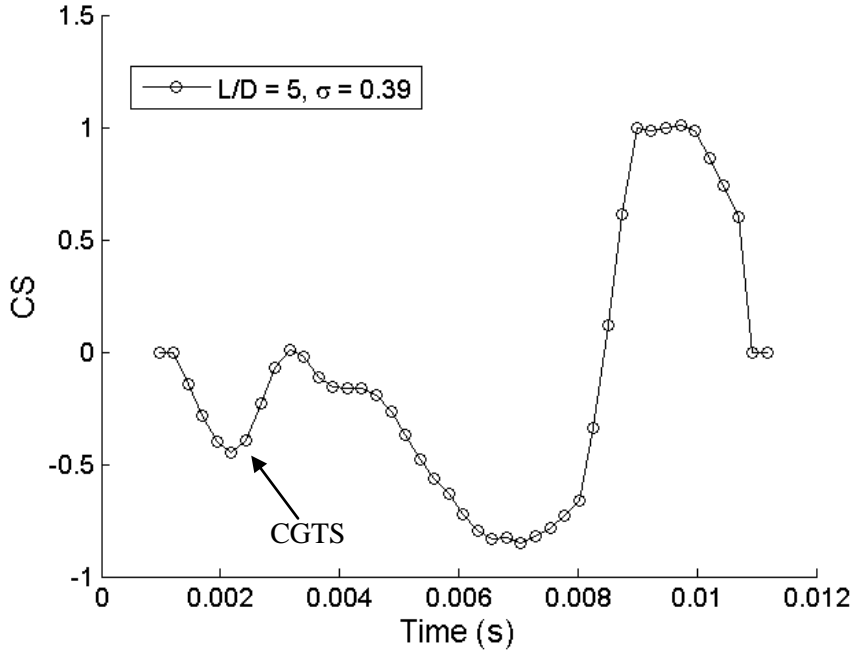


Figure 5.6: Change Point Analysis of Figure 5.5 showing the computed location of the CGTS.

5.5 Non-Dimensional Time Scale

The time scale is non-dimensionalized as shown in Equation 5.5. \bar{U}_p is the running mean projectile velocity, $t_{critical}$ is the time of CGTS in physical units, and D is the projectile diameter.

$$\frac{H}{D} = \frac{\bar{U}_p t_{critical}}{D} \quad 5.5$$

Equation 5.5 has significance in the scaling of the vortex ring behavior, where a slug of fluid is pushed by a piston through a bore of diameter D over length H . Gharib et. al. (Gharib et al. 1998; Mohseni and Gharib 1998) have shown that the scaling parameter H/D (where H is the equivalent stroke length and is equal to the numerator of Equation 5.5), termed the formation time, appropriately scales the vortex ring time scale before pinching off from the feeding jet. They suggest that, subject to several assumptions, the formation number ranges between $3.6 < H/D < 4.5$. Their model is based on the Kelvin-Benjamin variational principle (Benjamin 1976), which defines a limiting process for the maximum circulation the vortex ring can incur before it pinches-off. We explore this concept in association with the present effort motivated by the notion that the egress of the projectile is equivalent to the typical vortex ring experiments where a piston-driven motion results in the formation of a vortex ring. At its estimated pinch-off time

the vortex ring will contain the maximum circulation thus imparting the largest pressure drop to small bubbles present in the flow.

5.6 Results and Discussion

The experimental results are presented in three sections. The first discusses the archetypal (pure hydrodynamic) partial supercavity development process. The second discusses deviations from the archetypal process through the process of gas leakage. The third section presents the data supporting the notion of a critical time scale for supercavity development over impulsively translated bodies.

5.6.1 *The Archetypal Cavity Formation Process*

Figure 5.7 shows the cavity (A_c) to projectile (A_p) area ratio for all projectiles as a function of the formation time. Qualitatively, two distinct development regimes are observed based on the formation time value for which the growth of the cavity appears to dramatically increase. The first occurs for smaller area ratios whose cavities tend to develop at formation times of approximately 3 or greater. The second regime is denoted by very large area ratios that are generated at formation times less than 2. In the second regime the area ratios can reach upwards of 13. These cases, such as $L_p/D_p=2.5$ $\sigma=0.18$ and $L_p/D_p=2.5$ $\sigma=0.25$ in Figure 5.7 are indicative of a cavity growth process different from the majority of the other cases shown in Figure 5.7 and will be discussed in more detail in the next section.

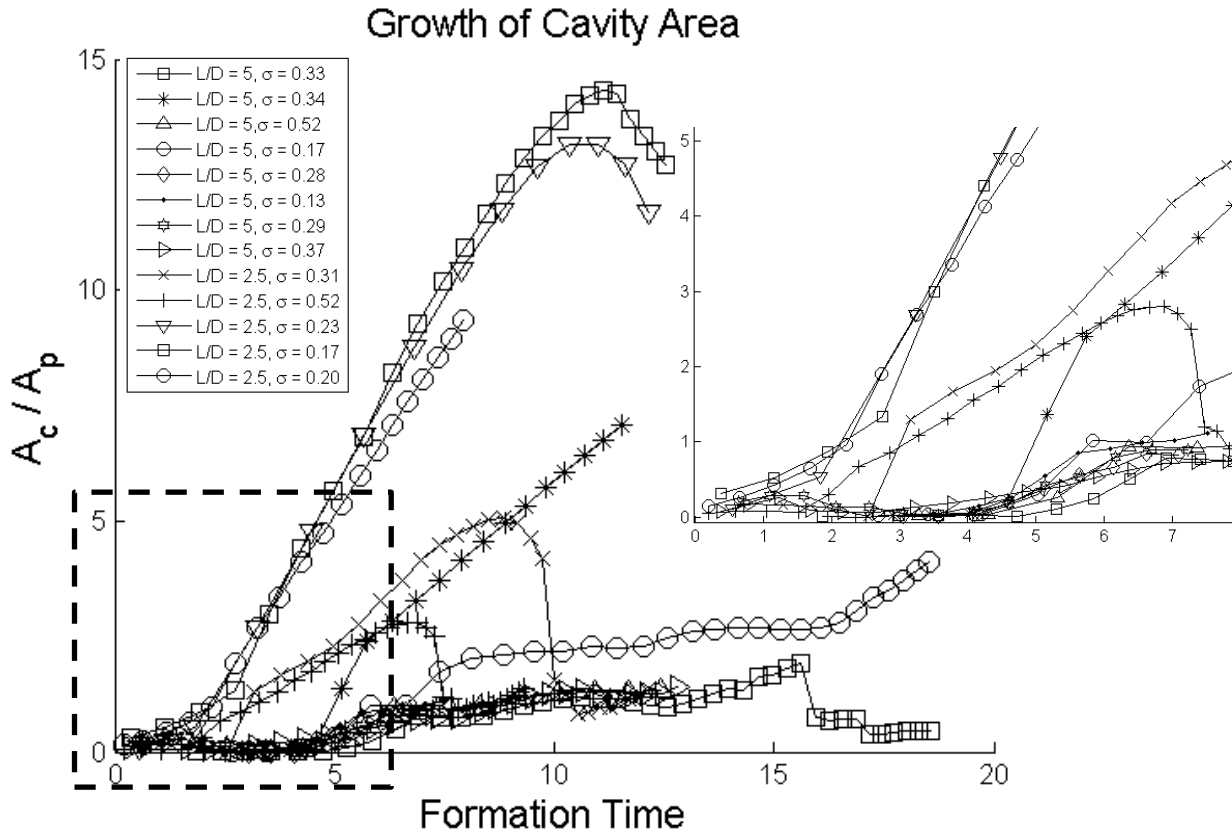


Figure 5.7. Plot of area ratios for all tested projectiles against the formation time. Inset picture shows zoomed-in detail. Note the clear division between two regimes which seems to occur near a formation time of 3.

We consider those cases where the growth and formation of partial cavities have a CGTS greater than 3 as archetypal and this is supported by the qualitative observations and image analysis of these respective cases. An example of the archetypal cavity formation process is shown in Figure 5.8 for the same test case shown previously, that of an aspect ratio 5 blunt projectile with maximum speed of 24 m/s ($\sigma=0.33$). The images are shown at 0.24 ms intervals. In image A, the edge-detected outline of the barrel exit is seen centered about position (0,0). The projectile position is superimposed over the images. The location of the projectile is estimated using the projectile tip location and knowledge of the projectile geometry. Image A shows the first small cavity as appearing downstream of the projectile forebody. The arrows are used to denote the cavity position as some noise appears which can resemble small cavities in some of the processed images. Only by studying the photographic data can the two be separated, although generally structures near the projectile, which do not move over time, indicate noise as opposed to a cavity. A good example of this is the object located at approximate coordinates (1,2) which remains stationary throughout the images. In images B-E, this initial cavity

translated with the projectile, maintaining its size and position downstream of the forebody. In image F an additional small cavity formed upstream of the initial cavity and the two merged and grew in size in image G. In images H-I the cavity expanded in volume upwards along the projectile body and in image J the projectile is covered approximately 50% by the cavity.

Careful observation of the raw images reveals the presence of small bubbles that are generated at the front of the body as the flow separates around the sharp corner. The bubbles are so small that the image processing does not capture them and they can only be discovered through careful study of the photographic images. These bubbles are entrained by the vortex ring downstream of the forebody where they grow independently and/or merge to form a larger cavity which loiters for some time. Figure 5.5 shows that the bubble area remains constant before rapidly expanding in volume. The identification of the mechanism and the time scale that governs this transition from stable bubble to rapid growth is explained and discussed in the following sections.

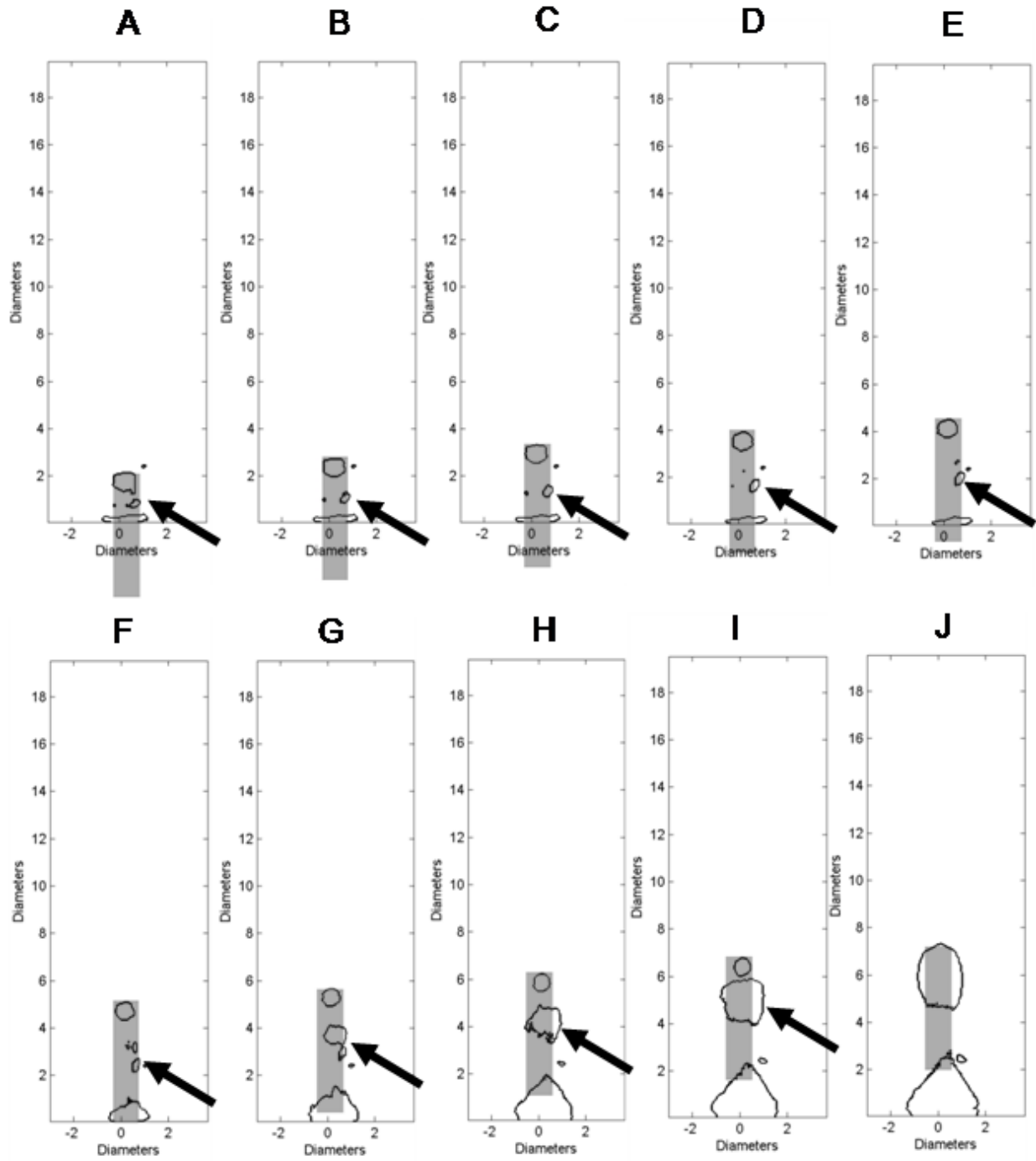


Figure 5.8. Supercavity development over aspect ratio 5 blunt projectile with maximum speed of 24 m/s ($\sigma=0.33$). The images are shown at 0.24 ms intervals. Growing cavity is denoted by arrows. Note the forebody of the projectile is covered by small bubbles in images A-I. The formation time (CGTS) of the test case was computed to be about 4.3.

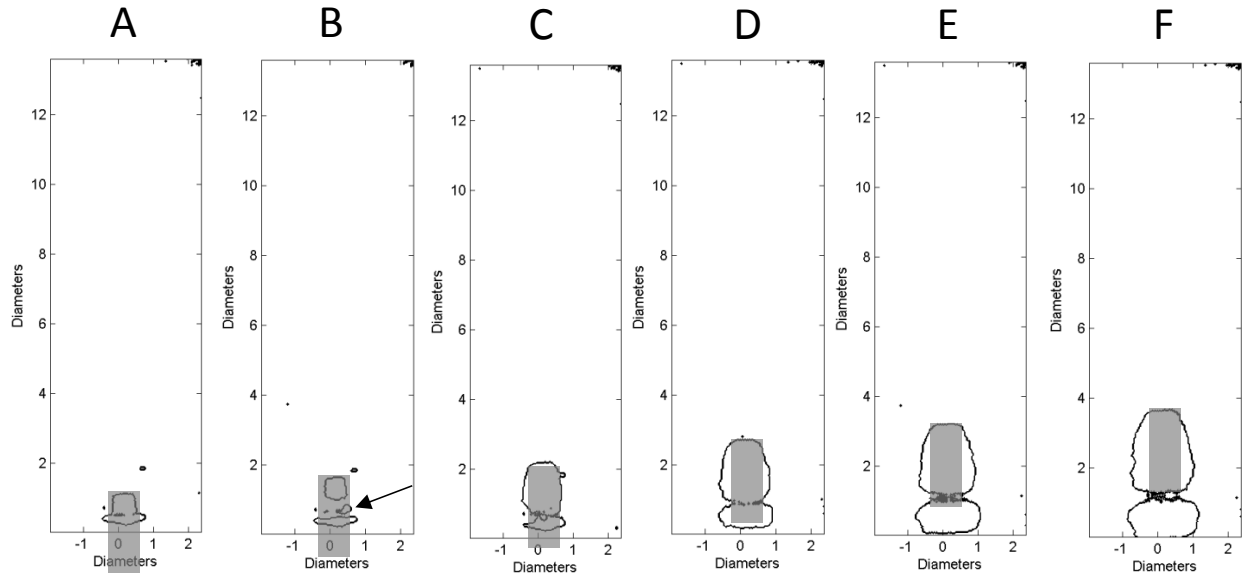


Figure 5.9. Cavity development for projectile of aspect ratio of $L_P/D_P=2.5$ and $\sigma=0.18$ shown at $\Delta t=0.24\text{ms}$. Initial cavity is shown by arrow. Note the forebody of the projectile is covered by bubbles in images A and B.

5.6.2 The Gas Leakage Effect

For the cases with low formation time as shown in Figure 5.7, it is difficult to distinguish the development process. Instead, the projectile is nearly instantly supercavitating the moment it leaves the barrel as shown in Figure 5.9. Here the cavity and estimated projectile position is shown at 0.24 ms intervals for a projectile aspect ratio of $L_P/D_P=2.5$ and $\sigma=0.18$. In image A, the projectile forebody has just begun to exit the barrel. In image B, a small cavity is seen (arrow) which by image C has already expanded to cover the whole projectile as shown in the subsequent images. This progression of events differs greatly from the previous paradigm and the small CGTS is explained by gases leaked from the barrel and contaminating the flow field adjacent to the projectile. This gas leakage occurred at some time between images B and C. The effect of premature supercavitation due to the barrel-gas contamination is termed the gas leakage effect and is responsible for the premature transition of the initial cavity into the developed supercavity at low formation numbers. This process is similar to a ventilated supercavity although the actual mechanism is different since in this case the ventilation source is off the body.

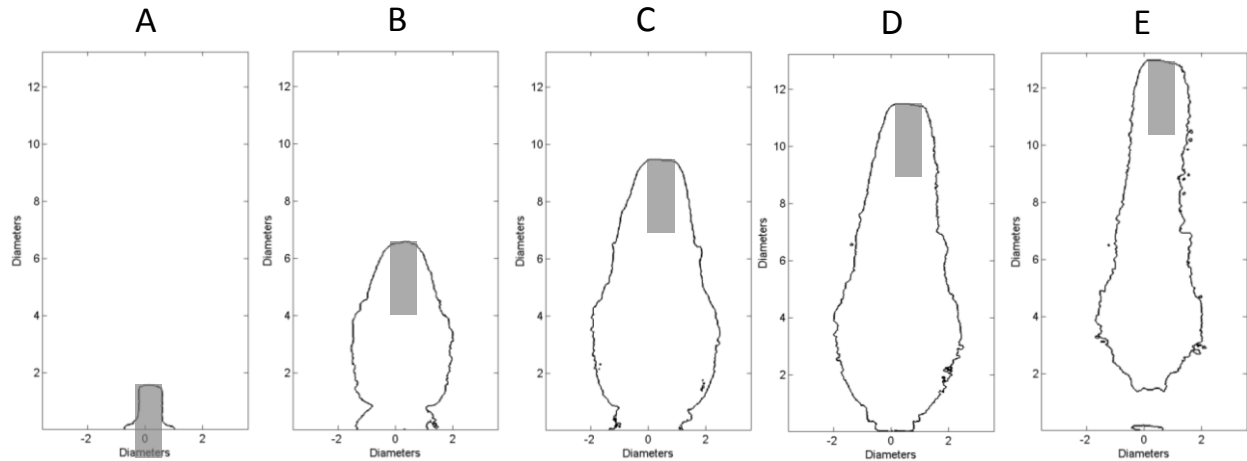


Figure 5.10. Supercavity development over projectile ($L_p/D_p=2.5$ $\sigma=0.25$) and corresponding cavity development shown at 1.6 ms intervals. Note that the cavity extends from the projectile forebody to the barrel in images B-D.

Cases of large area ratios that suddenly reach a maxima and decline, such as $L_p/D_p=2.5$ $\sigma=0.18$ and $L_p/D_p=2.5$ $\sigma=0.25$ in Figure 5.7, are attributed to the gas leakage concept. The large area ratios measured are due to cavities remaining attached to the barrel as the projectile translates downstream as shown in Figure 5.10. Thus the cavities are subjected to a large flux of expanding barrel gases that prevent the cavity from closing. Here the projectile ($L_p/D_p=2.5$ $\sigma=0.25$) and corresponding cavity development are shown at 1.6 ms intervals. The supercavity gases stay attached to the barrel as the projectile translates downstream until image E. This pinch-off and shedding of the supercavity gases is reflected in Figure 5.7 as the decrease in the cavity area ratio at a formation time of approximately 10. Note that all of the $L_p/D_p=2.5$ projectiles experienced the gas leakage effect. This is rationalized by the fact that the longer projectiles essentially plug the barrel gases from escaping during cavity development, and thus do not allow barrel gases to contaminate the cavity development region downstream of the forebody as was pointed out for Figure 5.7. The shorter projectiles do not provide the same level of sealing and hence barrel gases are able to contaminate the flow field and do not allow the supercavity to develop through normal hydrodynamic mechanisms. This rationale also explains why the time scales are drastically different between the two regimes: since both large and small aspect ratio projectiles had the same diameter and were shot at nearly the same range of velocities (Reynolds numbers), the viscous mechanisms responsible for the partial cavity development do not change between the different aspect ratios. Thus, in order for the two projectiles to have different time scales an alternative mechanism must be responsible. In this

case, the high-pressure barrel gases were drawn into the low-pressure separated flow region behind the projectile forebody, causing nearly instant supercavitation through ventilation.

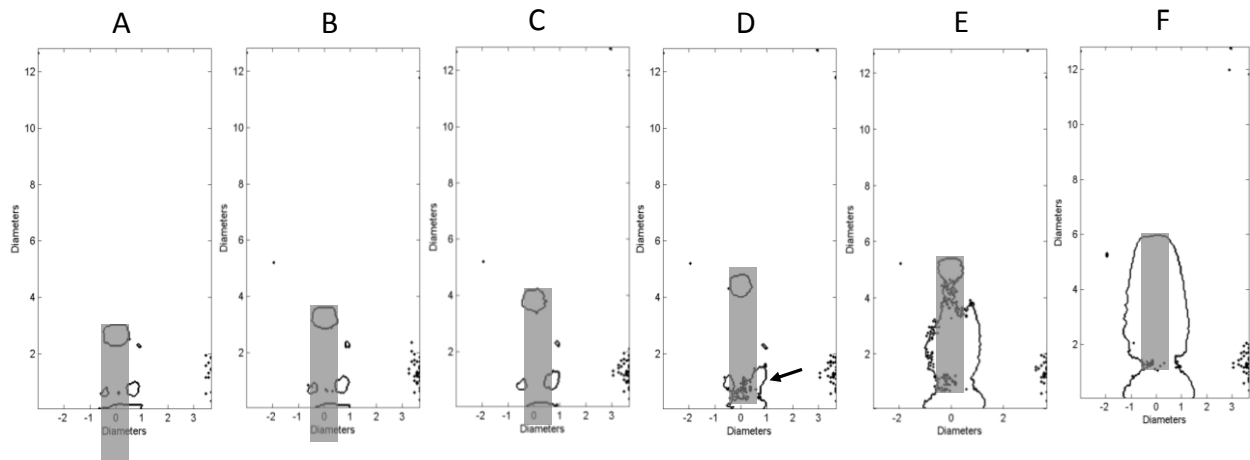


Figure 5.11. Supercavitation development over projectile of $L_P/D_P=5$ and $\sigma=0.34$ shown at 1.6 ms intervals. Initial cavities are clearly seen in images A-C, which interact with barrel gases in image D (arrow).

In addition to the two regimes shown, a third regime exists, termed pseudo gas leakage. Here the initial cavity formation is governed by natural processes, but gas leakage is responsible for the large scale supercavitation formation. An example of this process is shown in Figure 5.11 for the $L_P/D_P=5$ $\sigma=0.34$ projectile. Images A-C show the natural cavitation process unfolding; two distinct cavitation regimes are seen that remain relatively stationary with respect to the projectile forebody. Images A-C show the initial expansion of the stable gas bubbles just prior to envelopment of the projectile. In image D, the projectile just clears the barrel and high-pressure barrel gases are seen to interact with the natural cavities (arrow). The cavity rapidly expands at this time, resulting in full supercavitation (image F). Proof of the gas leakage effect is manifested as the supercavitation gases remained attached to the barrel. The CGTS was not diminished however, as the natural expansion of the vortex ring core began just before this leakage process. This behavior was also observed for the projectile case $L_P/D_P=5$ $\sigma=0.17$. Full supercavitation was only observed for projectiles with gas leakage.

5.6.3 Critical Time Scale for Partial and Supercavitation Formation

Since the development of cavitation can be ascribed to either A) viscous flow over a streamlined body or B) separated flow, the CGTS is plotted against the Reynolds number in Figure 5.12. Note that only 13 test cases are shown. The cases for which the image quality of the initial bubble is poor were omitted from the critical time scale analysis. The two regimes, archetypal ($3 < \text{CGTS} < 4.5$) and gas leakage ($\text{CGTS} < 3$), are readily seen. The two pseudo-gas

leakage cases are also shown with arrows. One case was an outlier ($L_P/D_P=5$ $\sigma=0.37$) with a CGTS of about 3.2. The reason for this divergence is unclear. It is possible that the merging of two smaller cavity bubbles occurred and the rapid increase in cavity area was perceived as the rapid area growth that defines CGTS.

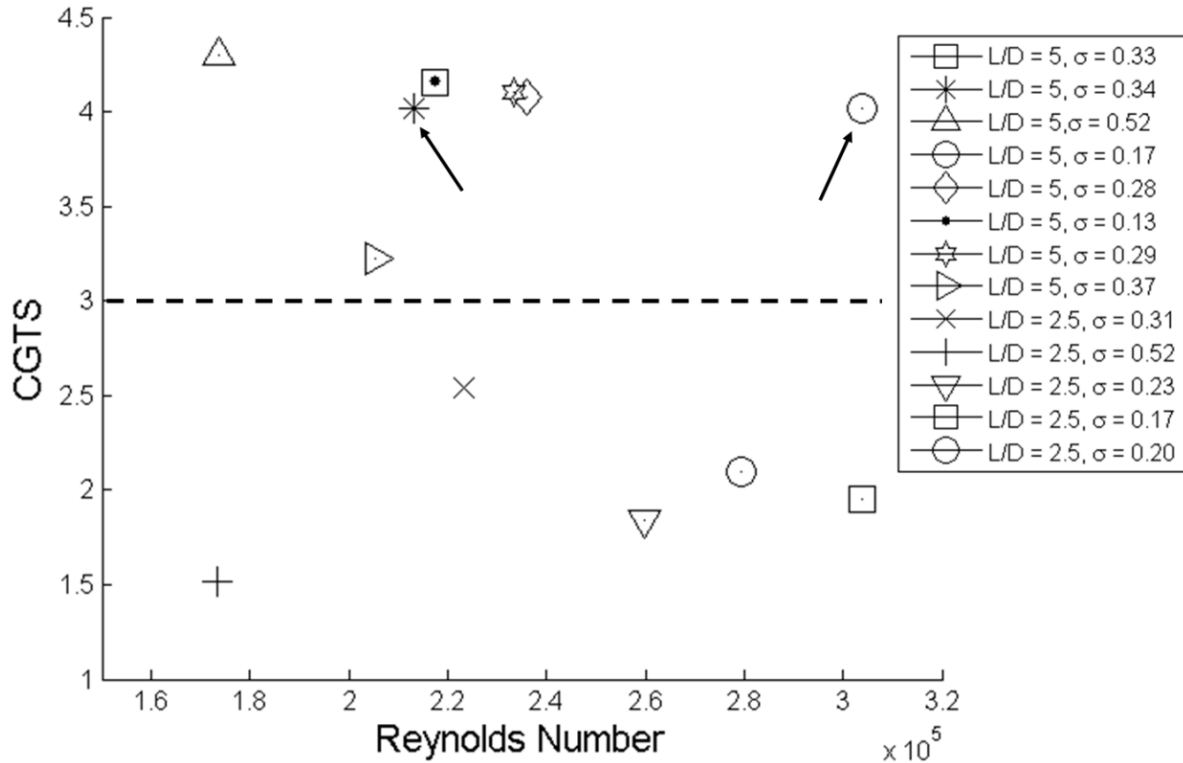


Figure 5.12. The critical time of the supercavity development process over the range of parameters tested.

As the projectile translates through the quiescent water just after barrel egress, flow stagnates at the forebody of the projectile and a laminar boundary layer develops. The boundary layer separates at the sharp corner of the forebody and rolls into a vortex ring. This vortex ring entrains micro bubbles and nuclei shed from the projectile front-edge into the vortex core where the low-pressure environment triggers and promotes vortex-induced cavitation. Here we calculate some critical parameters to estimate the conditions experienced by the small bubbles at the CGTS in an effort to rationalize the proposed mechanism. The circulation of the vortex ring is estimated using the method of Glezer (1988) and is given in Equation 5.6. Θ is a constant denoting the influence of the velocity program and is defined in Equation 5.7, t is a running time, and $t_{critical}$ is the physical time corresponding to CGTS.

$$\Gamma = \theta \frac{\bar{U}_P^2 t_{critical}}{2} \tag{5.6}$$

$$\theta = \int_0^1 \frac{U_p^2}{\bar{U}_p^2} d\left(\frac{t}{t_{critical}}\right) \quad 5.7$$

Introducing the pressure coefficient and modeling the vortex as a Lamb vortex yields Equation 5.8, which for a Lamb vortex $C_{p,min} = (R/a)^2 - 1.74$ where R denotes the radial position. The vortex core radius is given by a and in the context of these experiments is the initially small cavity seen downstream of the fore end. Using this cavity radius as the core radius $C_{p,min} = -0.74$. The pressure just outside the vortex core (P_{min}) which drives the cavity growth is computed from the definition of the pressure coefficient and is given in Equation 1.8.

$$C_{p,min} = \frac{2 P_{min} - P_{\infty}}{\rho \left(\frac{\Gamma_{max}}{2\pi a}\right)^2} = \frac{16\pi^2 a^2 P_{min} - P_{\infty}}{\rho \Gamma_{max}^2} \quad 5.8$$

As no measurements of the water quality were taken we will estimate the water condition here. According to Henry's law, water saturated with air at atmospheric pressure yields a concentration of 15 ppm dissolved air content. The critical tensile water strength is then (Arndt 1995) given by Equation 5.9 where p_s is the saturation pressure, β is Henry's constant (nominally 6700 Pa/ppm for air), and C_g is the dissolved gas content (in ppm). Note that p_s is greater than the vapor pressure of water which denotes gaseous, as opposed to vaporous, cavitation.

$$P_{\infty} - P_{v_c} \leq p_s = \beta C_g \quad 5.9$$

The data of Rouse and McNown (1948) was also examined in an attempt to understand the pressure field downstream of the blunt forebody and its effect on the cavity development. Rouse and McNown conducted a multitude of experiments on a stationary zero caliber ogive over a range of cavitation indices and took detailed pressure measurements along the body. We have tabulated their results including only the minimum pressure measured on the body at a given cavitation index, the idea being that the minimum pressure will be the driving factor to promote cavitation on a large scale. As their measurements only cover a range of the Reynolds numbers encountered here their minimum pressure curve is linearly extrapolated to lower Reynolds numbers as a rough estimate.

The experimental results and the two pressure conditions, namely 1) the saturation pressure given by 15 ppm air dissolved in water and 2) the data of Rouse and McNown for the pressure inside the separation bubble are shown together in Figure 5.13. Circles denote archetypal cavity

development cases and diamonds denote cases which appear to instantaneously supercavitate through gas leakage. Note that since the rapid growth of initially small bubbles was not observed for the gas leakage cases, the first observation of full supercavitation was reported as the CGTS. Therefore for these cases of gas leakage it is likely that the pressures estimated here are well below what was actually experienced. In fact, it is likely that the pressures were much higher than the saturation pressure, but all gas leakage cases have pressures well above the pressures reported by Rouse and McNown. Based on this data it is likely that for these cases the pressure field has little to do with determining the supercavity growth, which supports the idea of supercavity growth through the gas leakage effect.

As can be seen from Figure 5.13 the pressure measurement data of Rouse and McNown indicates the minimum pressure in the separated flow region is greater than that experienced by the initially small cavitating bubbles at CGTS for many of the test cases. Cases for which this does not hold are 1) three cases at $Re \sim 1.75 \times 10^5$, 2.3×10^5 , and 3.4×10^5 , the first of which had an unusually low CGTS (3.22) that can be seen in Figure 5.12 and 2) the gas leakage cases. In all cases the estimated vortex pressure never reached the vapor pressure, but many of the test cases sustained pressures lower than what was reported by Rouse and McNown. Therefore, it is likely that the CSGT was caused not by the separated flow pressure but rather the vortex pressure field.

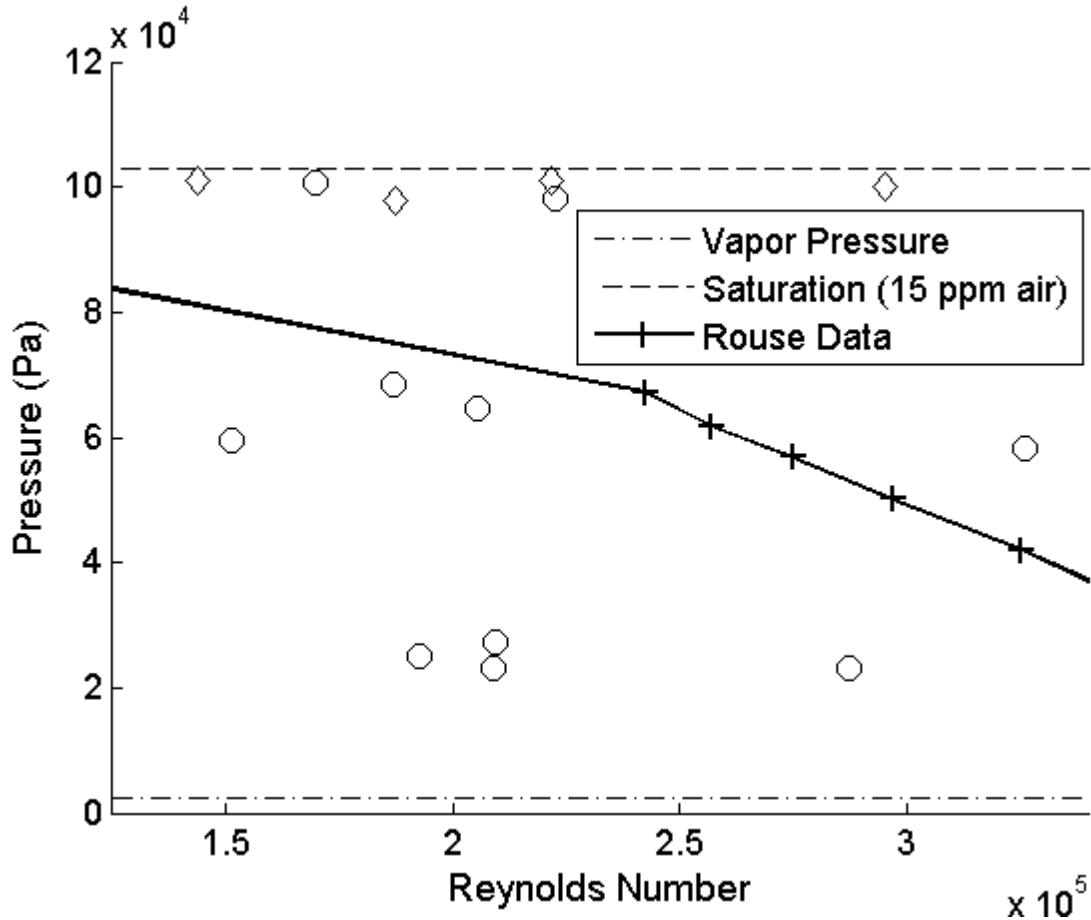


Figure 5.13. Predicted pressures which can drive the CGTS. Circles represent archetypal development cases and diamonds represent gas leakage cases.

To further disprove the argument of the separated flow pressure and re-entrant jet controlling the CGTS we compute the maximum time scale for the advection of a bubble from the fore end of the body to the reattachment point and then its travel back toward the fore end. A similar phenomenon was observed by Arakeri and Acosta (1973) in their studies of cavity development over static bodies tested in a water tunnel facility. This time is computed from Equation 5.10, where U_P is the projectile velocity, L_C is the distance between the fore end and the initial small cavity, and U_j is the re-entrant jet velocity. The re-entrant jet velocity can be calculated from the Bernoulli equation along a streamline. σ is computed using the cavity pressure as opposed to vapor pressure and estimations of the cavity pressure are taken from the data of Rouse and McNown (1948). We compute this time scale for all test cases where the projectile was not immediately supercavitating upon egress from the barrel. Using t_j as the time in which to compute the CGTS we arrive at the maximum formation time which should be observed if the re-entrant jet were responsible for the generation of the cavity. As is shown in Figure 5.14 in all

cases the observed CGTS is much greater than that due to the re-entrant jet model. The observed CGTS is shown with a filled marker and the CGTS calculated from the re-entrant jet is shown with an open marker. A vertical line connects each case to show the difference between the two values. The Reynolds number is computed from the velocity of the projectile at the experimentally observed CGTS. These calculations indicate the re-entrant jet has already carried bubbles from the reattachment point to the forebody in the separated flow region before the CGTS is observed experimentally. Also, the speed of cavity growth is up to four times the translational velocity of the projectile which is many times higher than the re-entrant jet velocity. It is clear from this analysis that the rapid growth of the initially small cavities is not due to the re-entrant jet.

$$t_j = \frac{2L_c}{U_j} = \frac{2L_c}{U_p \sqrt{1+\sigma}} \tag{5.10}$$

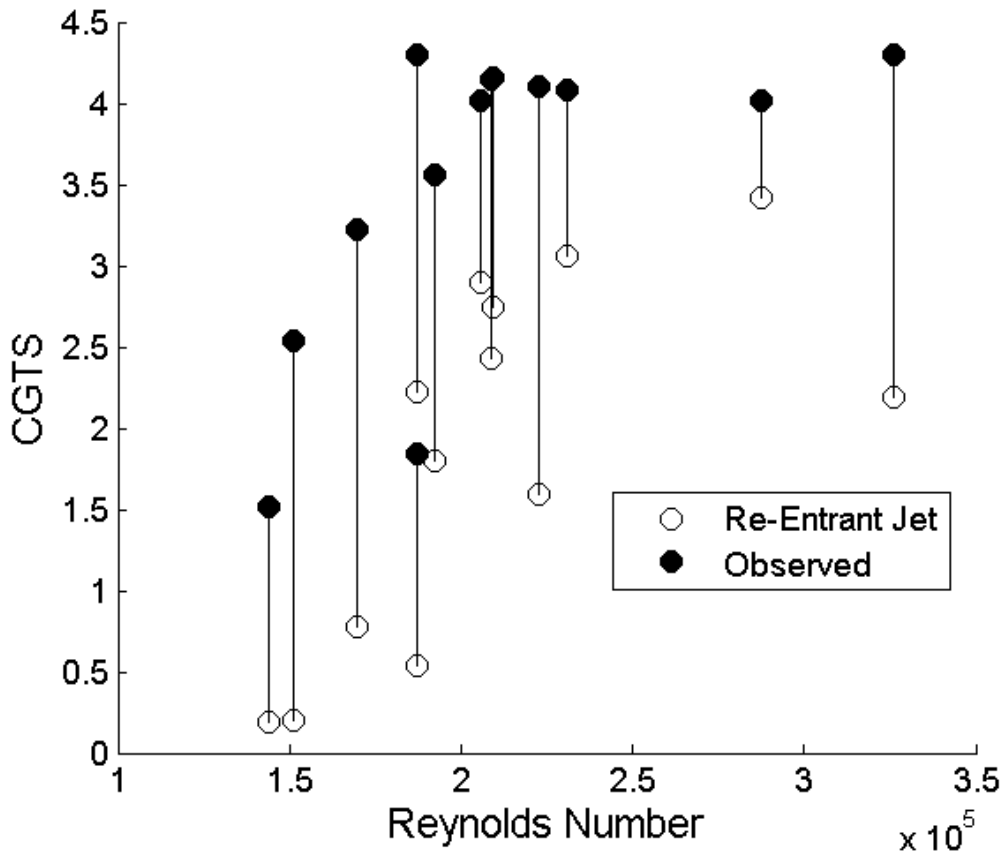


Figure 5.14. The maximum recirculation time scale computed from the digital images. In all cases the actual CGTS was greater than would be expected if the re-entrant jet were responsible for rapid cavity growth.

It is also possible that the expanding gases which drive the projectile could play a role in initiating the rapid bubble growth through a large pressure perturbation on a bubble near its

critical radius. The expansion of the large vaporous bubble behind the projectile upon egress in Figure 5.8 and the corresponding growth of the initial cavity occur coincidentally at or near the same time for this test case. However, it appears from the experimental data that these events are coincidental, as several test cases show rapid growth of the initial cavity prior to the barrel gases leaking into the flow field. Future tests must consider an alternative mechanism to launch the projectiles to completely decouple the two phenomena of gas leakage and bubble growth.

5.7 On the Similarity Between the Formation Number for Vortex Rings and the CGTS

The CGTS reported here for the archetypal development process is remarkably similar to the values reported by Gharib et al. (1998) to describe the time scale of vortex ring formation. In that work the vortex ring pinch off was shown to occur for a formation number of approximately $3.6 < H/D < 4.5$ and was subject to a number of assumptions and input flow conditions. This was explained through the use of the Kelvin-Benjamin variational principle, which denotes the maximum circulation that the vortex ring can attain. As will be shown, the CGTS reported here is similar to the formation number in magnitude only; the physical mechanisms responsible for the CGTS are quite different from the formation number and we will show here that it is erroneous to conclude the two mechanisms are equivalent.

Given the estimation of the vortex ring strength by Equations 5.6-5.7 and the formation number proposed by Gharib et al (1998) these equations are combined to yield Equation 5.11, which relates the velocity program, vortex circulation, and the mean running projectile velocity to the formation number.

$$\frac{H}{D} = \frac{\bar{U}_p t_{critical}}{D} = \Gamma_{max} \left(\frac{2}{D\theta\bar{U}_p} \right) \quad 5.11$$

Assuming the minimum pressure P_{min} seen near the core of the vortex in Equation 5.8 is the vapor pressure of water we solve for the theoretical formation number which is given in Equation 5.12. The vortex core radius a is taken as the mean core radius observed experimentally.

$$\frac{H}{D} = \left(\frac{2}{D\theta\bar{U}_p} \right) \sqrt{\frac{16\pi^2 a^2}{\rho} P_{\infty} - P_{min}} \quad 5.12$$

Figure 5.15 shows the theoretical CGTS versus the running mean projectile velocity. The theoretical curves shown correspond to the vapor pressure of water with $\Theta=4/3$ (ramp) and

$\Theta=1.1$, which cover the range of theoretical to experimental values of Θ observed in the experiments. Note the confirmed cases of gas leakage fall far below the theoretical CGTS. All other values are very close to the theoretically predicted CGTS. The reason for the outlier at $U_p \sim 8$ m/s CGTS ~ 3.22 is unclear, although it may correspond to some degree of unconfirmed gas leakage. It is interesting to note that the CGTS observed for the archetypal cases is essentially constant with increasing U_p . This trend indicates a limiting process – in this case the vortex pressure – which governs the CGTS.

It is therefore not necessary to consider the energetic processes presented by the Kelvin-Benjamin variational principle to explain the CGTS. The phenomenon may be explained through the vortex pressure generated near the core when a body is impulsively accelerated from rest. The CGTS time scale is coincidental with regards to the time scale observed by Gharib et al (1998) for the pinch off of vortex rings for the range of pressures considered here. If the ambient pressure was raised or the water quality was such so as to have a greater tensile strength the required time scales would deviate from those shown here.

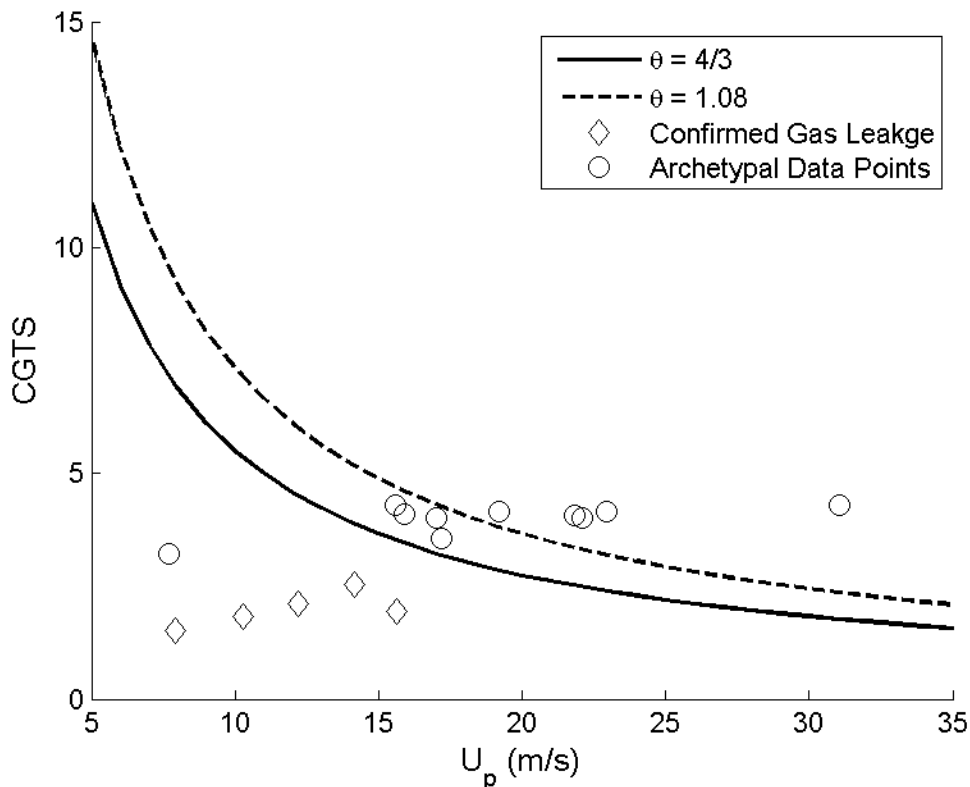


Figure 5.15. Theoretical values for the CGTS as a function of the running mean velocity. The experimental data is shown as either confirmed gas leakage or archetypal formation processes.

5.8 Conclusions

A critical time scale that describes the spontaneous growth of small-scale cavities into developed partial or supercavitation over blunt free flying cylindrical slug projectiles was observed experimentally. The initially small cavities appeared downstream of the projectile forebody and grew up the projectile. The critical growth time scale (CGTS), or the time at which the cavities rapidly grew in size, occurred approximately between 4 and 4.5. This is remarkably similar to the results of Gharib et al (1998), who show the dependence of vortex ring pinch off on a critical formation time of $3.6 < H/D < 4.5$. In addition to this archetypal formation process, two other processes were identified. The gas leakage supercavity process corresponds to a contamination of the projectile near-wake from propulsive gases. This interaction decreases the CGTS considerably, resulting in a supercavity development on a reduced time scale. Pseudo-gas leakage was also observed, in which case the CGTS is governed by the archetypal process due to purely hydrodynamic effects but the large scale supercavity development is due to propulsive gas contamination.

A plausible mechanism to explain supercavity development over translating projectiles was introduced. Bluff body separation over the blunt corner of the forebody produced a vortex ring whose circulation increased as the projectile accelerated due to the flux of vorticity from the blunt corner of the forebody. The vortex core was fed small nuclei that formed due to the separation at the blunt forebody. These small bubbles coalesced in the core of the vortex ring into an initially stable cavitating vortex ring core. At the critical growth time scale (CGTS) the initially stable cavitating vortex ring rapidly grew into a developed supercavity fully or partially enveloping the projectile. The small cavities grew from aft to fore as the supercavity developed, traveling at speeds up to 4 times the initial projectile velocity in part propelled also by the water entrainment jet at the aftbody. Vortex pressures were estimated and compared to experimental pressure measured on a zero caliber ogive at similar Reynolds numbers to show that the CGTS occurred at pressures lower than could be accommodated by a separated flow region. Additionally, it was shown that the re-entrant jet could not play a role in initiating the bubble growth as the maximum calculated time scale is still well below what was experimentally observed. It is therefore hypothesized that the CGTS corresponds to a critical vortex circulation, and thus pressure, necessary to initiate the unstable growth of small initially stable bubbles.

It was also shown that the CGTS is coincidental with the results of Gharib et al (1998) at the water quality and ambient pressures presented here. In fact, it is not necessary to consider the processes argued by Gharib et al for the current problem, which is purely based on reaching a critical vortex circulation necessary to surpass the tensile strength of water and induce unstable bubble growth.

5.9 References

- Amromin, E. and I. Mizine (2003). "Partial cavitation as drag reduction technique and problem of active flow control." Marine Technology and Sname News **40**(3): 181-188.
- Arakeri, V. H. and A. J. Acosta (1973). "Viscous Effects in the Inception of Cavitation on Axisymmetric Bodies." Journal of Fluids Engineering **94**(4): 8.
- Arndt, R. E. A. (1995). Vortex Cavitation. Fluid Vortices - Fluid Mechanics and its Applications. S. Green. Dordrecht, Kluwer Academic Publishers: 731-782.
- Arndt, R. E. A. (2002). "Cavitation in vortical flows." Annual Review of Fluid Mechanics **34**: 143-175.
- Benjamin, T. B. (1976). "The Alliance of Practical and Analytic Insights into the Nonlinear Problems of Fluid Mechanics. Applications of Methods of Functional Analysis to Problems in Mechanics." Lecture Notes in Math: 8-29.
- Blake Jr, F. G. (1949). "Onset of Cavitation in Liquids." Thesis (PH. D.)--HARVARD UNIVERSITY, 1949. Source: American Doctoral Dissertations, Source code: W1949: 0049.
- Brennen, C. E. and C. Earls (1995). Cavitation and Bubble Dynamics, Oxford University Press New York.
- Callenaere, M., J. P. Franc, J. M. Michel and M. Riondet (2001). "The cavitation instability induced by the development of a re-entrant jet." Journal of Fluid Mechanics **444**: 223-256.
- Gharib, M., E. Rambod and K. Shariff (1998). "A universal time scale for vortex ring formation." Journal of Fluid Mechanics **360**: 121-140.
- Glezer, A. (1988). "The Formation of Vortex Rings." Physics of Fluids **31**(12): 3532-3542.
- Gopalan, S. and J. Katz (2000). "Flow Structure and Modeling Issues in the Closure Region of Attached Cavitation." Physics of Fluids **12**(4): 895-911.
- Hinkley, D. V. (1970). "Inference about the change-point in a sequence of random variables." Biometrika **57**(1): 1-17.
- Hinkley, D. V. (1971). "Inference about the change-point from cumulative sum tests." Biometrika **58**(3): 509-523.
- Hrubes, J. D. (2001). "High-Speed Imaging of Supercavitating Underwater Projectiles." Experiments in Fluids **30**(1): 57-64.
- Huang, T. T. (1979). Cavitation Inception Observations on Axisymmetric Headforms. International Symposium on Cavitation Inception. New York, NY.
- Katz, J. (1984). "Cavitation Phenomena within Regions of Flow Separation." Journal of Fluid Mechanics **140**: 397-436.
- Keller, A. P. (1979). Cavitation Inception Measurement and Flow Visualisation on Axisymmetric Bodies at Two Different Free Stream Turbulence Levels and Test Procedures. International Symposium on Cavitation Inception. New York, NY.

- Kirschner, I. N., D. C. Kring, A. W. Stokes, N. E. Fine and J. S. Uhlman (2002). "Control strategies for supercavitating vehicles." Journal of Vibration and Control **8**(2): 219-242.
- Kondama, Y., S. Tamiya, N. Take and H. Kato (1979). The Effects of Nuclei on the Inception of Bubble and Sheet Cavitation on Axisymmetric Bodies. International Symposium on Cavitation Inception. New York, NY.
- Le, Q., J. P. Franc and J. M. Michel (1993). "Partial Cavities - Global Behavior and Mean Pressure Distribution." Journal of Fluids Engineering-Transactions of the Asme **115**(2): 243-248.
- Lin, G. J., B. Balachandran and E. H. Abed (2008). "Dynamics and control of supercavitating vehicles." Journal of Dynamic Systems Measurement and Control-Transactions of the Asme **130**(2): -.
- Matveev, K. I. (2003). "On the Limiting Parameters of Artificial Cavitation." Ocean Engineering **30**(9): 1179-1190.
- Mohseni, K. and M. Gharib (1998). "A model for universal time scale of vortex ring formation." Physics of Fluids **10**(10): 2436-2438.
- Plesset, M. S. and A. Prosperetti (1977). "Bubble Dynamics and Cavitation." Annual Reviews in Fluid Mechanics **9**(1): 145-185.
- Prosperetti, A. (1982). "A generalization of the Rayleigh–Plesset equation of bubble dynamics." Physics of Fluids **25**: 409.
- Rayleigh, L. (1917). "On the pressure developed in a liquid during the collapse of a spherical cavity." Phil. Mag **34**(200): 94-98.
- Rood, E. P. (1989). Mechanisms of Cavitation Inception. International Symposium on Cavitation Inception. San Francisco, CA.
- Rood, E. P. (1991). "Review -- Mechanisms of Cavitation Inception." Journal of Fluids Engineering **113**: 163-175.
- Rouse, H. and J. McNown (1948). Cavitation and Pressure Distribution Head Forms at Zero Angle of Yaw. Iowa City, State University of Iowa.
- Savchenko, Y. N. (2001). Supercavitation - Problems and Perspectives. Proc. 4th International Symposium on Cavitation, Pasadena, CA.
- Shi, H.-H., M. Itoh and T. Takami (2000). "Optical Observation of the Supercavitation Induced by High-Speed Water Entry." Journal of Fluids Engineering **122**: 806-810.
- Stutz, B. and J. L. Reboud (1997). "Experiments on unsteady cavitation." Experiments in Fluids **22**(3): 191-198.
- Stutz, B. and J. L. Reboud (2000). "Measurements within unsteady cavitation." Experiments in Fluids **29**(6): 545-552.
- Varghese, A. N., J. S. Uhlman and I. N. Kirschner (2005). "Numerical analysis of high-speed bodies in partially cavitating axisymmetric flow." Journal of Fluids Engineering-Transactions of the Asme **127**(1): 41-54.

6. CONCLUSIONS

This dissertation has provided an experimental study of the characteristics of the high speed gas-liquid interface. The usage of a global optical measurement technique has provided an interesting perspective on these flows as past researchers have only used point measurement techniques.

The implications of the basic research contained in this dissertation have been applied to the Water Piercing Missile Launcher (WPML). The WPML feasibility study process is reproduced below as Figure 6.1, and is composed of three major questions. In this dissertation each question was addressed in a separate section, and the major conclusions from each section are summarized below.

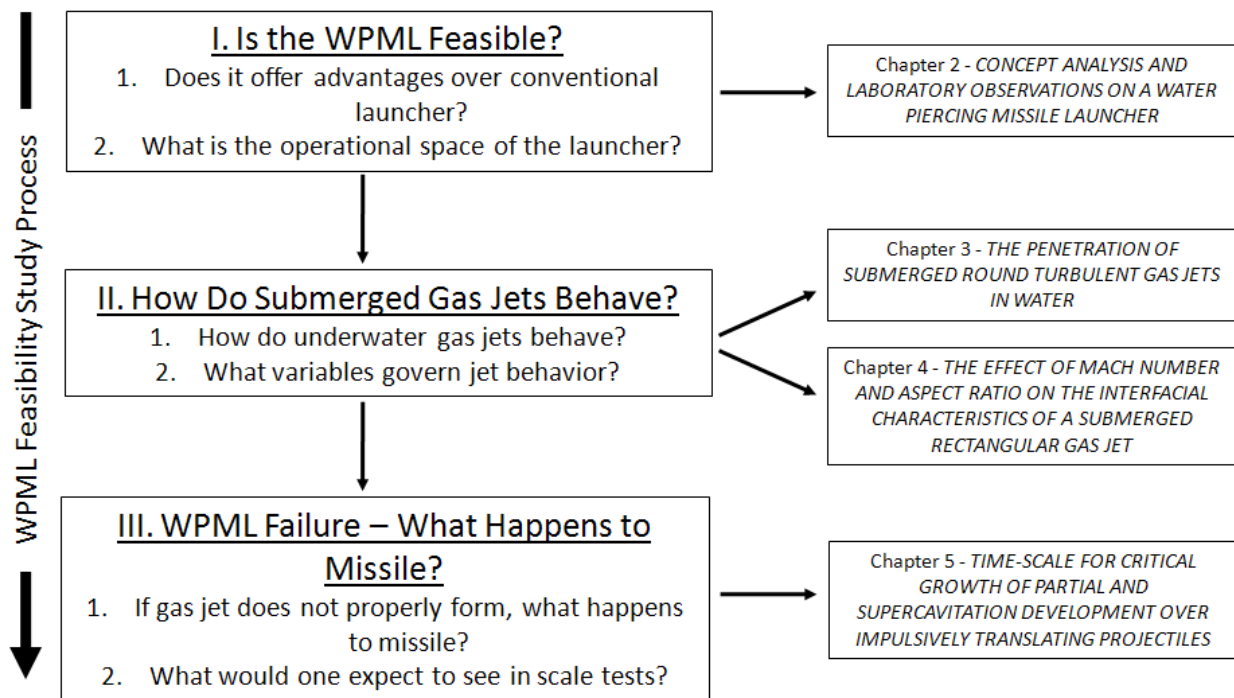


Figure 6.1. The WPML feasibility study process is divided into three sections. Each section is explored in greater detail in one of four chapters of this dissertation.

6.1 Is the WPML Feasible?

The WPML is an effective missile launcher in both surfaced and submerged roles and due to its scalable design can be applied to a wide range of missiles. Based on empirical evidence and the numerical simulations presented in this paper, the WPML concept is shown as a viable launcher for underwater bodies. The results indicate the optimal launch depth, in terms of maximizing launch depth while minimizing the missile restraint time, for a generic artillery

missile occurs at about 14 m depth for a 8 m/s submarine speed. The maximum launch depth occurs at about 20 m given a cross flow speed of 4 m/s and a missile restraint time of 4.5 s.

6.2 How Do Submerged Gas Jets Behave?

In Chapters 3 and 4 the effect of two variables, Mach number and injector geometry, were studied. The purposes of these studies were to learn the basic physics of how submerged gas jets behave. An optical, as opposed to probe, based measurement technique was utilized to record global instantaneous measurements of the gas jet. Using these techniques it was shown that submerged gas jets can maintain a significant presence without fracturing into multiple independent bubbles (pinch off). This penetration distance, as well as pinch off, was shown to be highly dependent on Mach number and mass flow rate. In the case of rectangular nozzles the aspect ratio also plays an important role. Higher Mach numbers increased the jet penetration distance and resistance to pinch off, which in the context of the WPML affords greater protection to the missile and therefore launch depth increases. These Chapters also demonstrated the basic principle crucial to a WPML launch: it is possible to sustain a continuous underwater high speed gas jet from a nozzle without pinch off occurring.

6.3 WPML Failure – What Happens to Missile?

In Chapter 5 projectiles were impulsively launched underwater to study the development of supercavitation. This study also simulated the effect of a failed WPML launch to understand what happens in the event the gas jet is improperly formed and the missile still accelerates out of the launch tube. It was found that projectiles launched impulsively are susceptible to cavitation which appears to be governed by the formation of a vortex ring. If high pressure gas is present near the wake of an underwater accelerating body during launch the gas can be rapidly drawn into the separated flow regime of the body. This causes an apparent “artificial supercavitation” scenario in which, with the exception of the forebody, the body is completely surrounded by gas. It is interesting to note that should this scenario occur the projectile might still be protected from water intrusion by rocket exhaust gases. Thus, even in the event of an unsuccessful gas jet formation the missile may still transition to external flight. This Chapter suggests an inherent redundancy might be present with the WPML.

6.4 Future Work

There are several areas in which work must continue to further understand the basic physics which govern the WPML. A brief list is provided below.

- In Chapter 2 a semi-empirical equation was used to predict the curvature of the gas jet in the presence of liquid cross flow. The constant C_L , which is necessary to compute the gas jet deflection, was computed from experimental data. It has yet to be determined however if this constant varies with WPML size. Therefore it is recommended to experimentally determine if this constant is size invariant.
- In Chapter 2 a power law relationship was fit to experimental data of the jet tip trajectory. Three sizes of WPML were used to determine this curve. However, the three WPMLs were of almost equal size. It is recommended to study the jet tip trajectory using several sizes of WPMLs of greatly varying size. It is also recommended that a theoretical analysis of the jet tip trajectory be completed.
- In Chapters 3 and 4, the effects of nozzle geometry and Mach number on the gas jet physics were studied. Hydrostatic pressure is also thought to play an important role, having an especially important role in governing pinch off. It is recommended to study the effect of hydrostatic pressure on the gas jet characteristics.
- Entrainment characteristics of submerged rectangular and round buoyant jets should be studied with the goal of prediction. Entrainment causes jet spreading which is particularly detrimental to the WPML concept, while also important to basic fluid mechanics research.
- In Chapter 3 the jet penetration was presented for one sized round injector. One of the great benefits of the WPML is its easily scalable design. However, there are no relationships to predict the effect of injector size on jet penetration. It is recommended to study these effects by constructing several sizes of round nozzles.
- In Chapter 4 the effect of both aspect ratio and Mach number on jet penetration was presented. There is clearly a gap in the jet properties as the aspect ratio is increased over the three sizes studied (2, 10, and 20). It is therefore recommended to repeat the

experiments using many more aspect ratios to find the point, if it exists, where aspect ratio ceases to govern jet behavior.

- The effects of cross flow on round, rectangular, and annular nozzles should be studied.
- In Chapter 5 an analysis of an impulsively launched projectile was presented. There are two aspects of this study which should be pursued further. First, a theoretical study of the vortex ring properties during projectile motion should be studied to better understand susceptibility of the flow to cavitation. Second, the gas leakage concept should be pursued further since it provides a low energy route to fully developed supercavitation which, in addition to supporting the WPML concept, could have many technological applications.

While much more work is necessary to completely understand the high speed gas-liquid interface and develop the WPML concept, this dissertation has provided a framework for its study. By utilizing an optical global measurement technique, as opposed to the point measurement techniques used by past researchers, new information on the behavior of submerged gas jets and accelerating submerged bodies has been gathered.

A conceptual analysis of the WPML the operational envelope of such a launcher was predicted and shown to be a viable submersible missile launcher. The basic physics of submerged gas jets was studied and from this analysis it was shown that submerged gas jets do have the characteristics to support a water piercing concept. Last, by studying the scenario of a poorly formed gas jet it was shown that the missile may entrain the exhaust jet gases to form a supercavity which, with the exception of the forebody, completely covers the missile and protects it from water intrusion. This supports the notion of perhaps an inherent redundancy system in the WPML.

7. APPENDIX A: IMAGE COLLECTION, PROCESSING, AND IMAGE ANALYSIS DETAILS

7.1 Introduction

In their efforts to understand the characteristics of submerged gas jets, past researchers have relied on point measurements such as electroresistivity probes to separate the liquid and gas phases for study [(Mori et al. 1982); (Ito et al. 1991)]. In these techniques the probe lingers at the measurement spot for some time and is then traversed in space. The sensing element can be a singular measurement point or be composed of several measuring points capable of simultaneous measurement at multiple spatial locations. In either case the probe itself is intrusive and only permits time-averaged whole-field measurements since the probe can only exist at one (or several) points in space at any given time. In such an unsteady and highly irregular flow field a global measurement is preferred since instantaneous information can be obtained. An example of a global measurement is high-speed photography, which has been used in the past [(McNallan and King 1982); (Loth and Faeth 1989)] to observe the interface, but the level of quantitative detail gathered from the recorded images was very low.

Since a major goal of this work was to study the interface motion itself, the technological limitations imposed by traditional measurement techniques were unacceptable. Thus high-speed photography was used to record the position and motions of the entire gas jet and the digital images were analyzed to extract the interface position. Thus direct and instantaneous global measurements of the interface were taken. This Appendix details the photographic measurements of the submerged gas jet and the steps taken to extract quantitative information from the digital images.

7.2 Photographic Measurement Details

Shadowgraph images of the submerged gas jet were recorded at a 1 kHz sampling rate. A Photron FASTCAM APS-RX in conjunction with a Canon VX-16 telephoto lens was used to digitally record shadowgraph images of the test section at 1 kHz sampling rate for 14 seconds. The 14 second recording period includes both the “start up jet” and the “quasi steady state” periods. The former is defined by the period of time just after the nozzle is turned on and the gas jet tip rises towards the free surface and the latter occurs once the jet tip has reached the free

surface. In this dissertation only the quasi steady state jet behavior was studied and the measurement period for this regime occurs after approximately the first $\frac{1}{2}$ s of time.

The Photron camera has a 10-bit complimentary metal-oxide semiconductor (CMOS) sensing element with 1024×1024 pixels. The camera was approximately 1.5m from the test section with yielded a typical image magnification between $388\text{-}477 \mu\text{m}/\text{pixel}$. Eight 250W halogen lamps evenly distributed over the test section were arranged behind a white sheet to distribute light evenly over the test section. A schematic of the rectangular jet system is shown in the left image of Figure 7.1 and the actual setup is shown on the right. The round jet setup is identical with the exception of the injector. Recorded images are a projection of the density variations seen in the test section. Unlike Schlieren photography which is sensitive to the 1st derivative of the index of refraction of the medium(s) which occupy the test section, shadowphotography is sensitive to the difference in the 2nd derivative of the index of refraction (Settles 2006). Thus the interface existing between air and water is very distinct. However, because the resulting shadowgraph image is a projection of the test section only two-dimensional information is recorded.

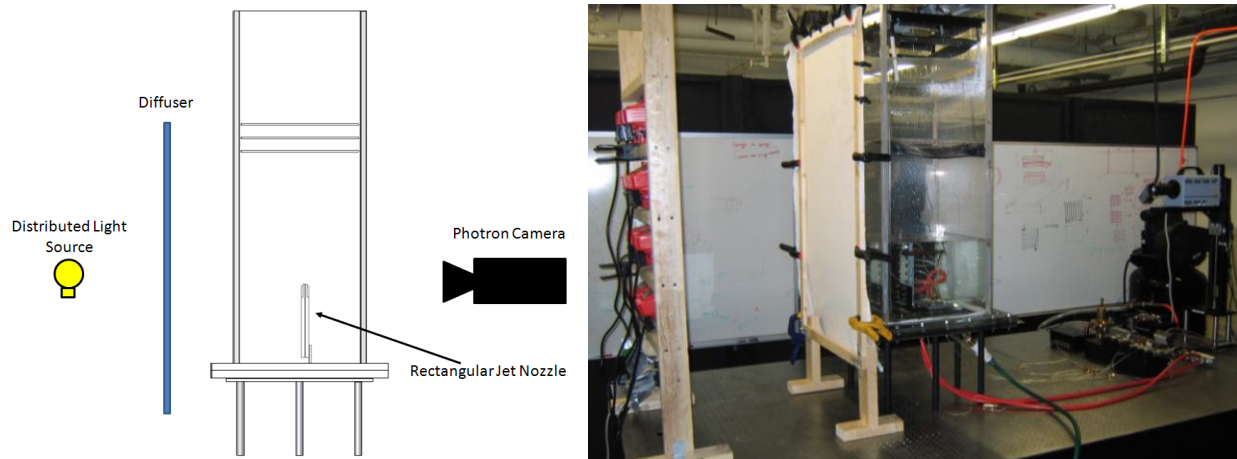


Figure 7.1. A schematic of the shadowphotography system is shown on the left and consists of a high-speed camera, a distributed light source, and a light diffuser (white sheet). On right is shown the actual test layout.

An example of the resulting shadowgraph images is shown in Figure 7.2. The white section is water and the dark section is the submerged gas jet. Note the clear distinction between the two phases which makes detection of the submerged gas phase relatively simple. One difficulty in accuracy determining the interface position is the presence of bubbles which are ripped from the gas jet. They are clearly not part of the continuous gas jet, yet linger near it and slowly rise. Their presence is ubiquitous across all Mach numbers and all nozzle designs tested (round and rectangular). An additional difficulty is due to the pinch-off phenomenon which may be seen in

Figure 7.2 at 1298ms. The once singular and continuous gas jet has now ruptured into two independent entities: a gas jet which remains connected to the nozzle exit and a large bubble which can now rise independently of the jet or re-attaches to the jet. Pinch-off presents a difficulty in that the main objective of this work was to analyze the interface of a continuous jet, and thus some confusion now arises as to what should be done with this independent bubble. The algorithm developed for this research can handle both entities separately, but for the purpose of this dissertation only the nozzle attached gas jet was studied.

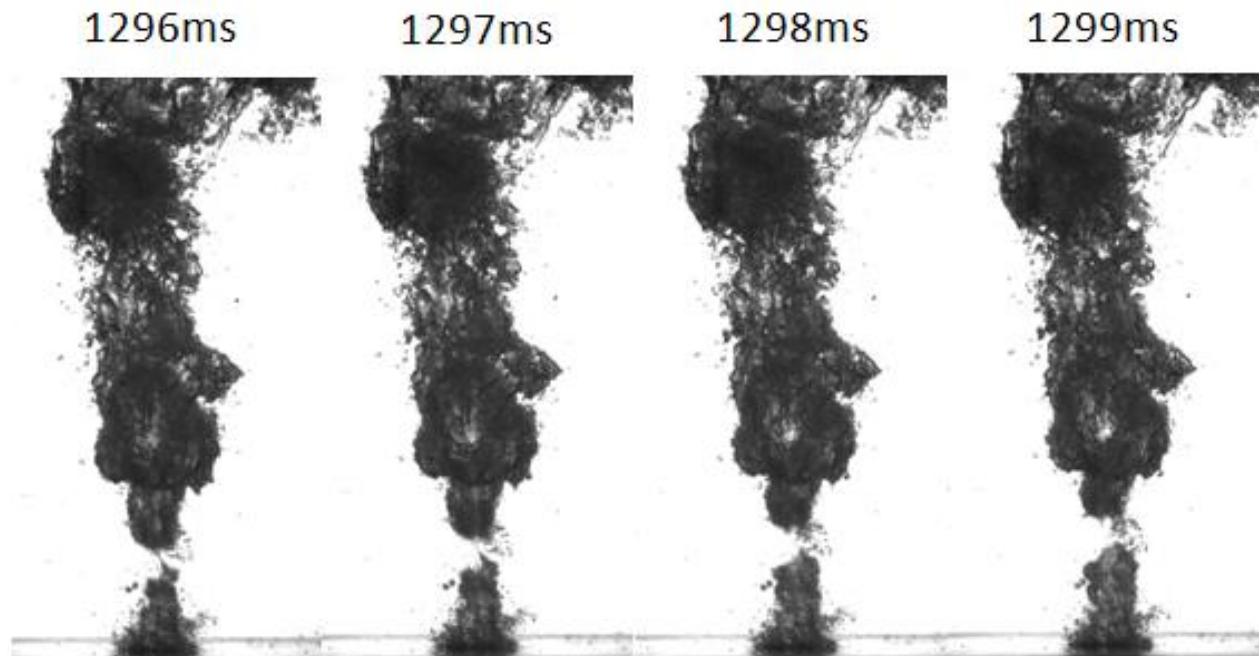


Figure 7.2. Recorded shadowgraph images for a Mach 0.8 round jet at several instances in time. Note the clear distinction of the phase interface.

7.3 Edge Detection Algorithm

As the main objective of this work was to analyze the interface motion from the acquired digital shadowgraph images an accurate determination of the interface is required. To accomplish this task a routine was implemented in MATLAB consisting of several well-known steps that are not unique to the field of image processing. The jet boundary is computed using seven steps:

1. Image digitization,
2. Median filter,
3. Image fill,

4. Morphological functions, and
5. Edge detection.

Each step is examined in greater detail below.

7.3.1 *Image Digitization*

Image digitization converts a grayscale or color image into a binary image. The primary difference between grayscale and binary images is the level of detail contained in the resulting image. The original images were grayscale which simply means each pixel is assigned a value between 0 and 255 by the high-speed camera. Binary images only have pixel values of 0 (black) and 1 (white). Thus this operation involves choosing a grayscale threshold such that the desired information is retained and noise is eliminated. In the present case this operation involves separating the gas and liquid phases. The MATLAB function “im2bw.m” converts a grayscale image into a binary image.

The task of choosing a suitable grayscale threshold is somewhat qualitative as is shown in Figure 7.3, but it is quite apparent that either too low of a threshold value (31% or 100/255) or too high of a threshold value (98% or 250/255) are not optimal thresholds. The lower (31%) threshold does not retain enough information and sections of the interface are clearly lost. The higher (98%) threshold permits some noise to be retained which can be difficult to remove, such as the many small black dots bordering the gaseous regions and the bottom of the tank next to the nozzle. The appropriate threshold can change depending on the fluid mediums, the level of background lighting, and the clarity of the tank side-walls. The medium (59%) threshold was used for image digitization of round jets and the high (98%) threshold was used for the rectangular gas jets. The medium threshold was used for the round jets as significantly more noise was present in the original images. This was primarily due to the fact that the round nozzles were attached to the base of the acrylic tank which can be seen in the original images. The rectangular nozzles were held some distance from the acrylic tank base and thus could not corrupt those images.

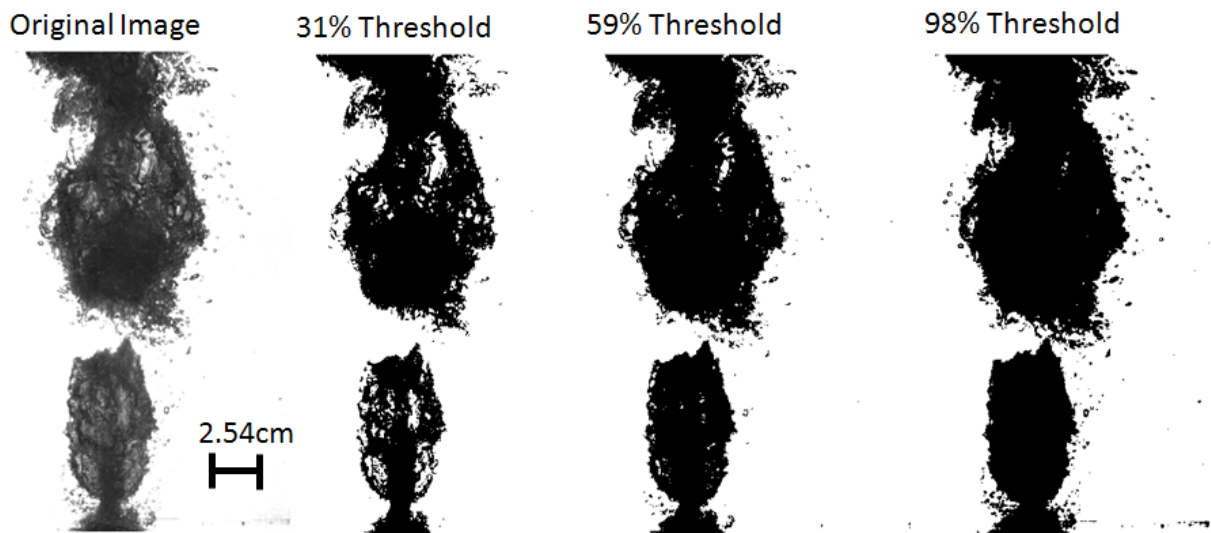


Figure 7.3. Various thresholds applied to the original image result in a varying level of information being filtered. The horizontal scale bar represents 0.0254m.

7.3.2 Median Filter

The median filter employs by $[n \times m]$ pixel median filter to the 2D image. To accomplish this task a $[n \times m]$ pixel rectangle is translated around the image where the center point value is updated based on the median value of the surrounding pixels. The MATLAB function “medfilt2.m” performs this operation. This image processing step is used for two purposes: 1) to remove image noise and 2) to remove small bubbles very near the interface. These bubbles are not part of the gas jet but rather were separated from the gas jet from unsteady processes or mixing.

An example of several window sizes for the median filter is shown in Figure 7.4. While it appears that there is no difference between the $[3 \times 3]$ and $[7 \times 7]$ filters in this image there are cases in which the $[3 \times 3]$ filter does not remove noise. Large filters such as the $[10 \times 10]$ size are not advisable as although they are capable of removing large bubbles separated from the gas jet they significantly smooth the interface. This is clearly seen in Figure 7.4 and represents a loss of interfacial information. Thus it is better to choose smaller, rather than larger, median filter sizes. The $[7 \times 7]$ filter size was used for both the round and rectangular jets. Through trial and error this size proved to be the most advantageous filter size as it removed most bubbles separated from the gas jet while preserving the interfacial shape.

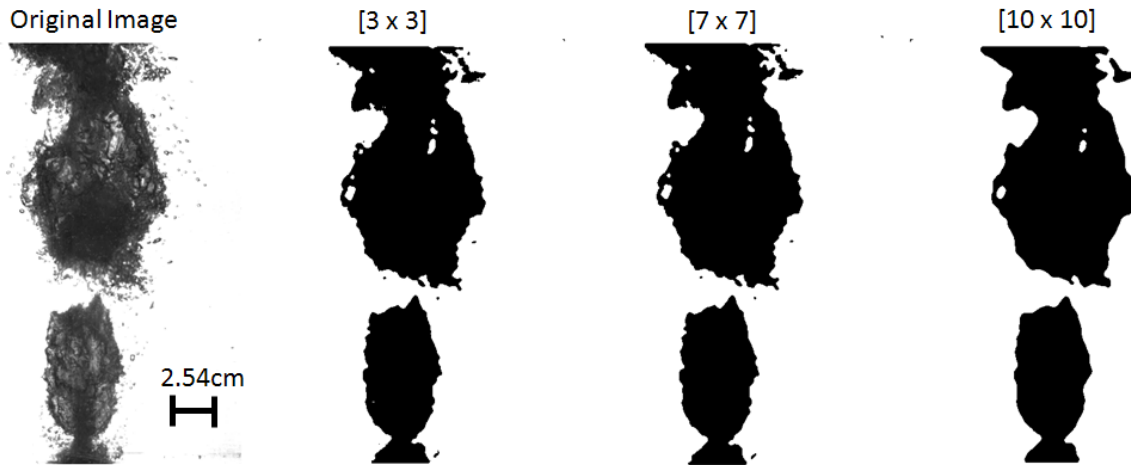


Figure 7.4. The median filter is used to smooth irregularities in the binary image. Only small median sizes are used to prevent filtering of actual interface data.

7.3.3 Image Fill

Due to the gas jets continually expanding and contracting there are regions of the gas jet composed of several shades. Although the image digitization step separated the gas and liquid phases, in some cases large holes exist in an otherwise continuous gas region. However, this dissertation makes use of time-averaged jet penetration curves to make several points, and these curves require that all regions of the gas jet remain black (0) and all regions of the ambient water remain white (1). Thus holes within the gas jet must be filled.

An example of filling holes within the continuous gas jet is shown in Figure 7.5. Observation of the original image reveals a light area within the pinched-off bubble and all steps up through the [7 x 7] median filter interpret this light region as a hole. Of course, this is merely a shortcoming of the steps up to this point to identify the gas phase within the surrounding liquid. The MATLAB function “imfill.m” fills all holes in the binary image by observing the connectivity of individual pixels. The background pixel value (white) is equal to the value of the holes within the bubble, yet there is no path from the holes to the ambient liquid one can take without first encountering the jet (dark pixels). MATLAB defines this scenario as a hole and automatically fills holes with the opposite pixel value.

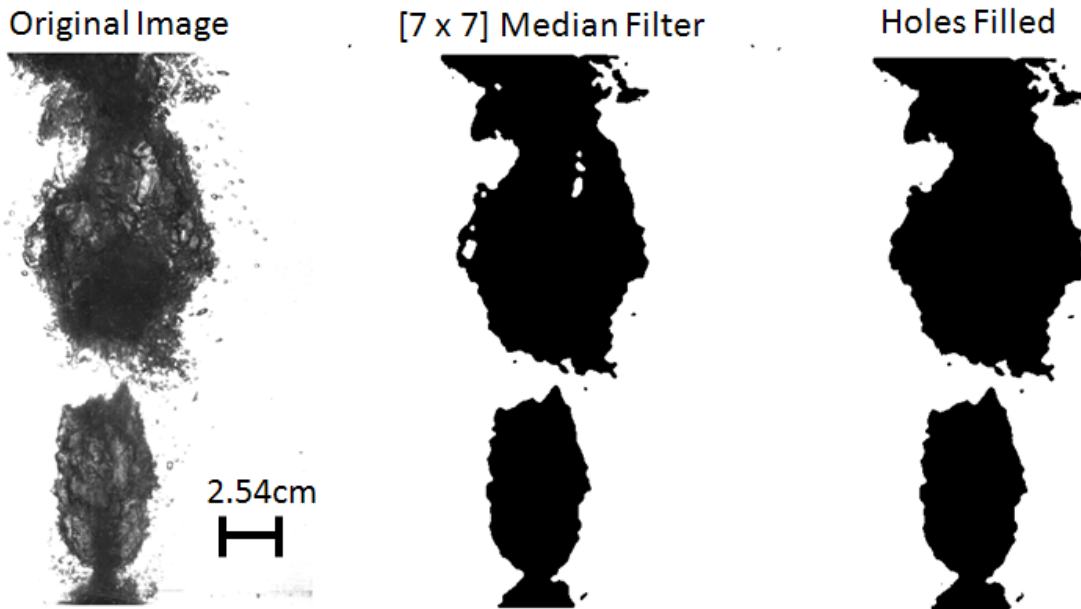


Figure 7.5. The digitization and other filtering operations can yield holes, or regions within the known gas jet identified as liquid. These regions are automatically identified and filled.

7.3.4 Morphological Functions

The last step before determining the jet boundary is a morphological opening of the image. Simply put, this step uses structuring elements, simple geometric shapes, to determine which parts of the image should be removed and which should remain. The geometric shape can be anything, such as a rectangle, diamond, or circular object and of any size. In this dissertation only circular shapes were used, since the primary reason for the inclusion of this step is to remove small independent bubbles. Essentially this operation consists of a circular element which is traversed through the image and any structures which are smaller than the circular element are removed from the image.

The morphological operation consists of two tasks: image erosion and image dilation. These tasks have the effect of removing small objects from the image, such as small bubbles which have broken off from the gas jet. In image erosion the circular element is traversed through the image and the center of the element (that particular pixel only) is set to the minimum value of all the pixels encountered within the element. This has the effect of removing information. The next step, image dilation, does the opposite and restores the prior boundary with the exception of those areas which were smaller than the geometric element. These steps exist in the MATLAB functions as “imerode.m” and “imdilate.m” for the erosion and dilation operations, respectively.

The morphological operation is shown in Figure 7.6 for the same test image used in the other cases. The leftmost image is the original unfiltered photograph. The image to the right of this image is the digitized, median filtered, and all holes filled processed image. The morphological operations are performed on this image. Several structuring element sizes were used with all elements disks. The effect of increasing the disk size is quite clear: small bubbles or other noise unrelated to the gas jet are removed. However, a trade-off exists between the size of element used and the resulting image. As the disk size is increased the interface is greatly smoothed and information is again lost. Through trial and error it was determined that a disk size of 6 was the maximum that should be used in order to prevent the loss of crucial interface shape and information. Any sizes over 6 simply smeared the interface too much, and thus both round and rectangular image processing tasks used a disk size of 6.

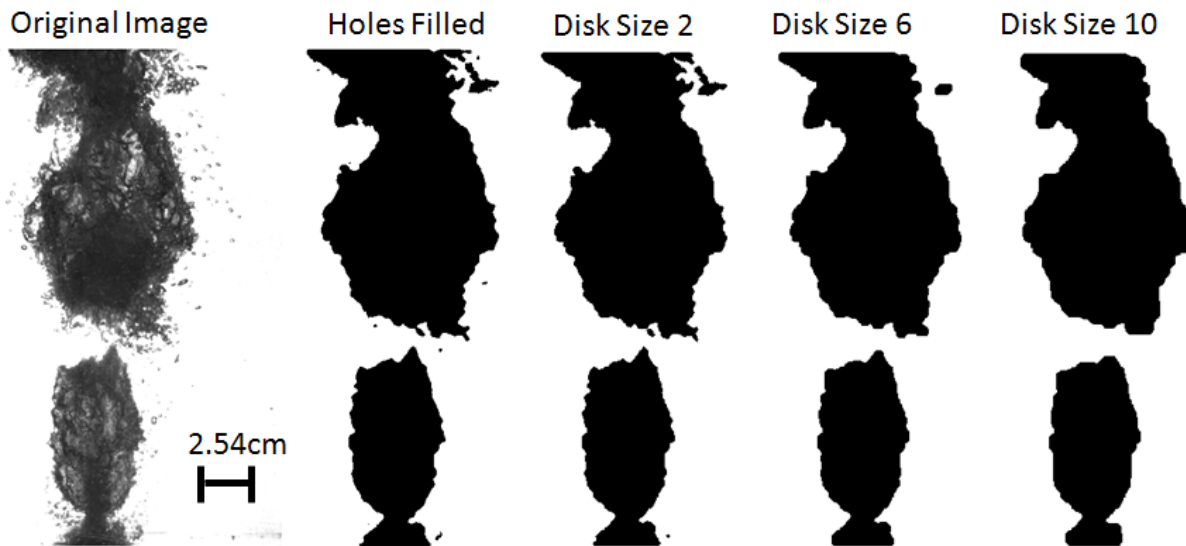


Figure 7.6. The morphological disk element is traversed around the image to filter small detached bubbles.

7.3.5 Edge Detection

The last step consists of edge detection. The MATLAB function “bwperim.m” finds the perimeter of a binary image, which is defined as any non-zero pixel which is adjacent to a zero value pixel. The algorithm thus searches adjacent pixels and forms the perimeter between dissimilar regions. The result of this calculation is shown in Figure 7.7 as the “Detected Perimeter”. Since this dissertation is only concerned with the interfacial motions of the orifice-attached jet, we seek only the perimeter which is nearest to the orifice location. The perimeter is located and its coordinates are saved to a text file.

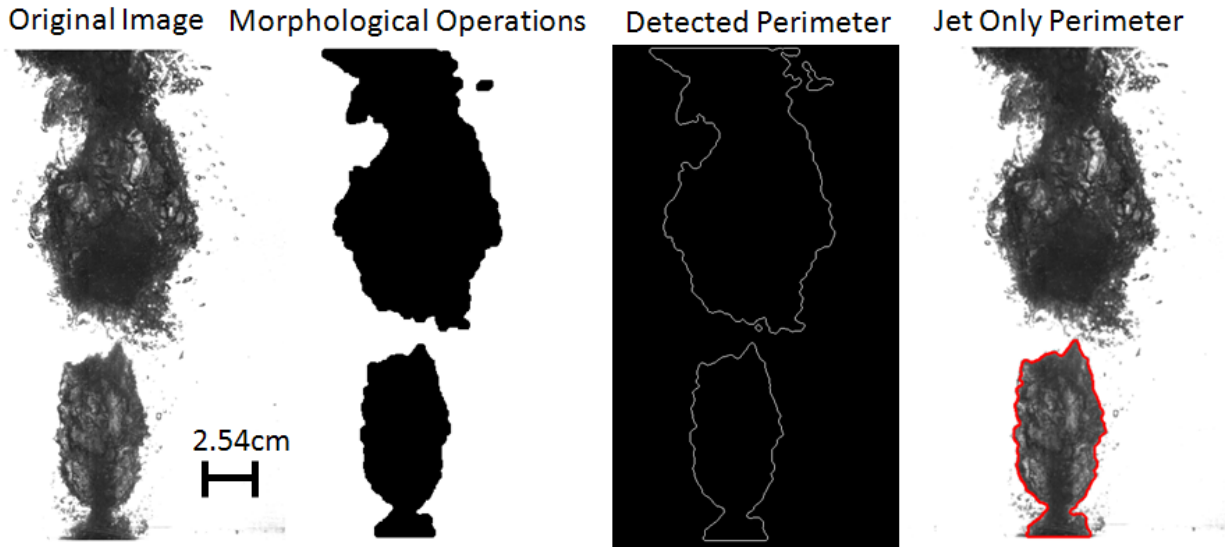


Figure 7.7. The final step consists of edge detection where the perimeter of the orifice-attached jet is determined. This perimeter is overlaid with the original image to show the degree of accuracy in determining the perimeter.

In summary, the individual steps are again shown in Figure 3.3. First the image is digitized based on a threshold pixel intensity to capture the gas phase and a 7x7 pixel median filter is applied to smooth any irregularities such as bubbles fractured from the jet. Next a circular disk morphological element was applied to the digitized image and after dilation and erosion the perimeter of the resulting structure was identified. As shown in Figure 3.3 the detected boundary agrees quite well with the experimental image. The edge detection code may be found in Section 7.5.

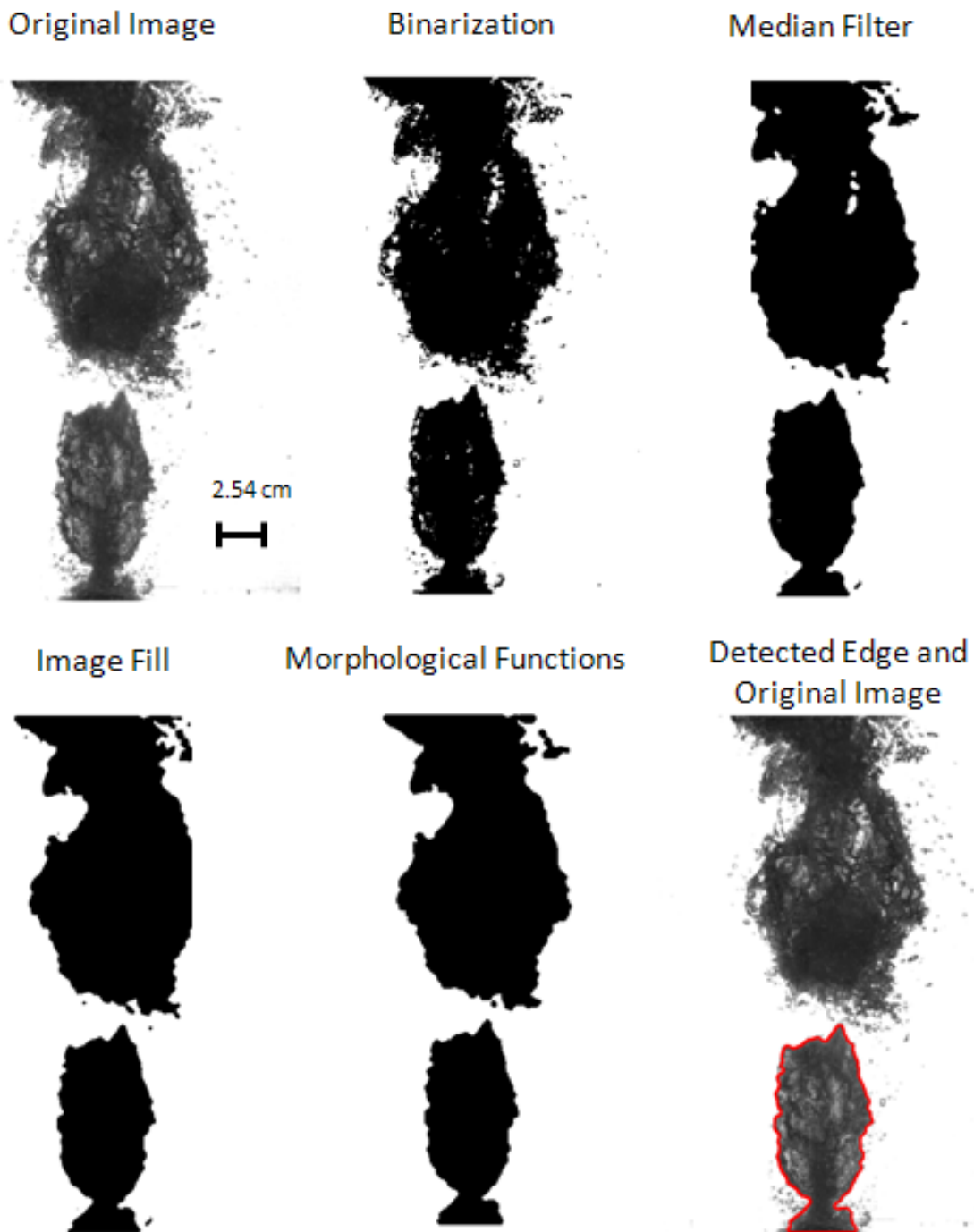


Figure 7.8. Steps used to detect the jet boundary. The process neglects outliers such as bubbles torn from the interface to accurately track the phase boundary. The horizontal scale bar represents 2.54 cm.

7.4 Image Analysis Steps

For all tests and time steps the orifice-attached perimeter coordinates were written to individual text files. The next step in the image analysis was to take these perimeter coordinates and analyze them. The jets were analyzed in several ways:

1. The jet pinch-off location was computed and
2. The jet penetration distance was computed.

Each of these analysis methods are presented in greater detail below.

7.4.1 Determination of the Jet Pinch-Off Location

Jet pinch-off refers to the scenario of a continuous gas jet breaking into multiple independent entities. Although the edge detection algorithm presented in this dissertation is capable of tracking all portions of the submerged gas phase, in this dissertation only the orifice-attached jet is analyzed. The location of the jet pinch-off is computed from the processed images.

First the jet perimeter is linearized and separated into left and right sides. Linearization implies that for each y coordinate position only one radial interface position is permitted. An example of this step is shown in Figure 7.9 where the x and y coordinates are shown in units of pixels. The nozzle exit is located at $(x,y)=(315,10)$. The original interface picture shows the computed interface position. However, in the linearized interface picture, for every axial position where the jet has multiple radial positions, only the outer jet position is taken. Additionally, the interface is separated into left and right sides. A comparison of the original and linearized interface positions is also shown. Note that at axial positions at which no interface exists, i.e. the jet has pinched-off, the interface position is given an x coordinate value of zero. The final step occurs in the last picture of Figure 7.9 where only the portion of gas jet attached to the nozzle is retained. All other axial positions are zero to an x coordinate of zero.

The interfacial data is padded both below and above with ten rows, all containing zeros, and thus both above and below of the interrogation region the data indicates the jet is pinched-off. This is primarily for data-processing to ensure that the entire interface is within the computation domain.

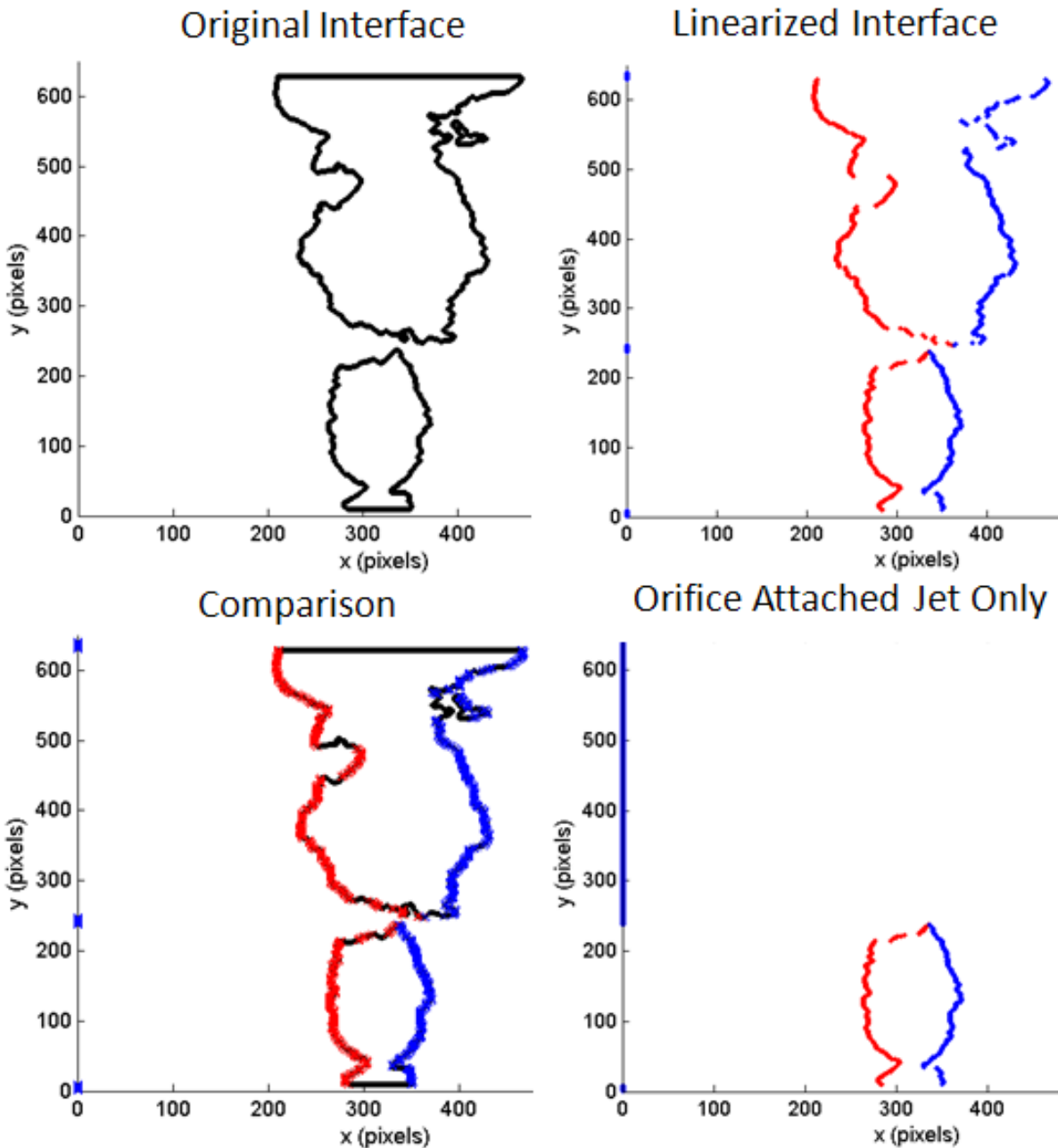


Figure 7.9. The computed jet interface positions are linearized and separated into left and right sides, denoted by the symbol color. Only the orifice attached jet is retained for study.

Thus it is quite easy to track all locations where the gas jet has pinched-off by simply recording the axial locations corresponding to an x coordinate value of zero. These values were recorded with the axial position of maximum jet continuity. In other words, if a gas jet were to pinch-off, the maximum axial position of the orifice-attached gas jet is recorded. These values are shown for a Mach 0.4 jet in Figure 7.10.

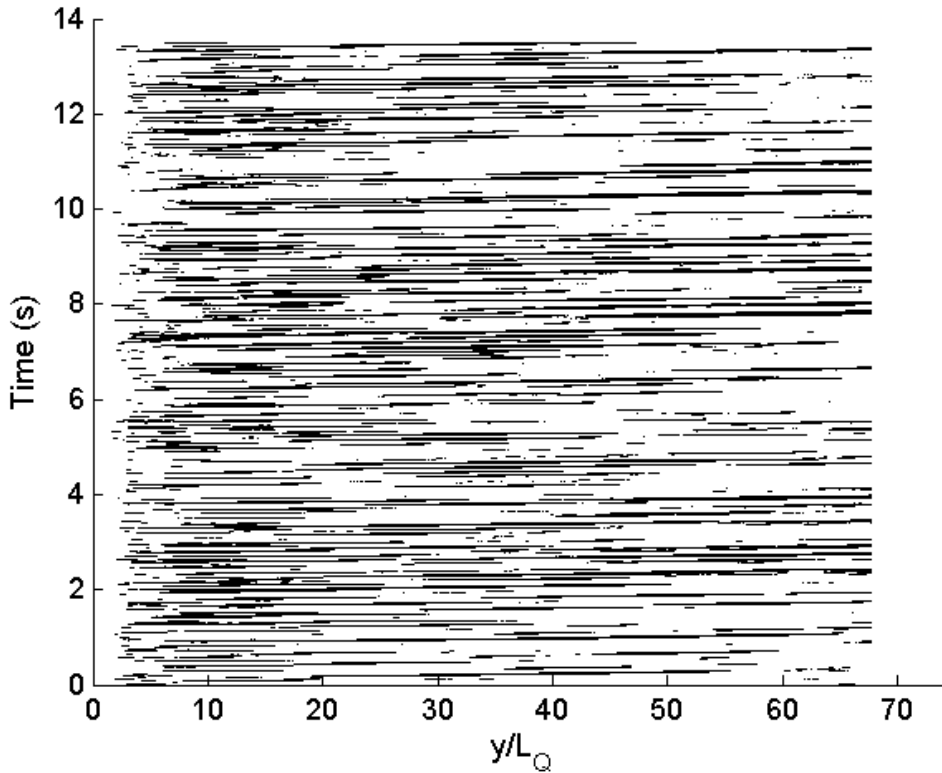


Figure 7.10. The minimum location where the gas jet became discontinuous is shown as a black dot. The x axis corresponds to axial position and the y axis corresponds to time. The slope of the black dots is the velocity of the pinch-off location.

At every axial position recorded the number of time the gas jet was discontinuous at that point was summed over time. The resulting curve is shown in Figure 7.11. The jet is primarily in a pinched-off configuration between $10 < y/L_Q < 30$. This analysis was done for all tests and all Mach numbers.

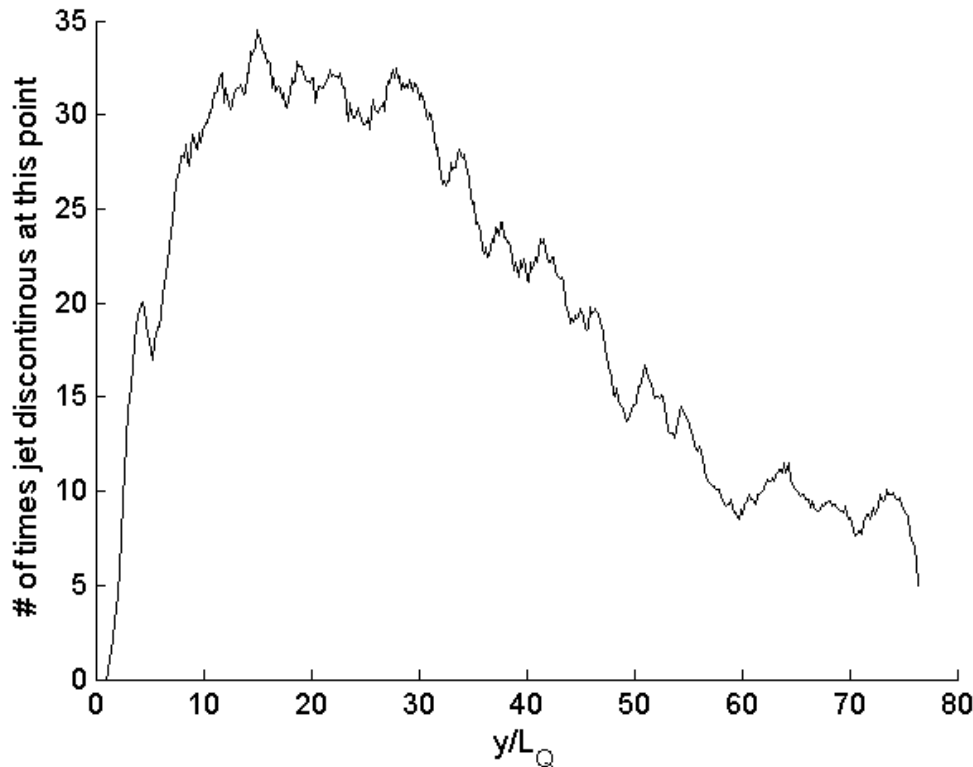


Figure 7.11. The axial position corresponding to the orifice attached jet position was recorded and summed for all times.

7.4.2 Computation of the Jet Penetration Distance

The gas jets tend to be very unsteady, with the gas jet as a whole oscillating in both size and position. Depending on the Mach number the gas jets may even pinch-off. While the unsteady interfacial motions are peculiar and interesting, there are several engineering disciplines which care less about the unsteady interfacial motions and more about the time averaged presence of the gas jet into the ambient water. In this dissertation the term jet penetration has been used to describe the jet location in a statistical sense. The steps taken to compute this value will now be described.

After the morphological functions are applied to the original photographs of the gas jet as shown in Figure 3.3, the resulting image is ready for jet penetration computation. The binary image is composed of only 0's and 1's, with a value of 0 and 1 indicating the presence of gas and water, respectively, for one instant in time. Each binary image is added to the last which results in an image with a spatially varying intensity. This is graphically shown in Figure 7.12 and Figure 7.13, which show the image addition for the first and last three time steps, respectively. Both the instantaneous and cumulative intensity images are shown. The color scale represents

the image intensity. The left images only add together portions of the jet which remain attached to the orifice, while the images on the right do not neglect any pinched-off sections. The resulting intensity fields are drastically different. Consider the final intensity plots in Figure 7.13 at 1000ms. The orifice only (left) plot clearly shows that the jet does not maintain a presence far downstream of the nozzle. If the pinched-off bubbles are not neglected (right plot) the downstream jet presence is calculated to be much higher. This is a fundamental difference between point measurement techniques, such as a submerged electroresistivity probe, and a global measurement such as the one presented in this dissertation. The image analysis allows one to distinguish between pinched-off bubbles and a continuous jet.

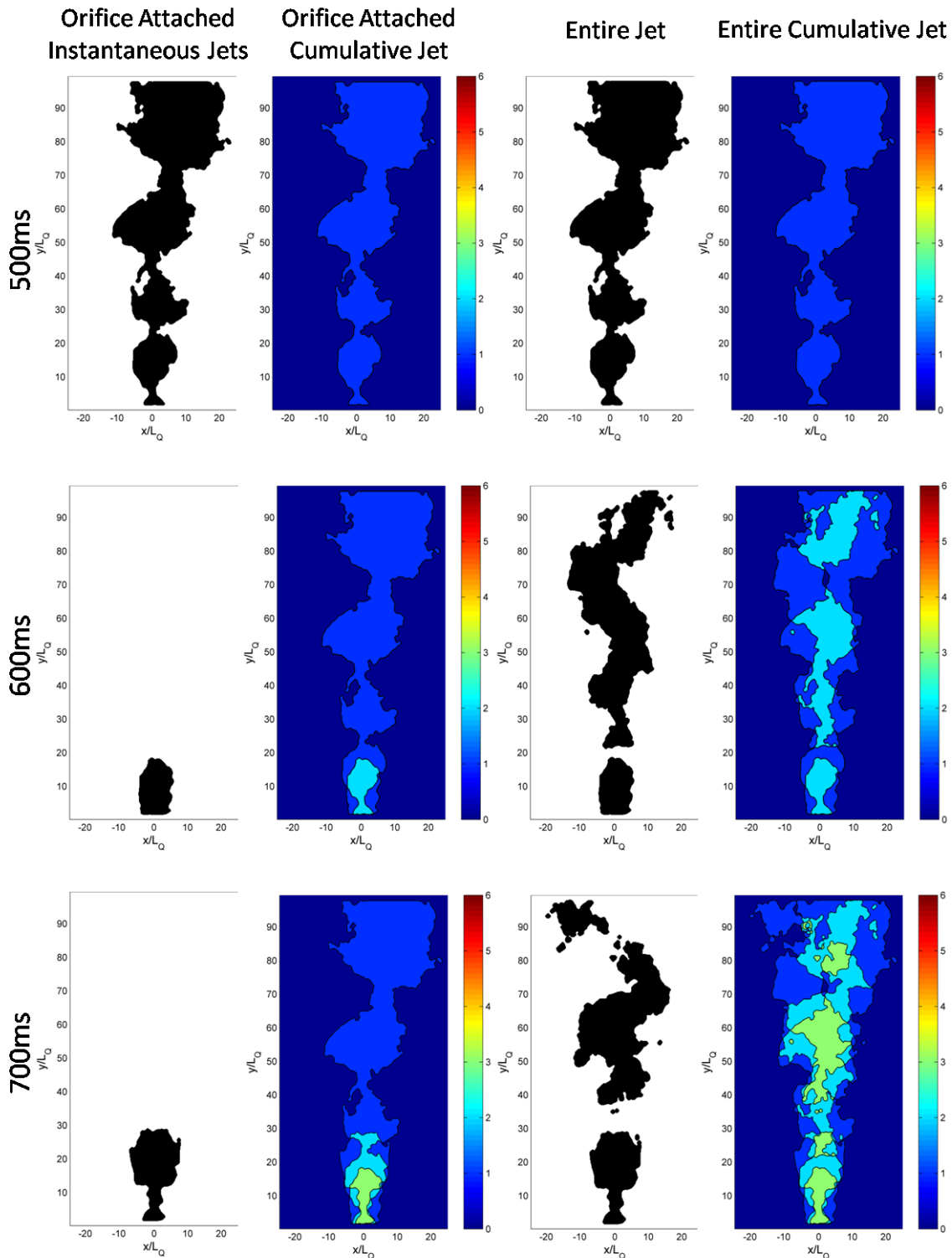


Figure 7.12. First three time steps of jet penetration determination, which is computed by binary image addition. The left images only add orifice attached jets together and all pinched-off bubbles are neglected in the image addition. In the right images no portion of the gas jet is neglected in the image addition.

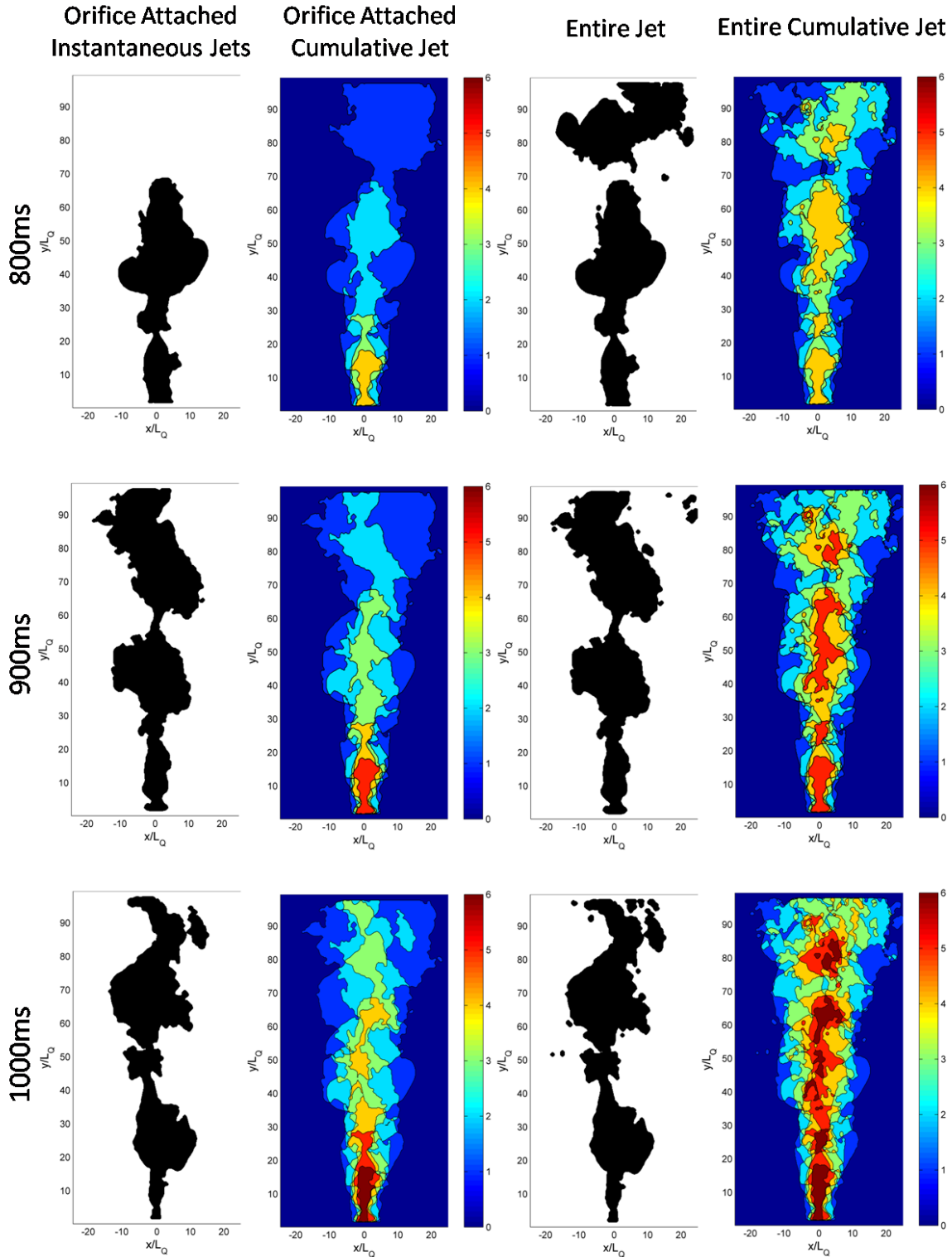


Figure 7.13. Last three time steps of jet penetration determination, which is computed by binary image addition. The left images only add orifice attached jets together and all pinched-off bubbles are neglected in the image addition. In the right images no portion of the gas jet is neglected in the image addition.

It is interesting to note that, in the absence of a global flow measurement technique, one cannot determine the true jet penetration distance. It is simply impossible to derive information without the measurement. By the very nature of the problem at hand the jet penetration is defined by global characteristics. Of course, the optical technique used in this dissertation is capable of reproducing or simulating probe based measurements. From the digitized images a value of 1 is located at each point in the field corresponding to the gas phase and 0 with the liquid phase. Consider a point $40L_Q$ downstream of the nozzle orifice along the nozzle centerline in a Mach 0.8 round jet flow. The response of an electroresistivity probe is shown in the left plot of Figure 7.14 while the response of the optical technique is shown in the right plot. A value of 1 indicates the presence of gas and 0 the presence of water. Clearly, the optical technique records the presence of water at this point much more. This is because as bubbles pinch off from the jet and rise independently the probe can only sense the presence of water or gas while the optical technique can impose the additional requirement of an orifice attached gas jet.

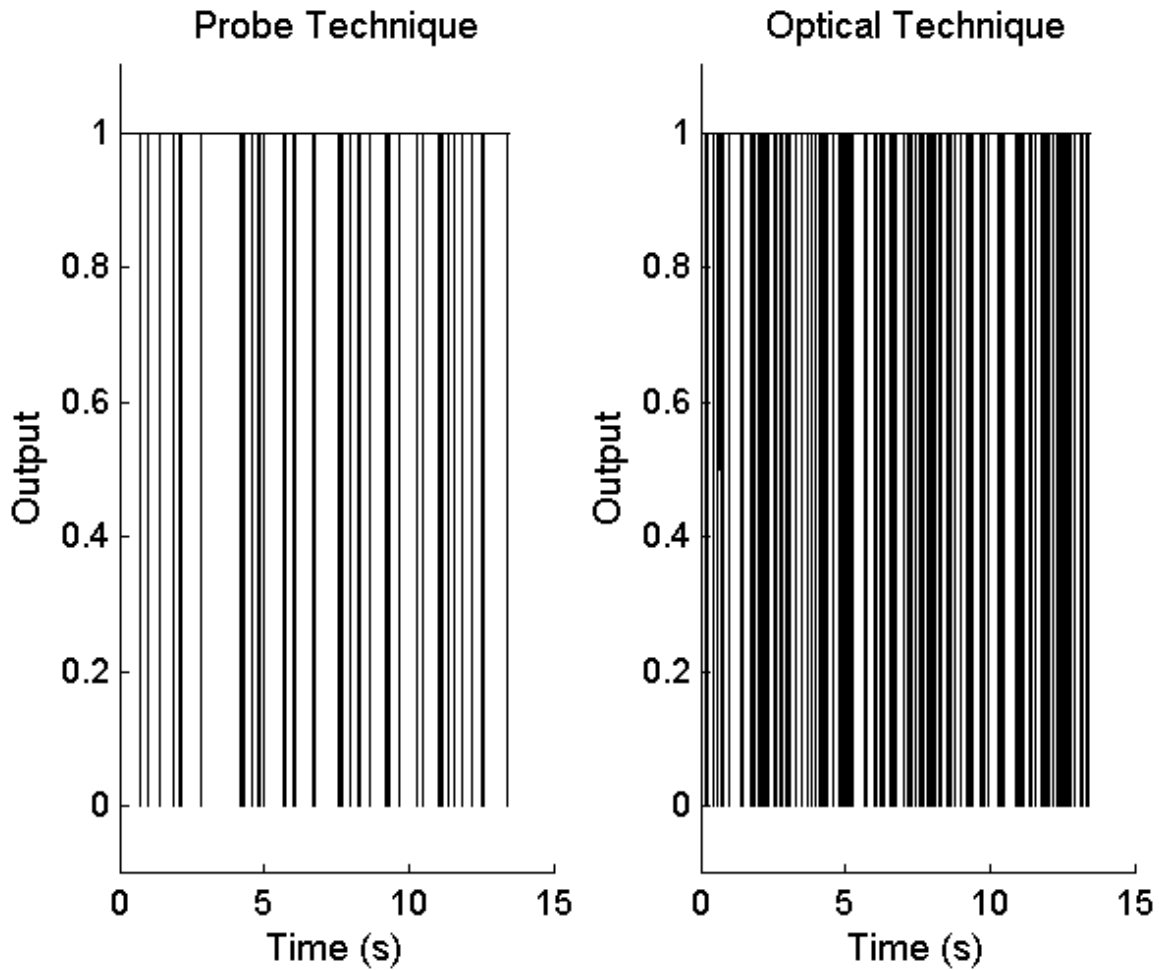


Figure 7.14. A comparison of probe (left) and optical (right) techniques for judging the presence of gas at a simultaneous point in space.

As an example consider Figure 7.15, which shows unprocessed images of a pinched off gas jet. The red circle denotes the position of the artificial probe. In images A-C the pinched off section of the gas jet fills the probe measurement point. In images D-G the bubble rises and moves away from the probe measurement point. In images H-L the orifice attached gas jet occupies the probe measurement point. If a probe based technique were used, the presence of gas would be detected in images A-C and it is impossible to know if this region of gas is continuous to the nozzle exit.

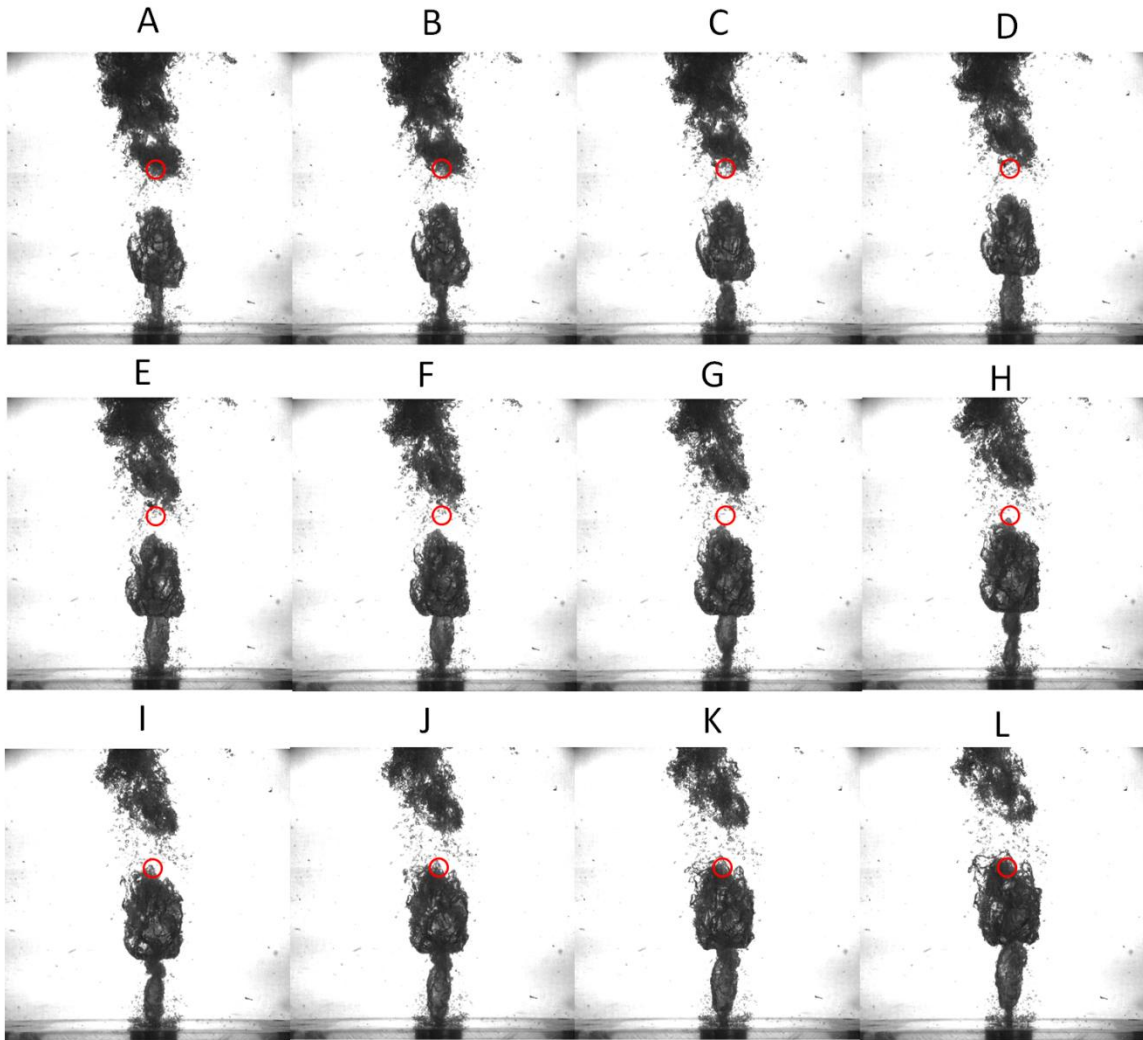


Figure 7.15. Unprocessed images are shown at 4 ms intervals. The red circle denotes the position of the probe. The gas jet tends to pinch off which is the source of the erroneous probe based measurements.

The simulated probe response and the optical response for this kind of system are shown in Figure 7.16. Note that in the optical technique, the presence of water is detected between approximately 1.830 to 1.888 s which corresponds to a pinched off jet. With the probe technique only a subset of this time (1.869-1.888s) is measured to be a pinched off jet. This is because the probe technique considers any portion of time where gas is measured to be an orifice attached jet, which is simply not true.

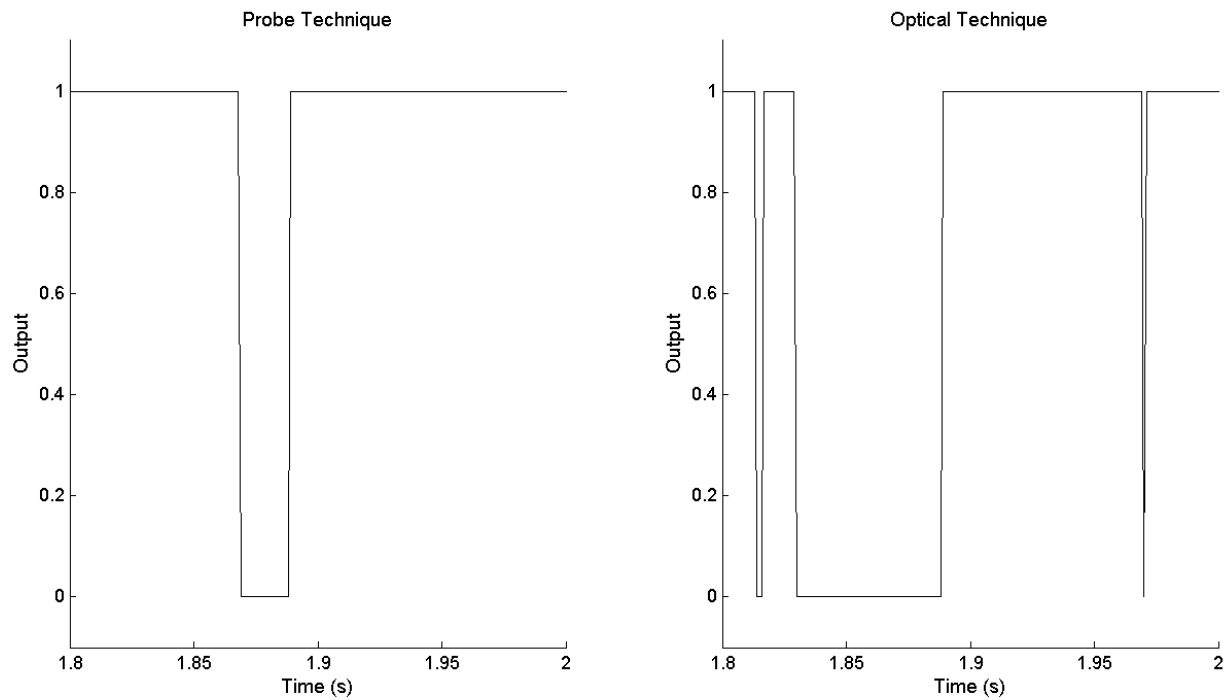


Figure 7.16. Simulated probe response (left) and the optical response (right) for the images shown in Figure 7.15.

7.5 Edge Detection Code

This code was written to automatically read in digital image files in MATLAB and compute the interface location. The code is broken into several functions which are called by the main file.

7.5.1 MATLAB Code: Write Detected Edges From Raw Images to .txt Files

```
clear all
close all
clc
q=1;

base_direct='Z:\WPML Data\Phase II\3-D Launcher\3D tubes\Experimental
Data\EIGHT INCH NOZZLE\'
sub_direct={'Mach 0.4','Mach 0.6','Mach 0.8','Mach 1.0','Mach 1.2','Mach
1.5','Mach 1.7'};

for big_count=1
if big_count==1
% AR2
mu=(2/(386.5-280))*0.0254;
filt_thresh=150;
filt_med=7;
morph_low=2;
morph_high=4;
```

```

vc1=50; % a and b are vertical crop
vc2=623;
hc1=150; % c and d are horizontal crop
hc2=550;
end

for j=1:7
subfolder=sub_direc{j};
if j<4
maxnum=3;
else
maxnum=9;
end

for i=1:maxnum
direc=strcat(base_direc,'RAW DATA/',sub_direc{j},'/test',num2str(i),'/');

c_1=1;
c_2=14000;
q=1;
save_direc=strcat(base_direc,'output/EDGES_',subfolder,'/test',num2str(i),'/');
);
mkdir(save_direc);

for count=1:14000
% call image to be processed
second=sprintf('%06s',num2str(count));
f_name=strcat('pic_',second,'.tif');
im1=imread(strcat(direc,'pic_001169','.tif'));

%crop
im2=im1(vc1(1,1):vc2(1,1),hc1(1,1):hc2(1,1));
im2_a=im2;
addon_b=255.*ones((vc2(1,1)-vc1(1,1))+1,10);
im2_a=[addon_b im2 addon_b];
dim_a=size(im2_a);
addon=255.*ones(10,dim_a(2));
im2=[addon;im2_a;addon];
[cols,rows]=size(im2);

% improfile %statistics on image
[P,Q]=imhist(im2);
% threshold/binarize original image using normalized image intensity
im4 = im2bw(im2, filt_thresh/255);
im4 = medfilt2(im4,[filt_med filt_med]);
im4 = imfill(~im4,'holes');

% morphological functions to filter
for g=morph_low:2:morph_high
se = strel('disk',g);
im4 = imerode(im4,se);
im4 = imdilate(im4,se);
end

BW2 = bwperim(im4);

```

```

y=206;
x=cols;

for b=cols:-1:1
if BW2(b,y)>0
x=b;
break
end
end

%%%%%%%%%%%%%%%%%%%%%%%%%%%%%%%%%%%%%%%%%%%%%%%%%%%%%%%%%%%%%%%%%%%%%%%%
% 1. only get jet positions attached to nozzle
col = round(y);
row = round(x);
boundary = bwtraceboundary(im4,[row, col],'S',8,inf);

mat_tester=isempty(boundary);
if mat_tester==0;
s_boundary_temp=size(boundary);
s_boundary(1,q)=s_boundary_temp(1,1);
jet_area(:,q)=bwarea(BW2);

%%% track true jet tip in time
y_tip=min(boundary(:,1));
x_temp=find(boundary(:,1)==y_tip);
x_tip=min(boundary(x_temp,2));
jet_tip_x(:,q)=x_tip;
jet_tip_y(:,q)=y_tip;
else
boundary=[0 0];
s_boundary(1,q)=1;
jet_area(:,q)=0;

%%% track true jet tip in time
y_tip=0;
x_temp=0;
x_tip=0;
jet_tip_x(:,q)=0;
jet_tip_y(:,q)=0;
end

temp_n=strcat(save_dir,sub_dir{j},'_test',num2str(i),'_frame_',num2str(count),'_orifice.txt');

dlmwrite(temp_n,boundary,'delimiter','\t','newline','pc','precision','%0f')

%%%%%%%%%%%%%%%%%%%%%%%%%%%%%%%%%%%%%%%%%%%%%%%%%%%%%%%%%%%%%%%%%%%%%%%%
% 2. orifice attached jet & fractured component
temp_n=strcat(save_dir,sub_dir{j},'_test',num2str(i),'_frame_',num2str(count),'_all.mat');
save(temp_n,'im4','-v6')
%%%%%%%%%%%%%%%%%%%%%%%%%%%%%%%%%%%%%%%%%%%%%%%%%%%%%%%%%%%%%%%%%%%%%%%%
%%%%%%%%%%%%%%%%%%%%%%%%%%%%%%%%%%%%%%%%%%%%%%%%%%%%%%%%%%%%%%%%%%%%%%%%

```

```

q=q+1;
end
q=q-1;

%%%%%%%%%%%%%%%%%%%%%%%%%%%%%%%%%%%%%%%%%%%%%%%%%%%%%%%%%%%%%%%%%%%%%%%%
% 1. save orifice attached jet
temp_n=strcat(save_direc,sub_direc{j},'_test ',num2str(i),'_orifice.mat');

save(temp_n,'cols','y','rows','jet_area','jet_tip_y','jet_tip_x','mu','q','s_
boundary','-mat','-V6')

%%%%%%%%%%%%%%%%%%%%%%%%%%%%%%%%%%%%%%%%%%%%%%%%%%%%%%%%%%%%%%%%%%%%%%%%
%%%%%%%%%%%%%%%%%%%%%%%%%%%%%%%%%%%%%%%%%%%%%%%%%%%%%%%%%%%%%%%%%%%%%%%%
end
end
end

```

7.5.2 MATLAB Code: Linearize Detected Edges for Data Analysis

```

clear all
close all
clc
q=1;

base_direc='/home/cweiland/Desktop/Gringotts_Mounted/WPML Data/Phase II/3-D
Launcher/3D tubes/Experimental Data/EIGHT INCH NOZZLE/';
Machnum={'Mach 0.4','Mach 0.6','Mach 0.8','Mach 1.0','Mach 1.2','Mach
1.5','Mach 1.7'};

%%%%%%%%%%%%%%%%%%%%%%%%%%%%%%%%%%%%%%%%%%%%%%%%%%%%%%%%%%%%%%%%%%%%%%%%
%%% LOAD IN .mat FILES WITH JET PARAMETERS FOR STUDY
%%% LOAD IN .txt FILES WITH JET BOUNDARY POINTS FOR STUDY
%%%%%%%%%%%%%%%%%%%%%%%%%%%%%%%%%%%%%%%%%%%%%%%%%%%%%%%%%%%%%%%%%%%%%%%%

for big_count=3 % cycle through Mach Number
if big_count<=3
maxnum=3;
else
maxnum=9;
end

for i=1:maxnum % cycle through test

% load in file for orifice attached data
load_direc=strcat(base_direc,'output/');
temp_mat=strcat(load_direc,Machnum{big_count},'_test',num2str(i),'_orifice','
.mat');
load(temp_mat);

% load in file to get im4 binary image size

temp_n=strcat(load_direc,'EDGES_',Machnum{big_count},'/test',num2str(i),'/',M
achnum{big_count},'_test ',num2str(i),'_frame_',num2str(1),'_all.mat');
load(temp_n,'im4')

```

```

[s1,s2]=size(im4);
Whole=zeros(s1,s2);
Imat=zeros(s1,s2);
clear im4

num=cols;
num_x=0;%198;

clear var*

i_RF=zeros(num,q,'double');
i_LF=zeros(num,q,'double');

i_La=zeros(num,q,'double');
i_Ra=zeros(num,q,'double');

Imat=zeros(s1,s2); % initialize matrix for orifice only attached jet position
calculation

for c=500:q%1:q
%%%%%%%%%%%%%%%%%%%%%%%%%%%%%%%%%%%%%%%%%%%%%%%%%%%%%%%%%%%%%%%%%%%%%%%%
%%%%%%%%%%%%%%%%%%%%%%%%%%%%%%%%%%%%%%%%%%%%%%%%%%%%%%%%%%%%%%%%%%%%%%%%
% orifice attached jet linear edges

temp_n2=strcat(load_dir,'EDGES_',Machnum{big_count},'/test',num2str(i),'/',
Machnum{big_count},'_test ',num2str(i),'_frame_',num2str(c),'_orifice.txt');
image=dlmread(temp_n2,'\t');

checkmat=isempty(image);
% test to make sure image contains an interface
if checkmat==0
image(:,2)=image(:,2)-num_x;
image(:,1)=(image(:,1)-num)*-1;
% find the maximum y-point in the jet edge (to correct for pinched jet
boundaries)
y_max=max(image(:,1));
for g=1:1:y_max
p=find(image(:,1)==g); % find x coordinate at height y
vv=max(image(p,2)); % find right side point
% find the INNER left side point
pp=min(image(p,2)); % find left jet point
test=isempty(pp);
if test==0
i_LF(g,c)=pp; % max x coord's
i_RF(g,c)=vv; % min x coord's
else
i_LF(g,c)=0;
i_RF(g,c)=0;
end
end
else
i_LF(1:1:y_max,c)=0;
i_RF(1:1:y_max,c)=0;
end
end

```

```

% orifice only attached mask
mask=poly2mask(image(:,2),image(:,1),s1,s2);
Imat=Imat+mask;

% add in additional zeros for pinched jet
i_LF((g+1):num,c)=zeros((num-g),1);
i_RF((g+1):num,c)=zeros((num-g),1);

clear image
%%%%%%%%%%%%%%%%%%%%%%%%%%%%%%%%%%%%%%%%%%%%%%%%%%%%%%%%%%%%%%%%%%%%%%%%
%%%%%%%%%%%%%%%%%%%%%%%%%%%%%%%%%%%%%%%%%%%%%%%%%%%%%%%%%%%%%%%%%%%%%%%%

%%%%%%%%%%%%%%%%%%%%%%%%%%%%%%%%%%%%%%%%%%%%%%%%%%%%%%%%%%%%%%%%%%%%%%%%
%%%%%%%%%%%%%%%%%%%%%%%%%%%%%%%%%%%%%%%%%%%%%%%%%%%%%%%%%%%%%%%%%%%%%%%%
% entire jet linear edges...
% A) add up where all gas exists to get % of time jet spent
% there...

temp_n=strcat(load_dirac,'EDGES_',Machnum{big_count},'/test',num2str(i),'/',M
achnum{big_count},'_test ',num2str(i),'_frame_',num2str(c),'_all.mat');
load(temp_n,'im4')
Whole=Whole+im4;

% consider entire jet and get all local pinch off points in
% time...image im4 contains all bubble positions
mat=bwperim(im4);
[a,b]=find(mat==1);
b=b-num_x;
a=(a-num)*-1;
checkmat=isempty(a);

if checkmat==0
for g=1:1:s1
p=find(a==g); % find x coordinate at height y
vv=max(b(p)); % find right side point
% find the INNER left side point
pp=min(b(p)); % find left jet point
test=isempty(pp);
if test==0
i_La(g,c)=pp; % max x coord's
i_Ra(g,c)=vv; % min x coord's
else
i_La(g,c)=0;
i_Ra(g,c)=0;
end
end
else
i_La(:,c)=0;
i_Ra(:,c)=0;
end
end
temp_n2=strcat(base_dirac,'output/eigth_',Machnum{big_count},'_',num2str(i),'
_orifice_perim.mat');
save(temp_n2,'i_RF','i_LF','Imat','mu','-v6');

```

```

temp_n2=strcat(base_dir,'output/eighth_',Machnum{big_count},'_',num2str(i),'
_all_perim.mat');
save(temp_n2,'i_Ra','i_La','Whole','mu','-v6');

clear i_RF
clear i_LF
clear i_La
clear i_Ra
clear Whole
clear Imat
end
end

```

7.6 References

- Abramovich, G. (1963). The Theory of Turbulent Jets. Cambridge, M.I.T. Press.
- Amromin, E. and I. Mizine (2003). "Partial cavitation as drag reduction technique and problem of active flow control." Marine Technology and Sname News **40**(3): 181-188.
- Antonia, R., L. Browne, S. Rajagopalan and A. Chambers (1983). "On the organized motion of a turbulent plane jet." Journal of Fluid Mechanics **134**: 17.
- Arakeri, V. H. and A. J. Acosta (1973). "Viscous Effects in the Inception of Cavitation on Axisymmetric Bodies." Journal of Fluids Engineering **94**(4): 8.
- Arndt, R. E. A. (1995). Vortex Cavitation. Fluid Vortices - Fluid Mechanics and its Applications. S. Green. Dordrecht, Kluwer Academic Publishers: 731-782.
- Arndt, R. E. A. (2002). "Cavitation in vortical flows." Annual Review of Fluid Mechanics **34**: 143-175.
- Batchelor, G. K. (1967). An Introduction to Fluid Dynamics, Cambridge University Press.
- Benjamin, T. B. (1976). "The Alliance of Practical and Analytic Insights into the Nonlinear Problems of Fluid Mechanics. Applications of Methods of Functional Analysis to Problems in Mechanics." Lecture Notes in Math: 8-29.
- Birkhoff, G. (1962). "Helmholtz and Taylor Instability." Proc. Sym. App. Math **13**: 21.
- Blake Jr, F. G. (1949). "Onset of Cavitation in Liquids." Thesis (PH. D.)--HARVARD UNIVERSITY, 1949. Source: American Doctoral Dissertations, Source code: W1949.: 0049.
- Brennen, C. E. and C. Earls (1995). Cavitation and Bubble Dynamics, Oxford University Press New York.
- Brodkey, R. S. (1967). The Phenomena of Fluid Motions, Dover.
- Callenaere, M., J. P. Franc, J. M. Michel and M. Riondet (2001). "The cavitation instability induced by the development of a re-entrant jet." Journal of Fluid Mechanics **444**: 223-256.
- Castillejos, A. H. and J. K. Brimacombe (1987). "Measurement of Physical Characteristics of Bubbles in Gas-Liquid Plumes .1. an Improved Electroresistivity Probe Technique." Metallurgical Transactions B-Process Metallurgy **18**(4): 649-658.

- Chawla, T. C. (1975). "Kelvin-Helmholtz Instability of Gas-Liquid Interface of a Sonic Gas Jet Submerged in a Liquid." Journal of Fluid Mechanics **67**(FEB11): 513-537.
- Chawla, T. C. (1975). "Rate of Liquid Entrainment at Gas-Liquid Interface of a Liquid Submerged Sonic Gas Jet." Nuclear Science and Engineering **56**(1): 1-6.
- Chen, K. and H. J. Richter (1997). "Instability analysis of the transition from bubbling to jetting in a gas injected into a liquid." International Journal of Multiphase Flow **23**(4): 699-712.
- Cieslinski, J. T. and R. Mosdorf (2005). "Gas bubble dynamics - experiment and fractal analysis." International Journal of Heat and Mass Transfer **48**(9): 1808-1818.
- Crow, S. C. and F. H. Champagne (1971). "Orderly structure in jet turbulence." Journal of Fluid Mechanics **48**(03): 547-591.
- Dai, Z. Q., B. Y. Wang, L. X. Qi and H. H. Shi (2006). "Experimental study on hydrodynamic behaviors of high-speed gas jets in still water." Acta Mechanica Sinica **22**(5): 443-448.
- Darmana, D., N. G. Deen and J. A. M. Kuipers (2005). "Detailed modeling of hydrodynamics, mass transfer and chemical reactions in a bubble column using a discrete bubble model." Chemical Engineering Science **60**(12): 3383-3404.
- Deo, R. C., J. Mi and G. J. Nathan (2007). "The influence of nozzle aspect ratio on plane jets." Experimental Thermal and Fluid Science **31**(8): 825-838.
- Dimotakis, P. E., R. C. Miakelye and D. A. Papantoniou (1983). "Structure and Dynamics of Round Turbulent Jets." Physics of Fluids **26**(11): 3185-3192.
- Epstein, M., H. Fauske, S. Kubo, T. Nakamura and K. Koyama (2001). "Liquid entrainment by an expanding core disruptive accident bubble - a Kelvin/Helmholtz phenomenon." Nuclear Engineering and Design **210**: 24.
- Fischer, H., E. List, R. Koh, J. Imberger and N. Brooks (1979). Mixing in Inland and Coastal Water. New York, Academic Press.
- Gharib, M., E. Rambod and K. Shariff (1998). "A universal time scale for vortex ring formation." Journal of Fluid Mechanics **360**: 121-140.
- Glezer, A. (1988). "The Formation of Vortex Rings." Physics of Fluids **31**(12): 3532-3542.
- Gopalan, S. and J. Katz (2000). "Flow Structure and Modeling Issues in the Closure Region of Attached Cavitation." Physics of Fluids **12**(4): 895-911.
- Gordeyev, S. V. and F. O. Thomas (1999). "Temporal subharmonic amplitude and phase behaviour in a jet shear layer: wavelet analysis and Hamiltonian formulation." Journal of Fluid Mechanics **394**(-1): 205-240.
- Gordeyev, S. V. and F. O. Thomas (2000). "Coherent structure in the turbulent planar jet. Part 1. Extraction of proper orthogonal decomposition eigenmodes and their self-similarity." Journal of Fluid Mechanics **414**(-1): 145-194.
- Gutmark, E. and I. Wygnanski (1976). "The planar turbulent jet." Journal of Fluid Mechanics **73**: 30.
- Helmholtz, H. v. (1868). "On discontinuous movements of fluids." Phil. Mag. **36**(4): 9.

- Hinkley, D. V. (1970). "Inference about the change-point in a sequence of random variables." Biometrika **57**(1): 1-17.
- Hinkley, D. V. (1971). "Inference about the change-point from cumulative sum tests." Biometrika **58**(3): 509-523.
- Hrubes, J. D. (2001). "High-Speed Imaging of Supercavitating Underwater Projectiles." Experiments in Fluids **30**(1): 57-64.
- Huang, T. T. (1979). Cavitation Inception Observations on Axisymmetric Headforms. International Symposium on Cavitation Inception. New York, NY.
- Ito, K., S. Kobayashi and M. Tokuda (1991). "Mixing Characteristics of a Submerged Jet Measured Using an Isokinetic Sampling Probe." Metallurgical Transactions B-Process Metallurgy **22**(4): 439-445.
- Katz, J. (1984). "Cavitation Phenomena within Regions of Flow Separation." Journal of Fluid Mechanics **140**: 397-436.
- Keller, A. P. (1979). Cavitation Inception Measurement and Flow Visualisation on Axisymmetric Bodies at Two Different Free Stream Turbulence Levels and Test Procedures. International Symposium on Cavitation Inception. New York, NY.
- Kelvin, W. (1871). "Hydrokinetic solutions and observations." Phil. Mag. **42**(4): 15.
- Kirschner, I. N., D. C. Kring, A. W. Stokes, N. E. Fine and J. S. Uhlman (2002). "Control strategies for supercavitating vehicles." Journal of Vibration and Control **8**(2): 219-242.
- Kitscha, J. and G. Kocamustafaogullari (1989). "Breakup Criteria for Fluid Particles." International Journal of Multiphase Flow **15**(4): 573-588.
- Kondama, Y., S. Tamiya, N. Take and H. Kato (1979). The Effects of Nuclei on the Inception of Bubble and Sheet Cavitation on Axisymmetric Bodies. International Symposium on Cavitation Inception. New York, NY.
- Krothapalli, A., D. Baganoff and K. Karamcheti (1981). "On the mixing of a rectangular jet." Journal of Fluid Mechanics Digital Archive **107**(-1): 201-220.
- Laughlin, J. and W. Brooks (1996). Adaptation of the Army Tactical Missile System to Undersea Operations, Lockheed Martin.
- Le, Q., J. P. Franc and J. M. Michel (1993). "Partial Cavities - Global Behavior and Mean Pressure Distribution." Journal of Fluids Engineering-Transactions of the Asme **115**(2): 243-248.
- Liepmann, H. and A. Roshko (1957). Elements of Gasdynamics. New York, John Wiley & Sons.
- Lin, C. C. and D. J. Benney (1962). "On the Instability of Shear Flows." Proc. Sym. App. Math **13**: 24.
- Lin, G. J., B. Balachandran and E. H. Abed (2008). "Dynamics and control of supercavitating vehicles." Journal of Dynamic Systems Measurement and Control-Transactions of the Asme **130**(2): -.
- Loth, E. (1988). Study of Underexpanded Turbulent Air Jets in Water. Ann Arbor, The University of Michigan. **PhD**.

- Loth, E. and G. M. Faeth (1989). "Structure of Underexpanded Round Air Jets Submerged in Water." International Journal of Multiphase Flow **15**(4): 589-603.
- Loth, E. and G. M. Faeth (1990). "Structure of plane underexpanded air jets into water." AICHE Journal **36**(6): 818-826.
- Lozanova, M. and P. Stankov (1998). "Experimental investigation on the similarity of a 3D rectangular turbulent jet." Experiments in Fluids **24**(5): 470-478.
- Matveev, K. I. (2003). "On the Limiting Parameters of Artificial Cavitation." Ocean Engineering **30**(9): 1179-1190.
- McNallan, M. J. and T. B. King (1982). "Fluid-Dynamics of Vertical Submerged Gas Jets in Liquid-Metal Processing Systems." Metallurgical Transactions B-Process Metallurgy **13**(2): 165-173.
- Mohseni, K. and M. Gharib (1998). "A model for universal time scale of vortex ring formation." Physics of Fluids **10**(10): 2436-2438.
- Mori, K., Y. Ozawa and M. Sano (1982). "Characterization of Gas-Jet Behavior at a Submerged Orifice in Liquid-Metal." Transactions of the Iron and Steel Institute of Japan **22**(5): 377-384.
- Ozawa, Y. and K. Mori (1986). "Effect of Physical-Properties of Gas and Liquid on Bubbling Jetting Phenomena in Gas Injection into Liquid." Transactions of the Iron and Steel Institute of Japan **26**(4): 291-297.
- Plesset, M. S. and A. Prosperetti (1977). "Bubble Dynamics and Cavitation." Annual Reviews in Fluid Mechanics **9**(1): 145-185.
- Prosperetti, A. (1982). "A generalization of the Rayleigh–Plesset equation of bubble dynamics." Physics of Fluids **25**: 409.
- Quinn, W. (1991). "Passive Near-Field Mixing Enhancement in Rectangular Jet Flows." AIAA Journal **29**(4): 4.
- Quinn, W. (1992). "Turbulent Free Jet Flows Issuing from Sharp-Edged Rectangular Slots: The Influence of Slot Aspect Ratio." Experimental Thermal and Fluid Science **5**: 12.
- Rayleigh, J. (1879). "On the instability of jets." Proc. Lond. Math. Soc. **10**: 10.
- Rayleigh, L. (1917). "On the pressure developed in a liquid during the collapse of a spherical cavity." Phil. Mag **34**(200): 94-98.
- Rood, E. P. (1989). Mechanisms of Cavitation Inception. International Symposium on Cavitation Inception. San Francisco, CA.
- Rood, E. P. (1991). "Review -- Mechanisms of Cavitation Inception." Journal of Fluids Engineering **113**: 163-175.
- Rouse, H. and J. McNown (1948). Cavitation and Pressure Distribution Head Forms at Zero Angle of Yaw. Iowa City, State University of Iowa.
- Ruzicka, M. C., J. Drahos, J. Zahradnik and N. H. Thomas (1997). "Intermittent transition from bubbling to jetting regime in gas-liquid two phase flows." International Journal of Multiphase Flow **23**(4): 671-682.

- Sahai, Y. and R. I. L. Guthrie (1982). "Hydrodynamics of Gas Stirred Melts .1. Gas-Liquid Coupling." Metallurgical Transactions B-Process Metallurgy **13**(2): 193-202.
- Sano, M., H. Makino, Y. Ozawa and K. Mori (1986). "Behavior of Gas-Jet and Plume in Liquid-Metal." Transactions of the Iron and Steel Institute of Japan **26**(4): 298-304.
- Savchenko, Y. N. (2001). Supercavitation - Problems and Perspectives. Proc. 4th International Symposium on Cavitation, Pasadena, CA.
- Settles, G. (2006). Schlieren and Shadowgraph Techniques. Berlin, Springer.
- Sfeir, A. (1979). "Investigation of Three-Dimensional Turbulent Rectangular Jets." AIAA Journal **17**(10): 5.
- Sforza, P., M. Steiger and N. Trentacoste (1966). "Studies on Three-Dimensional Viscous Jets." AIAA Journal **4**(5): 6.
- Shapiro, A. (1953). The Dynamics and Thermodynamics of Compressible Fluid Flow. New York, John Wiley & Sons.
- Shi, H.-H., M. Itoh and T. Takami (2000). "Optical Observation of the Supercavitation Induced by High-Speed Water Entry." Journal of Fluids Engineering **122**: 806-810.
- Stutz, B. and J. L. Reboud (1997). "Experiments on unsteady cavitation." Experiments in Fluids **22**(3): 191-198.
- Stutz, B. and J. L. Reboud (2000). "Measurements within unsteady cavitation." Experiments in Fluids **29**(6): 545-552.
- Subramaniam, K., R. N. Parthasarathy and K. M. Chiang (1999). "Three-dimensional temporal instability of compressible gas jets injected in liquids." Aiaa Journal **37**(2): 202-207.
- Tam, C. and A. Thies (1993). "Instability of rectangular jets." Journal of Fluid Mechanics **248**: 23.
- Trentacoste, N. and P. Sforza (1967). "Further Experimental Results for Three-Dimensional Free Jets." AIAA Journal **5**(5): 6.
- Tross, S. (1974). Characteristics of a Turbulent, Two-Phase, Submerged, Free Jet. Mechanical Engineering. University Park, The Pennsylvania State University. **Masters Thesis**.
- Tsuchiya, Y. and C. Horikoshi (1986). "On the spread of rectangular jets." Experiments in Fluids **4**(4): 197-204.
- Varghese, A. N., J. S. Uhlman and I. N. Kirschner (2005). "Numerical analysis of high-speed bodies in partially cavitating axisymmetric flow." Journal of Fluids Engineering-Transactions of the Asme **127**(1): 41-54.
- Wang, H. W. and A. W. K. Law (2002). "Second-order integral model for a round turbulent buoyant jet." Journal of Fluid Mechanics **459**: 397-428.
- Weiland, C. and P. Vlachos (2007). Experimental Study of the Stability and Trajectory of a High Speed Gas Jet Under the Influence of Liquid Cross Flow. ASME Joint U.S.-European Fluids Engineering Meeting. San Diego, CA.
- Weiland, C., P. Vlachos and J. Yagla (2005). A Novel Launcher for Submarine Self-Defense. 4th Biennial National Forum on Weapon System Effectiveness. Austin, TX, AIAA.

- Wraith, A. and M. Chalkly (1977). Advances in Extractive Metallurgy. M. Jones. London, IMM.
- Yagla, J. (1997). "Concentric Canister Launcher." Naval Engineers Journal **109**(3): 18.
- Yagla, J., J. Basic, S. Koski, B. Myruski, C. Weiland and P. Vlachos (2008). Launcher Dynamics Environment of a Water Piercing Missile Launcher. 24th International Symposium on Ballistics. New Orleans, LA, NDIA.
- Yagla, J., K. Deloach and C. Weiland (2004). The Water Piercing Missile Launcher. 21st International Symposium on Ballistics. Adelaide, Australia, NDIA.
- Yagla, J., M. Soifer, K. Deloach, C. Weiland and P. Vlachos (2006). The Water Piercing Missile Launcher. Submarine Technology Symposium. Laurel, MD, The Johns Hopkins University Applied Physics Laboratory.
- Zaman, K. B. M. Q. (1999). "Spreading characteristics of compressible jets from nozzles of various geometry." Journal of Fluid Mechanics **383**: 31.
- Zaman, K. B. M. Q., M. D. Dahl, T. J. Bencic and C. Y. Loh (2002). "Investigation of a 'transonic resonance' with convergent divergent nozzles." Journal of Fluid Mechanics **463**(-1): 313-343.
- Zhao, Y. F. and G. A. Irons (1990). "The Breakup of Bubbles into Jets During Submerged Gas Injection." Metallurgical Transactions B-Process Metallurgy **21**(6): 997-1003.

8. APPENDIX B: JET PENETRATION DATA

8.1 Introduction

The jet penetration was shown to be strongly dependent on both Mach number and aspect ratio (in the case of rectangular jets) in Chapters 3 and 4. This Appendix shows the individual jet penetration and performance for all cases tested. There is no discussion of the individual cases as these occurred in the body of the dissertation. Rather this Appendix is meant to serve as a repository of information for the curious reader. In each case, three trials of data were taken and thus each trial is shown for both the orifice attached only and entire jet.

It is important to note the differences between the optical method used in this dissertation and the probe methods typically employed and discussed in Chapters 3 and 4. Visually this may be described in the plots which follow. As an example, consider Figure 8.1 and Figure 8.2, which show the time averaged gas presence contours for orifice attached only gas jets (neglect pinched off bubbles) and the entire flow field, respectively. Clearly, a large discrepancy exists between the cases. The apparent jet presence increases drastically when pinched off bubbles are not neglected. Of course, the WPML operation requires a continuous gas jet presence to be maintained from the nozzle to the free surface, and thus probe measurements are useless to this end. Instead, only orifice attached gas jets are considered and this demonstrates the mean jetting length – or the statistical presence a gas jet maintains from the nozzle to some position in the ambient liquid – across all test cases. From this one can surmise the useful length of each gas jet test condition.

In some of the cases pertaining to whole field measurements, in which pinched off bubbles are not included, there are erroneous measurement spots away from the jet. Consider Figure 8.24 which shows a jet presence near the legend. Of course this is not gas but rather an artifact of the shadowgraph images having uneven lighting intensity. When analyzed these portions are automatically ignored, and should be ignored by the reader here.

8.2 Round Jets

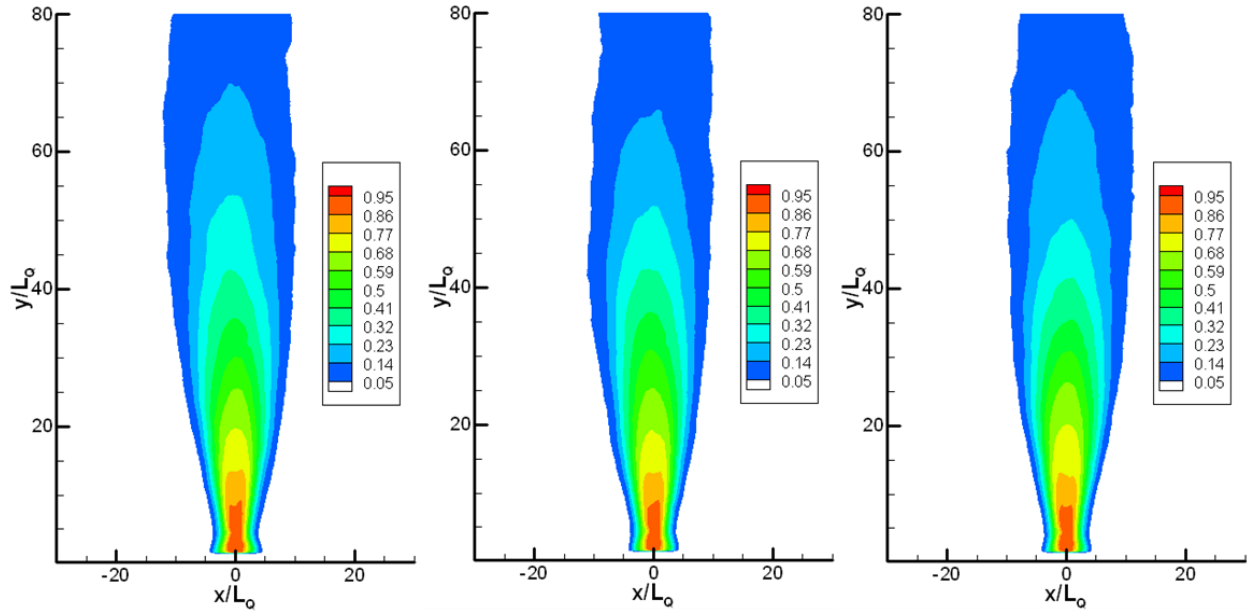


Figure 8.1. Mach 0.4 jet penetration trials: orifice attached jets only.

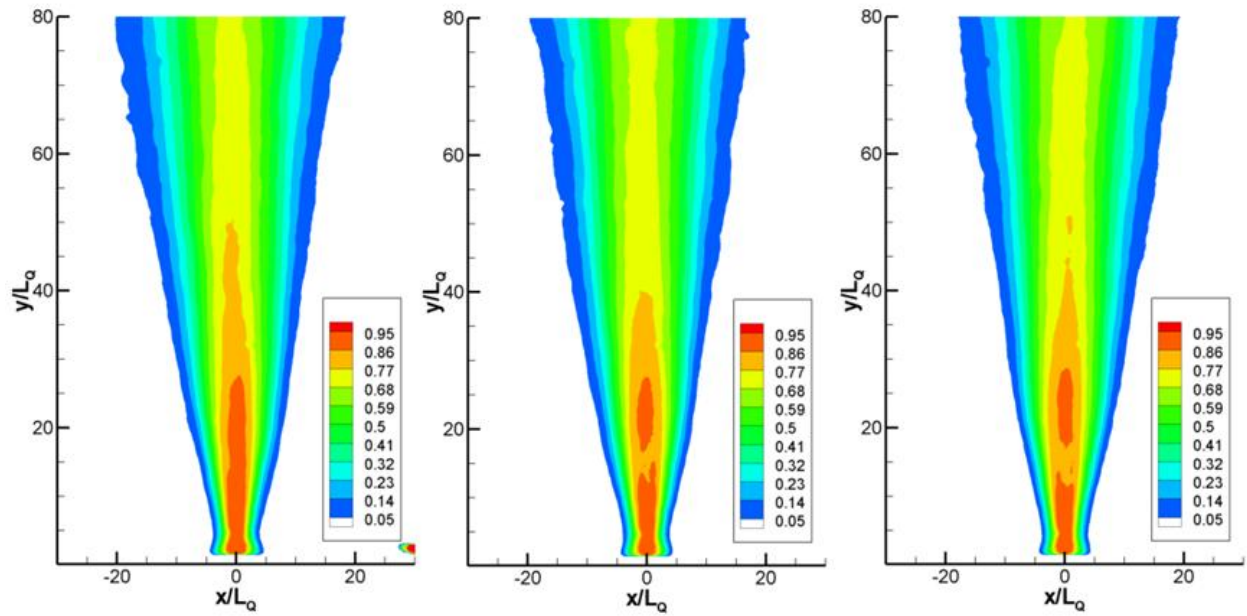


Figure 8.2. Mach 0.4 jet penetration trials: entire jet.

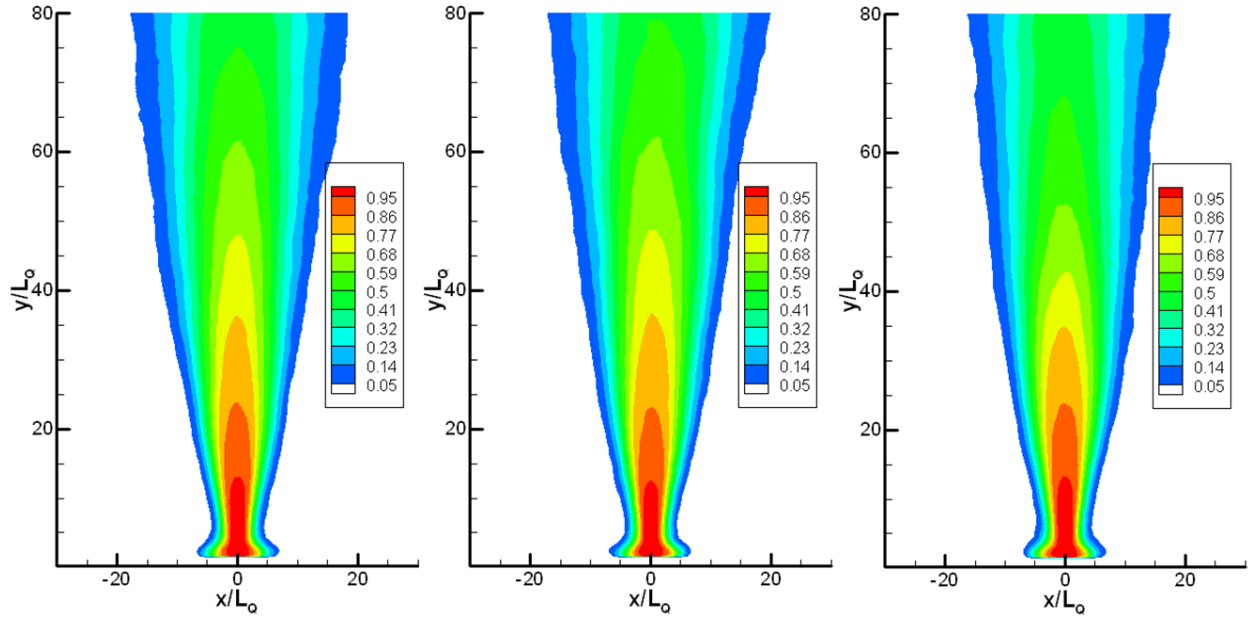


Figure 8.3 Mach 0.6 jet penetration trials: orifice attached jets only.

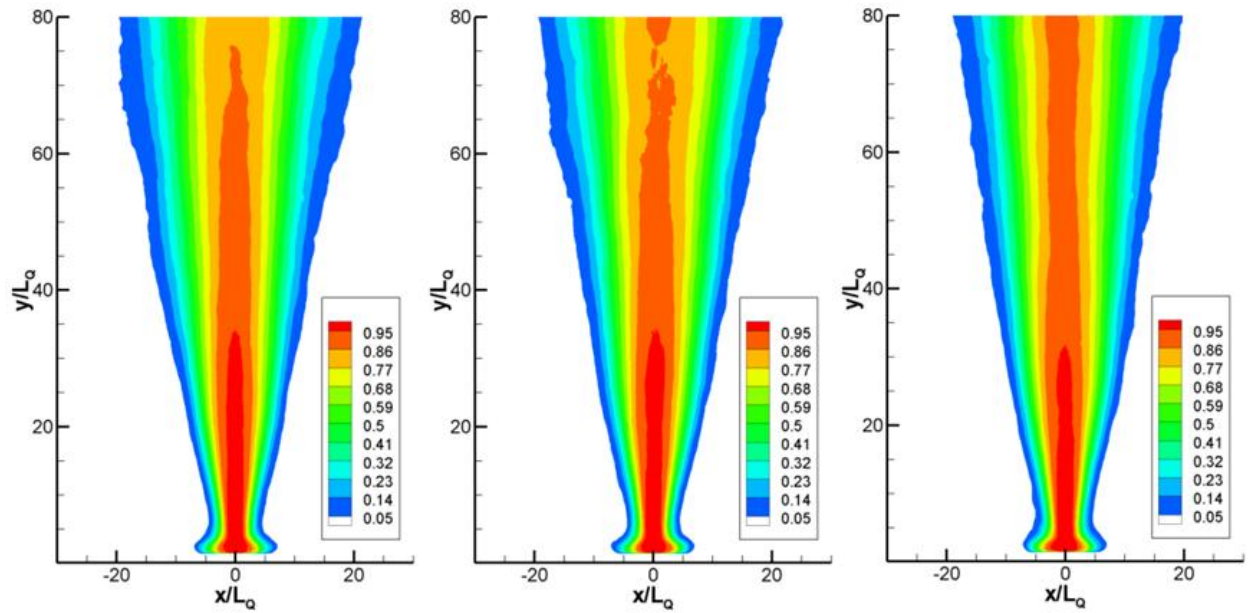


Figure 8.4. Mach 0.6 jet penetration trials: entire jet.

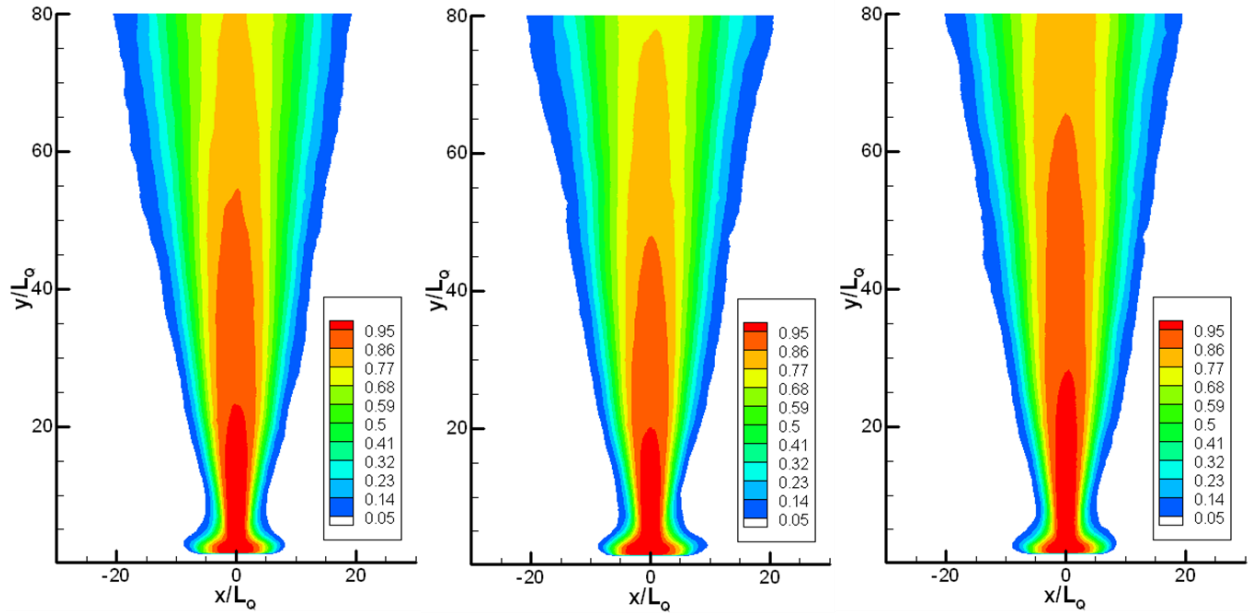


Figure 8.5. Mach 0.8 jet penetration trials: orifice attached jets only.

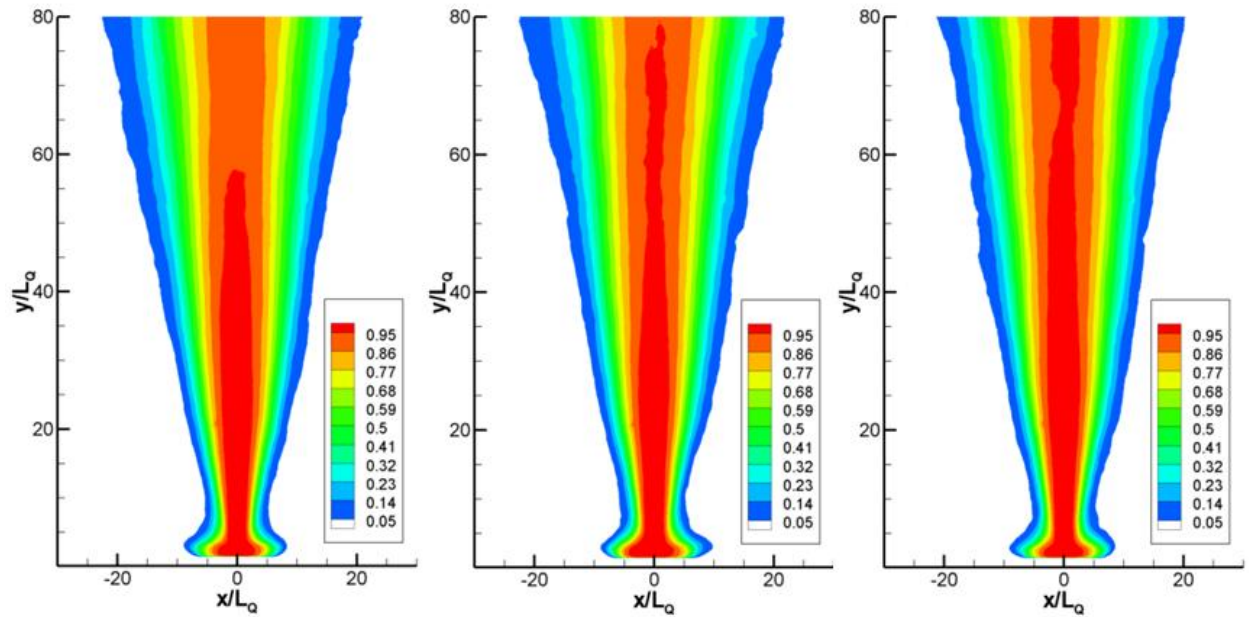


Figure 8.6. Mach 0.8 jet penetration trials: entire jet.

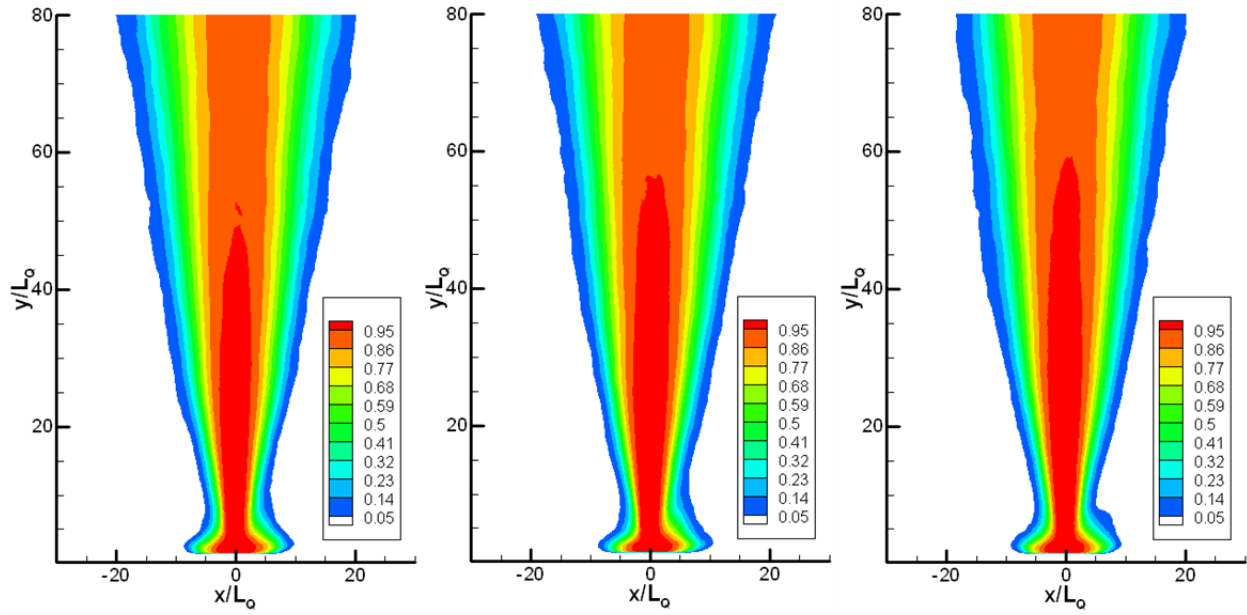


Figure 8.7. Mach 0.9 jet penetration trials: orifice attached jets only.

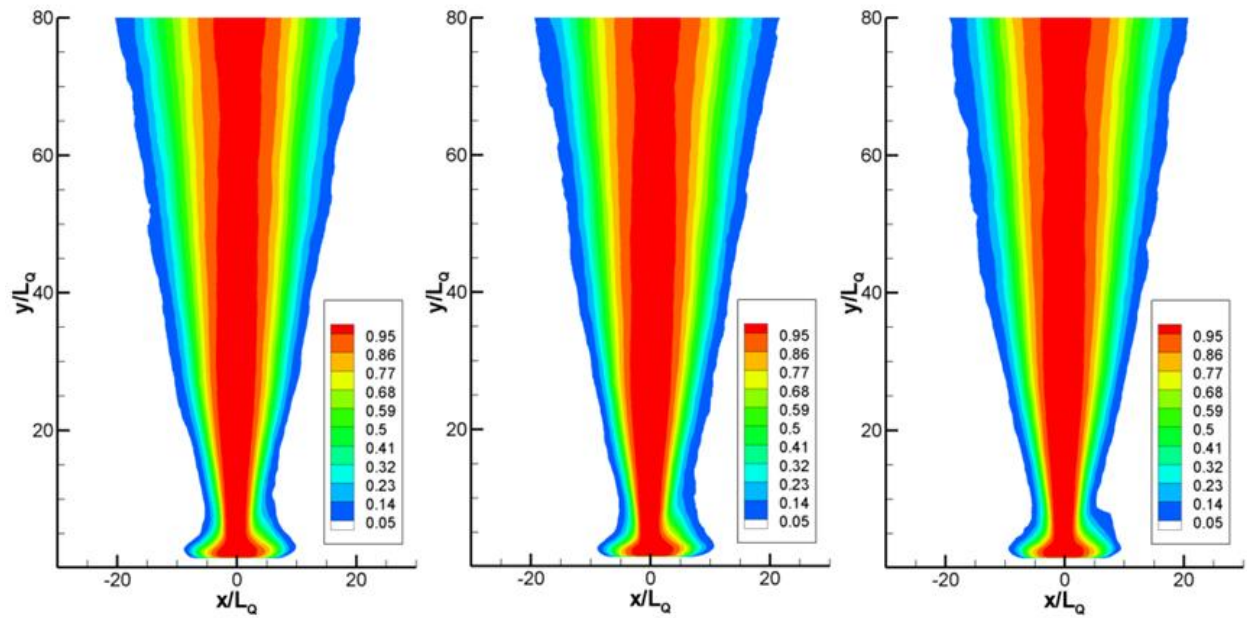


Figure 8.8. Mach 0.9 jet penetration trials: entire jet.

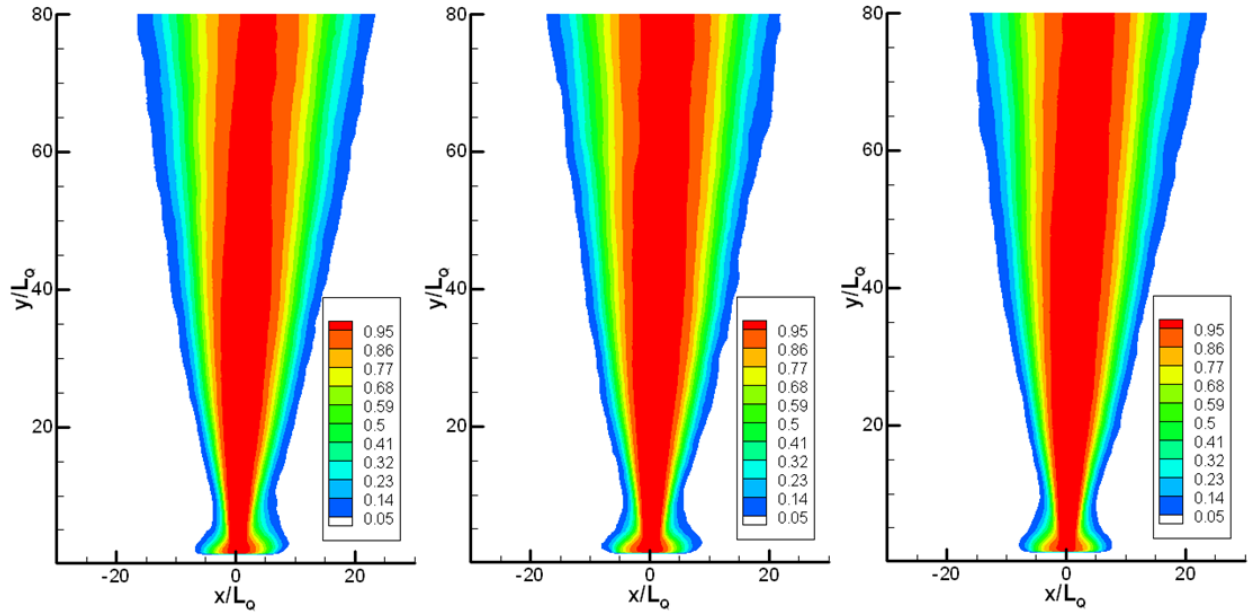


Figure 8.9. Mach 1.1 jet penetration trials: orifice attached jets only.

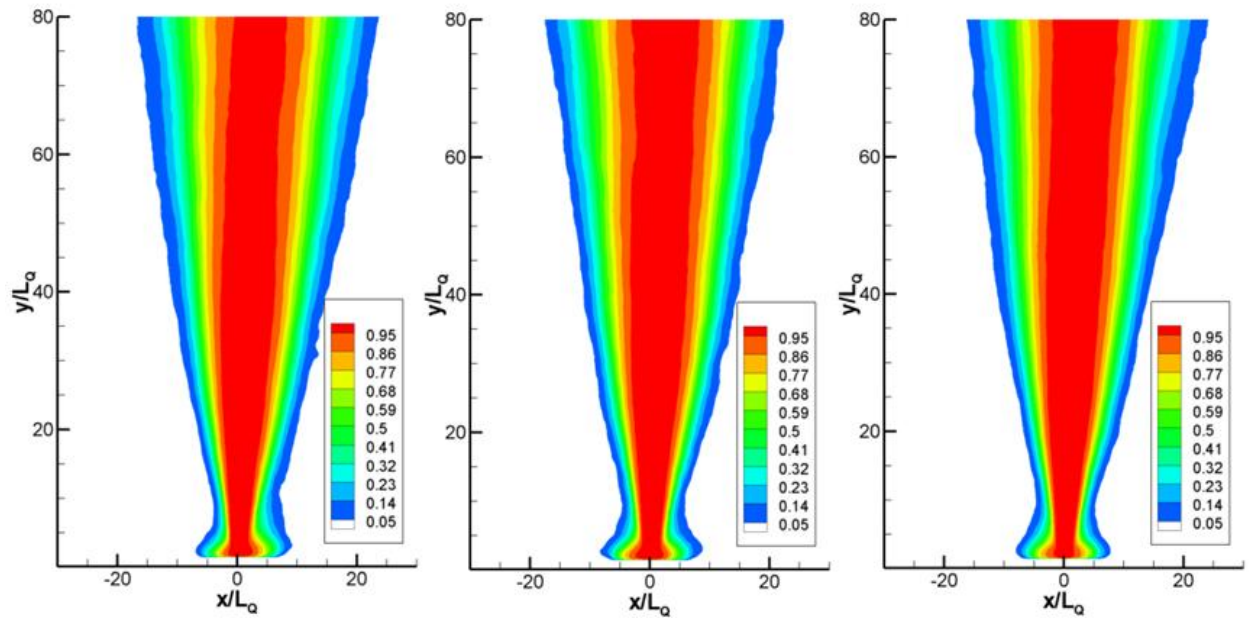


Figure 8.10. Mach 1.1 jet penetration trials: entire jet.

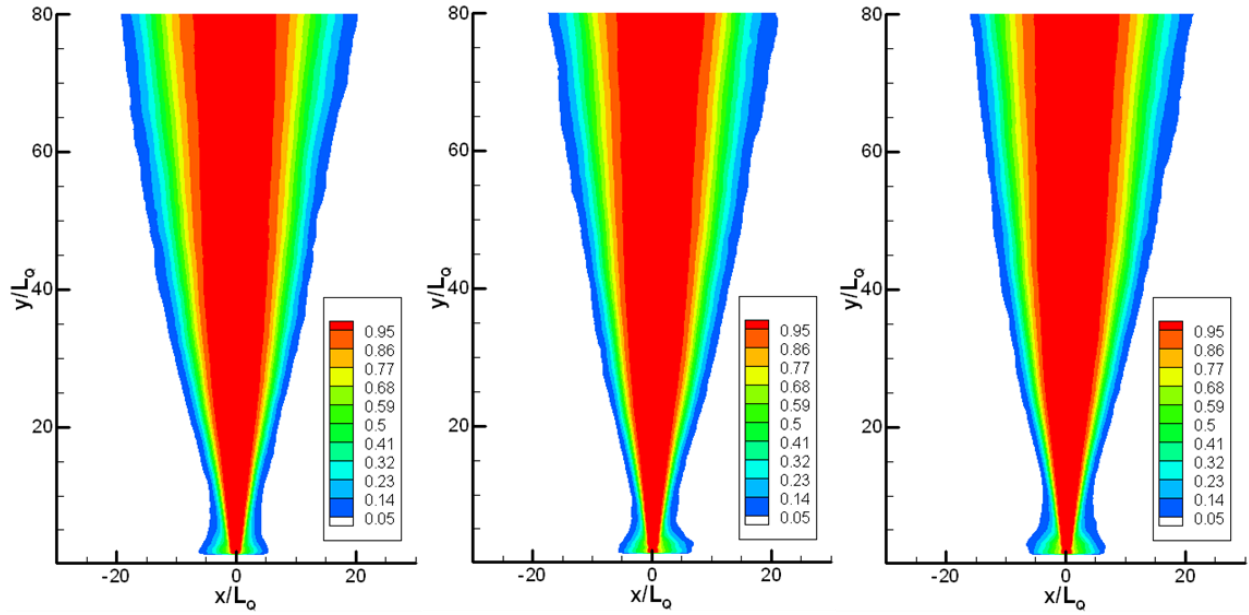


Figure 8.11. Mach 1.8 jet penetration trials: orifice attached jets only.

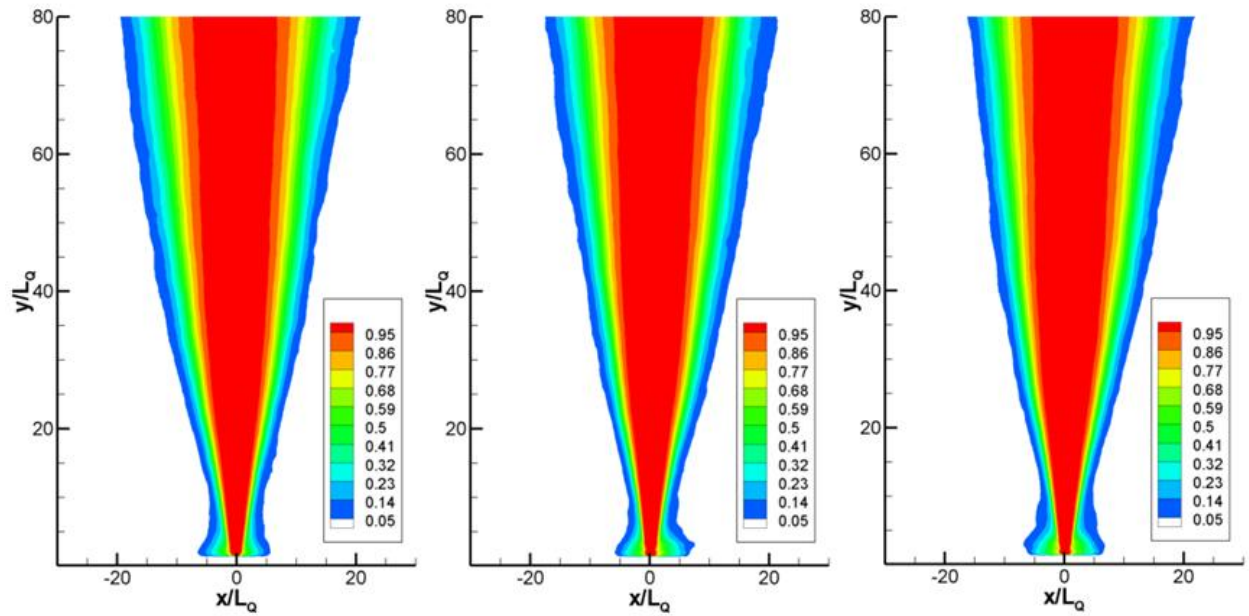


Figure 8.12. Mach 1.8 jet penetration trials: entire jet.

8.3 Rectangular Jets – Aspect Ratio 2

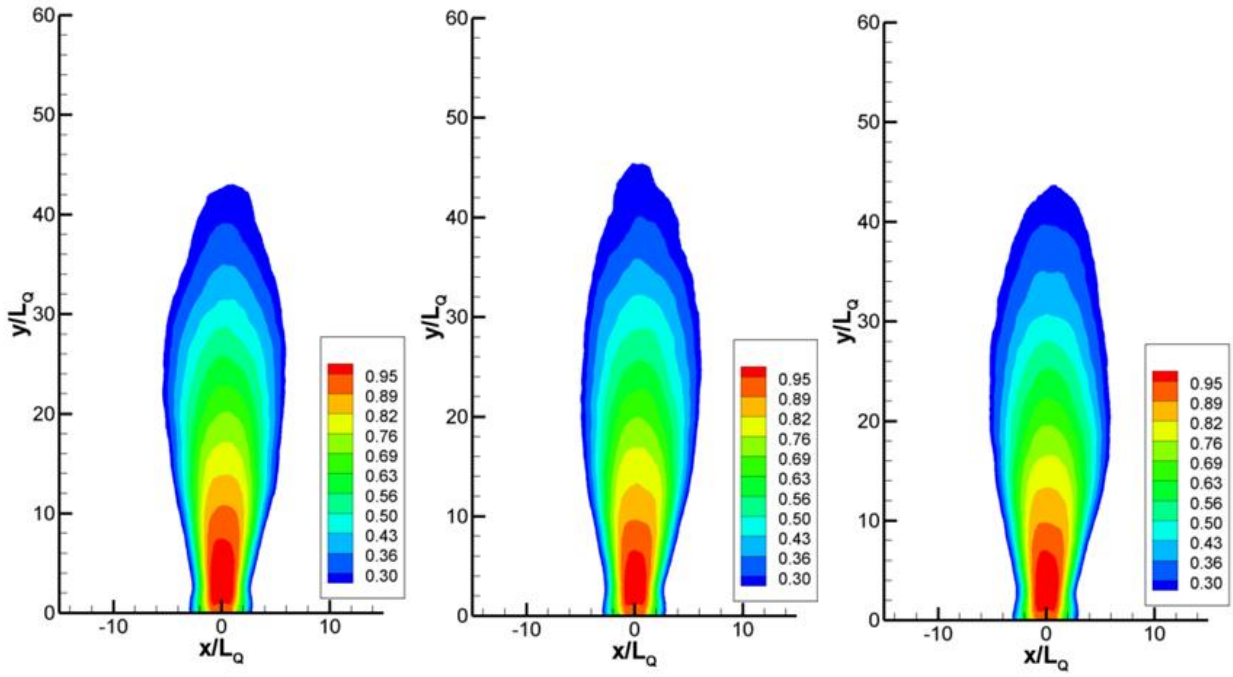


Figure 8.13. Mach 0.5 jet penetration trials: orifice attached jets only.

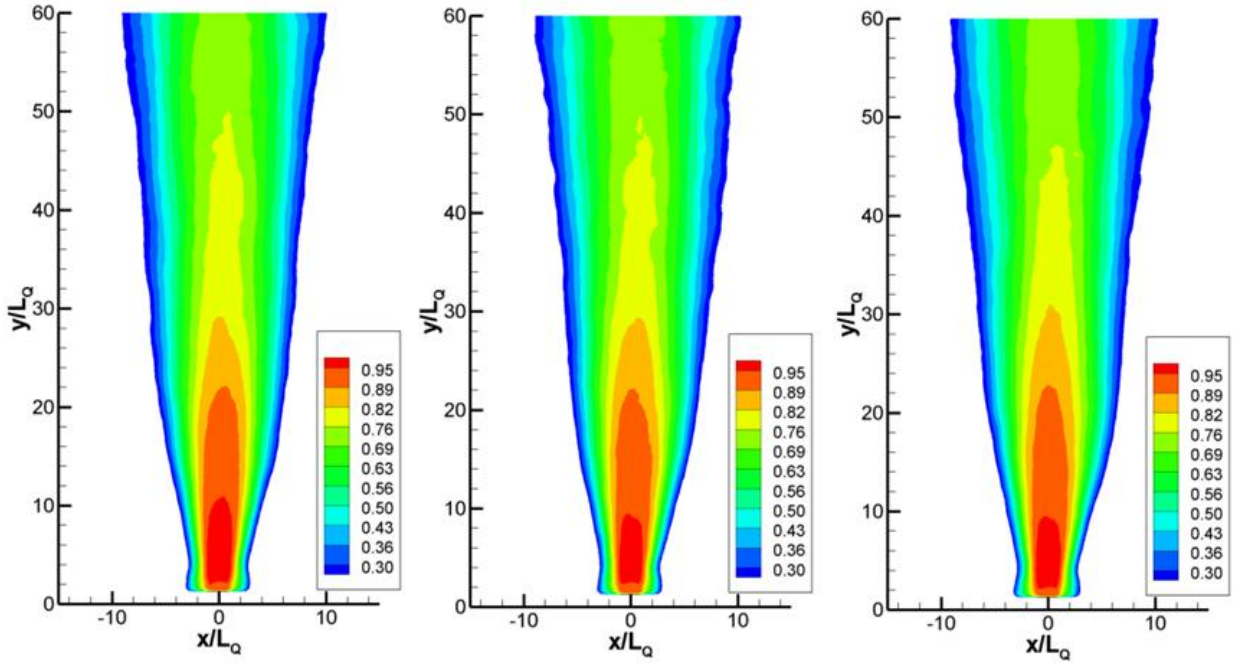


Figure 8.14. Mach 0.5 jet penetration trials: entire jet.

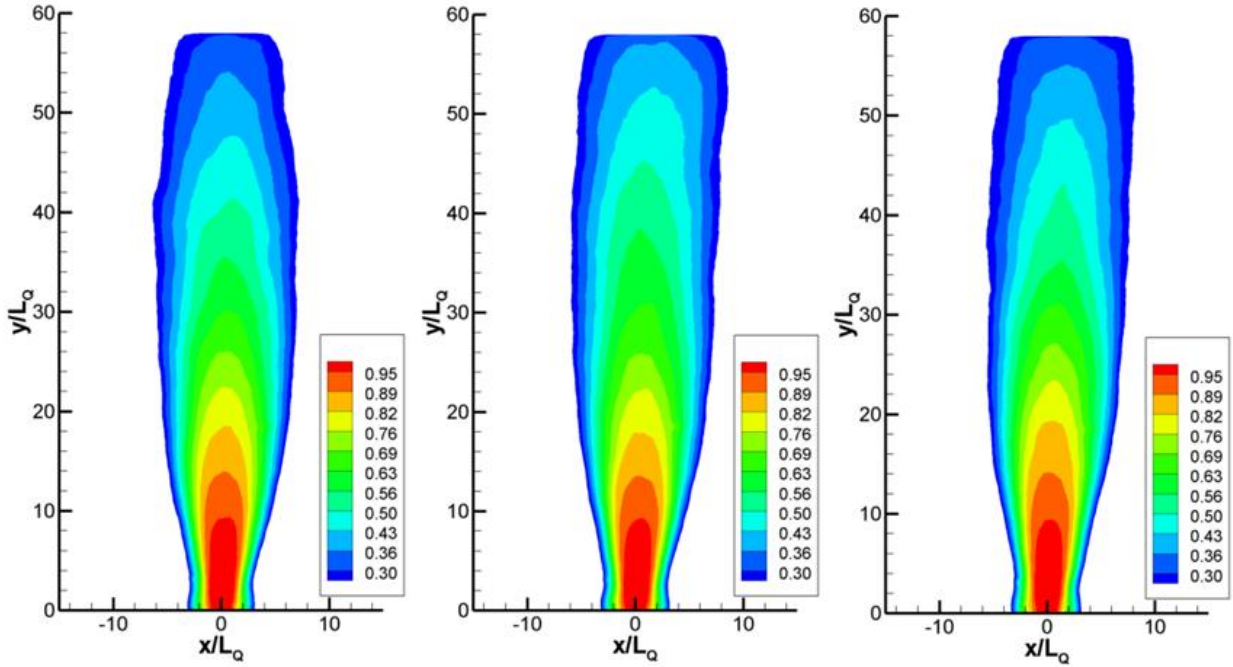


Figure 8.15 Mach 0.6 jet penetration trials: orifice attached jets only.

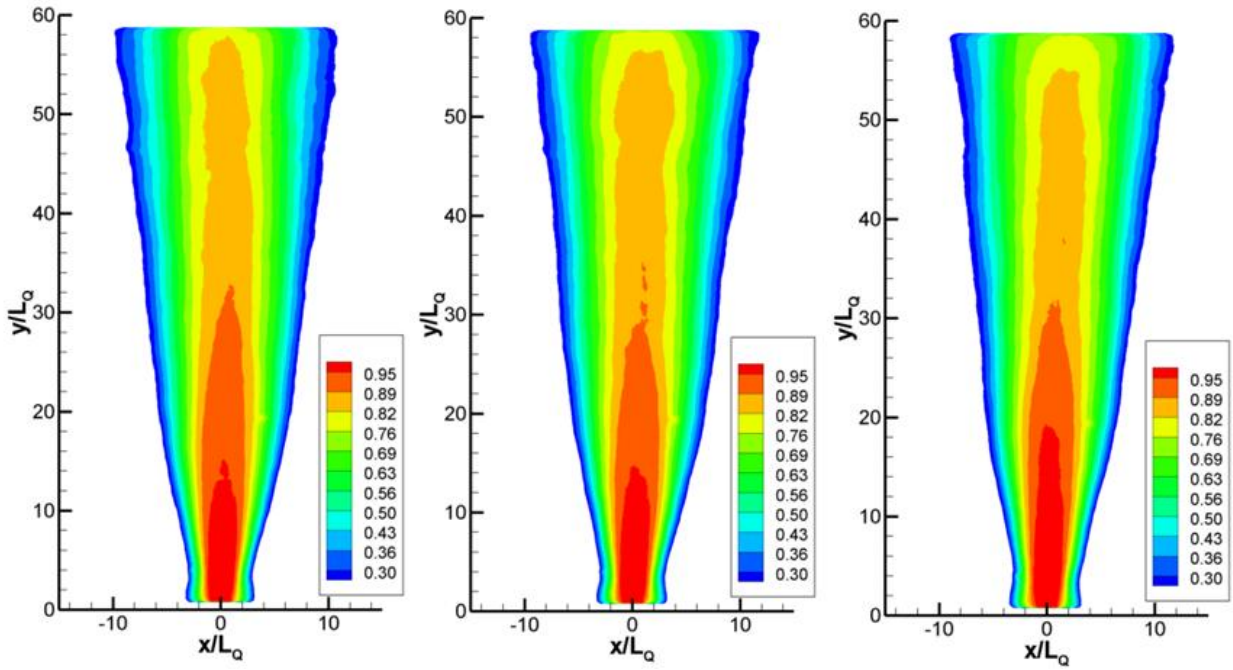


Figure 8.16. Mach 0.6 jet penetration trials: entire jet.

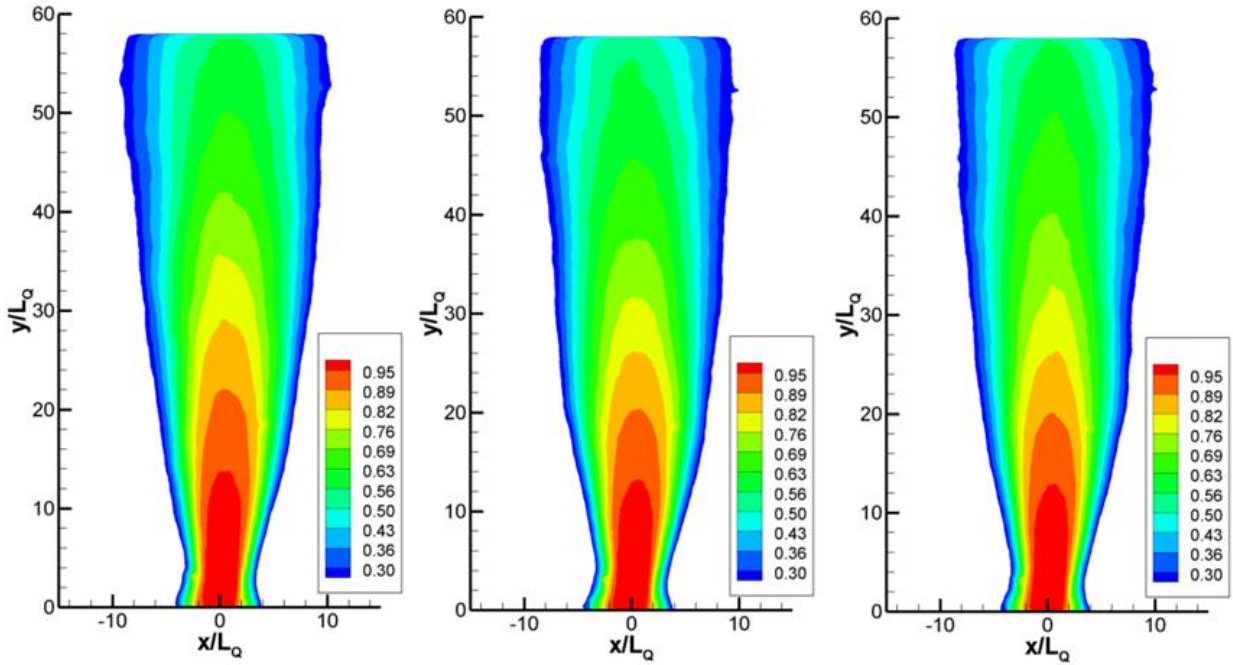


Figure 8.17. Mach 0.8 jet penetration trials: orifice attached jets only.

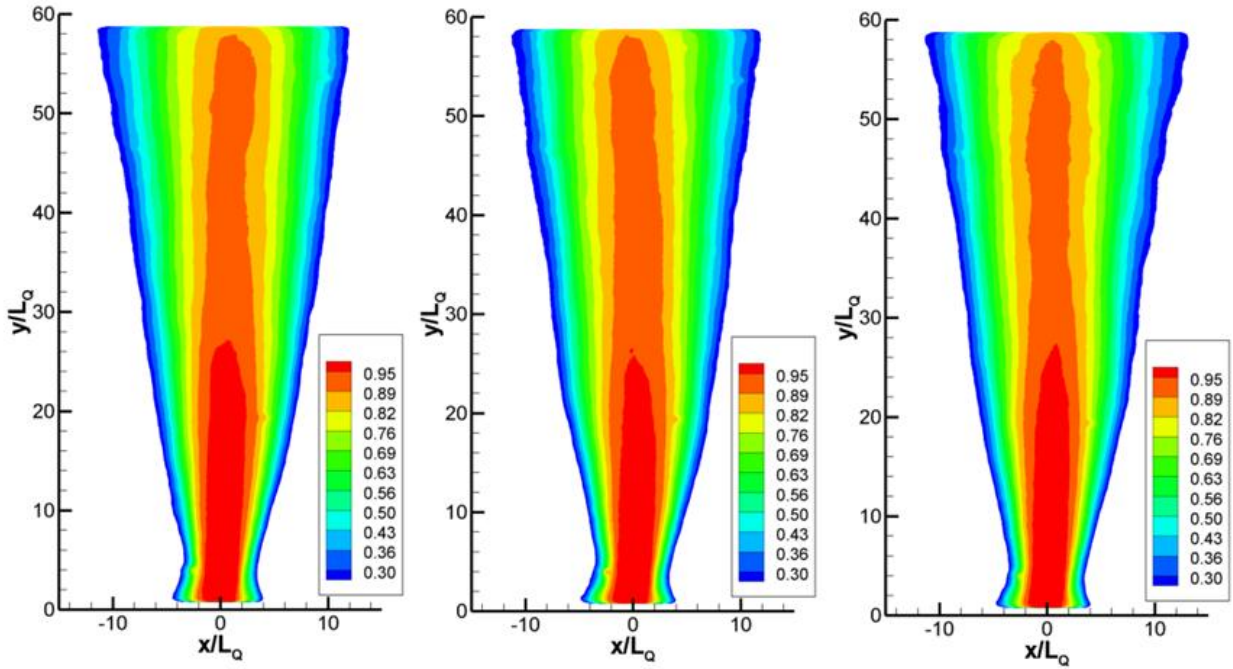


Figure 8.18. Mach 0.8 jet penetration trials: entire jet.

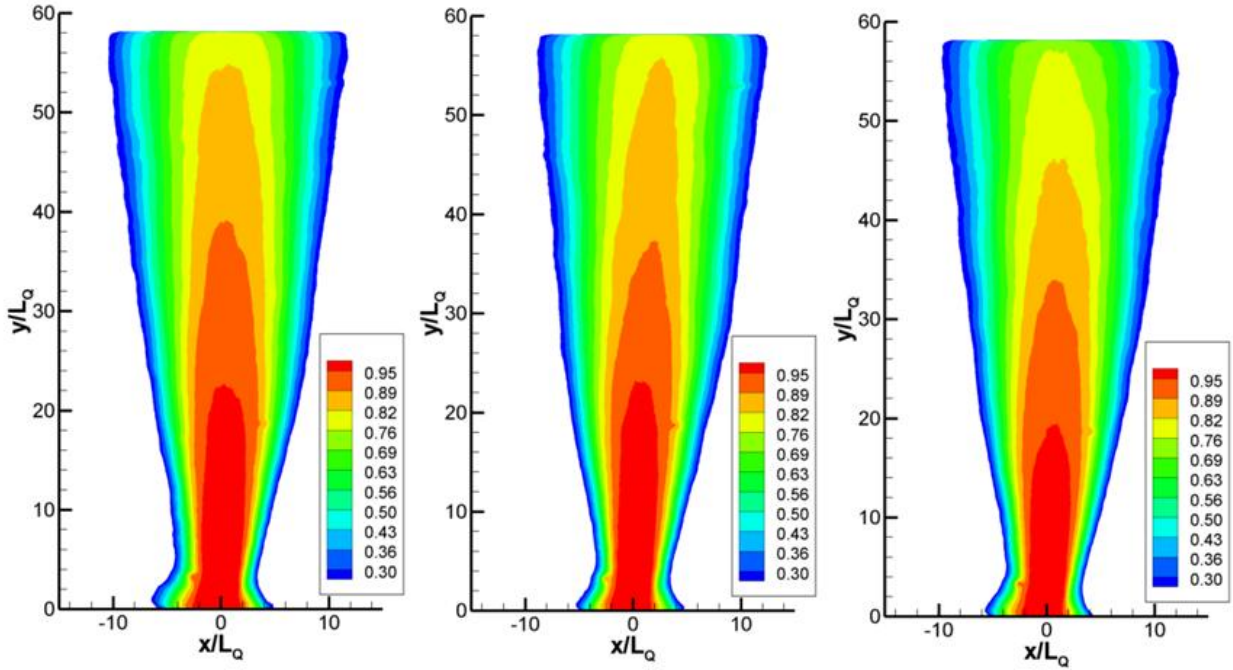


Figure 8.19. Mach 1.0 jet penetration trials: orifice attached jets only.

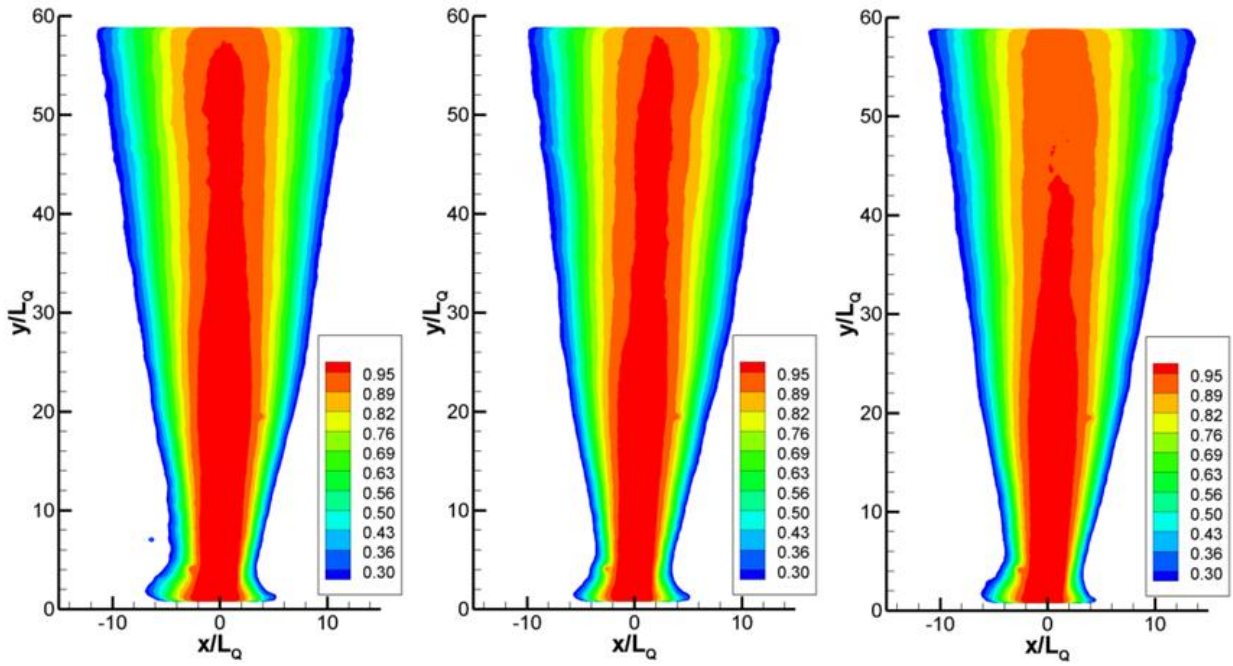


Figure 8.20. Mach 1.0 jet penetration trials: entire jet.

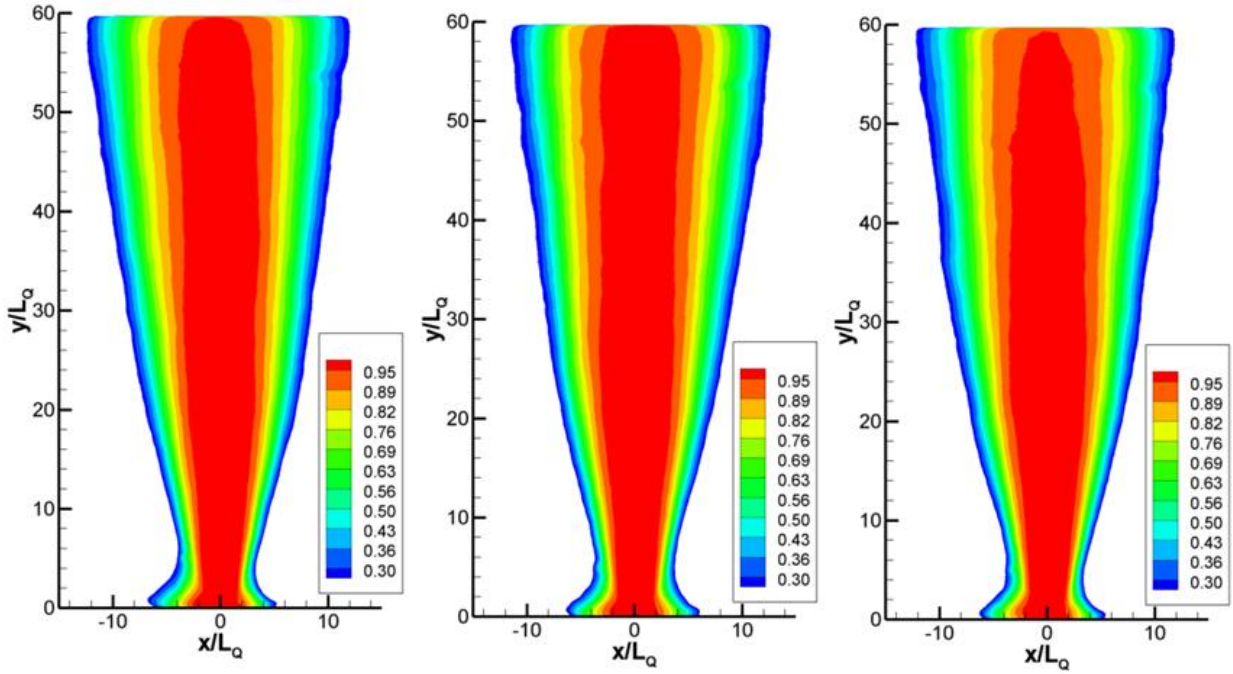


Figure 8.21. Mach 1.1 jet penetration trials: orifice attached jets only.

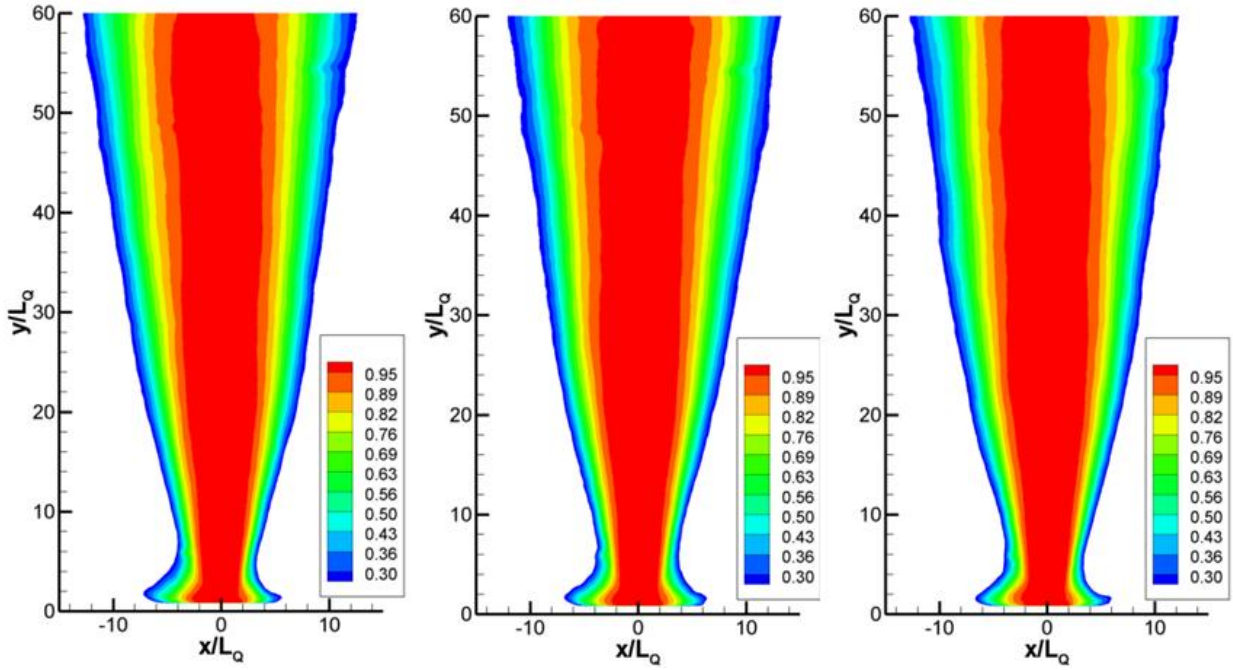


Figure 8.22. Mach 1.1 jet penetration trials: entire jet.

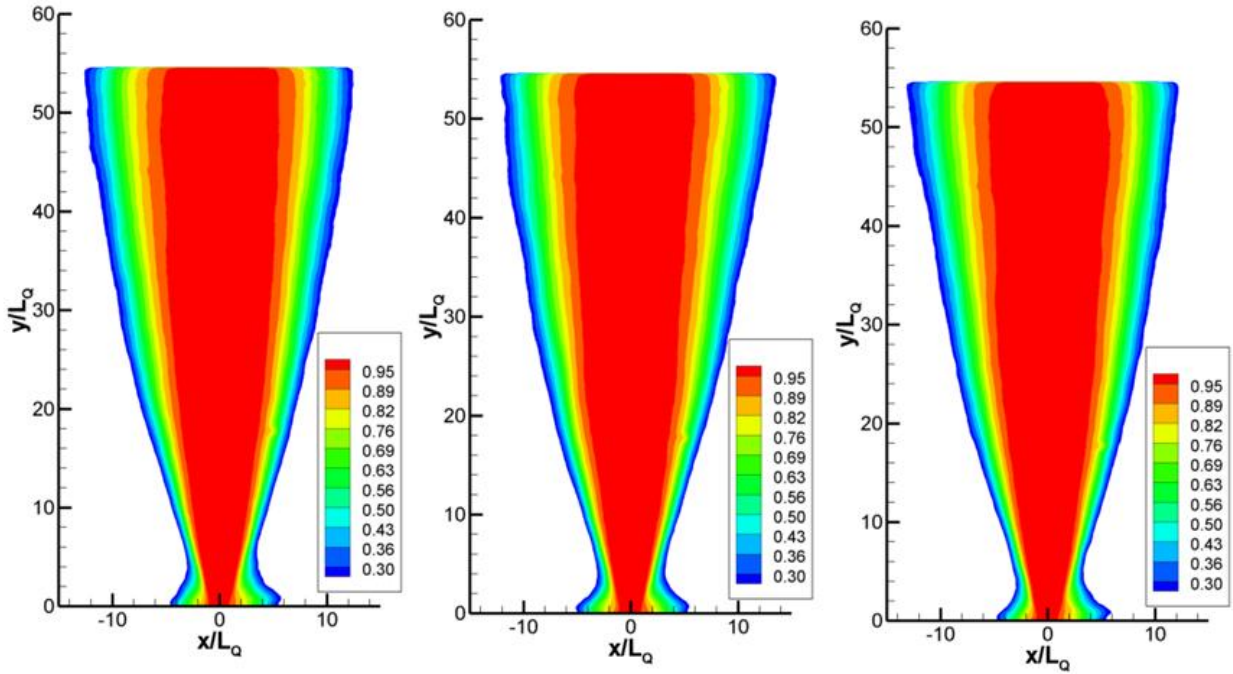


Figure 8.23. Mach 1.3 jet penetration trials: orifice attached jets only.

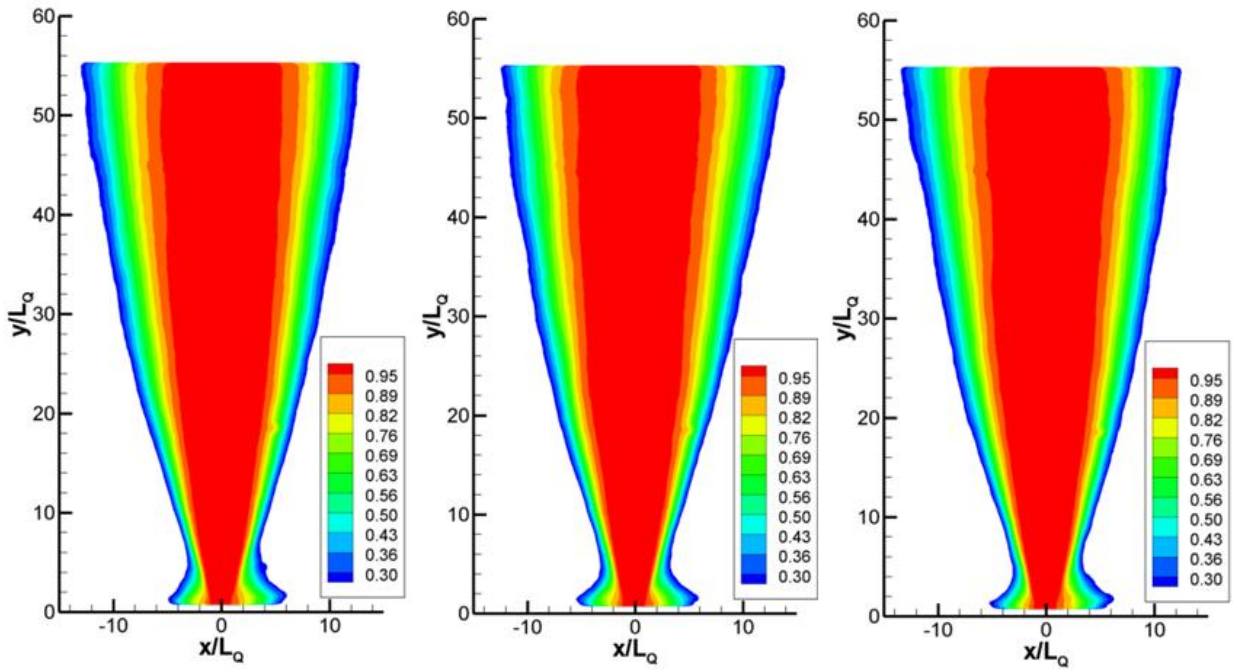


Figure 8.24. Mach 1.3 jet penetration trials: entire jet.

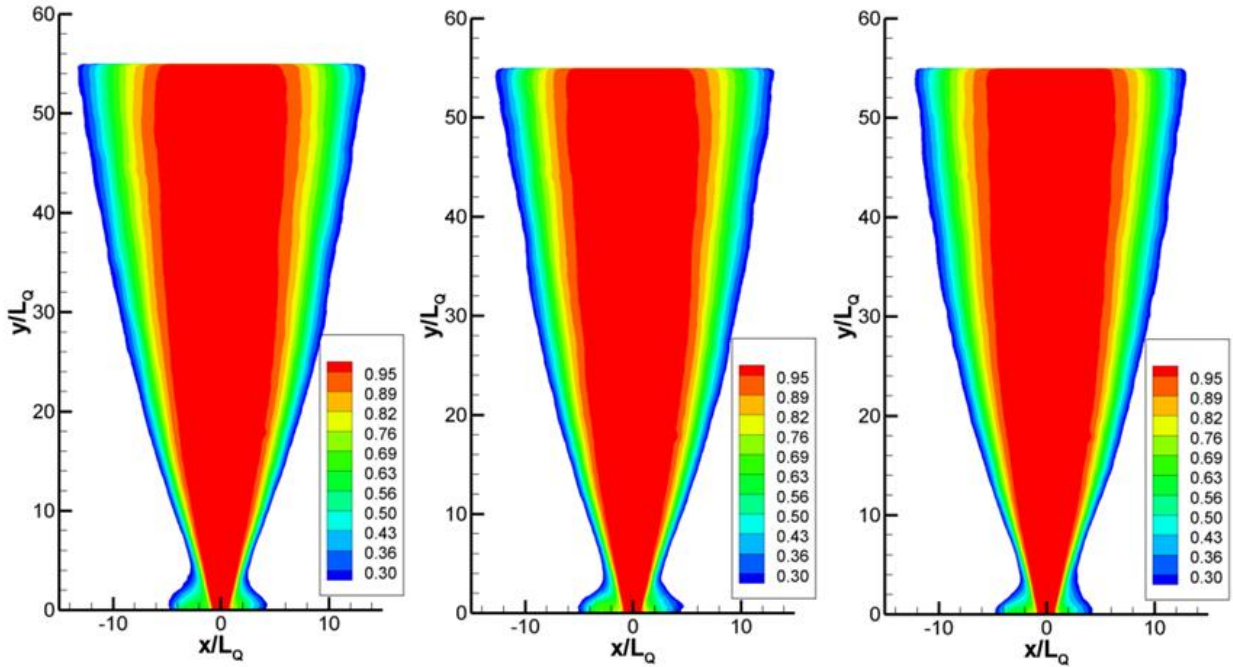


Figure 8.25. Mach 1.5 jet penetration trials: orifice attached jets only.

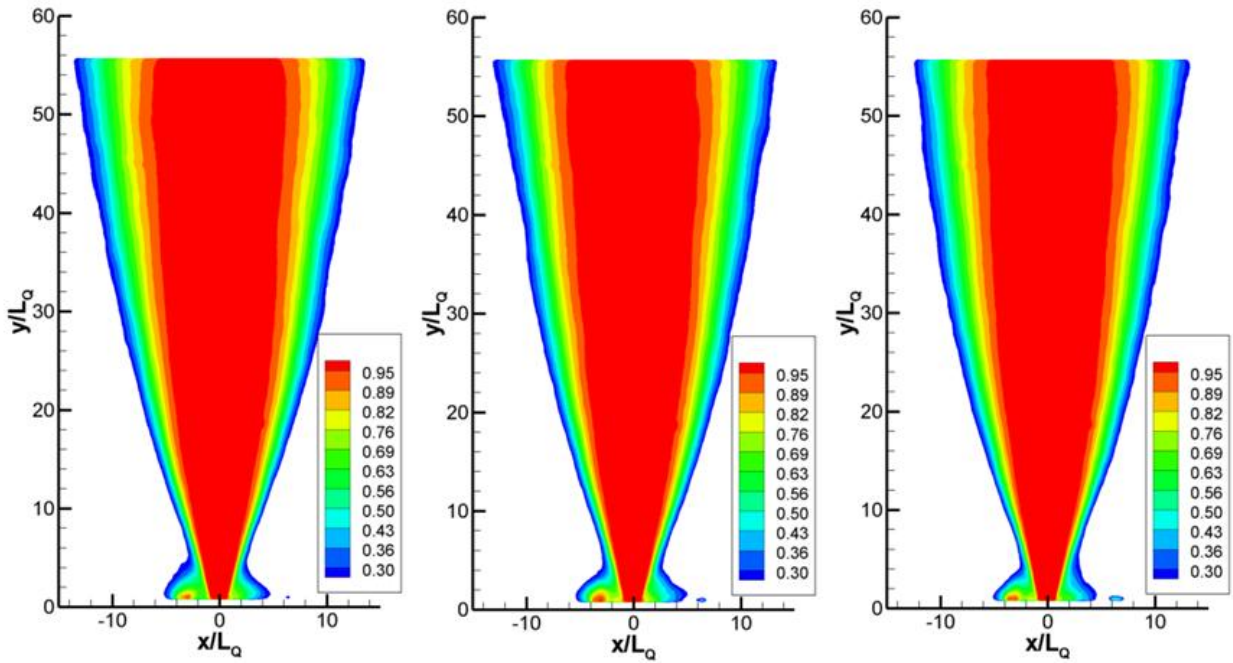


Figure 8.26. Mach 1.5 jet penetration trials: entire jet.

8.4 Rectangular Jets – Aspect Ratio 10

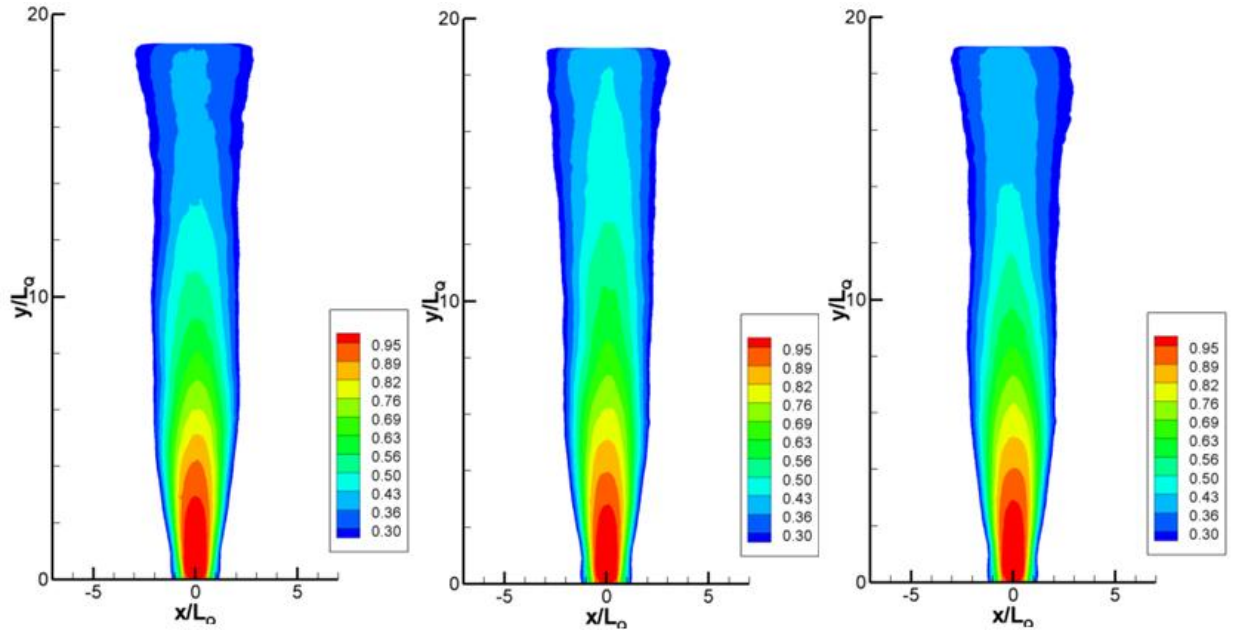


Figure 8.27. Mach 0.5 jet penetration trials: orifice attached jets only.

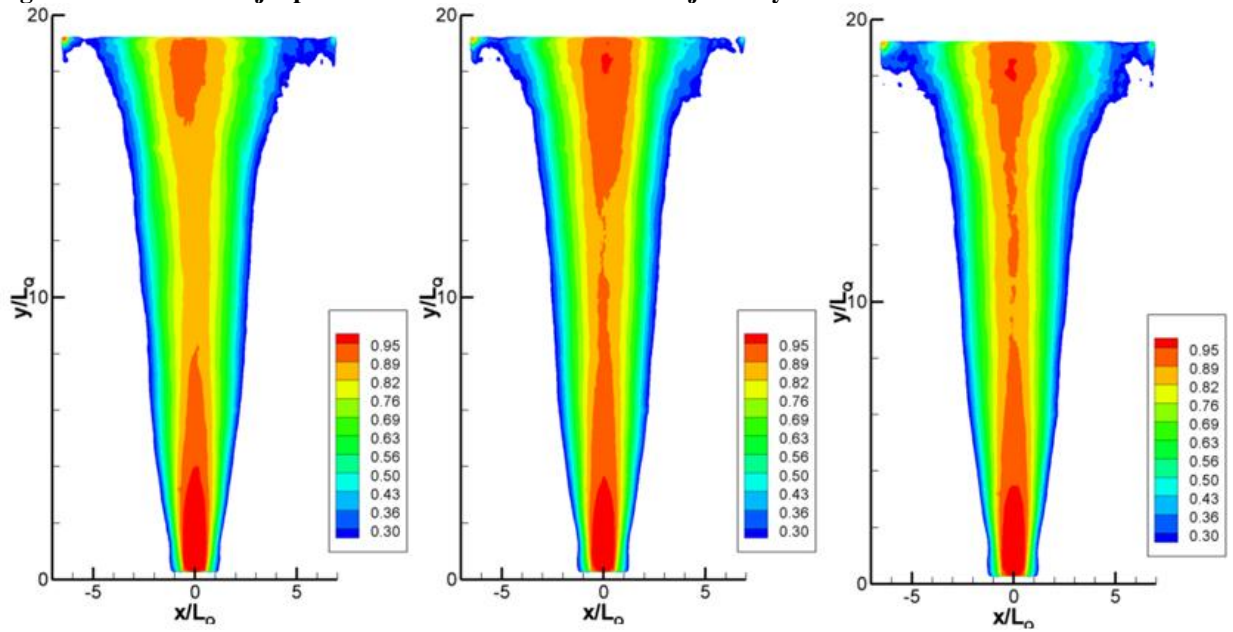


Figure 8.28. Mach 0.5 jet penetration trials: entire jet.

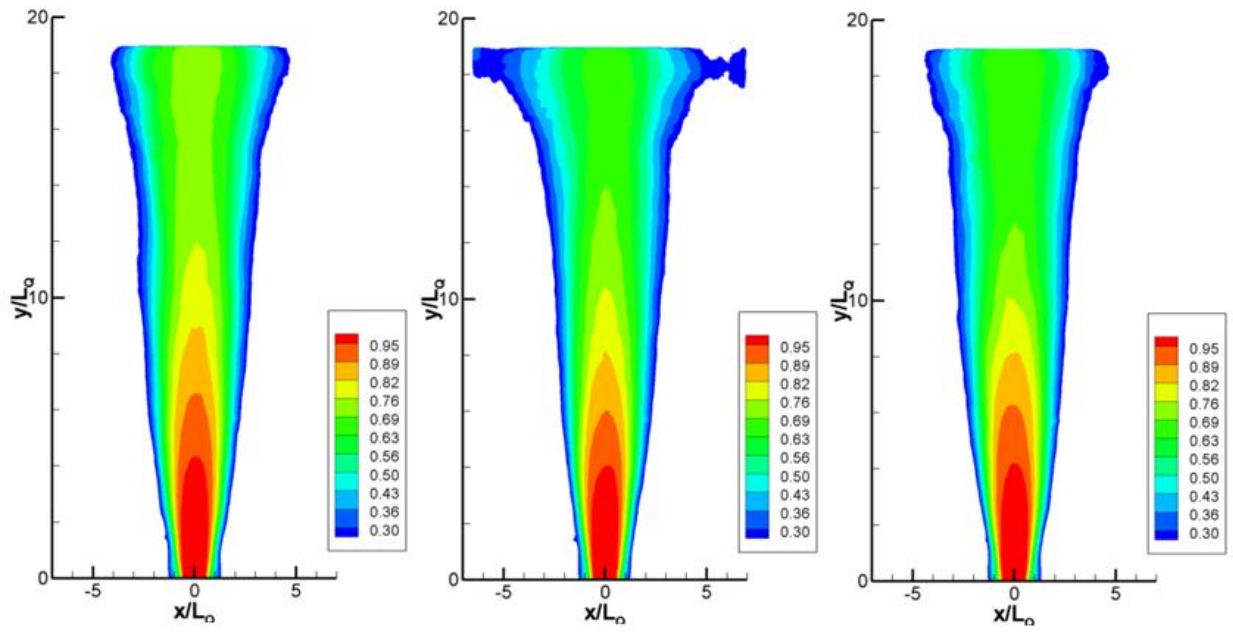


Figure 8.29 Mach 0.6 jet penetration trials: orifice attached jets only.

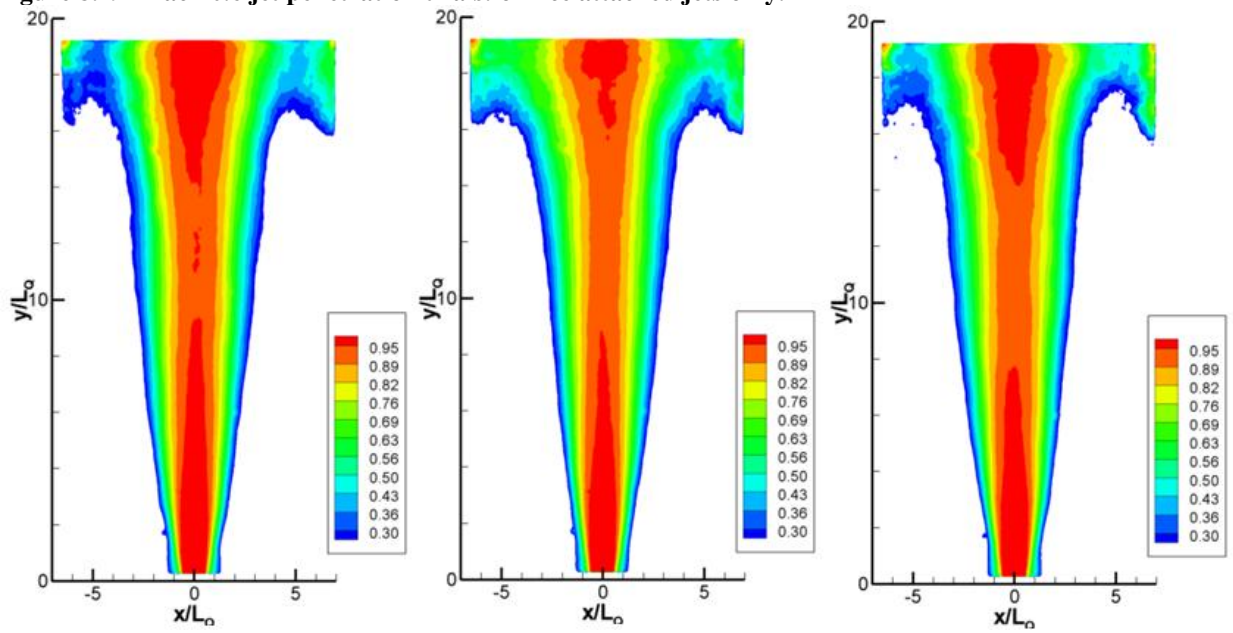


Figure 8.30. Mach 0.6 jet penetration trials: entire jet.

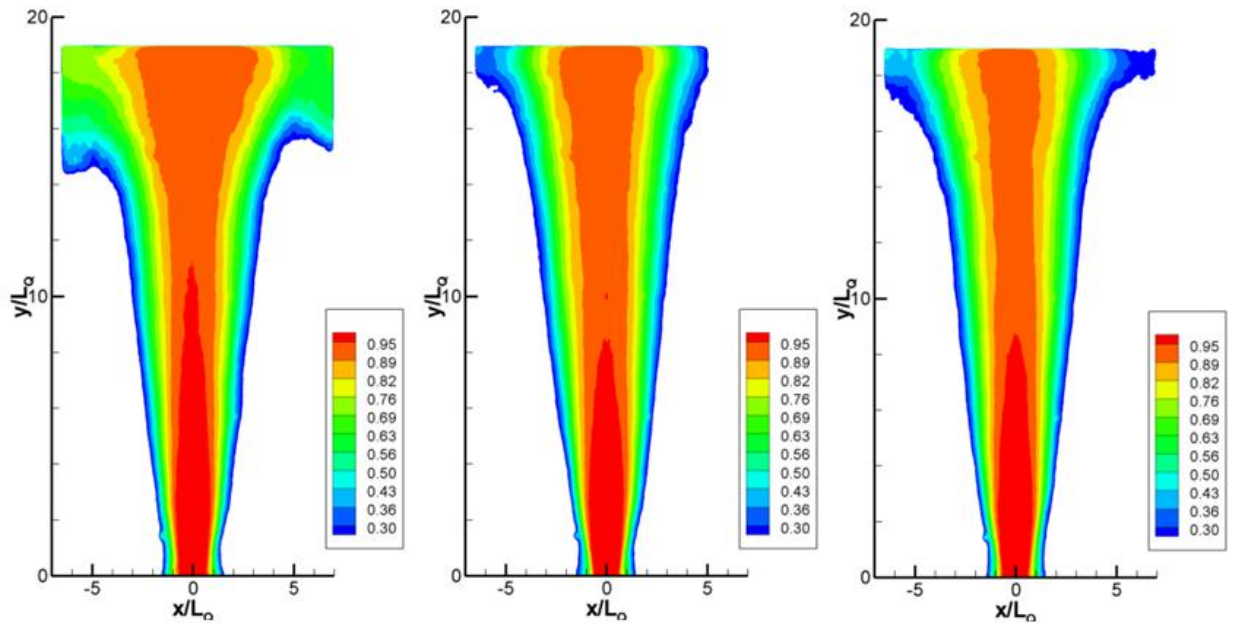


Figure 8.31. Mach 0.8 jet penetration trials: orifice attached jets only.

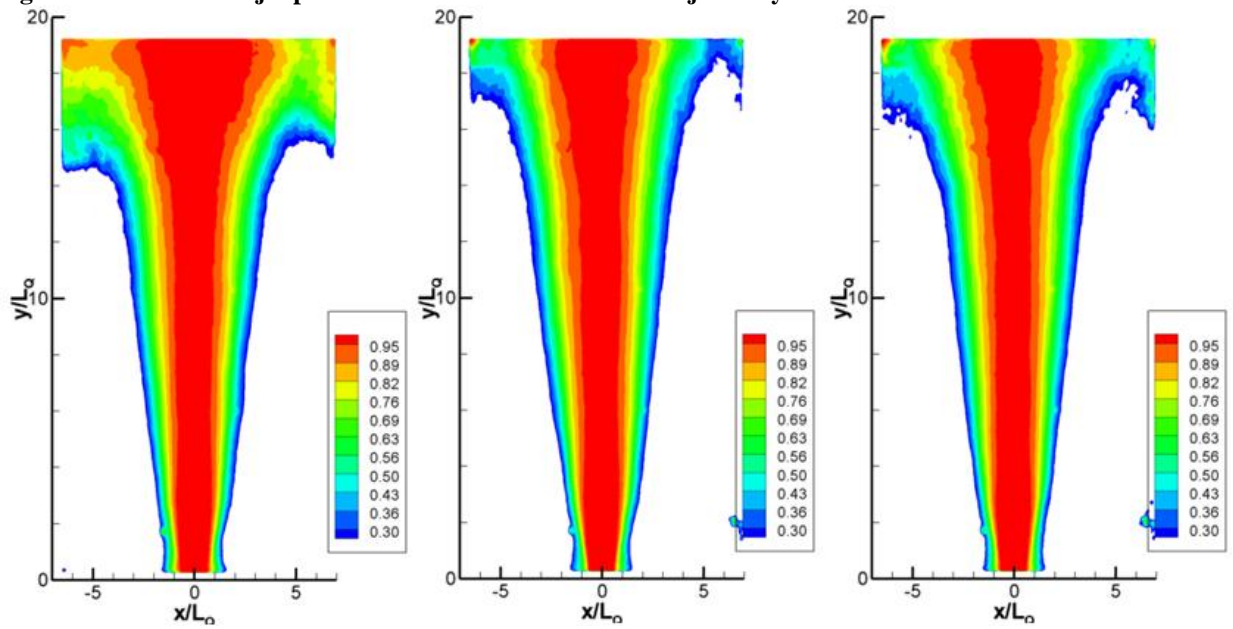


Figure 8.32. Mach 0.8 jet penetration trials: entire jet.

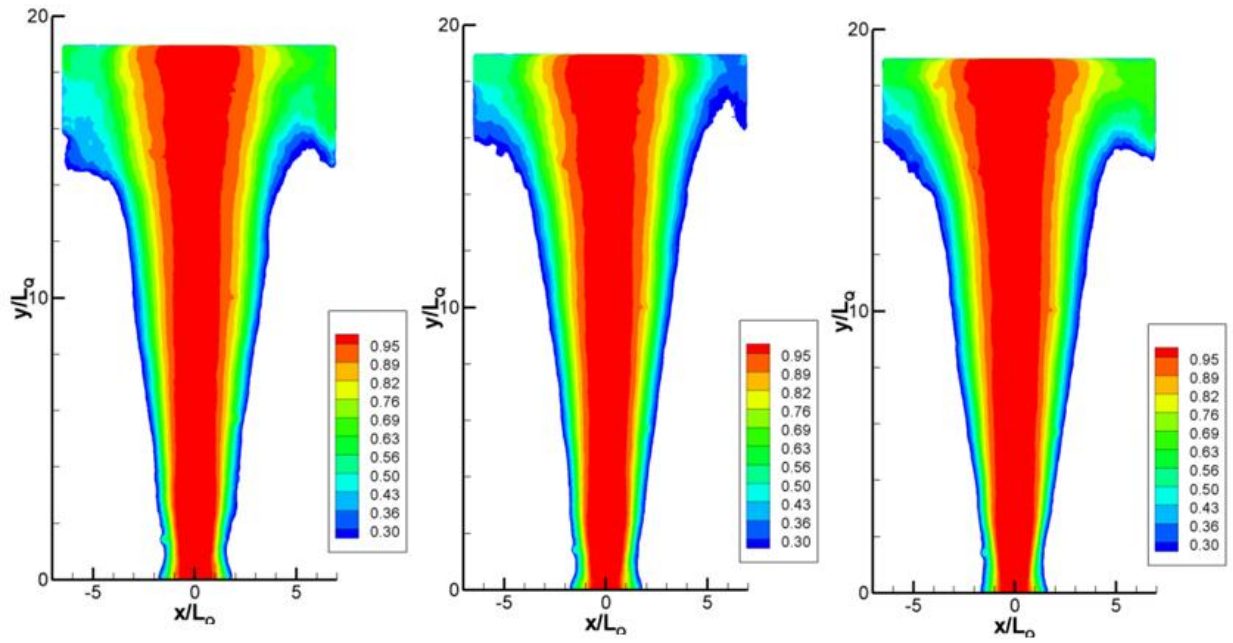


Figure 8.33. Mach 1.0 jet penetration trials: orifice attached jets only.

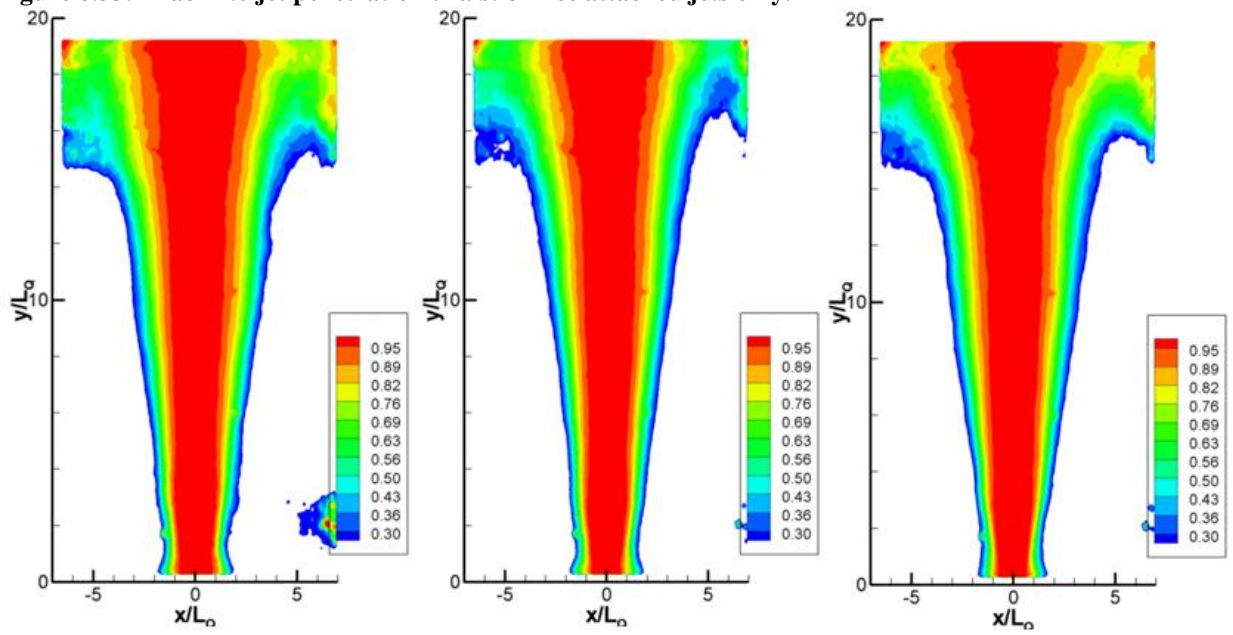


Figure 8.34. Mach 1.0 jet penetration trials: entire jet.

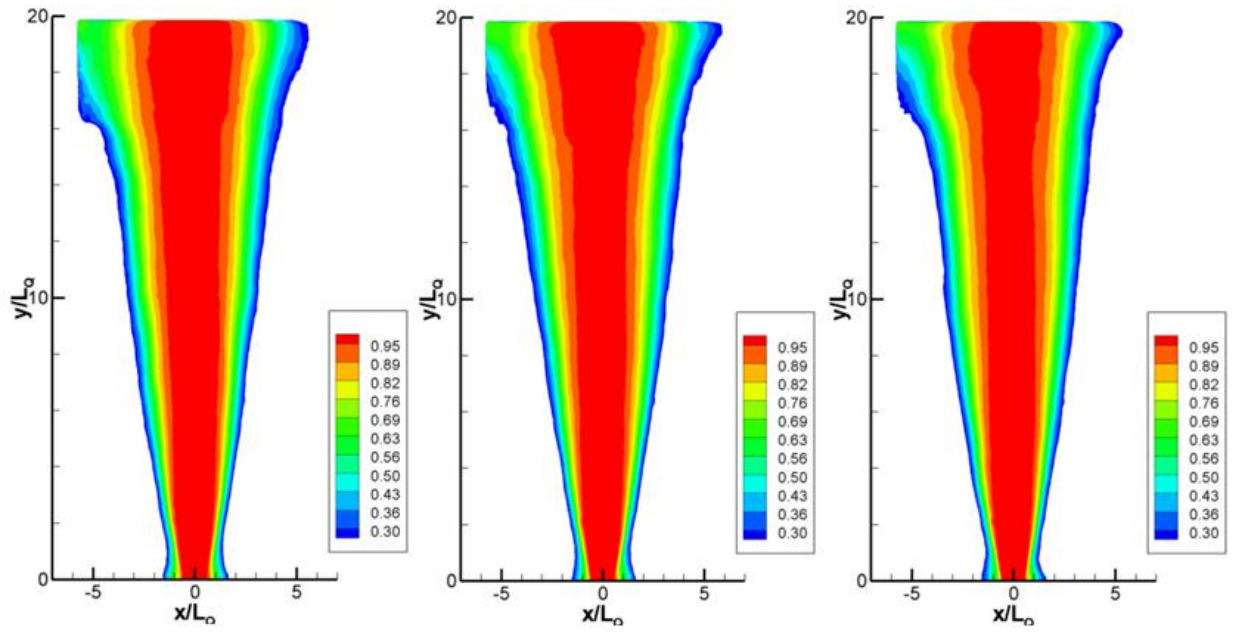


Figure 8.35. Mach 1.1 jet penetration trials: orifice attached jets only.

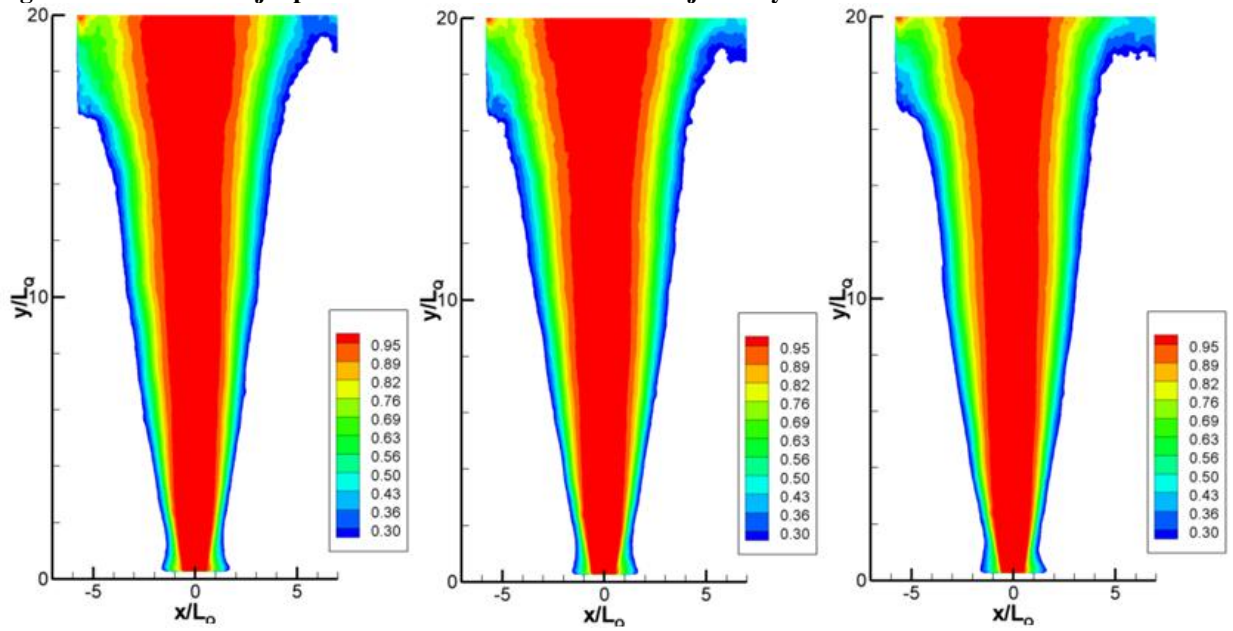


Figure 8.36. Mach 1.1 jet penetration trials: entire jet.

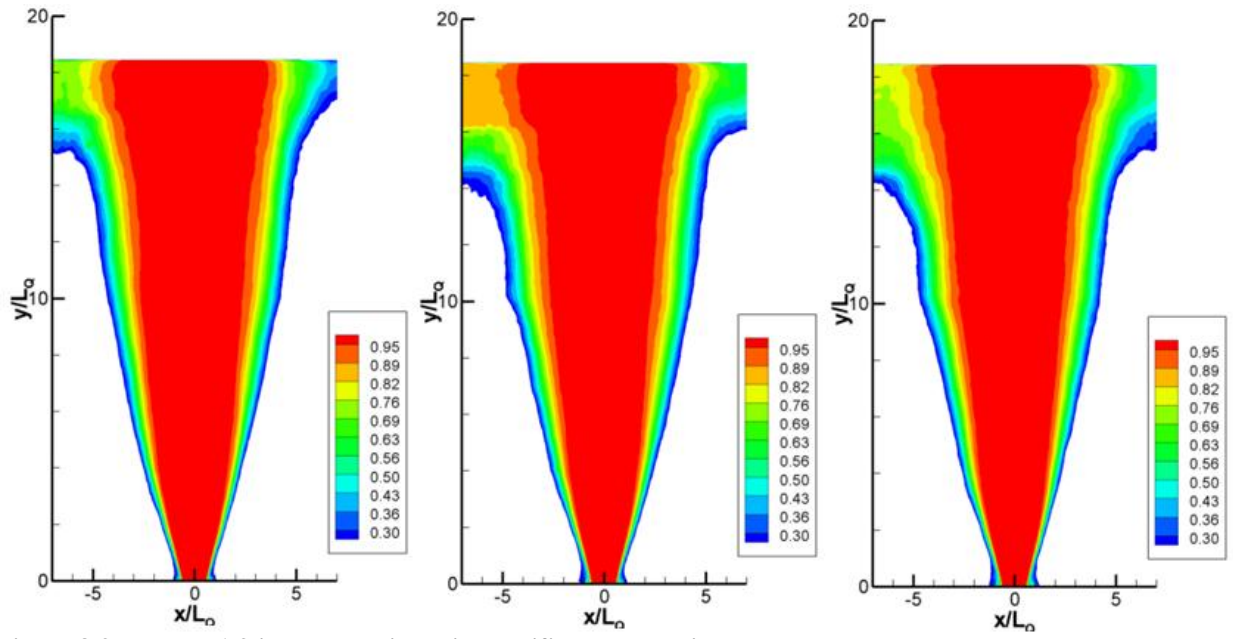


Figure 8.37. Mach 1.3 jet penetration trials: orifice attached jets only.

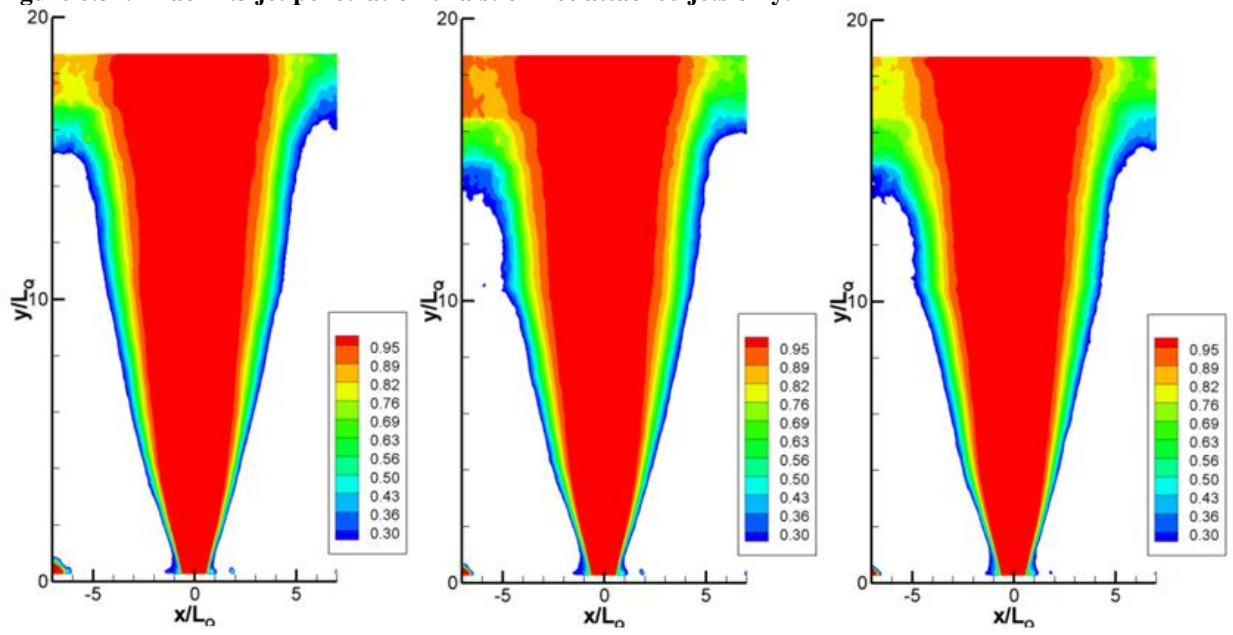


Figure 8.38. Mach 1.3 jet penetration trials: entire jet.

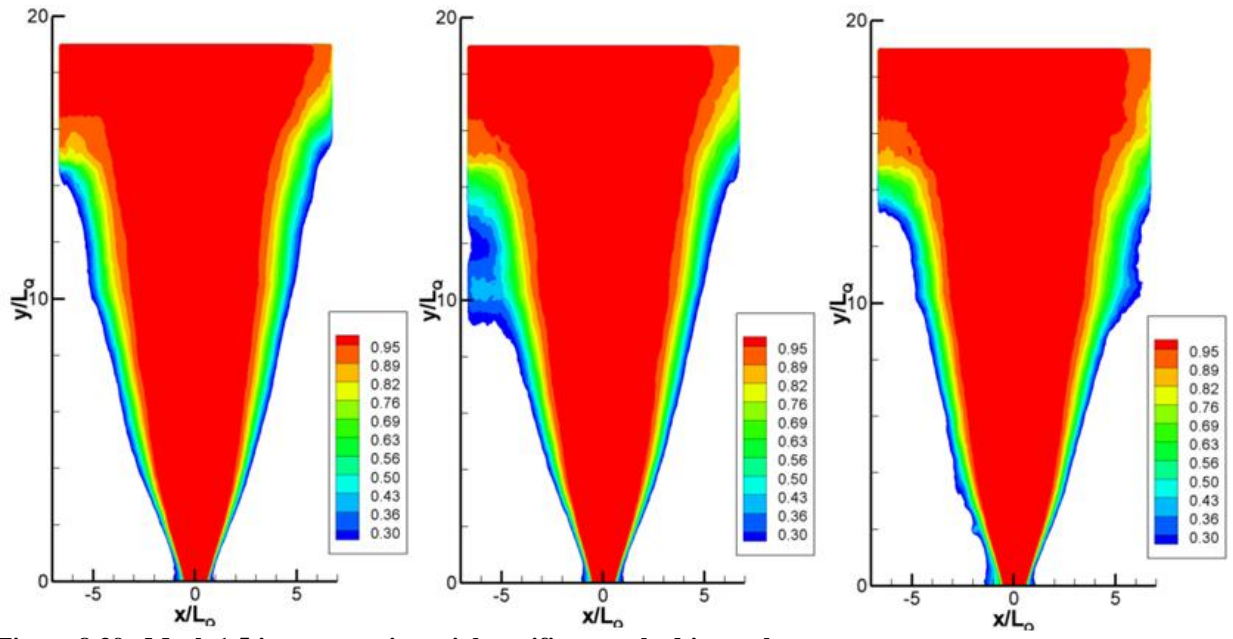


Figure 8.39. Mach 1.5 jet penetration trials: orifice attached jets only.

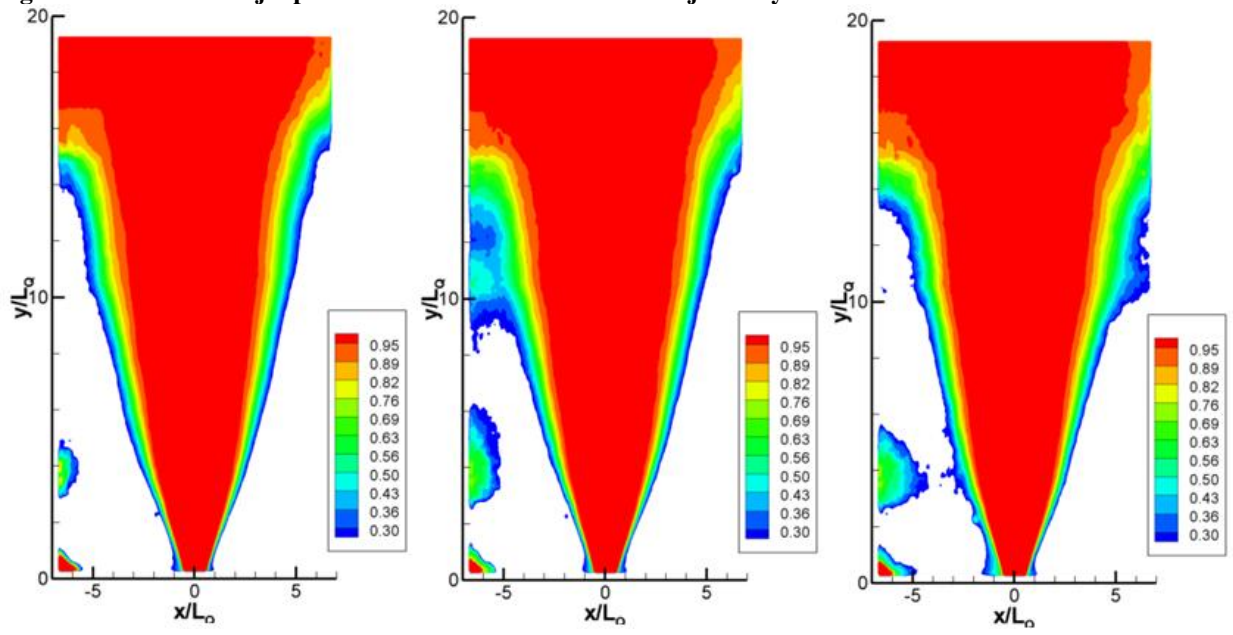


Figure 8.40. Mach 1.5 jet penetration trials: entire jet.

8.5 Rectangular Jets – Aspect Ratio 20

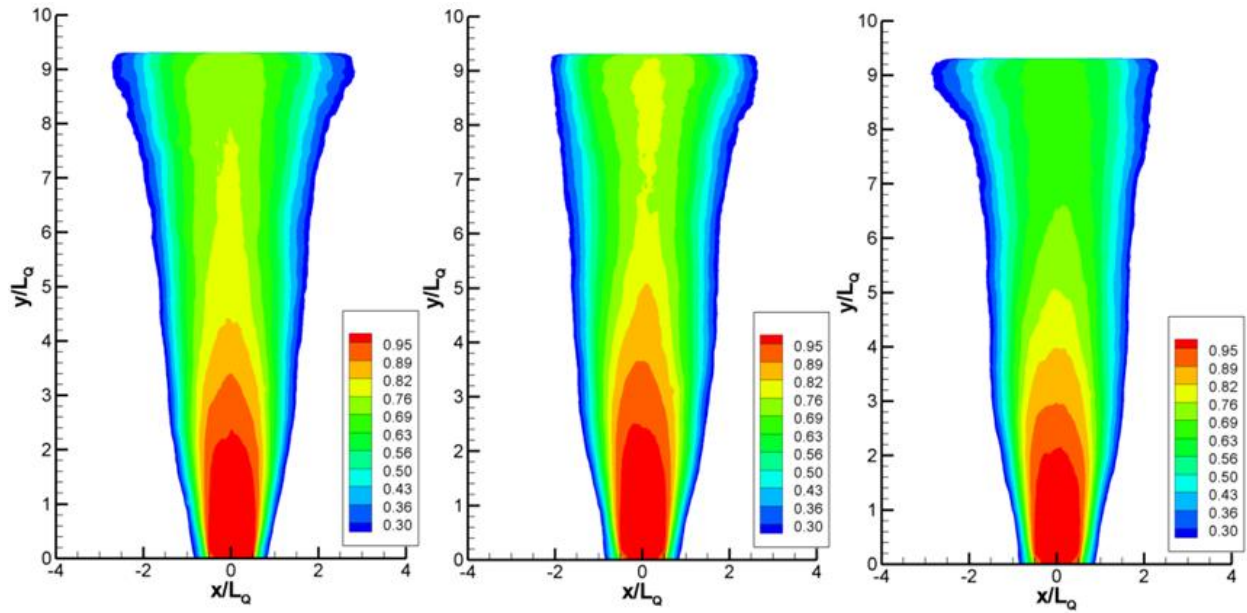


Figure 8.41. Mach 0.5 jet penetration trials: orifice attached jets only.

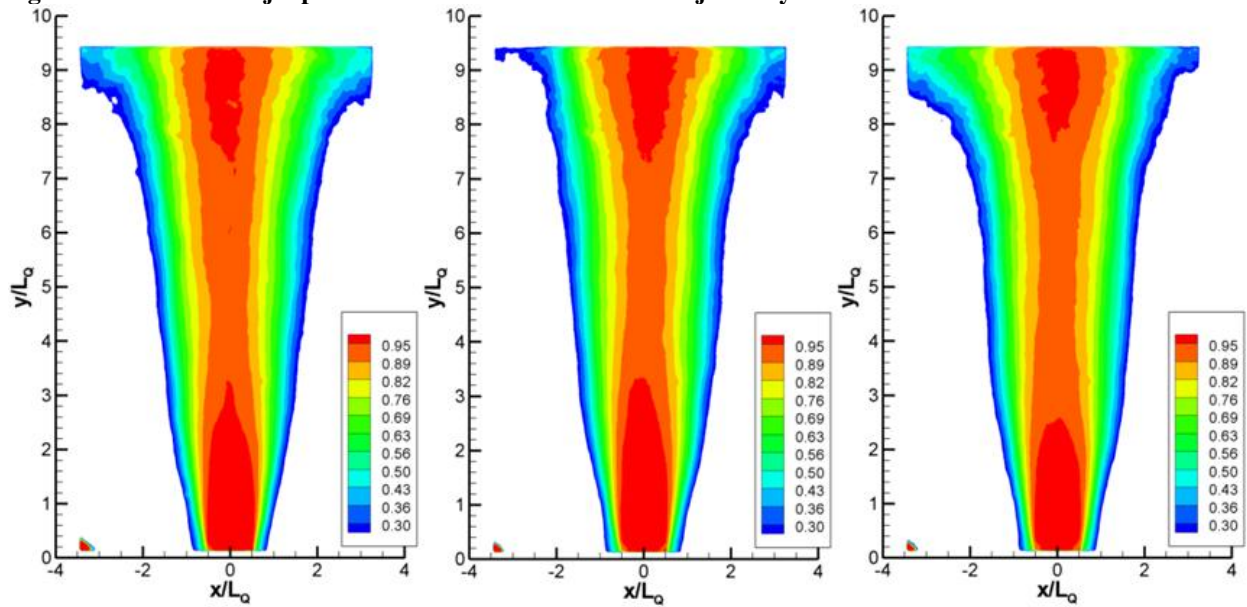


Figure 8.42. Mach 0.5 jet penetration trials: entire jet.

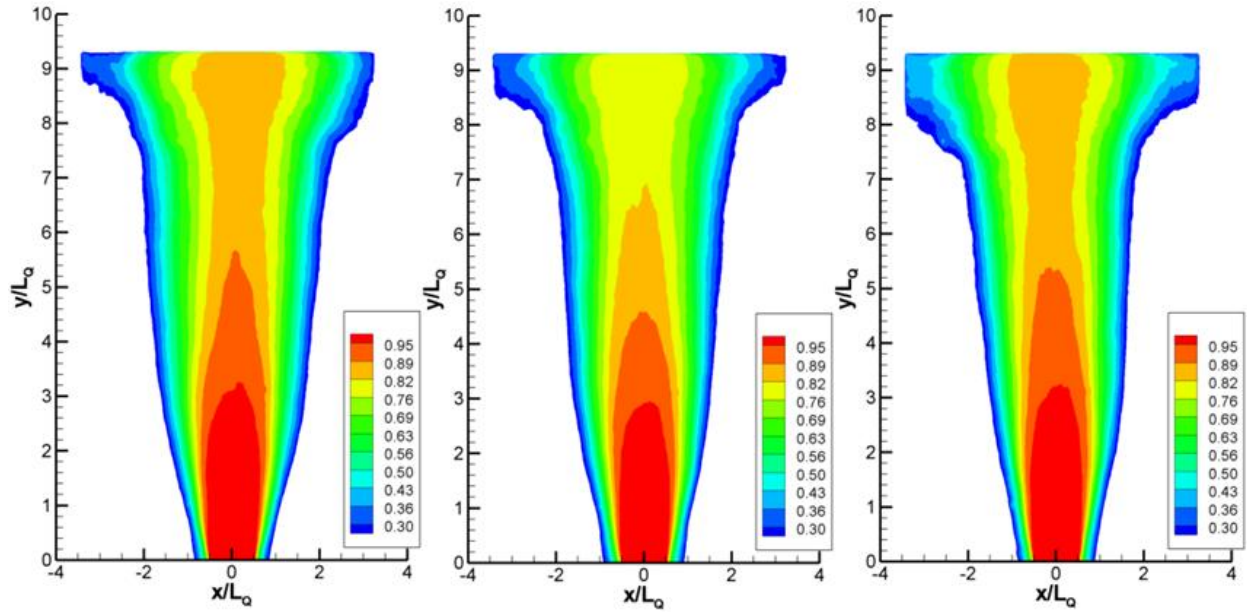


Figure 8.43 Mach 0.6 jet penetration trials: orifice attached jets only.

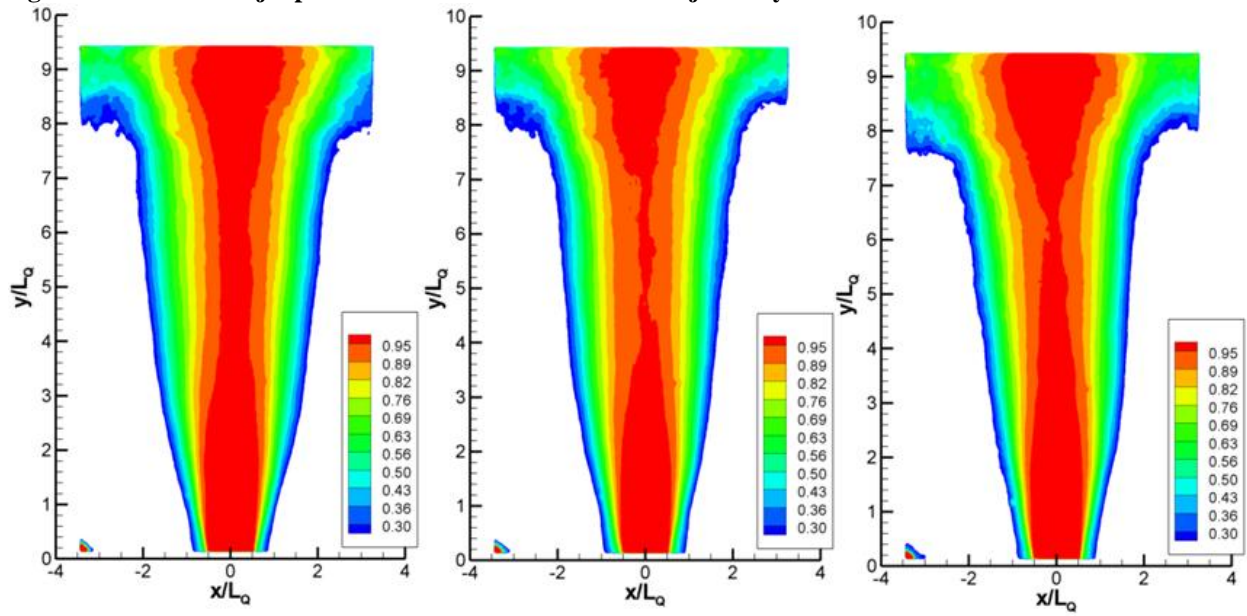


Figure 8.44. Mach 0.6 jet penetration trials: entire jet.

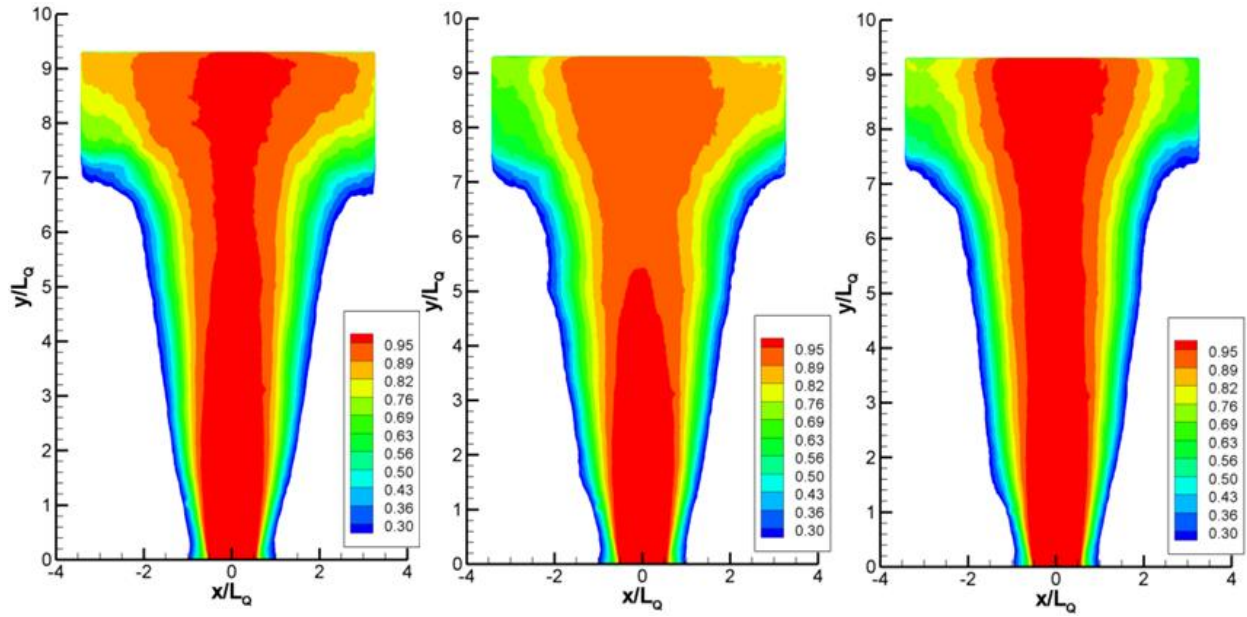


Figure 8.45. Mach 0.8 jet penetration trials: orifice attached jets only.

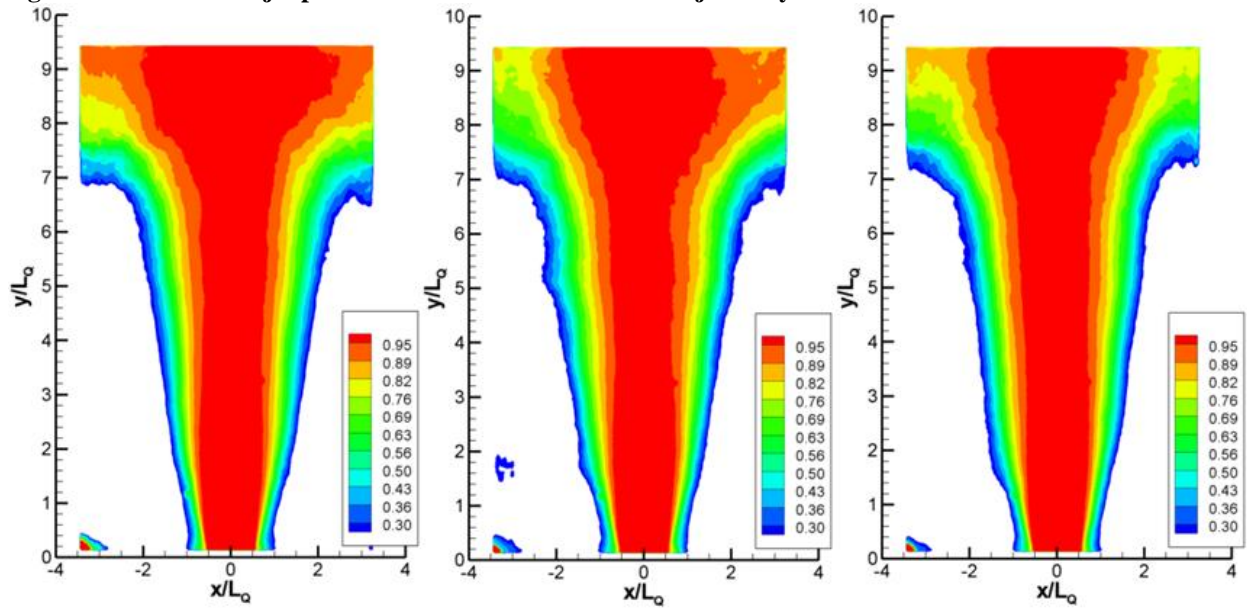


Figure 8.46. Mach 0.8 jet penetration trials: entire jet.

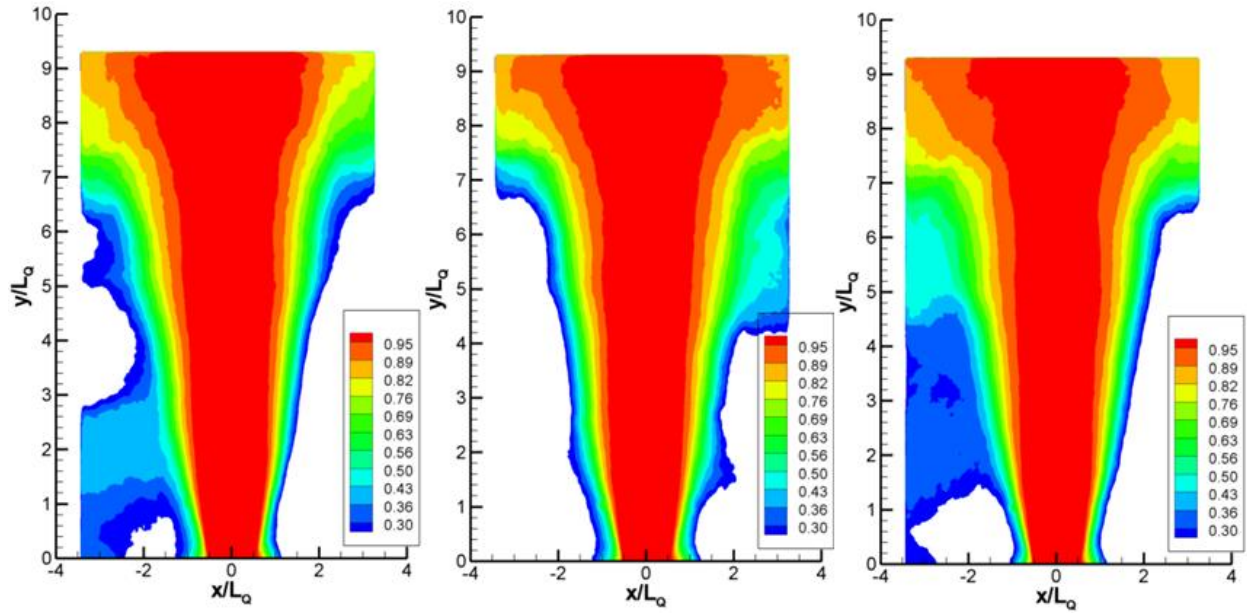


Figure 8.47. Mach 1.0 jet penetration trials: orifice attached jets only.

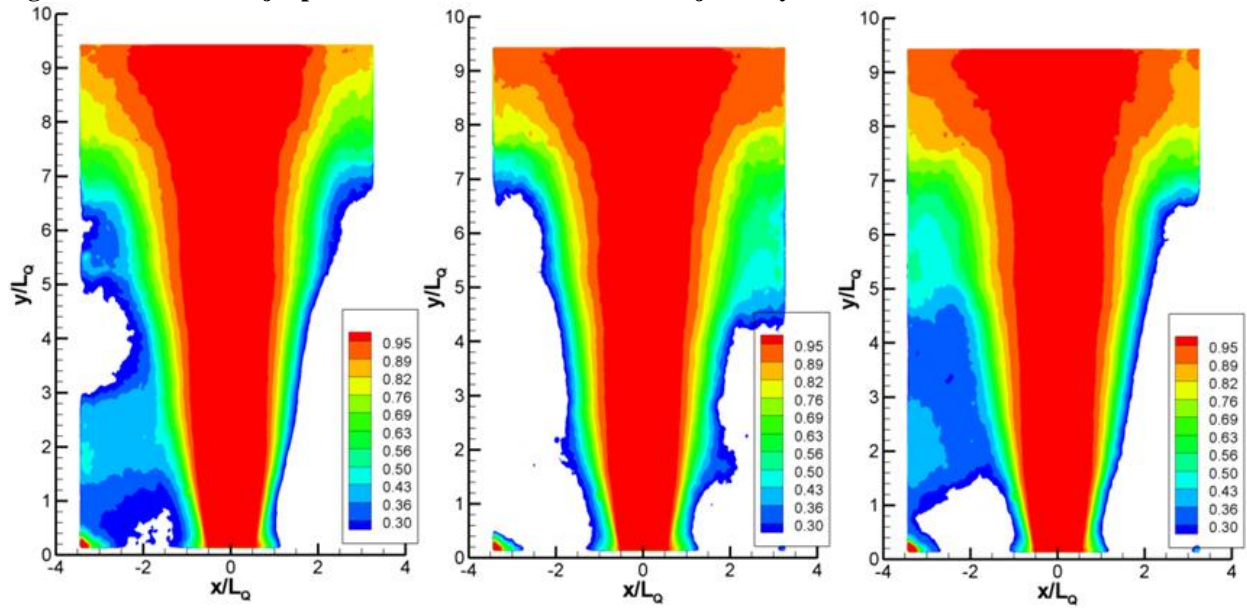


Figure 8.48. Mach 1.0 jet penetration trials: entire jet.

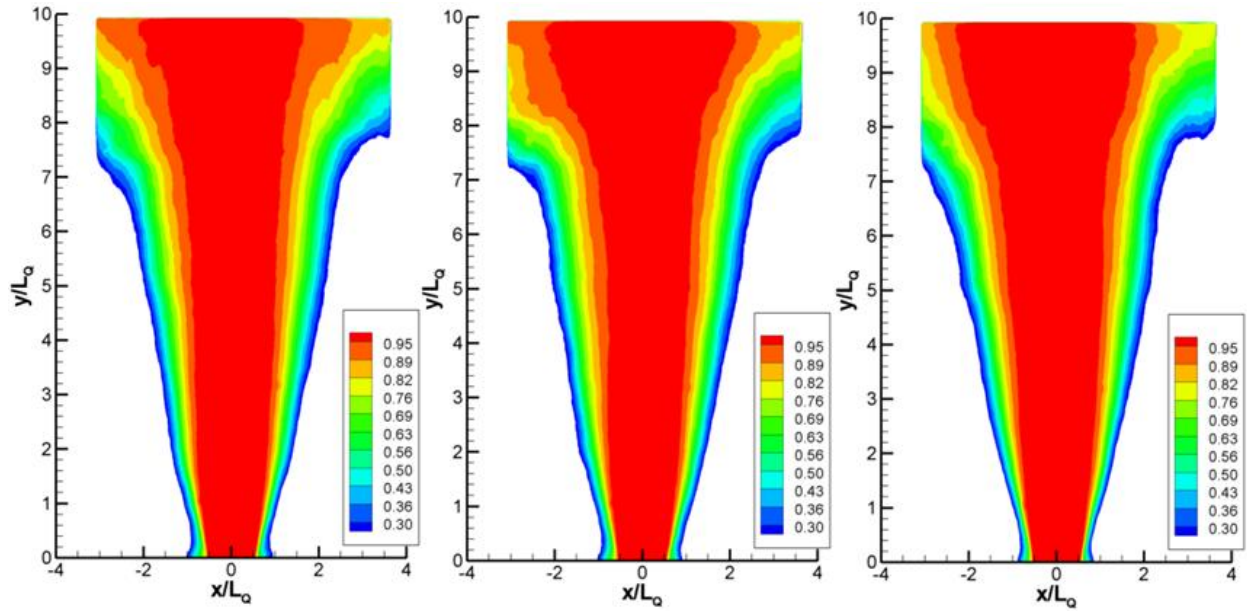


Figure 8.49. Mach 1.1 jet penetration trials: orifice attached jets only.

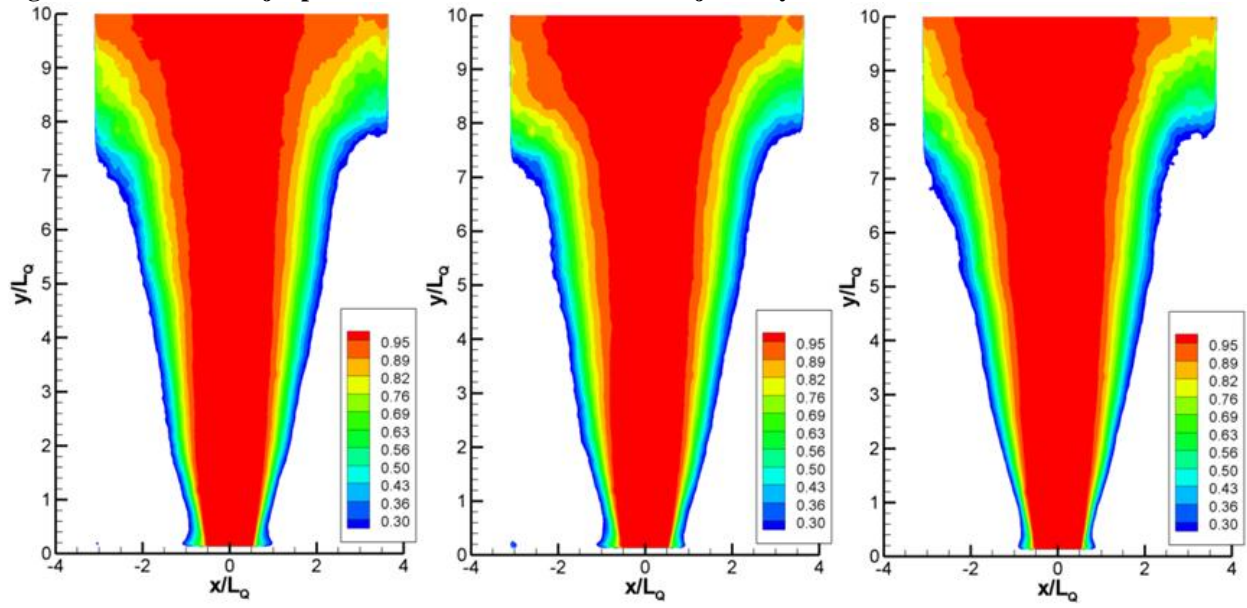


Figure 8.50. Mach 1.1 jet penetration trials: entire jet.

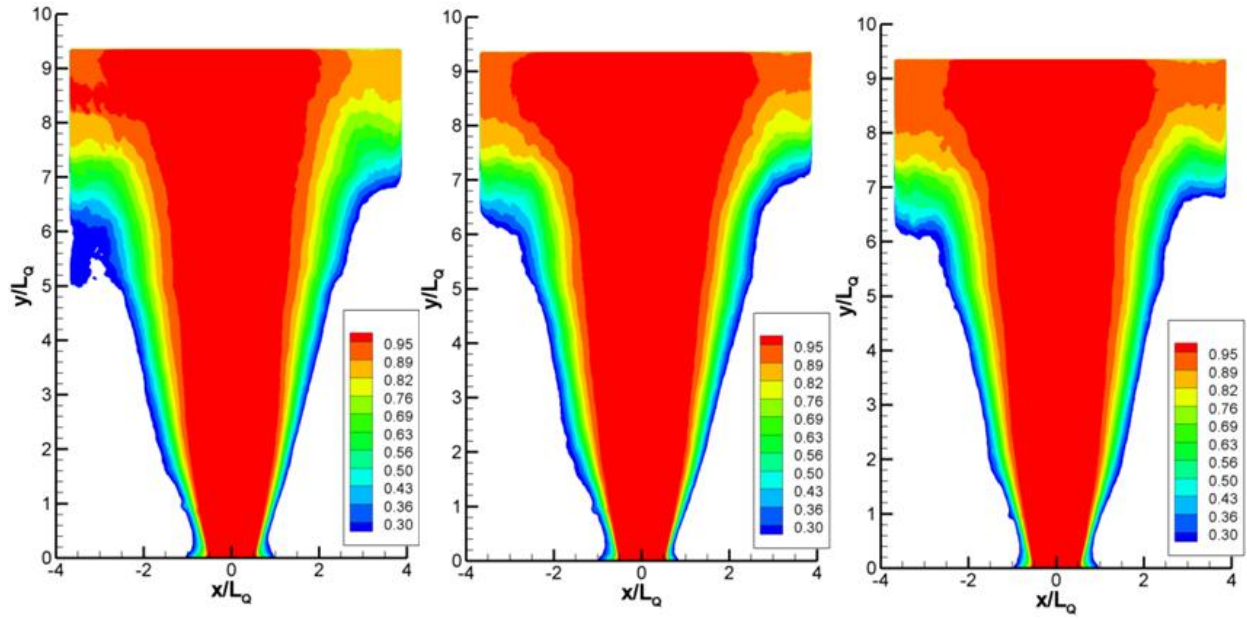


Figure 8.51. Mach 1.3 jet penetration trials: orifice attached jets only.

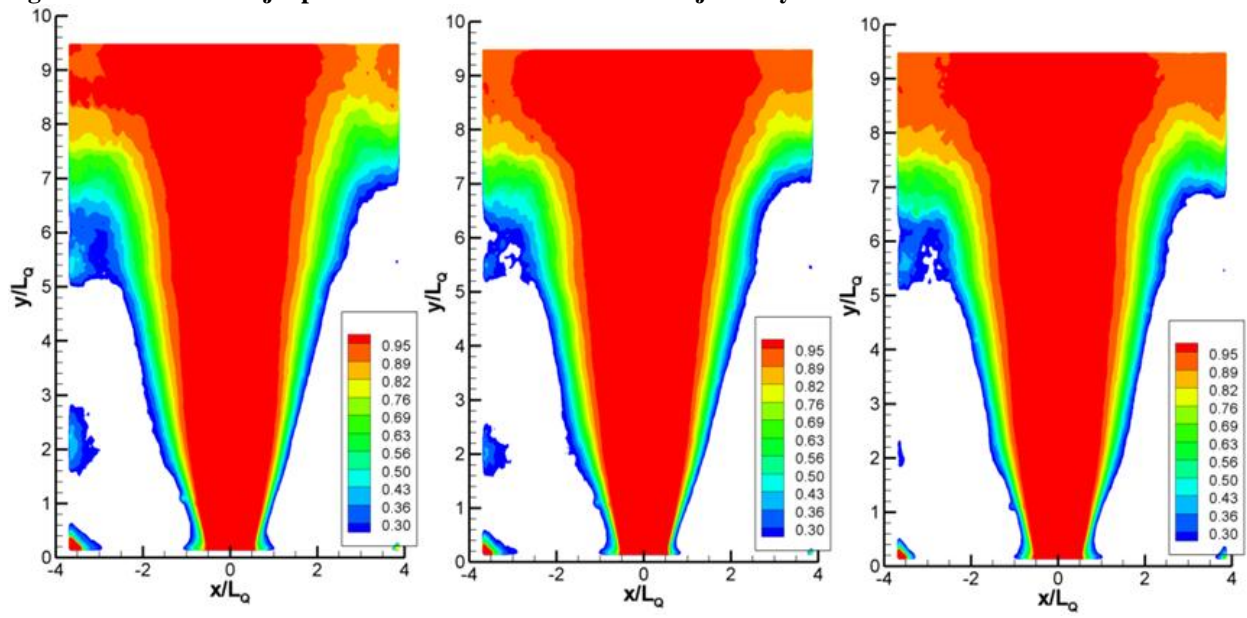


Figure 8.52. Mach 1.3 jet penetration trials: entire jet.

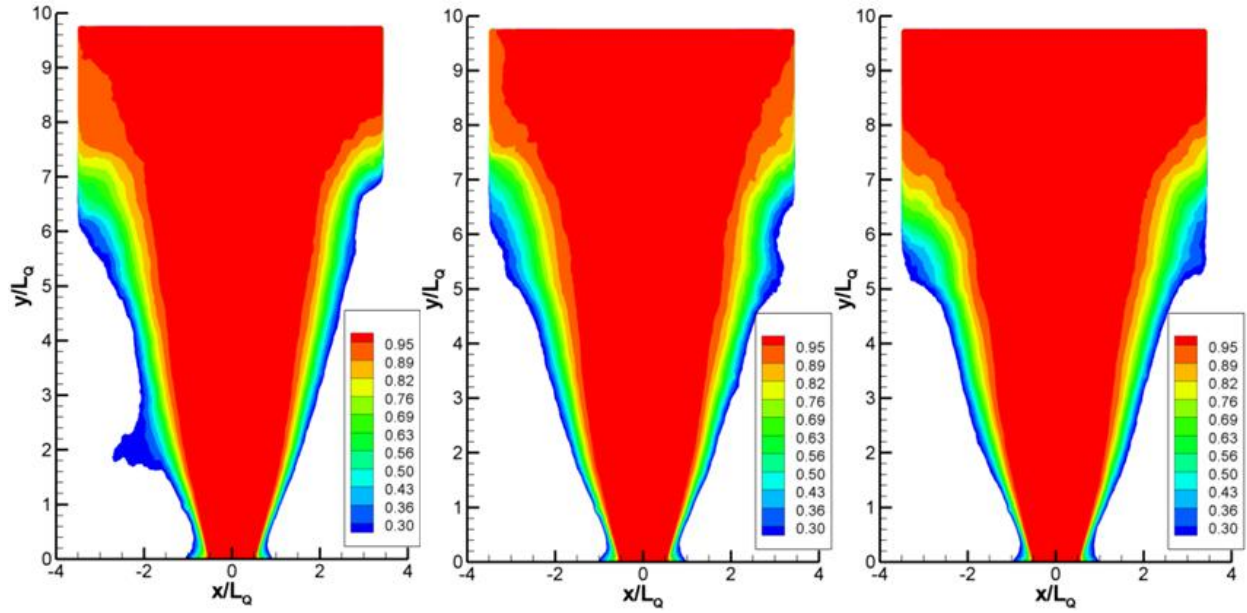


Figure 8.53. Mach 1.5 jet penetration trials: orifice attached jets only.

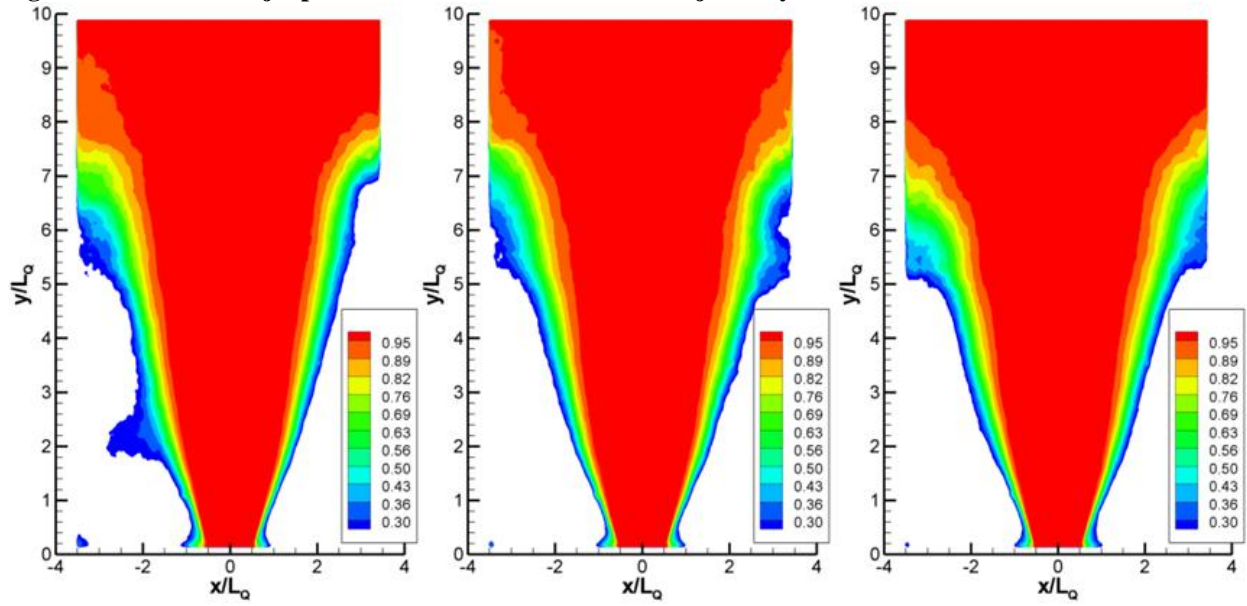


Figure 8.54. Mach 1.5 jet penetration trials: entire jet.